

Humboldt-Universität zu Berlin

D I S S E R T A T I O N

**Nanobionic Strategies for the
Implementation of Photosystem I into
Biohybrid Photoelectrodes**

Zur Erlangung des akademischen Grades

“Doctor rerum naturalium” (Dr. rer. nat.) in der Wissenschaftsdisziplin Biophysik

eingereicht an der Lebenswissenschaftlichen Fakultät

der Humboldt-Universität zu Berlin

von:

Dipl.-NanoSc. Kai Ralf Stieger

Präsidentin/Präsident

der Humboldt-Universität zu Berlin:

Prof. Dr.-Ing. Dr. Sabine Kunst

Dekanin/Dekan der Lebenswissenschaftlichen Fakultät

der Humboldt-Universität zu Berlin:

Prof. Dr. Bernhard Grimm

Gutachter/innen: 1. Prof. Dr. Fred Lisdat
 2. Prof. Dr. Holger Dobbek
 3. Prof. Dr. Frank Bier

Datum der mündlichen Prüfung: 23.06.2017

Zusammenfassung

In dieser Arbeit werden Strategien zur Entwicklung von biohybriden Photoelektroden, die Licht in elektrische Energie umwandeln, demonstriert und diskutiert. Der natürliche Photonen-transformierende Superkomplex der oxygenen Photosynthese aus *Thermosynechococcus elongatus*, das Photosystem I (PSI), kann durch die nicht-native Interaktion zum Redoxprotein Cytochrom *c* (Cyt *c*), erfolgreich funktional in Elektroden integriert werden. Hierfür wurden unterschiedliche Strategien entwickelt, z. B. bilden beide Biokomponenten unspezifische Komplexe in Lösung und assemblieren gemeinsam auf modifizierten Goldoberflächen. Aus der Kontaktierung des PSI mit einer thiol-modifizierten Goldelektrode *via* Cyt *c* ergeben sich unidirektionale kathodische Photoströme. DNA, als ein Polyelektrolytmatrixelement, kann zum Aufbau von 3D-Protein-Mehrschichtarchitekturen höherer Stabilität und Leistungsfähigkeit verwendet werden. Der Einsatz von mesoporösen Indium-Zinnoxid-Elektroden vergrößert die Photostromgenerierung um mehr als eine Größenordnung, wodurch sich hieraus skalierbare transparente Photobioelektroden mit hohen Quanteneffizienzen (bis zu 30%) erzeugen lassen.

Schlagwörter: Nanobionische Systeme, Biohybride, Protein-Protein Interaktionen, Photobioelektroden, Photostromgenerierung

Abstract

In this thesis, strategies are demonstrated and discussed for the development of biohybrid photoelectrodes transforming light into electrical energy. The natural photon-to-charge carrier converting super-complex from oxygenic photosynthesis of *Thermosynechococcus elongatus*, photosystem I (PSI), can be functionally implemented into such electrodes, due to the non-native interaction with the small redox protein cytochrome *c* (cyt *c*). Different strategies have been developed, e. g. both biocomponents form complexes in solution and self-assemble on modified gold-surfaces. The electrical connection of PSI to thiol-modified gold electrodes *via* cyt *c* results in unidirectional cathodic photocurrents of high efficiency. DNA, as a polyelectrolyte matrix element, can be used to build up 3D protein multilayer architectures of higher stability and performance. The use of mesoporous indium tin oxide electrodes further enhances the photocurrent generation more than one order of magnitude, thus resulting in scalable transparent photobioelectrodes of high quantum efficiencies (up to 30 %).

Keywords: Nanobionic Systems, Biohybrids, Protein-Protein Interaction, Photobioelectrode, Photocurrent generation

Table of Contents

Zusammenfassung.....	i
Abstract.....	i
Table of Contents	ii
List of Abbreviations.....	iv
1. Introduction	1
2. Objective of Thesis	2
3. Theoretical Background	3
3.1 Photosynthesis – a natural model	3
3.1.1 The photosynthetic electron transport (Z-Scheme)	5
3.1.2 Photosystem I – a biological semiconductor	9
3.1.2.1 Structure	9
3.1.2.2 Function	12
3.2 Protein electrochemistry – communicating with nature	14
3.2.1 Marcus theory	14
3.2.2 Cytochrome <i>c</i> – the versatile redox protein.....	17
3.2.2.1 Structure	17
3.2.2.2 Function	18
3.2.2.3 Electrochemistry	19
3.2.3 Strategies for the electrical coupling of proteins to electrodes....	22
3.3 Photobioelectrodes: design, construction and assembly	24
3.3.1 PSI on gold: strategies for immobilization and DET	26
3.3.2 Wired / mediated electron transfer of PSI with electrodes	27
3.3.3 Photosystem I on other conductive materials	28
3.3.4 Photobiovoltaic and photobioenzymatic systems.....	28
4. Results.....	31
4.1 Advanced unidirectional photocurrent generation <i>via</i> cytochrome <i>c</i> as reaction partner for directed assembly of photosystem I	31
4.2 Engineering of supramolecular photoactive protein architectures: Defined co-assembly of photosystem I and cytochrome <i>c</i> using a nanoscaled DNA-matrix.....	48
4.3 Biohybrid architectures for efficient light-to-current conversion based on photosystem I within scalable 3D mesoporous electrodes	79

5. Discussion	102
5.1 The interaction and communication between cytochrome <i>c</i> and photosystem I.....	102
5.2 Photobioelectrode performance and efficiency	108
5.3 Advantages and drawbacks of the cytochrome <i>c</i> / photosystem I photobioelectrodes.....	115
6. Outlook and Future Perspectives.....	120
7. Summary	122
8. References.....	125
Danksagung.....	141
Ehrenwörtliche Erklärung	143

List of Abbreviations

α	Charge transfer coefficient
μITO	Mesoporous indium tin oxide
2D	Two-dimensional
3D	Three-dimensional
A_0	Modified chlorophyll A_0
A_1	Phylloquinone A_1
ADP	Adenosine diphosphate
AFM	Atomic force microscopy
APTES	(3-Aminopropyl)triethoxysilane
ATO	Antimony tin oxide
ATP	Adenosine triphosphate
ATPase	ATP synthase
bRC	Bacterial reaction centre
Chl <i>a</i>	Chlorophyll <i>a</i>
CNT	Carbon nanotube
CV	Cyclic voltammetry
cyt b_6/f	Cytochrome b_6/f
cyt <i>c</i>	Cytochrome <i>c</i>
cyt c_6	Cytochrome c_6
DET	Direct electron transfer
DNA	Deoxyribonucleic acid
EQE	External quantum efficiency
ESI	Electronic supporting information
ET	Electron transfer
ETC	Electron transfer chain
Fdx	Ferredoxin
FET	Field effect transistor
FNR	Ferredoxin-NADP ⁺ -reductase
FRET	Förster resonance energy transfer
FTO	Fluorine doped tin oxide
F_x, F_A, F_B	Fe_4S_4 cluster X, A, B
GNP	Gold nanoparticle
IET	Intramolecular electron transfer

IMM	Inner mitochondrial membrane
I_p	Photocurrent density
IQE	Internal quantum efficiency
ISP	Iron sulfur protein
ITO	Indium tin oxide
ITO _{NP}	Indium tin oxide nanoparticles
J_{\max}	Maximum photocurrent
k_{ET}	Electron transfer rate
k_{ex}	Homogeneous electron transfer constant
K_M	Michaelis-Menten constant
k_s	Heterogeneous electron transfer constant
LB	Latex beads
LED	Light emitting diode
LHC	Light harvesting complex
M^+	Electron acceptor
MALDI-TOF	Matrix-assisted laser desorption/ionization - time of flight
MES	2-(<i>N</i> -morpholino)ethanesulfonic acid
ML	Monolayer
MU	Mercaptoundecanol
MUA	Mercaptoundecanoic acid
MV / MV ²⁺	Methyl viologen
NADP ⁺ /NADPH	Nicotinamide adenine dinucleotide phosphate
n_e	Number of carriers
NMR	Nuclear magnetic resonance
NP	Nanoparticle
n_p	Number of photons
NTA	Nitrilotriacetic acid
OCP	Open-circuit potential
OEC	Oxygen evolving complex
P_{700} / P_{700}^+	Luminal pigment dimer, chlorophyll <i>a</i> /chlorophyll <i>a'</i>
PASA	Sulfonated polyaniline
PC	Plastocyanin
PDB	Protein data bank
PET	Photosynthetic electron transport

Pheo	Pheophytin
pI	Isoelectric point
PO	Photosynthetic organisms
PQ	Plastoquinone
PQH2	Plastoquinol
PsaA - X	Protein subunit A - X of photosystem I
PSI	Photosystem I
PSII	Photosystem II
Q _A	Plastoquinone A
Q _B	Plastoquinone B
QE	Quantum efficiency
QI	Quantitative imaging
RC	Reaction centre
RC-LH1	Reaction-centre light harvesting-1 complex
ROS	Reactive oxygen species
rps	Revolutions per second
RT	Room temperature
SAM	Self-assembled monolayer
SEM	Scanning electron microscopy
SHE	Standard hydrogen electrode
SPR	Surface plasmon resonance
β-DM	β-dodecyl maltoside
<i>T. elongatus</i>	<i>Thermosynechococcus elongatus</i>
tBID	Cytosolic truncated protein BID
TCO	Transparent conducting oxide
T _e	Turnover number
Tris	Tris(hydroxymethyl)aminomethane
UV/Vis	Ultraviolet / Visible
ν	Scan rate
V _{oc}	Open-circuit voltage
W _{0.5}	Half peak width

1. Introduction

In the last 10,000 years, the evolution of mankind is basically driven by the exploitation of technologies leading towards a social, cultural and economical development. These innovations brought us to higher standards of living as well as a tremendous amount of knowledge. In spite of these achievements the elevation of societies is directly coupled to the opportunity of energy utilization and with this, the need to explore new kinds of energy resources. In this era, the main energy resource at present, fossil fuels, is finally getting depleted. The upcoming scarcity of them may even raise more political and economical crises. On the other side the current increasing utilization and dependency upon fossil fuels causes the climate to change, the rainforest to be destroyed and the environment to be polluted. A reasonable consequence on account of this negative prospect is the strong necessity of alternative concepts to harness energy in a sustainable and renewable fashion. One option is to make use of the abundant solar energy provided by our sun, which has the potential to power the entire humanity. In one hour the sun provides the earth with more energy as humanity uses in one year.¹

Along with efforts to produce photovoltaic devices (e.g. silicon solar cells), artificial photosynthesis, a new emerging field, has been introduced to research based on a better understanding of the natural phototrophic organisms, such as plants and cyanobacteria, converting solar energy, carbon dioxide and water to carbohydrates and oxygen. This biological machinery, mainly known as photosynthesis, provides us with the needed tools, concepts and components for the invention of a bio-based, sustainable and renewable economy. One first step has already been done by the elucidation of the basic processes in photosynthesis on a molecular level. The principles and properties in the main reaction of light absorption in phototrophic organisms have been addressed, and the tasks of specific proteins have been identified. Another important field of research has been emerged over the past 20 years, studying the connection of proteins with man-made technology. Protein electrochemistry allows us to communicate with the molecular machinery of nature, having the opportunity to combine advantages from artificial and natural processes to construct biohybrid devices. By using the successes in photosynthesis, protein electrochemistry and nanotechnology, we may finally be able to produce reasonable biohybrid semi-artificial systems, which utilize solar energy for the conversion into electrical energy, or for the production of energy-rich chemicals.

2. Objective of Thesis

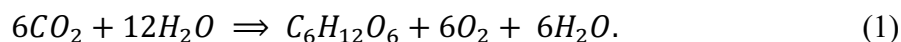
This thesis aims for the construction of a biohybrid electrode for the efficient conversion of light to electrical energy. For this purpose one key component from photosynthesis, the photosystem I (PSI), will be used as a natural light absorbing protein super-complex to harness solar energy for the conversion into an electrical current flow. To make use of such an electrode, the electrical connection as well as the surface immobilization of this super-complex has to be achieved. Hence, the novel idea is to use a small redox protein, cytochrome *c* (cyt *c*) for the connection and assembly of PSI to an inorganic electrode material. From this, the main development and optimization steps for the construction of such a system can be divided into the following groups:

1. Exploration of the electrical coupling and assembly conditions of cyt *c* and PSI on the electrode and their molecular interaction,
2. Understanding the photo-induced signal chain and the photo-physical and electrochemical properties of the constructed biohybrid electrodes,
3. Optimization of the electrode performance and efficiency by introducing other components or materials,
4. Elucidating limiting factors of these electrodes and the potential for application.

3. Theoretical Background

3.1 Photosynthesis – a natural model

The process of converting solar radiation into chemical energy by nature is described as photosynthesis, which started to evolve over the last 3.5 billion years on earth.² Hereby, plants, algae and photosynthetic bacteria¹ are transferring the thermodynamically low energy molecule carbon dioxide (CO₂) into reduced energy rich carbohydrates by utilizing solar irradiation.³ The photosynthetic organisms (PO) can be divided into two groups: anoxygenic PO and oxygenic PO. Organisms from the first group are purple bacteria, green gliding bacteria, green sulfur bacteria and gram positive bacteria, which use the light energy to oxidize molecules other than water without the release of oxygen.⁴ Reaction centres (RC) are the components of photosynthesis, where the light reaction takes place. In the anoxygenic PO only one type of reaction centre (RC, light-converting protein) in each organism exists, but differs strongly among the various species. The RC can be more photosystem I-like (heliobacteria, green sulfur/green gliding bacteria) or photosystem II-like (purple bacteria).⁵ However, all these organisms use bacteriochlorophyll and carotenoids for the light absorption mainly in the infrared region (700 – 1000 nm). In the second group, the oxygenic photosynthesis, organisms like plants, algae and cyanobacteria oxidize water, while releasing oxygen, to reduce CO₂. This process is divided into two main reaction cycles, which are either light-dependent⁶ (light reaction) or light-independent⁷ (Calvin-Benson cycle). The net reaction can be formulated as the following:



In plants, the photo-active cell contains the “power plant” of photosynthesis, the chloroplast.⁸ It is believed, that this organelles evolved from endosymbiotic reactions with cyanobacteria.⁹ Inside of a cyanobacterium, or in the chloroplasts of plants, a special membrane, the thylakoid membrane, can be found, dividing two reaction spaces, the stroma (outer plasmatic phase) and the lumen (inner plasmatic phase).^{10,11} In the thylakoid membrane the bound super-protein complexes photosystem II (PSII), photosystem I (PSI), cytochrome b₆/f (cyt b₆/f) and the ATP

¹ Halobacteria (archaea) are omitted in this description, because they do not use a reduction/oxidation chemistry, and cannot use CO₂ as their carbon source, while their light conversion differs fundamentally from higher organisms.⁴

synthase (ATPase) are involved in the photosynthetic electron transport chain and maintaining/using the proton gradient between the stromal and luminal reaction spaces.^{12–15} A general scheme is shown in Fig. 1.

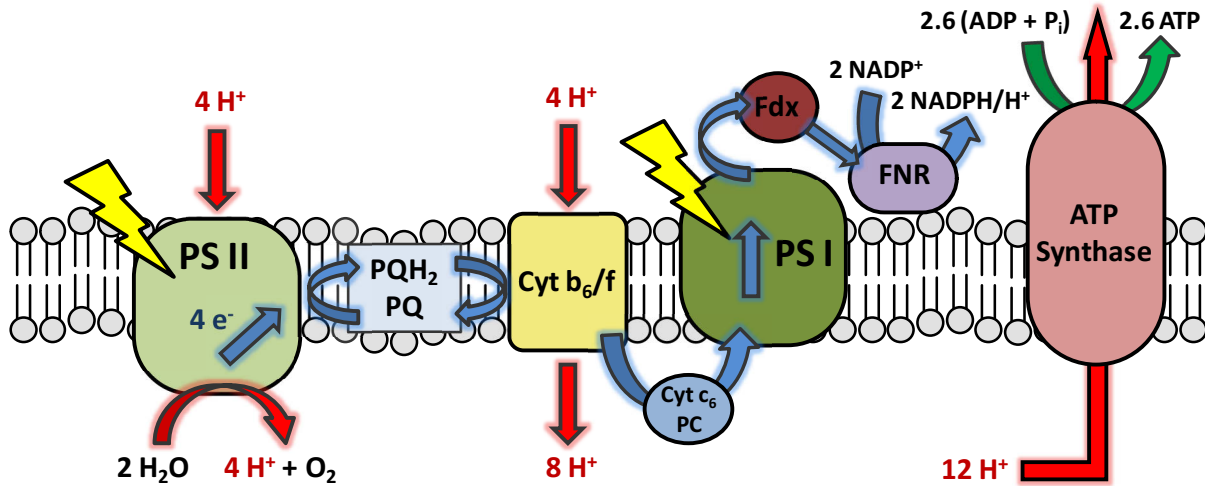
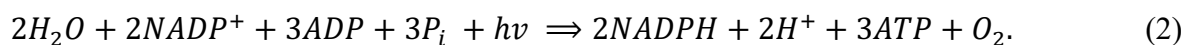


Fig. 1: Schematic representation of the photosynthetic electron transport chain (PET) in the thylakoid membrane of chloroplasts. The reaction starts with the absorption of light (yellow thunderbolts) and the oxidation of water at photosystem II (PSII), producing molecular oxygen. Electrons are transferred *via* plastoquinone (PQ) to the cyt b_6/f complex and *via* cytochrome c_6 (cyt c_6) or plastocyanin (PC) to photosystem I (PSI). After another light absorption electrons are further transferred to ferredoxin (Fdx) and finally to the ferredoxin-NADP⁺-reductase (FNR) to produce nicotinamide adenine dinucleotide phosphate (NADPH) (indicated with blue arrows). The PET results in a proton gradient driving the chemiosmotic synthesis of adenosine triphosphate (ATP) by the ATP-Synthase (indicated with red arrows).

The photosynthetic electron transport (PET) starts with the light-dependent excitation of PSII, whereas 4 photons are consumed to oxidize 2 water molecules at the PSII integrated Mn_4CaO_5 -cluster. This reaction yields molecular oxygen, 4 protons and 4 electrons.¹⁶ Due to an intramolecular electron transfer cascade (IET) in PSII, 2 electrons are transferred one-by-one to one PSII-associated plastoquinone (PQ) reducing the lipophylic aromatic compound to plastoquinol (PQH_2).^{17,18} The molecule is able to diffuse through the lipid double layer membrane to finally gets re-oxidized by the cyt b_6/f complex.^{19,20} In this reaction protons are pumped from the stromal to the luminal side of the membrane, being one of the reasons for the photosynthetic proton gradient.²¹ At the luminal side of the cyt b_6/f complex electrons are transferred to plastocyanin (PC), a redox protein with a tetrahedral coordinated copper ion.²² In cyanobacteria or green algae under copper shortage, this function can be taken over by a heme c containing redox protein, cytochrome c_6 (cyt c_6).²³ Due to a further light absorbing step in PSI an intramolecular electron-hole pair is generated.²⁴ The hole can be restocked *via*

the reduced PC or cyt c_6 , while the excited electron is transported to the stromal side, whereat the electron is transferred to the redox protein Ferredoxin (Fdx).²⁵ Fdx is able to shuttle one electron per molecule from PSI to the Ferredoxin-NADP⁺-reductase to finally reduce Nicotinamide adenine dinucleotide phosphate (NADP⁺ to NADPH).²⁶ For this reaction 2 electrons are needed to produce one molecule NADPH. During the PET a proton gradient between the luminal and stromal side is produced.²¹ Due to this concentration gradient, excess protons on the luminal side are flowing back through the ATP-Synthase, whereas the phosphorylation of adenosine diphosphate (ADP) to adenosine triphosphate (ATP) takes place.²⁷ Both products, ATP and the reducing agent NADPH are needed for the assimilation of CO₂ forming glucose in the Calvin-Benson cycle.⁷ The net reaction for the light reaction can be formulated as the following:



3.1.1 The photosynthetic electron transport (Z-Scheme)

The most remarkable feature of the light reaction of photosynthesis is the electron transport over multiple components, which effectively exchanging electrons with each other. To transport electrons over either a wide potential or a spatial range in natural systems, redox chemical reactions are responsible. Their corresponding redox potentials describe the tendency to be oxidized or reduced by another species. The excitation of a molecule by light results in a change in its redox potential, which depends on the electronic structure of the molecule. In nature the highest oxidation and reduction potential can be found in the PET, whereas PSII manages the water oxidation and PSI provides a high reduction potential for the reduction of NADP⁺.^{25,28} The Z-scheme displays the energy level of the transported electrons along a chain of redox-reactions, starting at the water splitting and finally ending up with the reduction of NADP⁺. As a peculiarity of photosynthesis, on the route of electrons along the redox chain the energy states are shifted towards higher reduction potentials due to the photon excitation at P₆₈₀ and P₇₀₀, respectively. This reaction provides the necessary reduction potential for either the spatial transport of electrons, as for the reduction of NADP⁺.

In the following description, potentials are given against a standard hydrogen reference electrode (vs. SHE). The initial luminal redox-reaction, H₂O/O₂, with its redox potential of 0.93 V at pH 5 of the luminal environment, provides the electrons for the PET.^{29–31} Electron

transport can only occur, if light is first absorbed by the system. To collect and focus a higher amount of solar energy, light-harvesting complexes (LHC) consisting of membrane proteins and photosynthetic pigments are used widely by phototrophic organisms, mainly surrounding and transferring energy to the photosynthetic reaction centres by Förster resonance energy transfer (FRET).³² In plants LHC's associated with PSI and PSII are called LHCI and LHCII, respectively, purple bacteria use bacterial antenna complexes LH1-3, while cyanobacteria or red algae utilize phycobilisomes.^{33–35}

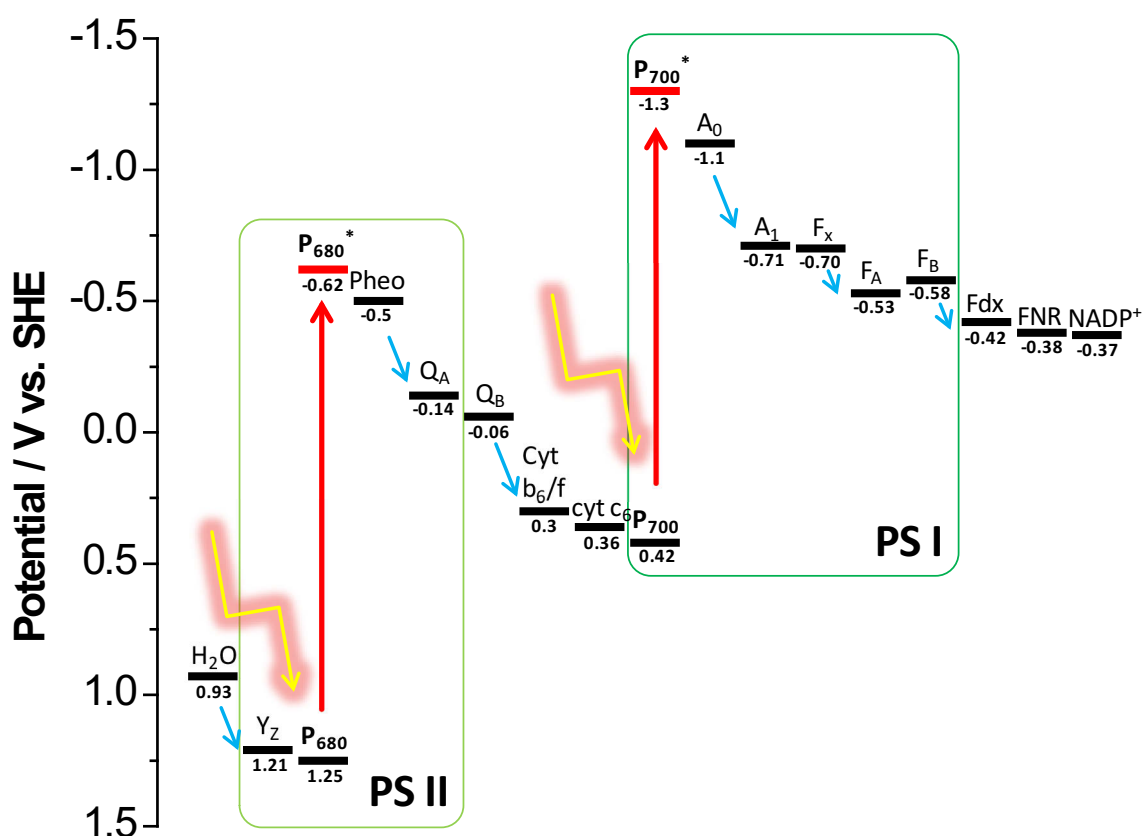


Fig. 2: Energy diagram (Z-scheme) of the light reaction in photosynthesis with the basic light converting components photosystem II (PSII, light green) and photosystem I (PSI, dark green). The redox potentials (displayed numbers in V) vs. a standard hydrogen electrode (SHE) under physiological conditions of the different species are plotted against the sequence of oxidation processes (from left to right). Blue arrows indicate the direction of electron flow, while red arrows show the change in potential of the P₆₈₀ and P₇₀₀ after light excitation (yellow arrow). For the sake of simplicity corresponding redox couples are denoted only as the molecule before chemical reaction (e. g. Pheo = Pheo/Pheo^{*}). For references see text.

When light is absorbed by the antenna system and this energy is transferred to the RC, first the very fast (~ 1.5 ps) excitation of a chlorophyll *a*, the P₆₈₀, occurs transferring the molecule to its excited state, P₆₈₀^{*}.³⁶ Instantly (after 3-5 ps) the primary electron acceptor pheophytin

(Pheo) gets reduced by P_{680}^* resulting in the state $P_{680}^{++}/Pheo^-$ (1.25/-0.5 V).³⁶⁻⁴¹ The intramolecular movements of the electrons in PSII are managed *via* the electron stabilizing acceptor plastoquinone A ($Q_A/Q_A^{\cdot-}$, -0.14 V) to the stromal located protein-bound quinone B (Q_B/Q_BH_2 , -0.06 V).^{42,43} The reaction occurs in two reduction and two protonation steps to form first a semihydroquinone ($Q_B^{\cdot-}$) and next the protonated hydroquinone (Q_BH_2).⁴⁴ The time scale of this reaction is ranging from 200-400 μ s for the reduction to $Q_B^{\cdot-}$ to 800 μ s to form Q_BH_2 . The protein-bound Q_BH_2 is then replaced by an oxidized Q_B , releasing Q_BH_2 into the membrane-embedded plastoquinone pool. P_{680}^+ , which has the strongest oxidation potential of +1.25 V in the PET, abstracts one electron from a proximal manganese cluster (Mn_4CaO_5 -cluster) by means of a 12.4 Å distant tyrosine residue (Y_Z).^{45,46} The above described reaction occurs 4 times, whereby the Mn_4CaO_5 -cluster is oxidized to a $Mn_4CaO_5^{4+}$ -cluster.^{41,47} New insights have shown, that there are 4 water molecules coordinated to this cluster in the dark state, 2 are bound by a Ca^{2+} ion, whereby another 2 are bound to an outer manganese (see Fig. 3).⁴⁸ The catalytic mechanism is not yet fully understood, but it is believed, that during the transition of the states S_0 - S_4 and back to S_0 (Kok-cycle), 4 protons and 1 O_2 molecule are released and 4 e^- are transferred subsequently to P_{680} .^{48,49} The complex nature of water splitting at the Mn_4CaO_5 -cluster, which are divided into 4 reaction states and their regeneration, have different reaction kinetics (30 μ s – 1.4 ms).⁵⁰ This causes the water oxidation to be the rate-limiting step in the electron transfer kinetics in PSII.

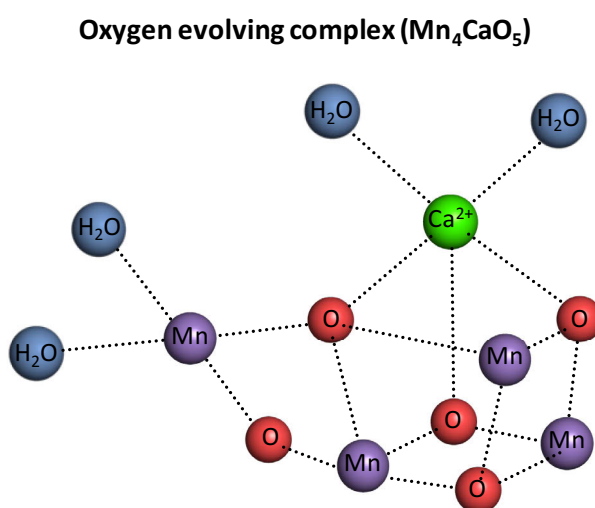


Fig. 3: Structure visualization of the oxygen evolving complex (OEC) from photosystem II, consisting of 4 manganese ions (Mn, purple), 5 oxygen atoms (O, red), a calcium ion (Ca^{2+} , green), while 2 water molecules (H_2O , blue) are coordinated to an outer manganese and 2 to a calcium ion. To show the three dimensionality of the OEC, coordination of the atoms has been visualized with dashed lines. Structure information used from Suga *et al.* 2014, PDB: 4UB6.⁴⁸

The two photosystems are electrical connected *via* diffusional redox shuttles. The membrane embedded $\text{Q}_\text{B}\text{H}_2$ pool reduces the cyt b_6/f complex with a redox potential of +0.3 V by diffusion to the acceptor side (1.5 - 5 ms).^{19,51–53} Here, $\text{Q}_\text{B}\text{H}_2$ is oxidized in two concerted reactions of proton-coupled electron transfer by a bifurcated reaction pathway.⁵⁴ However, the slowest step in PET is not determined by diffusion of $\text{Q}_\text{B}\text{H}_2$ but by the proton-coupled electron transfer in the high potential redox chain, where electrons are finally transferred to the iron sulfur protein (ISP, $\text{Q}_\text{B}\text{H}_2/\text{ISP}_{\text{ox}}$, 10 - 20 ms).^{51,55} Electrons from the ISP are then transferred over the cytochrome f to the redox proteins, cyt c_6 or PC (0.36 V), which diffuse to the luminal located electron donor docking side of the PSI.⁵⁶ The time scale of the electron transfer from cyt b_6/f complex to PSI is 150 – 500 μs .¹³ After light excitation of the primary electron donor, P_{700} , to the P_{700}^* state (-1.3 V), charge separation occurs, where in 100 fs electrons are transferred to the primary electron acceptor A_0 (-1.1 V). This leaves P_{700} in the oxidized state, P_{700}^+ with a redox potential of +0.42 V. After 30-35 ps electrons are transferred from the primary electron acceptor further to a phylloquinone A_1 (vitamin K_1 , -0.71 V).^{57–60} The intramolecular rate-limiting step here is the asymmetrical electron transfer to the central Fe_4S_4 -cluster (F_x , -0.7 V), which takes about 200 ns.^{61–63} From there, the terminal electron acceptor are the Fe_4S_4 -cluster F_A and F_B (-0.53 V, -0.58 V), whereas the electron is extracted in 500 ns from F_B to the diffusible redox protein ferredoxin (Fdx).^{64–67} With a redox potential of -0.42 V under physiological conditions, Fdx is able to reduce in a two electron transfer step the ferredoxin- NADP^+ -reductase (-0.38 V) further reducing NADP^+ to NADPH , which is utilized in carbon dioxide fixation.^{68–71} Nonetheless Fdx can also transfer electrons in a cyclic reaction to the cyt b_6/f complex, increasing the proton gradient and thus ATP production without accumulating NADPH .⁷² The Fdx reduction potential displays the entire usable photosynthetic reduction potential provided by the excitation of light and can additionally be used by phototrophic organisms for the production of other energy rich compounds. For example, reduced Fdx can be used for nitrite/nitrate reduction (nitrite reductase) in the N_2 fixation, glutamate synthesis (glutamate synthase), hydrogen production (hydrogenases), sulfite reduction (sulfite reductase) or thioredoxin reduction for the regulation of chloroplast localized enzymes.^{25,73,74}

3.1.2 Photosystem I – a biological semiconductor

In matter the excitation by light populates energy-rich states, which often relax to their ground states in very short time (\sim ns) under fluorescence and/or thermodynamic heat conversion. To use the light energy, semiconductor materials produce excitons (excited electron-hole couple), where electrons can be spatially separated from holes leading to an electrical usable energy. The biological equivalent to this is photosystem I (PSI), which is a multi-protein super-complex being one of the thylakoid-membrane light-converting components of natural photosynthesis. The function of PSI is to conduct a charge separation by light excitation, by which electrons are transported from the luminal to the stromal side of the thylakoid membrane. Having a high reduction potential these electrons provide the energy for CO₂ fixation. The most important feature of PSI is the ability to stabilize excited states in time after light absorption by separating spatially the resulting electron-hole pair. Hence, this super-complex shares similarities with charge-separating materials, but the high efficiency of PSI results from its in-built electron chain. In contrast, electron transfer in a semiconductor arises from the population of intrinsic conductive states, in which the charge carriers can move freely through the material. However, the basic working principles are very much alike, making PSI the biological variant of a semiconductor.

3.1.2.1 Structure

In the cyanobacteria *T. elongatus* first structural information of PSI could be gained in 1993 at a resolution of 6 Å.⁷⁵ This could be refined to 4 Å in the following years.^{76,77} Jordan *et al.* achieved in 2001 the highest resolution of 2.5 Å.⁷⁸ The super-complex can be present in a monomeric, dimeric and trimeric form, however in plants only the monomeric form is found, whereas in cyanobacteria the trimeric form is more likely.^{79–82} The cyanobacterial PSI trimer has a molecular mass of 1.068 MDa (356 kDa for each monomer), while one monomer consists of 12 protein subunits (PsaA-X) and a total of 127 cofactors comprising 96 chlorophylls, 22 carotenoids, 4 lipids, 2 phylloquinones, 3 Fe₄S₄ cluster and a putative Ca²⁺ ion.^{63,78} The lateral dimension of the trimeric PSI is 220 Å in diameter, its total height is 90 Å, while 45 Å of the complex is inside of the membrane.⁶³ The core subunits of PSI, located in the centre, with a high homology are PsaA and PsaB (80 kDa), both consisting of 11 transmembrane helices and building a heterodimer.⁸⁰ They contain the most components of the electron transport chain, 6 chlorophylls, 2 phylloquinones and one Fe₄S₄ cluster (P₇₀₀, A₀, A₁, F_x).^{63,83} The stromal side of the complex is formed by membrane extrinsic subunits PsaC,

PsaD, PsaE. All three subunits providing a stromal hump, by which ferredoxin can bind to each monomeric PSI independently.⁸³ PsaC (9.8 kDa) contains the terminal Fe_4S_4 cluster F_A and F_B , which are coordinated by cysteine residues.⁸⁴ PsaD (15.6 kDa) and PsaE (8 kDa) are responsible for anchoring and locating PsaC at the stromal side of the complex, and are actively involved in the docking process of Fdx to the acceptor side.^{85–87} The membrane exposed hydrophobic subunits PsaF, PsaJ, PsaK and PsaX are located distal side of the trimeric complex, stabilizing the core antenna system of PSI and play an important role by forming interactions with the peripheral antenna system.⁸³ PsaL and PsaI are the subunits responsible for the interconnection of the monomeric PSI complexes forming the trimer, while the subunit PsaM is located at the interface between two monomers.^{63,88}

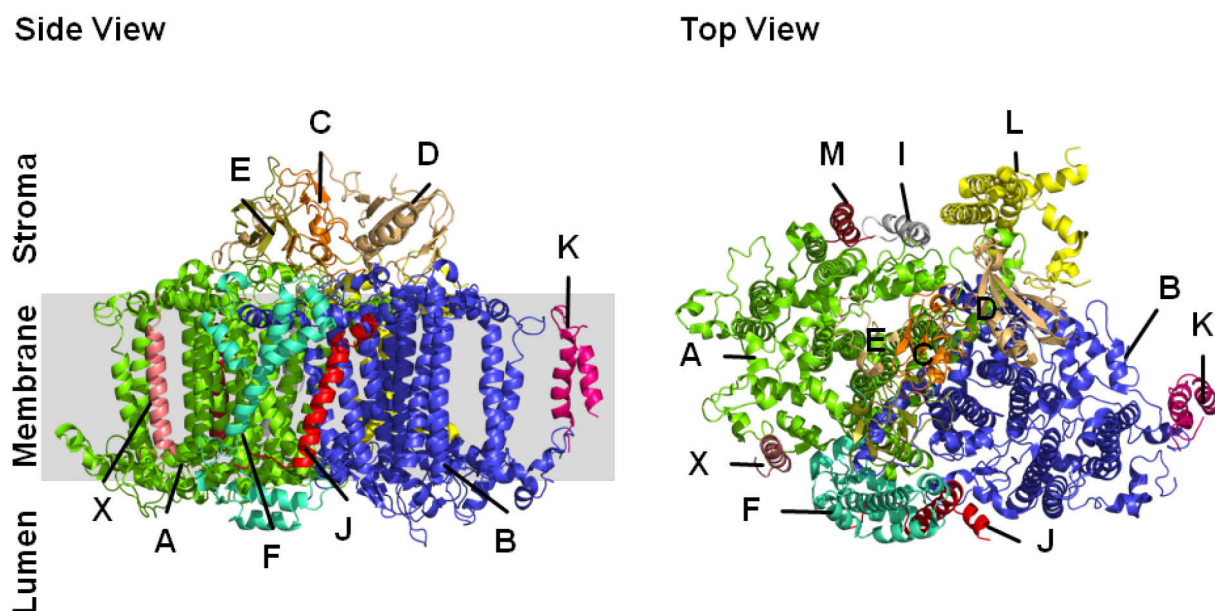


Fig. 4: Crystal structure visualization of monomeric photosystem I (PSI) and their protein subunits displayed as secondary structure: PsaA (A, green), PsaB (B, blue), PsaC (C, orange), PsaD (D, blue), PsaE (E, dark yellow), PsaF (F, cyan), PsaI (I, light grey), PsaJ (J, red), PsaK (K, magenta), PsaL (L, yellow), PsaM (M, dark red), PsaX (X, light pink). The complex is displayed as side view (left) in the membrane and in top view (right). Structure information used from Jordan *et al.* 2001, PDB: 1JB0.⁷⁸

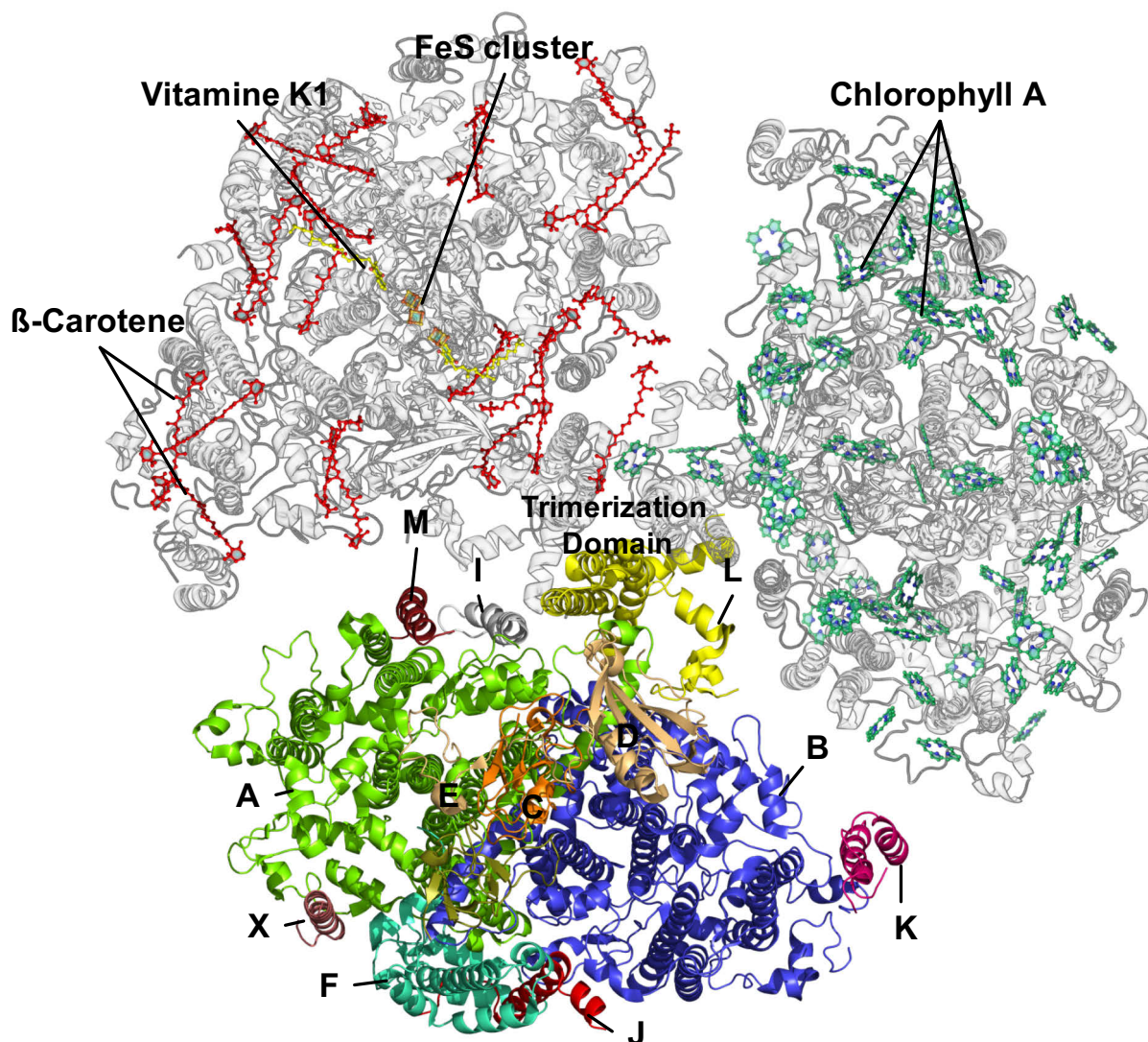


Fig. 5: Crystal structure visualization of trimeric photosystem (stromal view perpendicular to the membrane plane) with monomers representing I) the secondary structure with subunits (bottom, for colour indication see Fig. 3), II) the location of the core antenna system consisting of 90 chlorophyll *a* and 6 chlorophyll *a* from the electron transfer chain (right top, green), III) the location of cofactors containing 22 β -carotenoids (red), 3 Fe_4S_4 cluster (orange), and 2 phylloquinones (vitamin K_1 , yellow) without lipids. Structure information used from Jordan *et al.* 2001, PDB: 1JB0.⁷⁸

For all Chl *a* molecules the distances between Mg^{2+} - central ions ranges between 7-16 Å resulting in a fast Förster resonance energy transfer.^{78,89} The Chl *a* molecules are spatially organized in two parallel membrane intrinsic planes building up a energy transferring network.⁷⁸ On the contrary this network is well separated from the ETC Chl *a* molecules, while only two Chl *a* have proximal distance to the ETC and thus be considered the energy transfer connection between the antenna system and the ETC.⁷⁸ The energy from light excitation is transported to the core of PSI, where it is trapped at the P_{700} .^{90,91} The β -carotenoids are distributed over the PSI similar to Chl *a*, however they are in close contact to

the headgroups of Chl *a* ($< 3.6 \text{ \AA}$).⁷⁸ This ensures an efficient energy transfer to Chl *a* after their light excitation (typically in the green gap of Chl *a*, 450-570 nm).⁹²⁻⁹⁴ Moreover they are supposed to photoprotect the antenna system by quenching Chl *a* triplet states by a charge transfer mechanism.⁹² Due to π - π stacking with Chl *a* molecules a fine tuning of the absorption properties is possible.⁷⁸ Moreover, in cyanobacteria trimerization of PSI is necessary for the efficient light-converting efficiency under low light intensities, hence the cooperativity in photon absorption in a trimeric form of PSI is enhanced compared to its monomeric form.^{95,96}

3.1.2.2 Function

In the natural system PSI functions as a light-driven *cyt c₆* (PC):Fdx oxidoreductase, whereby electrons are transferred from the luminal to the stromal side of the thylakoid membrane. For one complete reaction only one electron is hereby transferred. First a photon is absorbed by the PSI antenna system network and transferred to the reaction centre (RC) and the ETC. This is generated by two different mechanisms: 1. The long-ranged direct energy transfer by a Förster mechanism, 2. The short-ranged exchange of excitons by a Dexter mechanism. The high quantum efficiency ($\sim 100\%$) and fast rates of this process can not solely be explained by Förster/Dexter theory, since between Chl *a* molecules in the network a wide heterogeneous coulomb coupling exist and could be better understood in combination with the Redfield theory approach.^{25,97-99} The ETC itself contains 6 Chl *a* molecules, while the P_{700} is attributed to be the “special pair”, where 2 Chl *a* molecules are paired in parallel and charge separation takes place. The P_{700} got its name from the red-shifted absorption maximum at 700 nm. The ETC is split into two branches A and B, where each branch have another 2 Chl *a* molecules ($A_{A/B}$, $A_{0A/B}$) and 1 phylloquinone ($A_{1A/B}$). It is argued how the light collection antenna transfers their energy to the RC and what part of the RC is first excited. One study suggests that charge separation is processed by A_A and A_0 is the first electron acceptor, while in a second step P_{700} is oxidized by A_A .¹⁰⁰ Another study supports the basic idea of P_{700} being the primary electron donor with fast charge separation ($< 100 \text{ fs}$) to yield the P_{700}^+/A_0^- state.⁵⁸ Nonetheless the electron gets accepted by the secondary electron acceptor phylloquinone A_1 (10-30 ps).^{58,67} From here, an asymmetrical electron transfer occurs to the first Fe_4S_4 cluster F_x . From A_{1B} to F_x the electron transfer is around 25 times faster than from A_{1A} to F_x (18 ns vs. 160 ns).^{60,101} Nevertheless in PSI both branches A and B are active for the electron transfer, however in cyanobacteria branch B is 4 times less used in the electron transfer process.^{102,103} From F_x an irreversible electron transfer occurs to F_A and further to F_B which is

not faster than 500 ns.^{25,59} However the transported electron in the ETC is able to recombine with the hole located at the P_{700} . The recombination takes place by emitting fluorescence and their half-life times can be measured to 3-10 μ s ($A_0:P_{700}$), 10 μ s ($A_1:P_{700}$), 500 μ s ($F_x:P_{700}$) and 10 ms ($F_B:P_{700}$) respectively. This relatively stable electron-hole pair in PSI in comparison to the typical time scale in semiconductor materials (\sim ns) making it highly efficient. The kinetics of the ET of $F_{A/B}$ to the diffusible electron acceptor Fdx involves three different first order half-life times with varying amplitudes at different pH ($t_{1/2} = 0.5, 20$ and 100 μ s). The fastest phase comply with the single ET from $F_{A/B}$ to Fdx, whereas the slower phases correspond to different PSI/Fdx complex formations.^{24,64,104} The mechanism on which the reduction of P_{700} by cyt c_6 or PC takes place, depends strongly on the organism and can range from an oriented collision model (type I) to a transient complex formation with a proper reorientation step of the redox center (type III).^{105,106} Nevertheless, half-life times can be relatively fast ($< 1 \mu$ s) or slow ($\sim 20 \mu$ s), whereby the rate constants of ET reaction increase from cyanobacteria to plants, leading to the conclusion, that evolution has been improving the reduction rate of PSI over time.^{106–108}

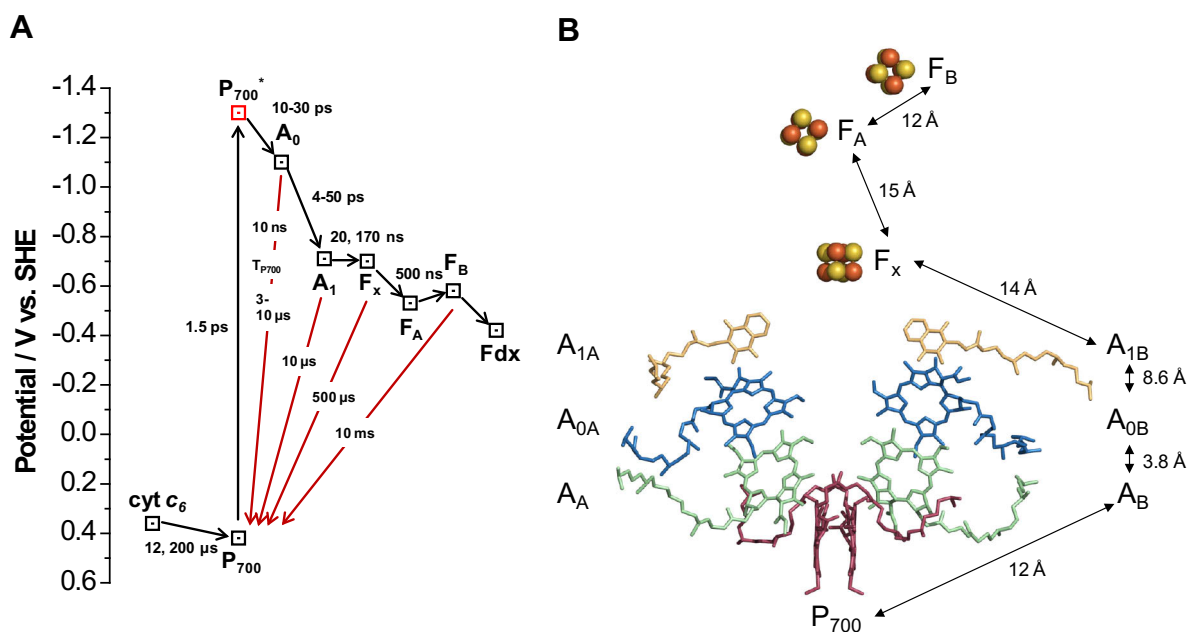


Fig. 6: (A) Energy diagram of the electron transport chain (ETC) in photosystem I (PSI) with forward (first number) and backward (second number) half-life time for the electron transfer process. Black arrows indicate the way of electrons, while red arrows indicate the relaxation of electrons to their ground state in P_{700} , with their half-life times of fluorescence decay.²⁴ (B) Intrinsic electron transport chain of photosystem I (PSI) with 3D visualization of cofactors involved. Branches A and B are indicated in subscript letters. The Mg^{2+} - Mg^{2+} distances or distances between the π -plane of the respective molecule are indicated with black arrows. Structure information used from Jordan *et al.* 2001, PDB: 1JB0.⁷⁸

3.2 Protein electrochemistry – communicating with nature

Protein electrochemistry displays the research branch in which proteins are either investigated by electrochemical methods or coupled with artificial electrical transducer materials (electrodes). The last chapter has shown that many important molecular processes in nature are conducted by the electrical communication of different proteins and redox molecules with each other. To mimic and make use of certain components of these processes artificial interfaces with electrodes have to be developed to establish the communication with nature. Therefore this research field is addressing the understanding and construction of bio-based sensors, fuel cells and photovoltaic devices, which benefit from the efficiency of natural systems.

3.2.1 Marcus theory

For the effective connection of biomolecules with electrodes, the Marcus theory enables the possibility to understand the exchange of electrons between two redox species in solution or between redox species and transducer materials in polarisable solvents. Chemical reactions can be understood by theories developed by Arrhenius and Eyring, whereby the reaction between two educts takes place according to a collision model, further passes a transitional state and forming the product. Besides a pre-exponential factor and the temperature, the activation energy of this transitional state is one parameter, which determines the reaction rate. Redox reactions, however, involve an electron hopping from one species to another. The change of the molecules during this event includes the formation or rearrangement of bonds, changes in binding lengths, angle or distortion of chemical groups in the molecules (inner sphere) and the reorganisation of solvent shell, the arrangement of water and ions around the transition complex (outer sphere). The electron hopping is much faster than the movement of solvent molecules (Born-Oppenheimer approximation), which means that the positions of atom nuclei and solvent molecules before and after the electron transfer are the same (Frank-Condon principle). The movements of atom nuclei are small, leaving the consequence that electron transition rates are highly dependent on the polarization of the solvent. The energy needed for the reorganisation of solvent molecules during transition of one electron ($\Delta e = 1$) to result in the configuration of the product molecule corresponds to the outer reorganisation energy λ_{out} . Nonetheless in redox reactions often also the inner sphere components are changed in the product molecules, due to different charge situation in the product molecules, as for example changing ligand distances from a central transition metal ion. This means, that

an electronic transition has also an inner reorganisation energy λ_{in} . The two kinds of reorganisation energies are considered to be independent from each other, consequently adding up to the total reorganisation energy λ ($\lambda = \lambda_{out} + \lambda_{in}$). Thermal fluctuations are needed for the electron transition to overcome the energy barrier, which would result in vanishing electron transfer rates at $T = 0$ K (see Arrhenius equation). However, experimentally observed ET rates in the low temperature region are getting constant ($k_{ET} \neq 0$). This means that an additional component in ET reactions is present and a quantum-mechanical approach is needed. Here, the nuclear motion can couple to the electron motion, where electron tunneling can occur between the ground level in the reactant potential and a vibrational level in the product curve. The influence of the electron tunneling on k_{ET} depends on the strength of electronic coupling between the reacting species, which decides whether electron transfer follows an adiabatic or non-adiabatic path. Included in the classical theory of Marcus, the electron transfer rate k_{ET} can therefore be formulated as the following semi-classical equation:

$$k_{ET} = A \cdot e^{-\beta r} \cdot e^{\frac{-(\Delta G^0 + \lambda)^2}{4\lambda RT}}, \quad (2)$$

with the electron transfer rate k_{ET} depending on the reorganization energy λ , the free Gibbs energy ΔG^0 (potential difference between reactants), the temperature T , the ideal gas constant R and the adiabatic term ($A \cdot e^{-\beta r}$) with the distance between reactants r , a pre-exponential factor A and the electron tunnel constant β . From equation 2 it is obvious that k_{ET} will increase exponentially with decreasing distance between reactants (r) and increases exponentially with the potential difference between reactants (ΔG^0).

The value of the solvation reorganization energy λ_{out} is inverse proportional to the refractive index of the medium (or their static and optical dielectric constants), the distance between the reacting molecules and their electrostatic radii. This means also that for short distances or electrostatic radii of reacting species, λ_{out} is small, which makes k_{ET} high. As a consequence for k_{ET} the physicochemical properties of the surrounding medium are very important to consider. One aspect is the choice of the solvent. For many ET processes a high polarisability of solvent molecules can improve k_{ET} . Further influencing parameters are the viscosity η of the medium, which determines the orientational freedom and mobility of the reacting species, and the ionic strength, which has a direct impact on the conductivity σ and the dielectric constant ϵ .

The inner reorganisation energy λ_{in} can be seen as the sum of forces needed to change all coupled intramolecular vibrational modes from educt equilibrium state to product equilibrium state. This strongly depends on the molecular nature of the reacting species, thus in redox species their chemical structure and composition (e. g. ligands in a metal complex) have to be considered. A higher λ_{in} would consequently be present in molecules, where a high number of vibrational modes have to change, while electron transition takes place.

In this discription of the semi-classical electron transfer theory, the pre-exponential factor A is a complex function of various parameters, which includes the characteristic frequencies ν to pass the saddle point of the energy barrier, the temperature T , the reorganization energies λ_{in} and mainly λ_{out} . Therefore, also here the above mentioned physicochemical parameters of the medium influence A , like η , σ , and ε . Especially molecules in a surface-fixed state exhibit dramatic dependencies upon these properties, when electrons are exchanged with a transducer material. For instance, fixed charges on a surface can shield the applied electrical field, or a limited rotational freedom of the surface-bound molecule can hinder the ET process.

With the mathematical representation of equation 2, the adiabatic or quantum-mechanical term contains β and r , which are exponential factors. The parameter r equals the distance the electron must travel as the van der Waals distance between reacting species. The parameter β represents the nature of the intervening medium between reactants, because the electron may has to travel through bonds or free space, for example for sigma bonds β is 0.7 \AA^{-1} , between adjacent parallel heme groups β is 2 \AA^{-1} , while in proteins β is $1.1\text{-}1.4 \text{ \AA}^{-1}$.^{109,110} The negative value of β corresponds to the slope of a plot of $\log(k_{ET})$ vs. r . Which mechanism (non-adiabatic or adiabatic) is found to be dominant in certain situations depends on the electronic coupling, distance and kind of the coupling species. For example, the ET mechanism between two stacked heme groups with imidazole axial ligands is 100 % adiabatic for Fe-Fe distances of up to 11.8 \AA , above the adiabatic mechanism transfers into a non-adiabatic ET and the second term in equation 2 will be dominant.¹⁰⁹ In intramolecular ET reactions the electron tunneling is often predominant, due to a high electronic coupling and optimal distances between redox species resulting in fast ET reactions, which was long time underestimated especially for endergonic processes.¹¹¹ However, the electron transfer rate determines besides other factors the overall performance of a biohybrid electrode and is therefore needed to be improved for a reliable working system.

3.2.2 Cytochrome *c* – the versatile redox protein

Cytochrome *c* is a highly conserved small redox protein of about 12 kDa from the respiratory chain containing a protein-bound heme prosthetic group with a redox potential of about 0.255 V vs. SHE.¹¹² Its high stability either in solution or immobilized on a surface, as well as its strong dipole momentum, makes it ideal to be used for the interconnection of proteins with electrodes. It is one of the most investigated proteins in protein electrochemistry so far.

3.2.2.1 Structure

Cytochrome *c* from *horse heart* consists of 105 amino acids with a high number of them are lysins (18.1 %).¹¹³ This results in a basic pI of about 10 – 10.5.¹¹⁴ The secondary structure is determined by 5 α -helices intersected with β -turns (2 turns of type III, 4 turns type II).¹¹³ The redox-active heme group is located in the center of the protein, where it is coordinated by the axial ligands M80 (S-Fe) and H18 (N-Fe).¹¹³ The porphyrin ring of the heme *c* is bound covalently *via* a thio-ether to C14 and C17, tightly fixating the heme in the protein.¹¹³ The heme *c* consists of a protoporphyrin IX and central Fe^{2+/3+}-ion coordinated in the plane *via* the 4 pyrrole inherent N heteroatoms by their free electron pair. With the axial ligands (M80, H18) the Fe^{2+/3+}-ion has a coordination of six, thus resulting in an octahedron. The axial ligands play a major role in tuning the redox potential of the heme *c*, because of the kind of ligand and distance from the Fe^{2+/3+}-ion, depending on the protein.¹¹⁵ The vacuum surface potential of cyt *c* reveals, that the protein has an asymmetric potential distribution having a strong positive potential basically located around the heme binding pocket. At a physiological pH cyt *c* is therefore positively charged with a dipole momentum of 320 Debye in vertebrates.¹¹⁶ The electric field distribution of the protein is therefore one of the major reasons for the movement, binding to other proteins and orientation of cyt *c* on membranes in the natural system.^{116,117}

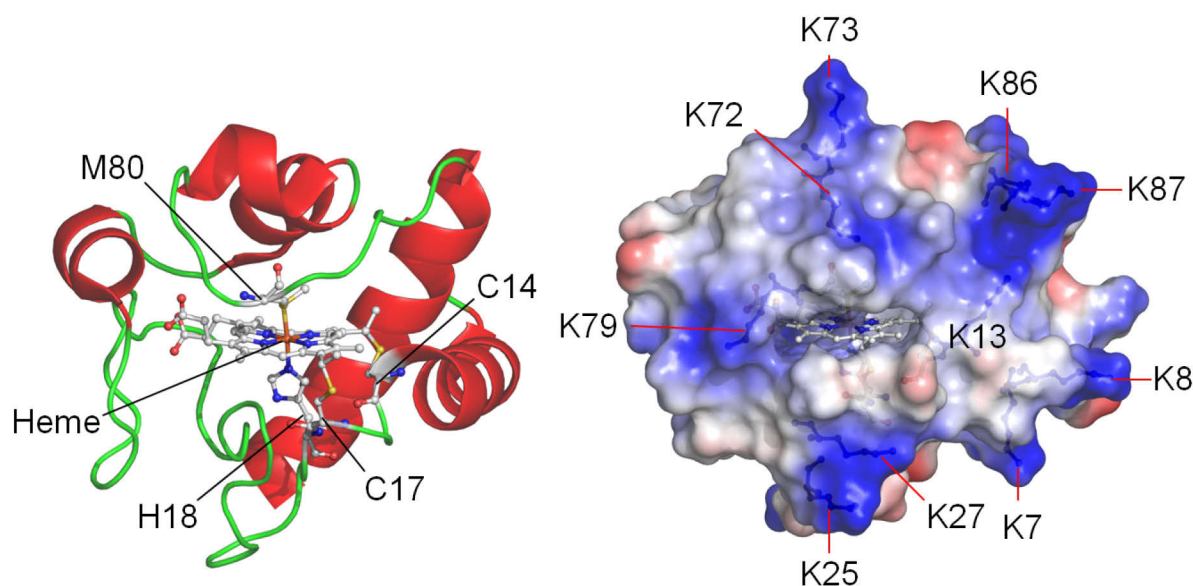


Fig. 7: Crystal structure visualization of cytochrome *c* from *horse heart*. The protein is displayed as a cartoon with secondary structure (left, α -helices = red, β -turn = green) including the bound heme (sticks and balls, atoms: C = white, Fe = orange, N = blue, O = red, S = yellow). The surface potential, calculated with vacuum electrostatics, is displayed indicating positive (blue) and negative (red) charged regions with the heme group with its binding pocket (right). Important lysine residues involved in the positive charge distribution are shown (sticks and balls, blue). Structure information used from Bushnell *et al.* 1990, PDB: 1HRC.¹¹³

3.2.2.2 Function

The highly conserved cyt *c* can be found in various organisms, ranging from eukaryotes, archaea and bacteria.¹¹⁸ Cyt *c*'s main function is to shuttle electrons in the electron transfer chain (ETC) of organisms, in eukaryotes it transfers electrons from the membrane-bound complex III (cytochrome *c* reductase) to complex IV (cytochrome *c* oxidase) in the respiratory chain (oxidative phosphorylation). Here, it is mainly located in the inner mitochondrial membrane (IMM). As can be seen from section 3.1, cytochrome *c* is involved in phototrophic organisms in the ETC of photosynthesis, as described previously. Besides this clear function in the ETC of organisms, cyt *c* was found to be involved in cell apoptosis. This is initiated in mitochondria, where the cyt *c* release into the cytosol is induced by a cytosolic truncated protein tBID, involving pro-apoptotic proteins, BAX and BAK, where pores are formed in the outer mitochondrial membrane.¹¹⁹ Cyt *c* then binds to the apoptotic protease activating factor-1 (APAF1), which activates heptamerization and binding to procaspase-9 forming an apoptosome.¹²⁰ Further natural functions can be seen as cyt *c* acts as a cardiolipin peroxidase. Additionally, cyt *c* is also included in detoxification of reactive oxygen species (ROS) in mitochondria, reacting with superoxide and peroxides.¹²¹ It is also involved in the removal of

cell toxic sulfite *via* shuttling electrons from sulfite oxidizing enzymes to the ETC in mitochondria.¹²²

3.2.2.3 Electrochemistry

Cyt *c* was ideal to be used as one of the first redox proteins communicating with electrodes due to the vast occurrence in cells, the high stability and the possibility of purification of this protein, becoming the model protein in protein electrochemistry. The electrochemistry of cyt *c* has a strong dependency upon electrode material and modification, as well as the adsorption of the protein to the electrode surface. At blank metal electrodes cyt *c* tends to adsorb and denaturise at the surface, leading to the prevention of clear and stable redox signals.^{123–125} Nevertheless, redox behaviour ranging from quasi-reversible to irreversible has been found on silver, gold, platinum, ITO and FTO but strongly depending on electrode pretreatment.^{125–128} Progress has been made by the introduction of adsorbed or chemisorbed promoter molecules, starting with 4,4'-bipyridine and derivatives, enhancing the electron transfer rates with the metal electrode.^{129,130} Since these preliminary research a vast amount of molecules, most of all thiol compounds, but also oligonucleotides, have been tested, improving and understanding the electron transfer of cyt *c* to metal electrodes.^{131,132} From this work, it was concluded, that hydrogen bonds or salt bridges from a bifunctional molecule to the heme-facial lysines of cyt *c* are beneficial for a fast electron transfer reaction.¹³¹ The introduction of negative charged carboxylic acid alkanethiol self assembled monolayers (SAM) resulted in non-destructive adsorption of cyt *c* with heterogeneous electron transfer rate constants (k_s) ranging from 0.1 to 0.4 s⁻¹.^{133,134} Interestingly, negative shifts of redox potentials (~45 mV) could be observed, when cyt *c* was bound to negatively charged surfaces, which was also found in the natural system.^{134–136} Nonetheless, the k_s of cyt *c* on carboxyl-terminated SAMs on gold electrodes has a strong dependence on ionic strength, pH and viscosity of the buffer solution, as well as the chain length of the SAM.¹³⁷ Here, the apparent k_s is an exponential function of the number of methylene groups ($n > 10$), obeying the Marcus theory, but levelling off at shorter SAM length ($n < 9$).^{137–139} In the latter case, the reorganization of cyt *c* becomes the rate-limiting step.¹³⁸ The extrapolation to infinitesimal short SAM length ($n = 0$) at low ionic strength results in an k_s of 5•10⁶ s⁻¹ being in the range of intramolecular electron transfer processes.¹³⁷ Moreover, the K13 in cyt *c* was found to be directly involved in the electronic coupling of the protein/SAM interface, since ET rates drop by 5 orders of magnitude, when this amino acid is replaced with alanine.¹⁴⁰ Interestingly, ET from cyt *c* to a metal electrode is coupled with a proton transfer step (reorganisation of hydrogen-bonding

network after reduction/oxidation), becoming the rate-limiting step for short SAM's ($< C_6$).¹⁴¹ While another study supports these findings, the k_s of cyt *c* is controlled by a long range tunneling, whereas at short SAM length the reaction is solvent/friction controlled.¹⁴²

A high stability and quasi-reversible electrochemistry of either covalently or adsorbed cyt *c* on mercaptoundecanoic acid was achieved, due to a better SAM formation on the surface compared to shorter molecules.^{133,143} The reduction of negative charges on the surface by mixing mercaptoundecanol to the SAM (1:3) yielded higher redox-active protein amounts as well as ET rate constants ($\sim 70 \text{ s}^{-1}$).¹⁴⁴ Nonetheless, the fixation of covalently bound cyt *c* decreases k_s to 40 s^{-1} , which was explained by the reduction in rotational freedom of the surface-bound protein.¹⁴⁴ The ligation of cyt *c*'s heme group to an pyridinyl- or imidazole-terminated alkanethiol resulted in a protein surface coverage one order of magnitude below a monolayer with a strong negative shift in redox potentials (up to $-415 \text{ mV vs. Ag|AgCl}$), but increased the ET rates up to 850 s^{-1} .¹⁴⁵ Due to the direct coordination of SAM-terminal groups to the Fe central ion in the heme group, a change in the electronic coupling or the reorganization energy is expected to be the reason for this high rate constants.¹⁴⁵

Until now, countless strategies have been applied for the electrical coupling of cyt *c* to electrodes by a variation of electrode materials and structure. Moderate ET rate constants of cyt *c* were found on nanostructured gold materials: colloidal gold-carbon paste electrodes (1.21 s^{-1})¹⁴⁶, gold nanoparticles-chitosan-carbon nanotubes (0.97 s^{-1})¹⁴⁷, L-cysteine modified gold electrodes (1.25 s^{-1})¹⁴⁸, nanoporous gold films (3.9 s^{-1})¹⁴⁹.

Using carbon materials, protein denaturation can be suppressed as compared with metal electrodes, but also pretreatment and surface modifications are beneficial. For instance, the ET of solution cyt *c* to an graphite electrode can be established without denaturation, but a high amount of oxygen modifications on the surface are needed generating high ET rates.^{150,151} Immobilisation of cyt *c* can be achieved by using nanostructured derivatives, which also result in moderate k_s values. This has been done using poly-3-methylthiophene/multi-walled nanotube glassy carbon electrodes (0.49 s^{-1})¹⁵², multi-walled nanotubes (4 s^{-1})¹⁵³, chitosan dispersed graphene nanoflakes (1.95 s^{-1})¹⁵⁴, graphene oxide (12.6 s^{-1})¹⁵⁵, polyaniline/multi-walled nanotube ITO electrodes (17 s^{-1})¹⁵⁶, and macroporous activated carbon electrodes (17.6 s^{-1})¹⁵⁷.

Furthermore, transparent conducting oxides have been directly used as electrode materials for the coupling of cyt *c* to the electrode. A prominent example is indium tin oxide (ITO), on

which the electrochemistry of cyt *c* has been investigated in solution¹²⁵ or adsorbed on the ITO surface either from solution or due to micro-contact printing.^{158–160} The k_s of adsorbed cyt *c* on planar ITO electrodes can be very different, with reported values of 4 s^{-1} or 18 s^{-1} under similar experimental conditions.^{158,159} Differences in conductivity of the ITO electrode can be found here, with a higher conductivity corresponding to a higher k_s value. Nevertheless, with mesoporous ITO electrodes, a larger amount of cyt *c* molecules have been coupled to the electrode, but due to the low intrinsic carrier density in such materials, ET rate constants were lower compared with planar ITO electrodes, for instance for mesoporous ITO (1.2 s^{-1}).¹⁶¹ A higher surface coverage and a k_s of 12 s^{-1} have been achieved, when cyt *c* was immobilized on nanosized columnar ITO structures.¹⁶² Other porous transparent conducting oxides have been used in combination with cyt *c*, exhibiting also a high assembled protein amount, but their k_s values are low, for example: mesoporous niobium oxide films (0.28 s^{-1})¹⁶³, NaY zeolite (0.78 s^{-1})¹⁶⁴, mesoporous antimony doped tin oxide (1.35 s^{-1} , 1.2 s^{-1})^{165,166}, sandwich structured SiO_2 gel boron-doped diamond electrode (1.39 s^{-1})¹⁶⁷, mesoporous SnO_2 (1 s^{-1})¹⁶⁸ and mesoporous silica thin films (1.33 s^{-1})¹⁶⁹.

Another aspect of cyt *c*'s electrochemistry is the possibility of electron self-exchange between cyt *c* molecules.¹⁷⁰ Hereby, electrons can be exchanged between equal cyt *c* molecules ($\Delta G^0 = 0$), being in different redox states (ferric or ferrous state).¹⁷⁰ First NMR studies in solution have revealed, that cyt *c* can self-exchange electrons with a rate constant (k_{ex}) of about $10^3\text{ M}^{-1}\text{ s}^{-1}$, which increased by one order of magnitude, when higher ionic strength is present.^{171,172} A simulation of the electron exchange between cytochromes has shown, that differences in the reorganization energy are dominant for disparities in the magnitudes of the apparent rate constant between these proteins.¹⁷³ Furthermore, the k_{ex} reaction dynamics are completely controlled by the electron transfer rather than by diffusion dynamics in solution.¹⁷³ Site-specific modifications of K13 and K72 increased k_{ex} by one and two orders of magnitude, respectively, implying that also electrostatic repulsion of cyt *c* molecules retarding the exchange process.¹⁷⁴ Based on this, layer-by-layer multilayer approaches have been developed exploiting the self-exchange process by using sulfonated polyanilines (PASA)^{175,176}, gold nanoparticles¹⁷⁷, DNA¹⁷⁸, or silica nanoparticles¹⁷⁹, whereby cyt *c* molecules far from the electrode could be electrically addressed. Nevertheless, ET rates in these multilayers depend strongly on the rotational freedom and molecular distances between the surface-confined cyt *c* molecules. Also the matrix element plays a crucial role in self-exchange, for example if silica nanoparticles are used, a k_{ex} of $1.99 \cdot 10^4\text{ M}^{-1}\text{ s}^{-1}$ have been achieved.¹⁸⁰ Nonetheless without a bulky matrix molecule, if cyt *c* is crystallized on modified

gold electrodes with the help of calixarenes the interfacial electron hopping between well-ordered bulky cyt *c* molecules can also take place and has been found in the range of 10^5 - 10^6 M⁻¹s⁻¹.¹⁸¹ The cyt *c* self-exchange has already been exploited for the connection of enzymes to electrodes, for instance, enzymes like bilirubin oxidase¹⁸², laccase¹⁸³, cellobiose dehydrogenase¹⁸⁴, fructose dehydrogenase¹⁸⁵ or sulfite oxidase^{186,187}. Feifel *et al.* 2014 were able to connect two enzymes, cellobiose dehydrogenase and laccase, in separated layers to a gold electrode, which can exchange electrons *via* cyt *c* with the electrode.¹⁸⁸

3.2.3 Strategies for the electrical coupling of proteins to electrodes

To date a vast number of different strategies for the electrical coupling of electro-active proteins has been developed. The different coupling strategies exhibit advantages and drawbacks with respect to the protein stability, the amount of connected proteins and the rate of electron exchange with the electrode. The basic strategies can be separated into three major groups: The direct, wired and mediated electron transfer. In the first group, electrons are exchanged with the electrode directly from/or to the electro-active group of the protein, without the need of an additional mediator. This is possible either because of a beneficial electrode material, or through an introduced layer on the surface (e. g. SAM). Here, theoretically ET reaction can be considered to be as fast as possible, because there is only one electron transfer step needed. Nonetheless, the distance between the redox-active group in the protein and the electrode can be rather long, due to the often deeply buried prosthetic groups in the protein structure, or random/poor orientation of the protein on the surface. Additionally, electronically coupling of redox centres of the protein with the electrode material can be very poor, which results in a higher activation energy, or decreased electron-tunneling rate, which increases the overpotential, thus energy, needed for an ET reaction. Hence, electrode material, surface modification or SAM molecules have to be carefully selected and tested for the each individual protein.

Typical examples for expedient electrode materials are mostly non-metal electrodes based on carbon (glassy carbon, pyrolytic graphite) or transparent conducting oxides (ITO, FTO). Metal electrodes (like gold or silver) are used in combination with alkanethiol modified SAM's, where orientation of the protein and ET rates can be controlled very well *via* the solution-exposed terminal groups of the SAM molecules and the length of the SAM. Nanostructuring often helps to increase the attractive forces between the electrode material and the protein, without a further modification of the electrode.¹⁸⁹

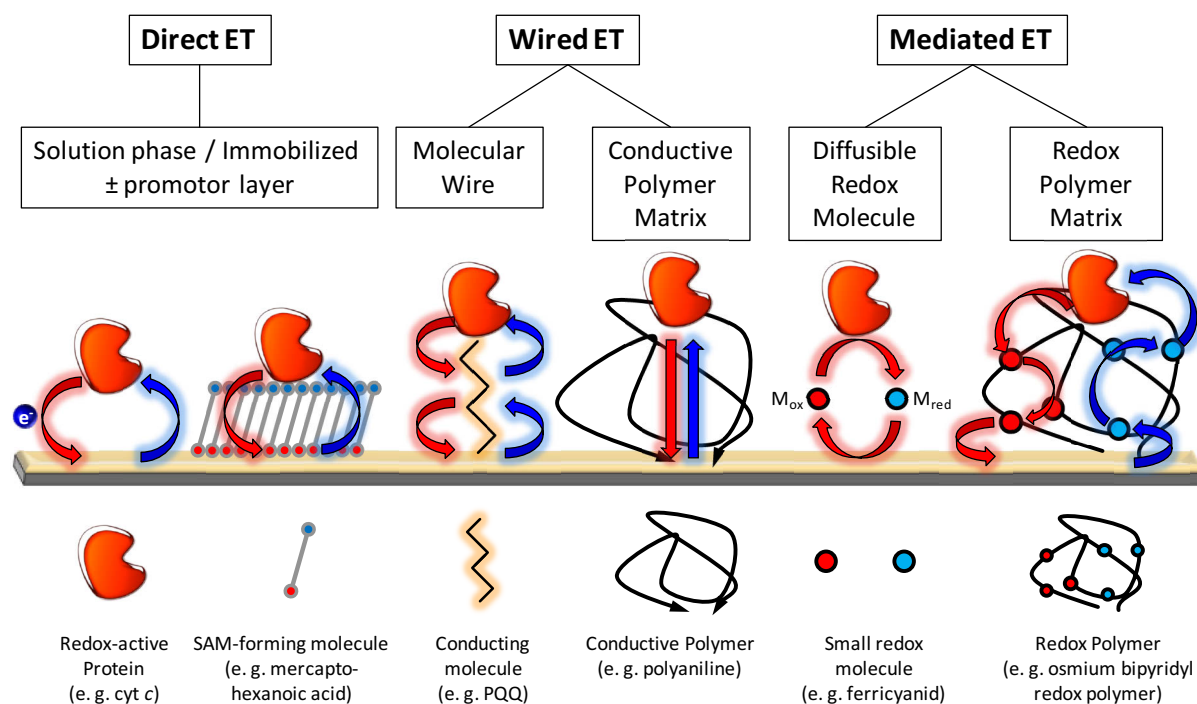


Fig. 8: Strategies for the electrical coupling of a redox-active protein to electrodes. These can be separated into three groups: direct electron transfer, wired electron transfer and mediated electron transfer. ET exchange reactions are displayed by arrows; red/blue arrows show anodic/cathodic current flow, depending on the electrode applied bias potential. The protein can be either immobilized on the electrode, as well in the solution phase.

The second and third group, the wired or mediated ET, show a higher variability of strategies. The ET reaction in the wired approach is guided through a coupled conducting molecule (molecular wire), respectively a conducting polymer, transporting electrons *via* the polymer matrix. The DET reaction can be accelerated by using a wire, which improves electron-tunneling probability and thus ET rates with the electrode. Here, diffusion-limitation is barely the case, because the electron is travelling through the wire much faster, as if a chain of redox reactions have to occur to transport the electron to the protein. This would extend the time needed for the electron forwarding to/from the electrode and lower the overall ET rate.¹⁹⁰

In the mediated approach, the ET is mediated by a redox molecule or shuttle, transporting electrons from/to the protein from/to the electrode. This can be achieved by diffusible molecules or by redox polymers, where electrons are transported *via* localized redox centres in the polymer matrix by an electron hopping mechanism. For strategies using redox mediators, ET reactions can only start at the respective redox potential of the mediator and the rate-limiting step is either the rate of redox reaction of the mediator with the protein or of the

mediator with the electrode. For application in sensors however these transfer steps have to be much faster than the substrate conversion rate of the enzyme.

With diffusible redox molecules or the conductive/redox-polymer matrix approach, the orientation of proteins does not play a major role and immobilization of active protein amount beyond monolayer coverage is relatively easy to perform. This gives the opportunity to boost the performance through an increased amount of electrically addressable proteins. Typical examples for also improving amount of proteins are polyanilines (conductive polymers, wired ET) or redox-hydrogels (redox polymers, mediated ET), which can entrap proteins on the surface and connect proteins to the electrode beyond a monolayer coverage.¹⁹⁰

3.3 Photobioelectrodes: design, construction and assembly

Photobioelectrodes consist of a biological light-to-current converting component, mainly from photosynthesis, and an artificial electrode material. The efficient connection of both components is the main focus in current research and a number of various strategies have been developed so far. Photobioelectrodes can be classified a) by their main current flow direction, being either anodic, cathodic or both depending on the applied potential, or b) by the nature of the photoactive component. This classification helps to further develop efficient photobiovoltaic or photobioenzymatic devices. In the first device upon illumination a voltage and current flow is generated between two coupled electrodes. At least one of them has to be either a photoanode or a photocathode, which transfers the solar energy into electrical energy. For enzymatic systems, the solar energy is transferred to an enzyme producing energy-rich chemicals. The kind of enzyme (oxidase, reductase) and thus the chemical reaction determines the kind of photoelectrode needed for the construction of such devices. Often the chemical reduction of molecules lead to the desired energy-rich state, whereas for this purpose the combination of a reductase with a photocathode is of special importance.^{191,192}

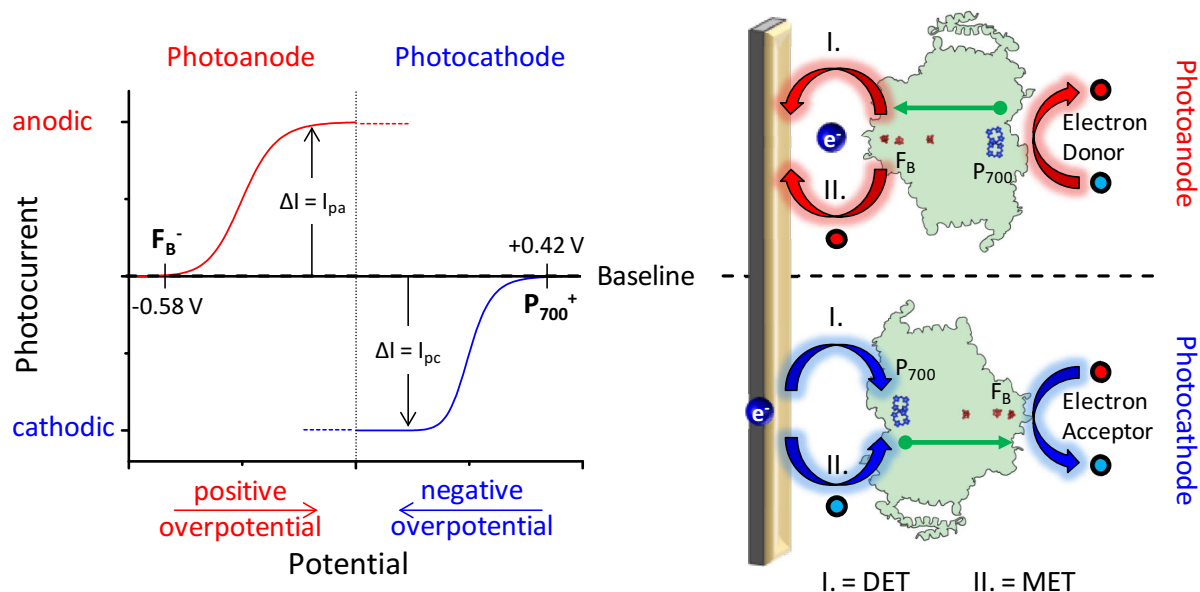


Fig. 9: Schematic representation of the basic principle of a photobioelectrode using photosystem I (PSI). **Left:** Photocurrent response depending on the applied electrode potential under illumination conditions. The plot can be separated into two situations, where solely cathodic (blue) or anodic (red) reactions at the start potentials of P_{700}^+ ($+0.42\text{ V}$) or F_B^- (-0.58 V) occur, with the cathodic photocurrent at negative overpotentials ($\Delta I = I_{pc}$ = negative) and anodic photocurrent at positive overpotentials ($\Delta I = I_{pa}$ = positive). Above or below the potentials of the PSI reaction centres, no photocurrent can be detected. A random orientation would nullify the photocurrent measured between potentials of P_{700}^+ and F_B^- (not shown). **Right:** Putative current flow for a PSI-using photoanode and photocathode in the presence of electron donor/acceptor molecules (red arrows: anodic current flow, blue arrows: cathodic current flow, green arrows: direction of intramolecular electron flow). The communication with the electrode is either established *via* a direct electron transfer (I. DET) or a mediated electron transfer (II. MET).

In this chapter, the focus is applied to photobioelectrodes using immobilized PSI as their light-to-current converting species. Due to the unidirectional electron-hole separation from the luminal to the stromal side of PSI (see chapter 3.1.3), the orientation and/or the direct coupling of the electron donor/acceptor site towards the electrode surface (F_B^- / P_{700}^+) is crucial for producing efficient photocathodes or photoanodes.¹⁹³ According to a mechanistic study, the majority of photocurrents are nullified if the fraction of orientation is below 80%.¹⁹⁴ Additionally, the overpotential at the electrode needed for the electron withdrawal has to be minimized according to the respective redox potential of the donor/acceptor side of PSI. This will maximize the usable potential gain during light excitation. In theory, when connecting the F_B^- to the electrode (either directly or *via* a mediator) an anodic photocurrent can be detected upon illumination. This means that for potentials $> -0.58\text{ V}$ a catalytic current at the electrode can be measured. Vice versa, when P_{700}^+ is connected to the electrode a cathodic photocurrent at potentials below $+0.42\text{ V}$ will be observed during illumination. In both cases, a suitable

electron donor or acceptor has to be present in solution. If random orientation or connection occurs, both photocurrent directions are suppressed by the opposing current direction. It has to be mentioned here, that the magnitude of photocurrent is also dependent on the electron donor and electron acceptor compound, which is not necessarily present in solution. Producing solely unidirectional, stable and high photocurrents with low onset potentials is the aim for developing photobioelectrodes.

3.3.1 PSI on gold: strategies for immobilization and DET

First investigations started to understand the orientation of PSI on short alkanethiols using -OH, -COOH, and -SH terminated SAMs on gold surfaces, resulting in a randomized orientation for all three terminal groups, having the highest uniformity (~70 %) on hydroxyl-groups.¹⁹⁵ Another strategy adsorbed PSI first on a mercaptohexanol SAM modified gold surface including a second step of backfilling hydrophobic methyl-terminated alkanethiols (C₂₂SH). This can mimic a thylakoid membrane, whereas the large membrane-protein can be trapped on the surface, resulting in a higher protein stability against various solvents.¹⁹⁶ Furthermore, the effect of surfactant on the PSI adsorption capacity has been investigated on polar, nonpolar and negatively charged alkanethiols, whereby especially Triton-X prevents PSI from adsorbing to the surface.¹⁹⁷ Ciobanu *et al.* 2007 were able to measure DET reaction of F_A, F_B and P₇₀₀ from immobilized PSI on hydroxyl-terminated alkanethiol modified gold electrode by cyclic voltammetry, unfortunately the produced photocurrents were very low (> 1 nA).¹⁹⁸

With the application of an electrical field, the adsorption of PSI onto a SAM-modified hydroxyl-terminated gold electrode results in a better control of the assembly morphology of PSI. Therefore, bulk aggregation of PSI on the surface could be prevented. Nonetheless, for a gravity-driven adsorption of PSI, at high protein concentrations, columnar aggregates on the surface were found, due to an enhanced protein-protein interaction. On the contrary lower concentrations lead to a uniform monolayer of PSI.^{199,200} Furthermore, an electrophoretic deposition of PSI on SAM-modified gold electrodes by applying a potential of -2 V for 5 min can yield a uniform and dense-packed PSI monolayer on various polar or charged terminal groups, nevertheless the ET is still slow ($\sim 5 \text{ e}^- \text{ PSI}^{-1} \text{ s}^{-1}$) and diffusible mediator molecules are needed for the generation of photocurrents in the low nA region.²⁰¹ Single amino acid mutation (Y635C) on the luminal side of PSI has been used to directly chemisorb PSI onto gold surfaces, while PSI could be assembled in 3 consecutive multilayer connected by

photoreduced platinum, interestingly, the photovoltage increased with the number of PSI/Pt layers up to 386 mV but no currents have been reported.²⁰² A covalent coupling approach have been done *via* binding PSI on a Au-SAM with terminal aldehyde groups producing imine bonds. Here, the arrangement of PSI molecules was carried out by a rapid assembly under vacuum. Even on an unmodified gold surface, cathodic photocurrents have been achieved up to 100 nA cm^{-2} .²⁰³ The same covalent-coupling approach has been used with PSI reacting from solution with a nanoporous gold leaf electrode, exhibiting photocurrents up to 800 nA cm^{-2} .²⁰⁴ SAM-modified gold nanoparticle (GNP) / PSI hybrids on gold electrodes show anodic photocurrents of 1600 nA cm^{-2} .²⁰⁵ The reconstitution at a surface-fixed molecular wire (vitamin K) binding to the A₁ quinone pocket of PSI in a GNP / PSI hybrid approach produced lower photocurrents.²⁰⁵ However, by leaving out the GNPs, evidence has been presented, that electron transfer *via* the molecular wire is faster, if directly coupled to a modified gold electrode.²⁰⁶ Both approaches have been used as photosensor, where excitation of PSI controls the voltage between gate and source in a field effect transistor (FET).^{207,208}

3.3.2 Wired / mediated electron transfer of PSI with electrodes

Efrati *et al.* 2012 uses PQQ in a covalent approach for the attachment and molecular wiring of PSI to gold electrodes. Here, depending on the applied potential, anodic ($\sim 60 \text{ nA}$) and cathodic ($\sim 20 \text{ nA}$) photocurrents can be produced.²⁰⁹ The cross-linking of PSI to gold surfaces can also been done with bis-aniline, either with and without Pt nanoparticles and Fdx as electron shuttle proposing an anodic multi-electron hopping mechanism up to 1000 nA .²¹⁰ The use of redox-polymers for the entrapment of PSI beyond a monolayer, and the electrical connection of the multilayered PSI molecules provided a strong improvement compared to the slow DET on monolayer electrodes. Another approach applies poly-benzyl viologen polymers for the layer-by-layer deposition and connection of PSI onto ITO, whereas anodic photocurrents could be achieved ($\sim 2.4 \text{ } \mu\text{A cm}^{-2}$).²¹¹ The entrapment of PSI was also achieved by electropolymerization of polyaniline in the presence of the protein, and has shown a moderate photocurrent density of $5.7 \text{ } \mu\text{A cm}^{-2}$, but a low turnover number of $1.4 \text{ e}^- \text{ s}^{-1} \text{ PSI}^{-1}$.²¹² By using polyvinylimidazole/Os(bpy)₂Cl₂ as the interconnector between a gold electrode and PSI, investigations on the behaviour of cyanobacterial trimeric and monomeric forms of PSI resulted in similar photocurrents and photo-bleaching stability, but for the monomeric form light-saturation occurs at lower light intensities.⁹⁶ In another study, Nafion is used in combination with Os(bpy)₂Cl₂, scavenging photo-holes and producing cathodic photocurrents ($2.5 \text{ } \mu\text{A cm}^{-2}$).²¹³ Badura *et al.* 2011 have used an osmium-based hydrogel entrapping PSI,

which produced strictly cathodic photocurrents up to $29 \mu\text{A cm}^{-2}$.²¹⁴ Furthermore, the modification of the osmium polymer adjusting their hydrophobic/hydrophilic balance could increase photocurrent densities (up to $70 \mu\text{A cm}^{-2}$), while a pH induced collapse of the hydrogel demonstrate even higher performances and one of the highest turnover numbers ($\sim 100 \mu\text{A cm}^{-2}$, $335 \text{ e}^- \text{ s}^{-1} \text{ PSI}^{-1}$).^{215,216}

3.3.3 Photosystem I on other conductive materials

Since gold surfaces can be used relatively well with respect to basic investigations of PSI assembly, other materials may provide a more sophisticated surface for building up biohybrid photo-electrodes. Various surface materials like n/p-doped silicon²¹⁷, GaAs²¹⁸, TiO_2 ²¹⁹, TiO_2/ZnO ²²⁰, CNTs²²¹, graphene²²², graphene oxide²²³, reduced graphene oxide²²⁴, organosilicate hydrogel²²⁵ and ITO²¹¹ have been exploited. Especially on semiconductor surfaces, not much attention was paid to verify intactness of PSI being the source of photocurrents. However this is necessary, since the used materials already have shown high photocurrents without PSI.^{217,220,224} The choice of diffusible electron acceptor/donor molecules was also critical, since these species show light-dependent reactions with electrodes as well and the occurring reactions at the electrode can be much more complex.^{191,226} One example on heavily p-doped Si / PSI macrolayer shows a high variance in reported photocurrent values, since high cathodic photocurrents of $875 \mu\text{A cm}^{-2}$ have been measured²¹⁷, but reporting only $15 \mu\text{A cm}^{-2}$ when used in a solid-state application²²⁷. If graphene oxide is used in the PSI macrolayer $140 \mu\text{A cm}^{-2}$ have been produced.²²³ The highest anodic photocurrent produced so far is 2.5 mA cm^{-2} , which relied on the electrosprayed deposition of PSI onto nanostructured TiO_2 . The base material itself exhibited already photocurrents up to 1.5 mA cm^{-2} , nonetheless being the top performance electrode so far.²²⁸

3.3.4 Photobiovoltaic and photobioenzymatic systems

As stated before, photobiovoltaic and photobioenzymatic devices are the long-term goal for investigating photo-biohybrid electrodes. They rely on the connection of two photoelectrodes (anode, cathode) or the integration of an additional enzyme/artificial catalyst for the production of interesting chemicals like hydrogen. Z-scheme mimicking electrode designs have already been presented, where both PSI and PSII are coupled on one electrode, or separated onto two electrodes (PSI-electrode, PSII-electrode). One approach has shown this by coupling platinized PSI onto an ITO electrode further cross-linking PSII *via* polyvinyl

pyridine/methyl pyridinium cyt *c* to PSI. The light-reaction splits water, but produced only photocurrents about 220 nA cm^{-2} .²²⁹ Another study used two osmium hydrogels with different redox potentials to integrate PSI and PSII on two separate electrodes in a photobioelectrochemical cell. Here, the anodic reaction of the PSII-electrode splits water, where protons and molecular oxygen can diffuse to the cathode half-cell being converted to water again during the PSI reduction reaction.²³⁰ Being the current and voltage-limiting half-cell, PSII-electrodes have been improved by using phenothiazine redox-polymers, increasing the cell power from nW cm^{-2} to $\mu\text{W cm}^{-2}$.²³¹

First examples have been shown for the conversion of solar to chemical energy. By this the excited electrons are transferred from PSI to protons *via* a catalytically active molecule (e. g. hydrogenase) in solution, forming hydrogen. This has been done by a variety of catalysts, resulting in different hydrogen evolution rates, including the use of a [NiFe]-hydrogenase (0.01 s^{-1})²³², cobaloxime (2.83 s^{-1})²³³, Pt nanoparticles (5.83 s^{-1})²³⁴, [FeFe]-hydrogenase (52.4 s^{-1})²³⁵. The NiFe-hydrogenase-PSI nanobiohybrid construct have been coupled *via* Ni-NTA in a monolayer to gold electrodes and was able to produce $120 \text{ pmol H}_2 \text{ s}^{-1} \text{ cm}^{-2}$.²³⁶ Another study have coupled Pt nanoparticles to the F_B cluster of an osmium-hydrogel entrapped PSI, which produced detectable hydrogen after light excitation, nevertheless the faradaic yield was low.²³⁷

Much more attention was drawn to biophotovoltaic cells based on a solid state or dye sensitized solar cell approaches. One of the first examples used a direct coupling approach to immobilize PSI stromally down *via* reconstitution of PsaD-His₆ on Ni-NTA gold surfaces with a organic semiconductor, tris(8-hydroxyquinoline) aluminium backed with a silver counter electrode. In the same study, another device has been produced with a very similar approach using bacterial reaction center (bRC). The study has not reported photovoltaic parameters for the PSI containing device, but the bRC device generated short circuit current densities of about $120 \mu\text{A cm}^{-2}$ under very high light intensities (10 W cm^{-2}).²³⁸ In another approach PSI was assembled on TiO_x on an ITO electrode and covered with a conductive polymer/fullerene mixture. As the counter electrode, either MoO_3/Al or LiF/Al has been used. The bulk heterojunction produced around $300 \mu\text{A cm}^{-2}$ and open circuit voltages of 390 mV. Nevertheless, the impact of using PSI was rather low, whereas the major performance (70-90 %) resulted from the other integrated components.²³⁹ The benefit from PSI was better visible in a system from Beam *et al.* 2015, who constructed a p-doped silicon/PSI/ZnO solid state photovoltaic cell, while depositing ZnO as the counter electrode on a PSI multilayer

using a chemical deposition process.²²⁷ By etching and roughening the p-doped silicon, they could improve short-circuit photocurrents by one order of magnitude up to $127 \mu\text{A cm}^{-2}$ ($V_{\text{OC}} = 214 \text{ mV}$).²²⁷ With electropolymerized polyaniline-PSI on ITO/TiO₂ with a Ag counter electrode, $72 \mu\text{A cm}^{-2}$ ($V_{\text{OC}} = 299 \text{ mV}$) have been achieved.²⁴⁰ Cross-linked PSI-LHCI on charged mesoporous hematite (Fe₂O₃) deposited as multilayer, was used as a dye-sensitized solar cell producing $56 \mu\text{A cm}^{-2}$ ($V_{\text{OC}} = 321 \text{ mV}$), but was also able to produce H₂ ($744 \mu\text{mol mg Chl}^{-1} \text{ h}^{-1}$), which was reduced at the Pt counter electrode.²⁴¹

However, many interesting systems have been produced so far, but the evaluation of photobioelectrodes is often very difficult. The reason for this can be seen by the usage of different experimental conditions with no uniform standard procedure (e. g. diffusible electron donors/acceptors, light intensities or electrode geometries). Additionally, not all information is provided by the corresponding study, hence making it challenging to classify the results and derive instructions for further development. In this thesis, this issue will be discussed more in detail in chapter 5.2.

4. Results

4.1 Advanced unidirectional photocurrent generation *via* cytochrome *c* as reaction partner for directed assembly of photosystem I

Authors: Kai R. Stieger, Sven C. Feifel, Heiko Lokstein and Fred Lisdat

Abstract

Conversion of light into an electrical current based on biohybrid systems mimicking natural photosynthesis is becoming increasingly popular. Photosystem I (PSI) is particularly useful in such photo-bioelectrochemical devices. Herein, we report on a novel biomimetic approach for an effective assembly of photosystem I with the electron transfer carrier cytochrome *c* (cyt *c*), deposited on a thiol-modified gold-surface. Atomic force microscopy and surface plasmon resonance measurements have been used for characterization of the assembly process. Photoelectrochemical experiments demonstrate a cyt *c* mediated generation of an enhanced unidirectional cathodic photocurrent. Here, cyt *c* can act as a template for the assembly of an oriented and dense layer of PS I and as wiring agent to direct the electrons from the electrode towards the photosynthetic reaction center of PSI. Furthermore, three-dimensional protein architectures have been formed *via* the layer-by-layer deposition technique resulting in a successive increase in photocurrent densities. An intermittent cyt *c* layer is essential for an efficient connection of PSI layers with the electrode and for an improvement of photocurrent densities.

Introduction

Artificial systems exploiting the features of natural photosynthesis are increasingly becoming a focus of current research.^{192,193} Particularly the two photosystems (PS) of the oxygenic photosynthesis have attracted the attention of researchers to build up new biohybrid solar energy-converting systems.^{211,230,242} In photosystem I (PSI) absorption of light results in charge separation with a quantum efficiency of nearly unity.²⁵ Moreover, PSI can be readily isolated from plants and cyanobacteria with a high yield, thus PSI is frequently used as a natural resource in biohybrid light converting entities.^{83,243,244} In such systems efficient

coupling of PSI with electrodes is essential. Besides the light-to-current conversion, PSI may also be used for light-driven redox and/or enzymatic reactions.

In the thermophilic cyanobacterium *Thermosynechococcus elongatus* (*T. elongatus*), PSI is a trimeric pigment-protein super-complex with 12 different protein subunits, harbouring 96 chlorophylls *a* (Chl *a*) – per monomeric subunit. Most Chls serve as light-harvesting antenna pigments and 6 Chls form the electron transport chain.⁷⁸ Electron transfer in PSI starts at a luminal pigment dimer, Chl *a*/Chl *a*' (P₇₀₀) finally leading to a reduction of the stromal-located terminal iron-sulfur-cluster (F_B).^{83,244}

To date several approaches of coupling PSI to gold surfaces have been described. One of them is the covalent fixation of PSI, which has been achieved mainly *via* amino-reactive surface chemistry in order to obtain fixation and a short distance of the reaction center to the electrode for direct electron transfer (DET).^{203,204} Improvements in surface enlargements by using meso- and nanostructured surfaces have been reported, for example coupling PSI with gold-nanoparticles²⁰⁵ and on nanoporous gold leaves²⁰⁴. A molecular wiring approach have been accomplished by reconstitution of PSI with vitamin K₁ derivatives.²⁰⁶ Application of crosslinked Platinum-nanoparticle/PSI composites with ferredoxin²¹⁰ or pyrroloquinoline quinone-linked PSI as a biohybrid relay assembly²⁰⁹ have also been reported. Additionally, PSI has been assembled in a non-covalent fashion onto different self-assembling monolayers (SAM) with terminal carboxyl-, hydroxyl- or amino-functions *via* adsorption.^{196–199,201,245,246} Nevertheless, DET from PSI to a transducer results rather often in minor photocurrent densities, mainly due to long electron tunneling distances between the reaction center and the electrode. Owing to the embedding of PSI in an Osmium-complex containing redox polymer such issues as long electron transfer distances and low active protein density have been overcome.²¹⁴ Recent investigations also address indirect electron transfer (IET) with various combinations of redox mediators in solution.²²⁶ However, in general current approaches result in photocurrent densities, which are orders of magnitude lower than those predicted by theoretical calculations, in particular, taking into account the high quantum efficiency of PSI, the fast intramolecular rate of charge separation (< 1 µs) and assuming an optimal PSI surface coverage of 0.5 pmol cm⁻².^{59,207} One reason is related to the lack of controlled orientation of PSI on the electrode surface¹⁹⁴, another may be the limited accessibility of mediator molecules to PSI.²²⁶

In the present work, we use cytochrome *c* (cyt *c*) as a tool for the assembly of PSI. The electrochemistry of this small redox protein (~12 kDa) and the adsorption processes onto modified gold-electrodes are quite well understood.^{137,144,247} Very recently, a similar attempt has been accomplished using a cyt *c* polymer complex to connect PSI to an electrode.²²⁹ In this study, we apply a different strategy by coupling cyt *c* *via* self-assembling monolayers, which provides a very stable and efficient electrical connection of cyt *c* with the electrode. We also address detailed investigations on the conditions under which cyt *c* can act as a protein scaffold for a non-covalent assembly of PSI, e. g. pH of buffer, PSI concentration and time period. Atomic force microscopy is used to elucidate the complex surface structure of the cyt *c* – PSI bilayer formation. Furthermore the capability for an efficient electron transfer in a surface-fixed state is explored, resulting in a unidirectional generation of photocurrents. In addition, we demonstrate a next step of development by building-up three dimensional cyt *c*/PSI architectures in order to obtain enhanced photocurrent densities. This novel approach displays the potential of cyt *c* to act as molecular protein scaffold for connecting PSI with electrodes, even if the biomolecules are immobilized rather far from the electrode surface.

Experimental Section

Isolation of Photosystem I from *T. elongatus*

Trimeric PSI has been isolated from *T. elongatus* essentially as described previously.^{248,249} The PSI containing fraction has been further purified by one or two sucrose gradient ultracentrifugation steps as required. Functionality of PSI has been assessed as light-driven electron transport from ascorbate-reduced 2,6-dichloroindophenol to methyl viologen (1,1'-dimethyl-4,4'-bipyridinium, MV²⁺) with a Clark-type electrode (Oxyview-1, Hansatech, King's Lynn, UK). Typical light-induced oxygen consumption rates were on the order of 3.5 $\mu\text{mol mg}^{-1} \text{ Chl } a * \text{min}^{-1}$. Fluorescence emission spectra measured at RT and 77 K indicated the integrity of the excitation energy transfer chain in PSI.

Preparation of Au-SAM/cyt *c*/PSI mono- and multilayer electrodes

Au-rod-electrodes (CHI) with an accessible geometrical surface of 0.0314 cm² have been cleaned with abrasive paper (P1200, P2500, P3000) and subsequently cycled between -0.2 and 1.6 V (vs. Ag|AgCl) in 100 mM sulfuric acid. Followed by an incubation for 48 h at RT with an ethanolic solution of a 3:1 mixture containing 11-mercapto-1-undecanol (MU, Sigma)

and 11-mercaptoundecanoic acid (MUA, Sigma). Afterwards the electrode has been incubated with 30 μM cytochrome *c* (horse heart, Sigma) in phosphate buffer (5 mM, pH 7) for 2 h. Subsequently the Au-SAM/cyt *c* electrodes have been incubated in the dark with purified 0.2 μM PSI trimer in phosphate buffer (5 mM, pH 7) over night at 4 $^{\circ}\text{C}$ and were finally ready for measurements.

In multilayer preparations the Au-SAM/cyt *c*/PSI electrodes have been alternately incubated with 30 μM cyt *c* solution for 2 h at RT and 0.2 μM PSI trimer solution for 2 h at RT in phosphate buffer (5 mM, pH 7). At all incubation stages cyclic voltammograms have been recorded to verify the assembly process.

Electrochemical experiments

Electrochemical measurements have been performed using a potentiostat (Zennium, Zahner) and an electrochemical cell containing 5 mL of a phosphate buffer (5 mM, pH 7) a Pt counter electrode and an Ag|AgCl (3 M KCl) reference electrode. Cyclic voltammetric measurements have been performed at a scan rate of 100 mV s^{-1} and in a potential range from +300 to -300 mV.

Photoelectrochemical experiments

Photoelectrochemical measurements have been performed using an integrated system (CIMPS, Zahner) containing a white LED light source (4300 K, Zahner) with a continuous change of intensity (max. 100 mW cm^{-2}), an electrochemical cell and a photodiode with feedback control to the light source *via* a potentiostat (PP211, Zahner). Electrochemical investigations have been carried out through a coupled potentiostat (Zennium, Zahner). In all experiments a Pt counter electrode and an Ag|AgCl (3 M KCl) reference electrode have been used in an aqueous solution containing phosphate buffer (5 mM, pH 7). As a soluble electron mediator MV^{2+} has been used at a final concentration of 250 μM . Photochronoamperometric experiments have been performed at RT and different potentials (-100 mV, 200 mV, 500 mV *vs.* Ag|AgCl), while using an illumination time of 30 s. Chopped light voltammetry experiments have been done at a scan rate of 2 mV s^{-1} from 250 mV to -300 mV with a light intensity of 60 mW cm^{-2} and a light period time of 15 s.

Atomic force microscopy

Atomic force microscopy (AFM) images have been taken in the quantitative imaging (QI) mode in phosphate buffer (5 mM, pH 7) by the use of an atomic force microscope (Nanowizard 3, JPK) and a cantilever (0.7 N m^{-1} , Bruker). In all experiments an unused planar gold-chip (Xantec) with an rms surface roughness of about 0.2 - 0.4 nm served as substrate. The new Au surface has been incubated for 48 h at RT with a freshly prepared ethanolic solution of a 3:1 mixture containing MU and MUA. After extensively washing the surface with ethanol and phosphate buffer (5 mM, pH 7) the chip first has been incubated for 2 h at RT with 30 μM cyt *c* in phosphate buffer (5 mM, pH 7) and second treated with 0.2 μM PSI in phosphate buffer (5 mM, pH 7) over night in the dark at 4 °C. At all incubation stages AFM-images have been taken.

Surface plasmon resonance

Surface plasmon resonance (SPR) experiments have been performed on a Biacore T100 (GE Healthcare) at a constant flow rate of 1 $\mu\text{L min}^{-1}$ and 25 °C. Before use, Au sensor chips have been cleaned with low pressure air plasma. The clean Au surface has been incubated 48 h at RT with a freshly prepared ethanolic solution of a mixture containing MUA and MU. After the thorough washing of the surface with ethanol and phosphate buffer (5 mM, pH 7) the chip was ready to use. First cyt *c* has been adsorbed on the thiol layer and subsequently PSI solutions of different pH and concentration have been flushed over the surface.

Results and Discussion

Assembly of photosystem I on cytochrome *c*

In a first attempt, the non-covalent assembly of PSI on a cyt *c* monolayer (cyt *c* ML) has been investigated. This idea is based on the natural situation in which plastocyanin or cyt *c*₆ can act as an electron donor of PSI.^{52,250} In addition, it has been shown that cyt *c*₆ can mediate the reactivity of PSI with electrodes in solution.²⁵¹ *T. elongatus*-PSI has a luminal-located binding site close to P₇₀₀ suited for cyt *c*₆ interaction.⁸³ Although cyt *c* from horse heart is rather different from cyt *c*₆, it provides the advantages of fast reactions at electrodes and a high isoelectric point²⁵² (10 – 10.5), which leads to a pronounced electrostatic adsorption on negatively charged SAMs and may also support an improved interaction with PSI.

Hence, we have investigated the assembly process of PSI on a cyt *c* layer by surface plasmon resonance (SPR). The sensorgram in Fig. 1 demonstrates the assembly of PSI on a MUA/MU-modified gold-surface (see experimental section) with and without a subjacent cyt *c* monolayer. First a rather fast adsorption of cyt *c* on the MUA/MU-SAM is observed. This results in a surface concentration of $15 \pm 1 \text{ pmol cm}^{-2}$ ($n = 5$), which reflects well the protein amount detected *via* electrochemistry: from cyclic voltammetric experiments (CV) the cyt *c* surface concentration can be calculated to be $14 \pm 0.8 \text{ pmol cm}^{-2}$ ($n = 9$), which is in agreement with other studies described previously.^{137,144,247}

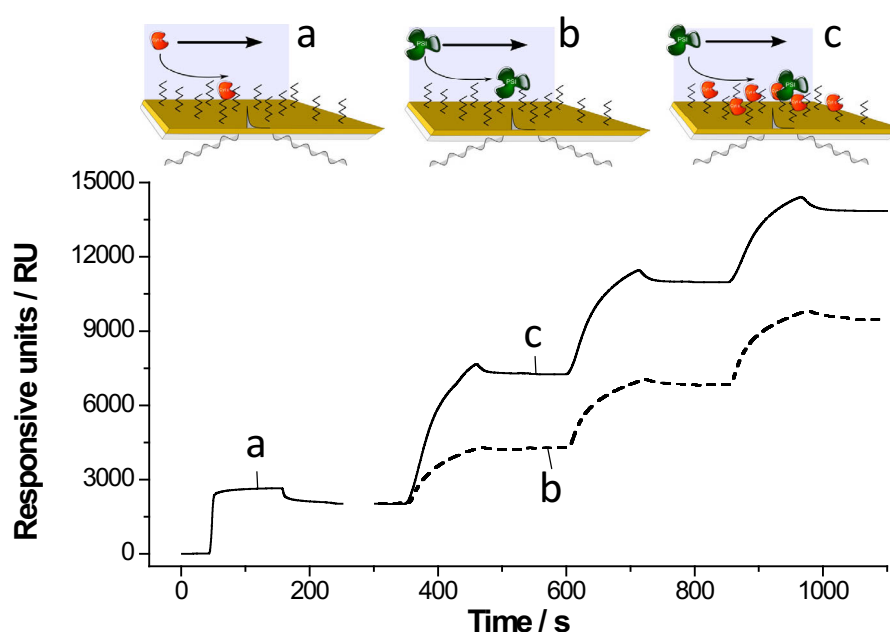


Fig. 1: Surface plasmon resonance (SPR) sensorgram of the assembly of cyt *c* and PSI on modified gold surfaces. (a) Deposition of cyt *c* on a SAM-modified gold surface, (b) Deposition of PSI on a SAM-modified gold surface and (c) Deposition of PSI on SAM-modified gold surface after deposition of cyt *c*. All experiments have been performed in phosphate buffer (5 mM, pH 7) in a flow system ($1 \mu\text{L min}^{-1}$). A mixture of 11-mercaptoundecanoic acid (MUA) and 11-mercapto-1-undecanol (MU) (1:3) have been used as SAMs for modification of the gold surface prior to the protein assembly.

The successful adsorption of PSI by injections on top of a cyt *c* ML can also be shown. In this experiment three subsequent PSI injections with intermittent buffer wash have been used in order to grant the system enough time for proper rearrangement on the surface and test for a potentially protein desorption (see Fig. 1). Given that 3 injection steps of PSI (2 min each) still result in a further mass increase, it can be concluded, that PSI exhibits a rather slow binding kinetics to the cyt *c* ML compared to the cyt *c* binding to MUA/MU. When PSI is flushed over a MUA/MU-modified surface a comparable slow adsorption behaviour can be

seen. However, a significantly reduced mass deposition is detected, demonstrating the importance of a subadjacent cyt *c* ML for an efficient PSI assembly process.

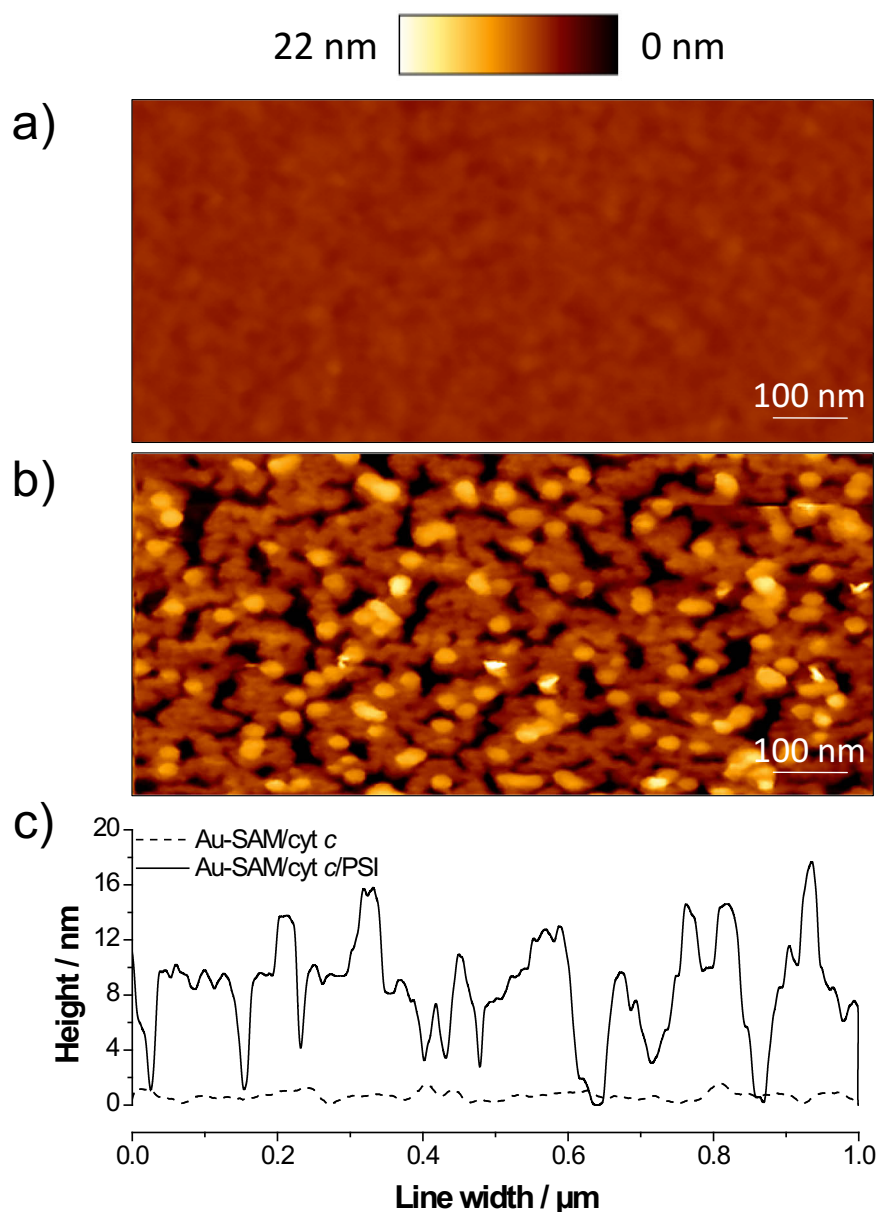


Fig. 2: Atomic force microscopy (AFM) images of cyt *c*/PSI assemblies on Au-SAM substrates. (a) AFM image of cyt *c* adsorbed to a SAM of MUA, MU (Au-SAM/cyt *c*). (b) AFM image of a PSI assembly on top of a cyt *c* monolayer (Au-SAM/cyt *c*/PSI). (c) Corresponding cross section graph of Au-SAM/cyt *c* (dashed) and Au-SAM/cyt *c*/PSI (solid) with a total line width of 1 μm . In (a) and (b) the colour scale is shown on the top of the Fig., ranging from 0 to 22 nm.

Further SPR experiments without intermittent buffer flow have been performed evaluating the best conditions for PSI adsorption onto a cyt *c* ML. When PSI is assembled with a concentration of 0.2 μM in a buffer with low ionic strength (5 mM phosphate buffer) at pH 7 most efficient protein deposition can be observed. Higher and lower concentrations of trimeric

PSI lead to a significant reduction of the assembly rate (see Fig. s1, ESI). Deposition experiments of PSI from a storage buffer (50 mM Tris, 0.04 % β -dodecyl-maltoside (β -DM), pH 8) also exhibits less mass accumulation due to the interaction of the detergent β -DM with the surface. Hence, a buffer exchange to low ion concentrations and a removal of β -DM have been performed.

A surface saturation with PSI can be achieved after an incubation time of 1 h resulting in a surface concentration of approximately 1 pmol cm^{-2} (see Fig. s2A, ESI). For PSI binding electrostatic forces are dominant at pH 7, due to a positive excess net-charge of cyt *c* and a prominent negative net-charge at the luminal side of PSI (see Fig. s3, ESI).^{199,253–256} A study of the pH-influence in the PSI deposition process on a cyt *c* ML, indicates clearly that a pH variation ranging from 8 to 6.5, has a quite strong impact on the PSI adsorption. This is due to the change in charge distribution on the protein surface (see Fig. s1A, ESI).

In order to confirm the deposition of PSI, AFM-measurements have been performed and are shown in Fig. 2. Because of the small size of cyt *c* and the formation of a densely packed monolayer, a rather low roughness can be found for the surface with the redox protein only. The PSI deposition however, changes the AFM-image compared to the cyt *c* layer displaying a dense structure with small gap-sections. Cross-section analysis has been carried out to elucidate the roughness-parameter for better comparison. The rms roughness for the cyt *c*-modified surface is about $0.3 \pm 0.1 \text{ nm}$ ($n = 3$). The roughness-value changes by one order of magnitude to $3.5 \pm 0.2 \text{ nm}$ ($n = 3$) for the deposition of PSI. The profile given in Fig. 2c and the increased roughness obviously confirm the deposition of a complete and rather compact layer of PSI. Additionally this is in very good agreement with the rather high surface concentrations found in SPR experiments.

Photocurrent generation of Au-SAM/cyt *c*/PSI electrodes

After verifying the successful assembly of trimeric PSI on cyt *c*-modified Au-surfaces, the functional properties of these cyt *c*/PSI systems have been investigated. First, we characterize the electrochemical properties of the cyt *c* layer with and without PSI on top by cyclic voltammetry. Following Fig. 3B, cyt *c* exhibits a quasi-reversible electrochemistry with a formal potential of $-8 \pm 4 \text{ mV vs. Ag|AgCl}$ ($n = 8$), a small peak separation of $12 \pm 2 \text{ mV}$ (at 100 mV s^{-1} , $n = 8$) and a surface slight conformational change around the heme group, altering the redox properties.

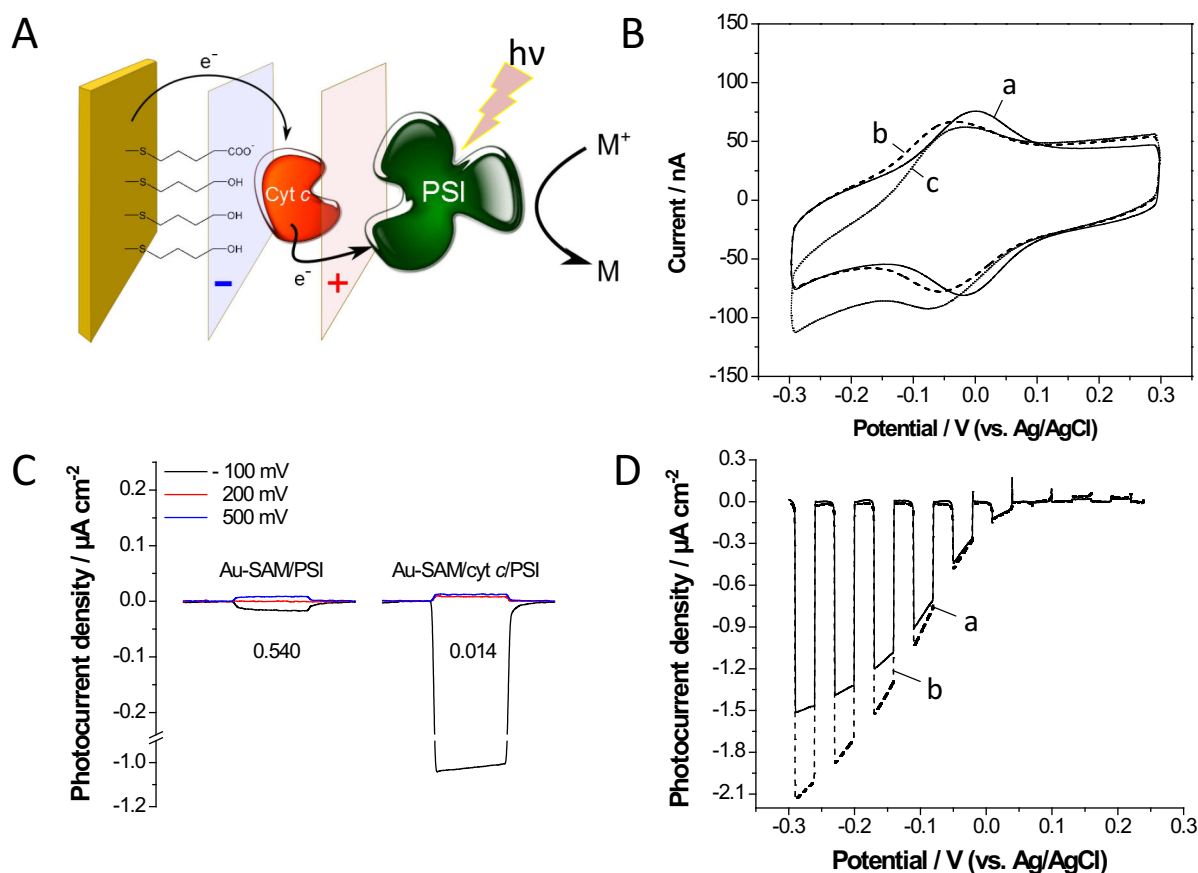


Fig. 3: Schematic electron flow in a cyt c/PSI assembly and photoelectrochemical experiments of Au-SAM/cyt c/PSI and Au-SAM/PSI: **(A)** After cyt c assembly on a MUA/MU-SAM PSI is deposited on the positively charged cyt c layer. Electrons can flow from the electrode *via* cyt c to PSI to reduce the reaction complex (P_{700}^+), when PSI is excited by light. A mediator (M) in solution oxidizes the reduced F_B^- iron sulfur cluster, which can be methyl viologen (MV^{2+}) and oxygen. **(B)** Cyclic voltammogram of (a) Au-SAM/cyt c and (b) Au-SAM/cyt c/PSI electrodes in the dark and (c) Au-SAM/cyt c/PSI electrode under illumination of 60 mW cm⁻² white light. **(C)** Photocurrent density generated at two assemblies Au-SAM/PSI and Au-SAM/cyt c/PSI at -100 mV (black), +200 mV (red) and +500 mV (blue) vs. Ag/AgCl with corresponding current ratio (anodic to cathodic). Please note the current axis has been interrupted for better visualization of the small photocurrents versus the cyt c mediated one. **(D)** Chopped light voltammetry of Au-SAM/cyt c/PSI (a) without MV^{2+} and (b) with MV^{2+} illuminated with white light of a power of 60 mW cm⁻². All measurements have been performed under aerobic conditions in phosphate buffer (5 mM, pH 7).

When the cyt c/PSI electrode is illuminated with a light-power of 60 mW cm⁻² a catalytic current with still detectable oxidation and reduction peaks is observed (Fig. 3B). It needs to be pointed out, that catalysis is rather efficient here, since it can be observed even at a higher scan rate (100 mV s⁻¹). The catalysis starts merely at the formal potential of cyt c, demonstrating that there is solely a photo-induced electron transfer from the electrode *via*

cyt *c* to PSI, which reduces the positively charged P_{700}^+ . This is schematically displayed in Fig. 3A.

Subsequently, the photocurrent has been measured at three different potentials (-100 mV, 200 mV and 500 mV *vs.* Ag|AgCl). The observations made are illustrated in Fig. 3C. Oxygen can oxidize the negatively charged iron-sulfur-cluster (F_B^-) located at the stromal side of the PSI (and thus can act as electron acceptor “ M^+ ” as illustrated in Fig. 3A). A significant photocurrent of $1 \mu A cm^{-2}$ can exclusively be observed at a negative polarization of the electrode (-100 mV *vs.* Ag|AgCl). At +500 mV *vs.* Ag|AgCl only a photocurrent of $13 nA cm^{-2}$ is found, as well as $9 nA cm^{-2}$ at +200 mV *vs.* Ag|AgCl, respectively. The ratio between anodic and cathodic photocurrents is calculated to be 0.014. This observation indicates a nearly unidirectional photocurrent generation, when PSI is assembled on a cyt *c* ML, emphasizing a rather well coverage of $14 \pm 0.8 pmol cm^{-2}$ ($n = 8$). The data verify the formation of a well-ordered cyt *c* ML and a fast electron transfer with the underlying electrode.

The subsequent adsorption of PSI on the cyt *c* ML can easily be recognized by a small potential shift towards lower potentials ($-45 \pm 2 mV$ *vs.* Ag|AgCl, $n = 5$). The interaction of PSI with cyt *c* in a surface-fixed state obviously results in a stabilized oxidation state of cyt *c* compared to the reduced one. Despite the potential change the transferred charge remains almost constant verifying that all previously accessible cyt *c* molecules are still electro-active, additionally without detachment from surface. However, the broadening of the half peak-width ($W_{0.5}$) of $75 \pm 3 mV$ ($n = 4$) to $83 \pm 3 mV$ ($n = 4$) indicates a change in the homogeneous state of the cyt *c* molecules in the monolayer to a slightly more heterogeneous one. After PSI deposition a change in the open circuit potential (OCP) can also be observed from 89 mV to 240 mV *vs.* Ag|AgCl. Although the measurements have been performed in the dark absorption of residual light cannot be completely excluded, which could result in cyt *c* oxidation and thus a shift in OCP. In summary these observations indicate a strong interaction, such as cyt *c* binds to the luminal side of PSI, which may cause an oriented PSI on the cyt *c* surface and a cyt *c*-mediated connection to the electrode.

To further evaluate the influence of cyt *c* on the photo-induced electron transport pathway a control electrode without cyt *c* has been prepared, taking into account that also other carboxyl-modified electrodes have been reported for PSI assembly and photocurrent generation.^{196–198,201,245,246} At a potential of -100 mV *vs.* Ag|AgCl such an electrode (Au-

SAM/PSI) generates only a rather small photocurrent of about 17 nA cm^{-2} . Additionally, a potential change to $+500 \text{ mV vs. Ag|AgCl}$ induces even smaller photocurrents, resulting in a ratio of anodic to cathodic current of 0.540. This clearly indicates that not only the magnitude of the photocurrent can be increased by the *cyt c* layer compared to the SAM approach, but also the proper orientation of immobilized PSI has been improved. Thus, the *cyt c*/PSI electrode can be considered as a biohybrid photodiode. Stability experiments of these electrodes reveal only about 20% loss in photo activity after 7 days stored at 4°C in buffer.

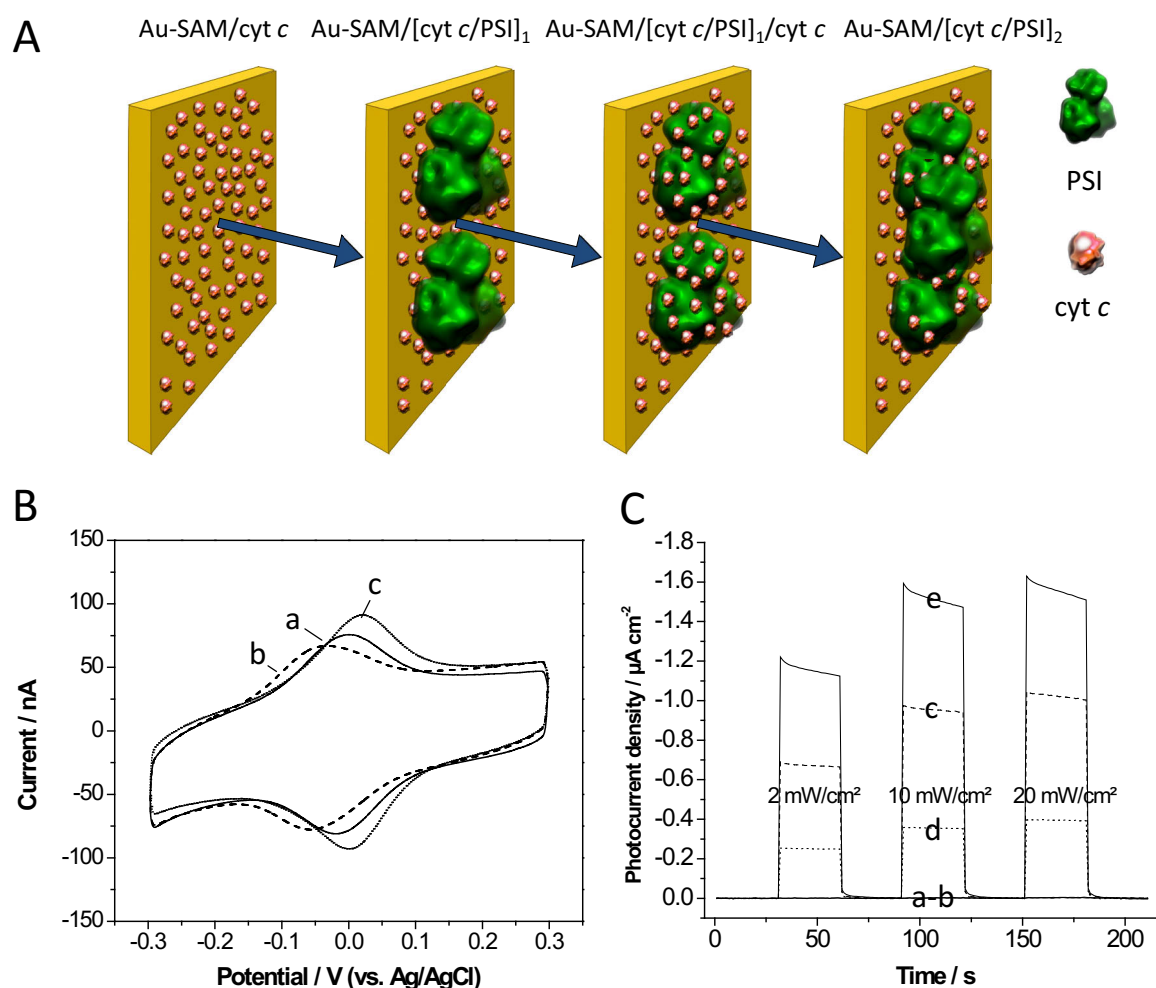


Fig. 4: (A) Scheme of the alternating assembly process of *cyt c*/PSI multilayers using the layer-by-layer technique and photoelectrochemical experiments of (*cyt c*/PSI) multilayers: (B) cyclic voltammogram in the dark with (a) *cyt c* monolayer electrode (Au-SAM/*cyt c*), (b) *cyt c*/PSI electrode (Au-SAM/[*cyt c*/PSI]₁) and (c) with a terminal *cyt c* layer on top of the *cyt c*/PSI electrode (Au-SAM/[*cyt c*/PSI]₁/*cyt c*). (C) Photochronoamperometric measurements of each successively added layer at three different light power (2 mW cm^{-2} , 10 mW cm^{-2} and 20 mW cm^{-2}) with (a) Au-SAM, (b) Au-SAM/*cyt c*, (c) Au-SAM/[*cyt c*/PSI]₁, (d) Au-SAM/[*cyt c*/PSI]₂ and (e) Au-SAM/[*cyt c*/PSI]₂/*cyt c* electrodes. Measurements have been performed under aerobic conditions and in phosphate buffer (5 mM, pH 7).

In a next characterization step the potential dependence of the cathodic photocurrent has been evaluated. In Fig. 3D a chopped light voltammetric experiment of an Au/SAM/cyt *c*/PSI electrode is displayed. Obviously the photocurrents are enhanced by decreasing the applied potential. In pure buffer oxygen acts as the electron acceptor in the system. Addition of the well-known electron acceptor MV²⁺ leads to an increase of the photocurrent and improves the withdrawal of electrons from the excited PSI. Notwithstanding, MV²⁺ is added to the solution, the potential dependence of the photocurrent is retained. The use of MV²⁺ has the advantage of not displaying any photochemical activity by itself or creating a shortcut with cyt *c*. Even though there is a strong MV²⁺ induced photocurrent enhancement at cathodic potentials, only tiny improvements are observed near the OCP. This observation is in accordance with the idea of a cyt *c* driven unidirectional assembly and the generation of an electron flow preferentially in one direction.

As a further characterization a light power dependence experiment without MV²⁺ has been performed with the Au-SAM/cyt *c*/PSI electrode (see Fig. s2B, ESI). In this case, already at low light intensities a fast rise in photocurrent is observed. The obtained curve is fitted with the Michaelis-Menten equation, an approach which has been proposed previously²¹⁴, assuming photons as substrate for PSI. However, the obtained fit is not accurate for low intensities. From the fit parameters a maximum photocurrent density of $0.97 \pm 0.01 \mu\text{A cm}^{-2}$ and a K_M of $2.4 \pm 0.1 \text{ mW cm}^{-2}$ can be derived.

Fig. 4B shows the cyclic voltammogram when cyt *c* is deposited on a cyt *c*/PSI electrode. The assembly process can readily be followed in the voltammetric analysis. Whereas the assembly of PSI on cyt *c* changes the potential of the underlying cyt *c* molecules as described before ($-45 \pm 2 \text{ mV vs. Ag|AgCl, } n = 5$), the subsequent assembly of cyt *c* on PSI results in a potential shift back to the positive direction ($11 \pm 3 \text{ mV vs. Ag|AgCl, } n = 5$) with a larger peak separation ($16 \pm 3 \text{ mV, } n = 5$). In addition, the electro-active amount of cyt *c* is increased to $28 \pm 3 \text{ pmol cm}^{-2}$ ($n = 5$). This demonstrates that the additionally deposited cyt *c* is in electrical contact with the electrode. The behaviour can be explained by interprotein cyt *c*–cyt *c* electron exchange as already has been verified previously in cyt *c* multilayers.^{175,179,257}

It also needs to be mentioned that a deposition of PSI on top of this layered system (Au-SAM/[cyt *c*/PSI]₂) decreases the redox potential again ($-2 \pm 4 \text{ mV vs. Ag|AgCl, } n = 5$). This effect is not as strong as with PSI deposited on the first cyt *c* layer, however reproducibly detectable. A further assembly step of cyt *c* on top of this layered system (Au-

SAM/[cyt *c*/PSI]₂/cyt *c*) shifts the redox potential back to a more positive potential of 16 ± 3 mV *vs.* Ag|AgCl ($n = 5$).

A functional analysis of the photocurrent generation with a successively assembled architecture of multiple layers (Au-SAM/[cyt *c*/PSI]₁/cyt *c*) at -100 mV *vs.* Ag|AgCl reveals a clear increase in photocurrent density compared to the Au-SAM/cyt *c*/PSI system. The use of cyt *c* as a surface confined electron shuttle on top of the cyt *c*/PSI layer enhances the cathodic photocurrent additionally by at least 11 %, indicating that not all previously immobilized PSI molecules are in electrical contact with the electrode. The additional cyt *c* molecules connect electrochemically some improperly orientated PSI molecules. Even higher photocurrents are generated when a two bilayer system with a terminal cyt *c* layer (Au-SAM/[cyt *c*/PSI]₂/cyt *c*) is analyzed, as illustrated in Fig. 4C. The resulting photocurrent is increased by 40 %. Further experiments at positive potentials do not lead to a significant rise in anodic photocurrent density, which also supports the idea of a cyt *c* – based connection of the P₇₀₀ complex in PSI with the electrode.

Even though the hybrid systems are assembled in a layer-by-layer fashion this does not result in well separated PSI and cyt *c* layers. Considering the size differences between PSI and cyt *c* and the observed photocurrent behaviour of the multilayered electrode, it can be concluded that the cyt *c* molecules assemble around the PSI (i.e. on the accessible area of the PSI-complex). At this point it needs also to be stressed, that the terminal cyt *c* assembly is essential for a reasonable photocurrent since the two bilayer system of Au-SAM/[cyt *c*/PSI]₂ turns out to generate less photocurrent output (reduction of 30 %, see Fig. 4C). This observation is in agreement with the behaviour found for a cyt *c* assembly on top of one bilayer system cyt *c*/PSI, which also results in an improved electrochemical connection of the large PSI complex with the electrode surface.

Conclusions

In the present study we have demonstrated the possibility of electrochemically connecting photosystem I with an electrode transducer *via* the electron carrier protein cytochrome *c* on MUA/MU-modified gold surfaces. Assembly studies have elucidated the formation of a dense PSI layer on such cyt *c* electrodes and an enhanced protein deposition compared to electrodes with only a SAM-layer. A cyt *c*/PSI system clearly displays enhanced photocurrent densities and also leads to a unidirectional photocurrent generation indicating a cyt *c* driven orientation

of PSI. A particular feature of this system can be seen in the finding that the process of assembly can be nicely followed *via* cyclic voltammetry, since the deposition of PSI changes the redox potential of cyt *c* noticeably.

Moreover, 3D architectures of cyt *c*/PSI have been accomplished based on the layer-by-layer deposition technique. In such multilayered systems, cyt *c* acts as a wiring agent between the separated PSI layers and the electrode. Owing to the well established communication between cyt *c* and the electrode and the high density of PSI molecules assembled on the electrode, rather large photocurrents have been achieved. This system highlights the importance of biomimetic approaches using natural building blocks to create artificial signal chains. It can also provide a biohybrid platform for the development of light driven enzyme cascades producing valuable chemical compounds.

Acknowledgements

We gratefully acknowledge the support of this research by the Bundesministerium für Bildung und Forschung BMBF, Germany (Biotechnologie 2020+, projects: 031A154A+B) and BBSRC/EuroCores (BB/J00823011).

Supporting Information

(I) Assembly Study of photosystem I on cytochrome *c* modified electrodes

1A) Dependence of protein deposition on pH

Assembly studies have been performed to verify the optimal conditions to deposit photosystem I (PSI) on cytochrome *c* (cyt *c*). First, SPR-experiments have been done showing the influence of pH on the assembly process. Cyt *c* has been injected for 120 s at a flow rate of 1 $\mu\text{L min}^{-1}$ in a concentration of 30 μM in phosphate buffer (5 mM) with different pH (6.5-8) on a prior modified mercaptoundecanoic acid / mercaptoundecanol (MUA/MU, 1:3) gold-chip. Afterwards PSI has been injected for 120 s at a flow rate of 1 $\mu\text{L min}^{-1}$ in a concentration of about 1.5 μM in phosphate buffer (5 mM) with corresponding pH. In Fig. S1A, the surface concentration after the injection step is plotted against the used pH. Here, the cyt *c* assembly exhibits a strong reduction in surface concentration at pH 6.5 compared to the other pH values. For the PSI adsorption a clear maximum was found at pH 7. For further studies, all experiments have been carried out at pH 7.

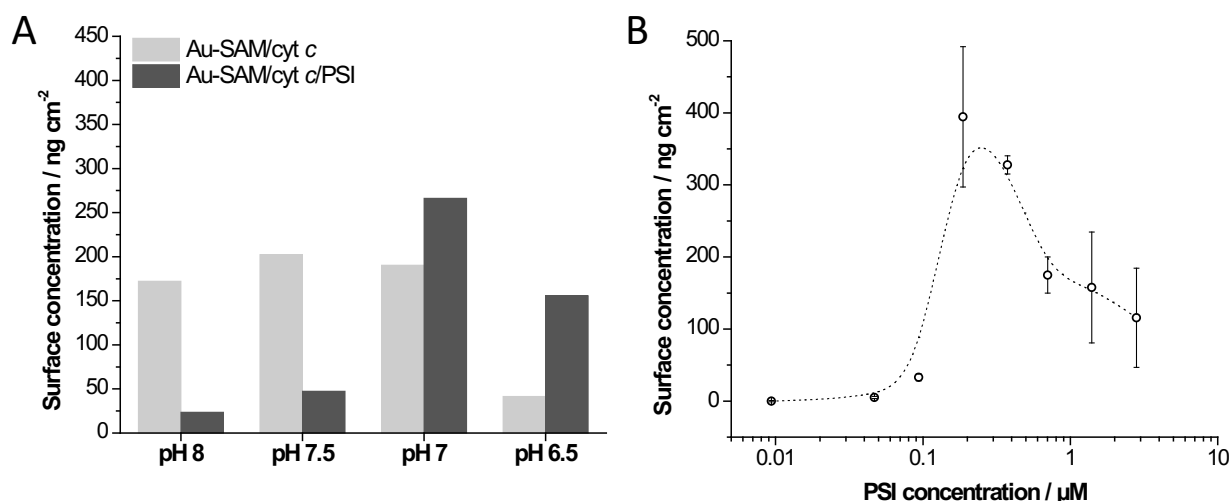


Fig. S1: Surface plasmon resonance (SPR) experiments to elucidate the assembly conditions of photosystem I (PSI) on a cytochrome *c* (cyt *c*) monolayer. Here, the pH of the assembly buffer was changed from pH 8 to pH 6.5 to verify the best interaction between cyt *c* and PSI. At pH 7 PSI concentration was changed to investigate the optimal protein concentration for the highest mass deposition. **(A)** Dependence of cyt *c* assembly (grey) on a mercaptoundecanoic acid / mercaptoundecanol (MUA/MU) 1:3 modified gold-surface and photosystem I assembly (black) on a MUA/MU/cyt *c* surface according to the pH of the assembly buffer. **(B)** Concentration dependence of PSI assembled on a MUA/MU/cyt *c* modified gold-surface. Surface concentration is calculated from responsive units (RU). For experimental details see text.

1B) Dependence of PSI deposition on concentration

In a next set of SPR experiments PSI has been injected for 120 s at a flow rate of 1 $\mu\text{L min}^{-1}$ at different concentrations to a surface with an adsorbed monolayer of cyt *c*. Prior to this injection the cyt *c* monolayer has been formed by injecting cyt *c* in a concentration of 30 μM for 120 s at a flow rate of 1 $\mu\text{L min}^{-1}$ in phosphate buffer (5 mM, pH 7) to a MUA/MU-modified gold chip. Fig. s1B shows the concentration dependence of mass deposition of PSI. The maximum surface concentration within this time frame can be achieved at a concentration of approximately 0.2 to 0.3 μM . Higher or lower concentrations decrease the rate of protein adsorption. For further experiments PSI has been used at a concentration of 0.2 μM .

2A) Time dependence of PSI deposition

In this SPR experiment the time dependent adsorption of PSI to a cyt *c* monolayer was studied for different time intervals. Here, a 0.2 μM PSI solution have been flushed over the surface from 2 until 120 min. The cyt *c* monolayer has been prepared by injecting cyt *c* to a MUA/MU-modified gold chip for 120 s at a flow rate of 1 $\mu\text{L min}^{-1}$ in phosphate buffer (5 mM, pH 7). The result is shown in Fig. s2A. The maximum surface concentration is

reached at about 60 min. The one-site-binding equation has been used to fit the curve, which exhibits a saturated surface concentration of 1085 ng cm^{-2} ($\sim 1 \text{ pmol cm}^{-2}$).

2B) Dependence of the photocurrent output of an Au-SAM/cyt *c*/PSI electrode on the light power

Photocurrent densities have been measured under various light intensities of a white light LED lamp (Zahner) ranging from either $0 - 20 \text{ mW cm}^{-2}$ and $0 - 60 \text{ mW cm}^{-2}$, without any additional electron acceptor in solution. This experiment has been performed under aerobic conditions in phosphate buffer (5 mM, pH 7). To fit the curves the Michaelis-Menten equation have been used considering PSI as photon converting enzyme and photons as substrate as previously proposed by Badura *et al.* 2011.²¹⁴ The light intensity is proportional to the photon concentration. In Fig. S2B the data and the fit are shown. At low light power the photocurrent densities do not follow the kinetic model.

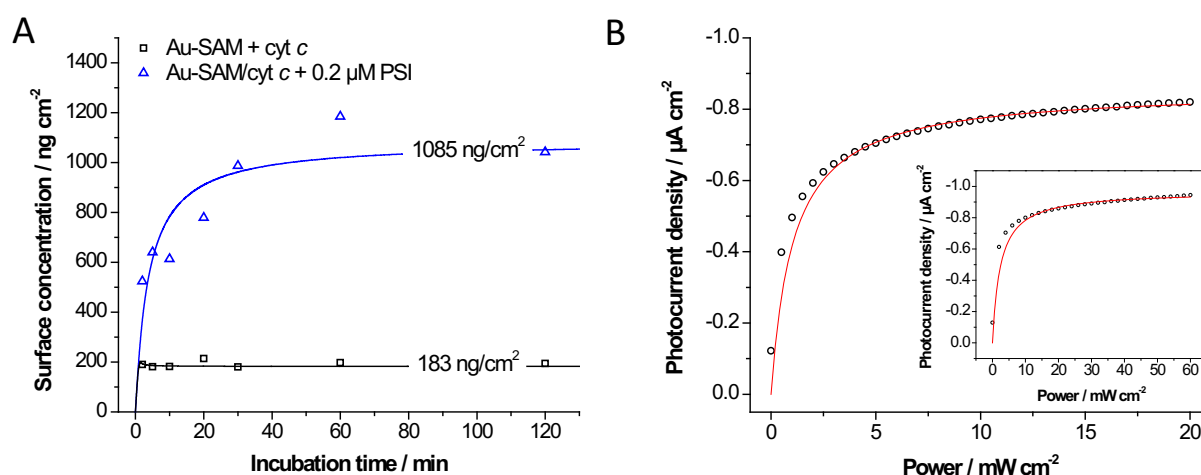


Fig. S2: (A) Surface plasmon resonance (SPR) experiment to elucidate the maximal mass deposition of photosystem I (PSI) on a mercaptoundecanoic acid / mercaptoundecanol (MUA/MU) 1:3 / cytochrome *c* (cyt *c*) modified gold-surface. Incubation time dependence of the assembled surface concentration of PSI on MUA/MU/cyt *c* modified gold-surface. The MUA/MU modified gold-surface had been in contact with the cyt *c* solution (black squares) before the MUA/MU/cyt *c* modified gold-surface has been in contact with the PSI solution (blue triangles). Surface concentration has been calculated from responsive units (RU). (B) Light intensity dependence vs. photocurrent density of a Au-MUA/MU/cyt *c*/PSI electrode without additional mediator (MV) in solution for two different sets of light intensities ($0 - 20$, $0 - 60 \text{ mW cm}^{-2}$). The data has been fitted using the Michaelis-Menten-equation. For experimental details see text.

(II) Surface potential calculations at monomeric photosystem I

Surface potential calculations of monomeric PSI (*T. elongatus*, PDB: 4FE1) has been done at pH 7 to verify the excess charge distribution of PSI and thus to support the basic idea of electrostatic assembly on cyt *c*. A similar calculation has been done by Mukherjee *et al.* 2011.¹⁹⁹ Here, the surface potential has been calculated from the crystal structure of Brunger *et al.* 2012²⁵³ (PDB: 4FE1) using the PyMOL Molecular Graphics System (PyMol, Version 1.7, Schrödinger, LLC.). Using PDB2PQR 1.8, pKa calculations have been performed by PROPKA at pH 7, while using PARSE as standard forcefield.^{255,256} The adaptive Poisson-Boltzmann Solver²⁵⁴ (APBS) was used with standard parameters (Temperature: 298.15 K, protein dielectric = 2.0, solvent dielectric = 78.0). For simplicity ionic strength and concentrations have been assumed to be 5 mM K⁺ (ionic radius = 133 pm) and 5 mM H₂PO₄⁻¹ (ionic radius = 213 pm). Fig. S3 shows the surface potential distribution in units of K_BT/e (from -5 to 5) of monomeric PSI in three different views (luminal, side, stromal) with the cytochrome *c6*/plastocyanin docking site⁸³ (black circle) at the luminal side of the PSI. These calculations verify the negative (red, luminal) and positive (blue, stromal) potential situation in PSI at pH 7 in a low ionic buffer system. It supports the idea of an orientated assembly of PSI on cyt *c* with a positive excess net-charge.

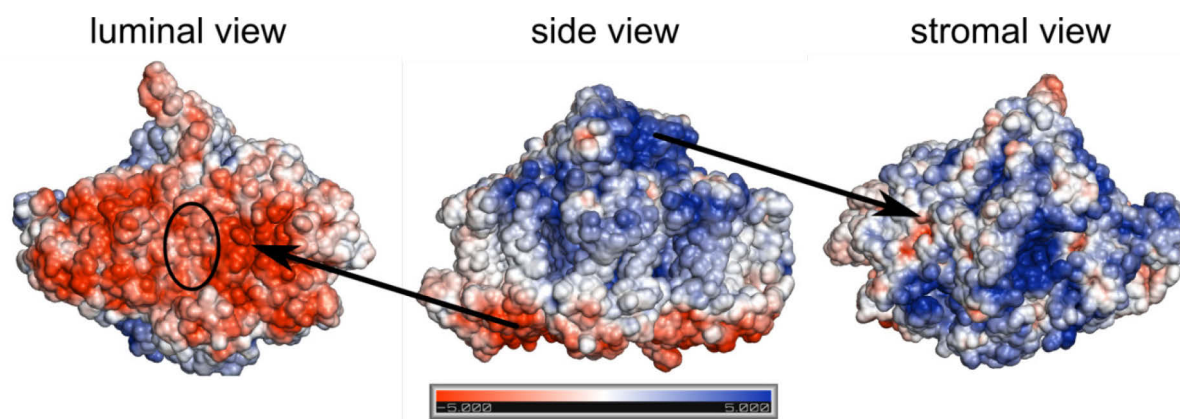


Fig. S3: Surface potential calculation of monomeric PSI (PDB: 4FE1) from three different viewpoints (luminal, side, stromal) in phosphate buffer (5 mM, pH 7). Colour bar range from a negative potential of -5 K_BT/e (red) to a positive potential of 5 K_BT/e (blue). The black circle shows the cytochrome *c6*/plastocyanin docking site. Calculations have been done with the use of PyMol V. 1.7, PDB2PQR V. 1.8, APBS V. 1.3. For citation see text.

4.2 Engineering of supramolecular photoactive protein architectures: Defined co-assembly of photosystem I and cytochrome *c* using a nanoscaled DNA-matrix

Authors: Kai R. Stieger, Dmitri Ciornii, Adrian Kölsch, Mahdi Hejazi, Heiko Lokstein, Sven C. Feifel, Athina Zouni and Fred Lisdat

Abstract

The engineering of renewable and sustainable protein-based light-to-energy converting systems is an emerging field of research. Here, we report on the development of supramolecular light-harvesting electrodes, consisting of the redox protein cytochrome *c* working as a molecular scaffold as well as a conductive wiring network and photosystem I as a photo-functional matrix element. Both proteins form complexes in solution, which in turn can be adsorbed on thiol-modified gold electrodes through a self-assembly mechanism. To overcome the limited stability of self-grown assemblies, DNA, a natural polyelectrolyte, is used as a further building block for the construction of a photo-active 3D architecture. DNA acts as a structural matrix element holding larger protein amounts and thus remarkably improving the maximum photocurrent and electrode stability. Investigating the photophysical properties, this system demonstrates that effective electron pathways have been created.

Introduction

Engineering advanced electrode surfaces by incorporation of biomolecules is a promising and emerging field of current state-of-the-art research. The defined assembly of specific biomolecules onto such surfaces allows the adjustment of the properties of these electrodes for a desired purpose. In different applications, they can be used as biohybrid electrodes in biosensing^{258,259} or for the enzyme-based synthesis of chemicals²⁶⁰. Furthermore bio-based electrical power generation is gained, when such bioelectrodes are used in bio-fuel cells²⁶¹ or photovoltaic devices.^{193,230,239,262,263} The construction of new functional systems applying defined biomolecular arrangements leads to a deeper understanding of the molecular interactions and the conditions influencing them. In addition a trend can be seen in the development of coupling strategies, which are of more general character and not only suited for a specialized system.

Learning from nature, the utilization of light-to-charge carrier converting proteins from oxygenic photosynthesis of plants and cyanobacteria becomes more and more successful and the construction of new biohybrid solar energy-converting devices has been started.¹⁹² In natural systems one of the light-converting “enzymes” is photosystem I (PSI).^{25,192} In the thermophilic cyanobacterium *Thermosynechococcus elongatus* (*T. elongatus*) PSI is a trimeric pigment-protein super-complex, consisting of 12 different protein subunits, harbouring 96 chlorophylls *a* (Chl *a*) – per monomeric subunit. Most Chls serve as light-harvesting antenna pigments and 6 Chls form an electron transport chain.⁷⁸ In PSI charge separation occurs at the luminal pigment dimer, Chl *a*/Chl *a*' (P₇₀₀) finally leading to a reduction of the stromally-located terminal iron-sulfur-cluster (F_B).^{25,83,244} Light-induced electron-hole pairs are restocked *via* cytochrome *c*₆ (cyt *c*₆), which reduces P₇₀₀, whereas the oxidation takes place at the F_B cluster, which is done by the redox protein ferredoxin (Fdx).⁵²

In the last years, significant efforts were undertaken for the efficient coupling of PSI with electrodes using a vast number of strategies.¹⁹¹ One issue to be addressed is the effective wiring of PSI to the electrode, which has been achieved by different surface design and chemistry.^{196–198,201,205,245,246,264,265} For instance, molecular wiring has been accomplished by reconstitution of PSI with vitamin K1 derivatives²⁰⁶, the application of cross-linked platinum-nanoparticle/PSI composites with ferredoxin²¹⁰ or linkage of pyrroloquinoline quinone to PSI.²⁰⁹ The connection of PSI *via* different π -systems²⁶⁶ on graphene has also been reported. A remarkable photocurrent density was shown by electrospray-deposited PSI on nanostructured TiO₂.²²⁸ Using the redox protein cytochrome *c* (cyt *c*) we²⁶⁷ and others²²⁹ have shown that the electrical wiring of PSI *via* an integrated protein matrix can be achieved.

Particularly, approaches for the integration of PSI beyond the two-dimensional limiting surface are of great interest, because they potentially allow the generation of higher photocurrents per geometrical electrode area. One strategy is the construction of multilayer PSI electrodes using the polyelectrolyte building block polybenzylviologen²¹¹ or poly-aniline composite films.²¹² Another PSI containing film has been shown *via* the integration into a cross-linked redox hydrogel using Osmium-complex containing polymers.^{214,216,231,268} This leads to a higher PSI concentration beyond the 2D arrangement.²¹⁶ Another photo-functional film could be obtained by the incorporation of PSI into a Nafion matrix.²¹³ A more simple method to develop PSI multilayer-like structures has been achieved by vacuum-assisted deposition of PSI suspensions on gold²⁰³, graphene^{223,224}, p-doped silicon²¹⁷ and others.²⁶⁹ Furthermore, an oriented multilayer formation was also confirmed by subsequently deposition

of platinized PSI.²⁰² Moreover, using agarose, the formation of a multilayer on charged hematite can be achieved.²⁴¹

Previously PSI and cyt *c* have been subsequently adsorbed onto each other to form multilayer architectures.²⁶⁷ Here we report the complex binding of cyt *c* with PSI for the first time. Based on this finding, we describe a time-controlled self-assembly process, due to the formation and adsorption of PSI:cyt *c* - complexes. In this study, we combine two strategies to develop a highly biocompatible, stable and sustainable light-to-current converting electrode by using the redox protein cyt *c*. To expand the accessible amount and stabilize the electrodes, we use DNA as a polyelectrolyte to provide a nanoscaled matrix for the PSI:cyt *c* - complexes on the electrode surface.

Here we exploit that cyt *c* binds with DNA *via* electrostatic interactions to form stable layered assemblies with a very large amount of electro-active protein.¹⁷⁸ In addition, it has been shown that other biomolecules, such as enzymes can be integrated into these architectures.^{182,257,270,271} The remarkable features of DNA significantly enhance the electro-active cyt *c* amount as compared to other nanoscaled building blocks, such as sulfonated polyanilines (PASA)¹⁷⁵, modified gold¹⁷⁷ or silica nanoparticles.¹⁷⁹ This renders DNA an interesting candidate to be applied in photo-bioactive electrode structures. In this study, we describe the construction of such biohybrid electrodes and investigate the striking features of these systems.

Experimental Methods

Isolation of Photosystem I from *T. elongatus*

Growth of *Thermosynechococcus elongatus* BP-1 and extraction of membrane proteins from thylakoids were performed according to Kern *et al.* 2005.²⁷² For the purification of PSI two chromatography steps were used. The first column was packed with Toyo Pearl DEAE 650 S (GE Healthcare) and pre-equilibrated with buffer A (20 mM MES-NaOH, pH 6.0, 20 mM CaCl₂, 0.02 % β -DM, 5 % glycerol). After sample loading and washing the column with buffer A, PSI was separated from PSII using a linear gradient with buffer B (20 mM MES-NaOH, pH 6.0, 20 mM CaCl₂, 0.02 % β -DM, 5 % glycerol, 100 mM MgSO₄). PSI containing peak eluted at 80-90 mM MgSO₄ was pooled and diluted with the same volume of buffer C (5 mM MES-NaOH, pH 6.0, 0.02 % β -DM). The second column was packed with Q-SepharoseTM Fast Flow (GE Healthcare) and pre-equilibrated with buffer D (5 mM MES-

NaOH, pH 6.0, 0.02 % β -DM, 60 mM MgSO_4). PSI Trimer was separated from remaining PSI Monomer by linear gradient with buffer E (5 mM MES-NaOH, pH 6.0, 0.02 % β -DM, 150 mM MgSO_4). The PSI Trimer eluted at 150 mM MgSO_4 . The fractions were pooled and concentrated in an Amicon stirring cell using a Biomax 100 membrane (Millipore). Finally, the PSI Trimer was crystallised by dilution with buffer C at 4 °C until a concentration of 5 mM MgSO_4 was reached. The crystals were collected by centrifugation (5 min, 4 °C, 4000 $\times g$), washed with buffer C, re-solubilized by adding buffer F (5 mM MES-NaOH, pH 6.0, 30 mM MgSO_4) and re-crystallised as described above. For the assembling experiments the crystals were dissolved in 100 mM phosphate buffer, pH 7.0 and diluted slowly to the final buffer concentration. The photochemical activity of PSI with cyt *c* as an electron donor was measured using a Clark electrode (Hansatech). In a final volume of 1 mL, the reaction mixture contained variable concentrations of cyt *c*, 5 mM phosphate buffer, pH 7.0, 0.05 % β -DM, 1 mM Na-ascorbate and 170 μM methyl viologen. Sample was incubated at 20 °C and saturated light (700 $\mu\text{mol m}^{-2} \text{s}^{-1}$). The reaction was started by adding of 20 nM PSI and the initial O_2 consumption (10 s) was measured. For the interaction of PSI with cyt *c* a catalytic rate of $20 \pm 1 \text{ s}^{-1}$ with a Michaelis-Menten constant of $23 \pm 3 \mu\text{M}$ can be determined (see Fig. S9).

Complex formation of PSI with cyt *c* in solution

PSI was mixed with cyt *c* in a ratio of 1:50. The reaction mixture containing 0.8 μM PSI, 40 μM cyt *c*, 5 mM phosphate buffer, pH 7.0, 1 mM Na-ascorbate and 0.02 % β -DM (final volume = 100 μL) was incubated for 2 min and 4 °C. A second reaction mixture was performed, in which 100 mM NaCl was added. Subsequently, the reaction mixture was applied to a Microcon YM-100 centrifugal filter (100,000 MWCO, Amicon) and centrifuged for 7 min and 4 °C to remove excess cyt *c*. The protein complex was washed 6 times with 400 μL buffer (see above) and analysed by MALDI-TOF. The determination of protein masses was carried out in linear mode using Microflex instruments (Bruker). An equal volume of 40 % acetonitrile, 0.1 % TFA in saturated sinapinic acid was mixed with protein sample in a ratio of 1:1.

Preparation of electrodes

Au-disk-electrodes (CHI) with an accessible geometrical surface of 0.0314 cm^2 have been briefly cleaned with abrasive paper (P1200, P2500, P3000) and subsequently cycled between -0.2 and 1.6 V (*vs.* Ag|AgCl) in 100 mM sulfuric acid. Au-chip-electrodes (Micrux, Spain)

with an accessible geometrical surface of 0.00785 cm^2 have been pre-cleaned in piranha solution ($1:3 \text{ H}_2\text{O}_2:\text{H}_2\text{SO}_4$) for 2 min. Afterwards, electrodes have been cycled between -1.5 and $1.6 \text{ V vs. Ag|AgCl}$ in 100 mM sulfuric acid, followed by an additional cycling between -0.2 and 1.6 V in 100 mM sulfuric acid. Subsequently, both electrode types have been incubated for 48 h at RT in an ethanolic solution of a 3:1 mixture containing 11-mercapto-1-undecanol (MU, Sigma) and 11-mercaptopundecanoic acid (MUA, Sigma). Afterwards the electrodes have been incubated in $30 \mu\text{M}$ cytochrome *c* (horse heart, Sigma) in phosphate buffer (5 mM , pH 7) for 2 h forming the cytochrome *c* monolayer (cyt *c* ML), according to Ge *et al.* 2002.¹⁴⁴ Before starting the assembly on the surface solutions with different molecular ratios of 1:20, 1:50, 1:100, 1:200 and 1:500 PSI:cyt *c* have been prepared in 5 mM phosphate buffer, pH 7 and these mixtures were allowed to equilibrate in the dark for 30 min at RT. For the preparation of PSI:cyt *c* – co-assembly (Au-cyt *c* ML-[PSI:cyt *c*]), the electrodes have been incubated in the PSI:cyt *c* solution in the dark at RT for various time scales, and were finally ready for measurements. In DNA-based preparations the Au-cyt *c* ML electrodes have been first incubated with 0.2 mg mL^{-1} calf thymus DNA (Sigma) in 0.5 mM phosphate buffer, pH 5 for 10 min. Afterwards the electrodes have been alternately incubated in PSI:cyt *c* solution (molecular ratio 1:100) for 20 min at RT in 5 mM phosphate buffer, pH 7, followed by an incubation for 10 min in 0.2 mg mL^{-1} DNA in 0.5 mM phosphate buffer pH 5 forming the first bilayer (PSI:cyt *c*/DNA). If not stated otherwise, 6x bilayer have been built up followed by 30 min incubation in phosphate buffer, pH 7 at 40°C for film stabilization. Finally the DNA-electrodes were ready for measurements or have been stored dry at 4°C in the dark. At all incubation stages cyclic voltammograms have been recorded to verify the assembly process.

Electrochemical experiments

Electrochemical measurements have been performed using the potentiostat CHI660E (CHI) and a custom-made electrochemical cell containing 1 mL of phosphate buffer (5 mM , pH 7) a Pt counter electrode and an Ag|AgCl (3 M KCl) reference electrode. Cyclic voltammetric measurements have been performed at a scan rate of 100 mV s^{-1} and in a potential range from $+300$ to -300 mV .

Photoelectrochemical experiments

Photoelectrochemical measurements have been performed using an integrated system (CIMPS, Zahner) containing a white LED light source (4300 K , Zahner) with adjustable

intensity (max. 100 mW cm^{-2}), an electrochemical cell and a photodiode with feedback control to the light source *via* a potentiostat (PP211, Zahner). Electrochemical investigations have been carried out through a coupled potentiostat (Zennium, Zahner). In all experiments a Pt counter electrode and an Ag|AgCl (3 M KCl) reference electrode have been used in an aqueous solution containing phosphate buffer (5 mM, pH 7). For most experiments no additional electron acceptor was used and air saturation of the solutions has been ensured. Photochronoamperometric experiments have been performed at RT and -100 mV *vs.* Ag|AgCl, while using an illumination time of 30 s and a light power of 20 mW cm^{-2} (white light source spectrum see Fig. S8). Light power dependent photocurrent experiments have been done using a power range of $0.5 - 20 \text{ mW cm}^{-2}$ using white light with and without 1 mM of the soluble electron acceptor methyl viologen (MV^{2+}).

Surface plasmon resonance

Surface plasmon resonance (SPR) experiments have been performed on a Biacore T100 (GE Healthcare) at a constant flow rate of $1 \mu\text{L min}^{-1}$ and 25°C . Before use, Au sensor chips have been cleaned with low pressure air plasma. The clean Au surface has been incubated 48 h at RT with a freshly prepared ethanolic solution of a mixture containing MUA and MU. After the thorough washing of the surface with ethanol and phosphate buffer (5 mM, pH 7) the chip was ready to use. First cyt *c* has been adsorbed on the thiol layer forming the cyt *c* ML. PSI:cyt *c* pre-complex mixtures (1:20 and 1:100) have been flushed over the surface with different injection times.

Scanning electron microscopy

Au-chip-electrodes (Micrux) have been used and 6x bilayer of Au-cyt *c* ML-[PSI:cyt *c*] and Au-ML-DNA-[PSI:cyt *c*/DNA] have been prepared, according to the previously described procedure in this study. Functionality of the assembly has been verified *via* photochronoamperometric measurements. To elucidate profile heights of the assembly, electrode surfaces have been carefully cut with an ultrasharp blade in order to obtain sharp edges. For visualization of morphology of the prepared electrodes scanning electron microscopy (JSM-6510, JEOL) has been employed. The acceleration voltage was 5 kV, which allowed a non-destructive irradiation of the biological surface. A working distance of 20 mm and a magnification of 10,000 and 20,000 fold were chosen. Images have been recorded under an approximate angle of 85° relative to the surface normal.

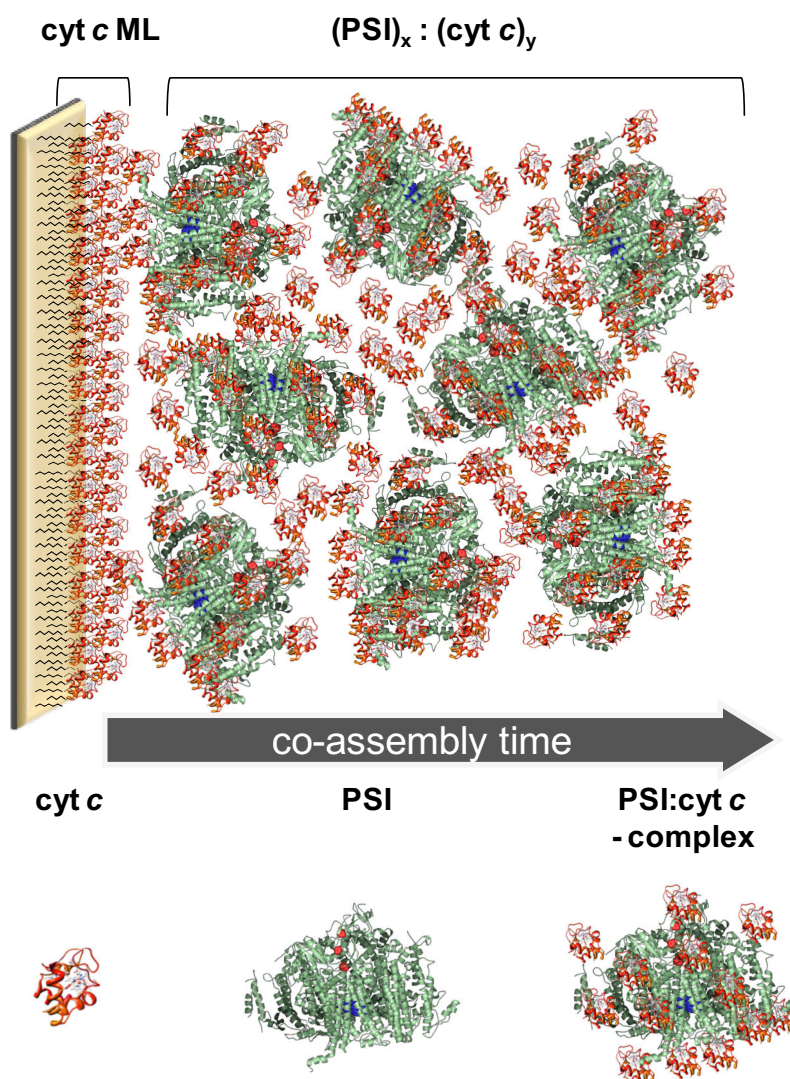
Results and Discussion

Co-assembly of cyt *c* and PSI: Au-ML-[(PSI)_x:(cyt *c*)_y]

It has been found, that PSI can be adsorbed onto cyt *c* and *vice versa*, indicating a strong interaction between both biomolecules.²⁶⁷ These proteins may also form a complex in solution with the opportunity to turn the interaction of cyt *c* and PSI into a time-controlled self-growing process. To verify pre-complex formation in solution, cyt *c* and PSI have been incubated together (see experimental details). The complexes have been purified afterwards *via* filtration to remove excess cyt *c*. Fig. S1 shows the MALDI-TOF analysis of the purified complexes, exhibiting a clear mass signal of cyt *c*. This indicates that cyt *c* has bound to PSI and cannot be removed, even by several washing steps. The main driving force for this interaction is of electrostatic nature since the same kind of experiments in the presence of 100 mM NaCl inhibits complex formation by lowering the interaction between the proteins. This verifies the complex formation in solution and is the starting point for assembling these complexes onto surfaces. Moreover, efficient electron transfer from a modified gold electrode *via* cyt *c* to PSI can be shown with both proteins in solution. (see Experimental Section and Fig. S9).

Scheme 1 illustrates the proposed concept of the co-assembly of PSI:cyt *c* complexes on an electrode. First, a cyt *c* monolayer (cyt *c* ML) is formed onto the thiol-modified gold to ensure the electrical communication of PSI with the electrode *via* the redox protein.²⁶⁷ The heterogeneous electron transfer from the electrode towards the surface-bound cyt *c* is fast ($k_s = 70 \text{ s}^{-1}$) and of quasi-reversible character providing a good basis for the subsequent electron transfer steps.

Under conditions of low ionic strength the PSI:cyt *c* complexes are found to adsorb onto a cyt *c* ML electrode and grow over time. This offers the opportunity to control the film thickness and thus the amount of PSI on the electrode with the assembly time. The molar ratio between both proteins (PSI:cyt *c*) in the complex solution turns out to be crucial for the mass deposition and adsorption behaviour. Using a fixed assembly time the molar excess of cyt *c* has been varied from 20 to 500. In order to control the functionality of the surface assembly of both compounds photochronoamperometric measurements have been chosen. They rely on the possibility to connect PSI effectively with electrodes *via* the electron donor cyt *c* and exhibit a nearly exclusive cathodic photocurrent.²⁶⁷



Scheme 1: Schematic representation of an Au-ML-[PSI:cyt *c*] electrode construction. The gold surface was modified with mercaptoundecanoic acid / mercaptoundecanol 1:3 (MUA/MU) adsorbing a monolayer of cyt *c* (cyt *c* ML). PSI and cyt *c* complexes were self-assembled with various molecular ratios of PSI to cyt *c* (*x*:*y*) for different time periods, allowing an increase of the photoactive protein amount on the electrode surface.

The functionality of electrodes prepared with different protein ratios can be seen from the data compiled in Tab. 1. The table displays major differences in photocurrent output for varying molar excesses of cyt *c* at a specific assembly time. Larger amounts of cyt *c* lead to an increase in photocurrent, which seems to level off at a 200-fold cyt *c* excess (see also Fig. S2).

Tab. 1: Photocurrent density achieved after 20 h of protein assembly onto an Au/MU:MUA/cyt *c* (cyt *c* ML) electrode from a mixture of PSI and cyt *c* with different molar ratios between PSI and cyt *c* (*n* = 3).

1:20 [$\mu\text{A cm}^{-2}$]	1:50 [$\mu\text{A cm}^{-2}$]	1:100 [$\mu\text{A cm}^{-2}$]	1:200 [$\mu\text{A cm}^{-2}$]	1:500 [$\mu\text{A cm}^{-2}$]
1.6 ± 0.4	3.2 ± 0.2	5.0 ± 0.9	7.4 ± 2.2	8.9 ± 0.2

Furthermore, the time dependence of the assembly of the PSI:cyt *c* complex has been studied at a fixed molar ratio (1:100) as given in Fig. 1. After a longer exposure time (44 h) a saturation of the photocurrent becomes visible. This indicates that either i) equilibrium of adsorption and desorption from/to the surface is reached during preparation, or ii) electron transfer to PSI molecules immobilized far away from the electrode surface is not sufficient anymore. Here, a hyperbolic function can be found to fit the data points giving characteristic parameters of the time-controlled co-assembly process ($K_{50} = 122 \pm 43$ min, $J_{\max} = 5.4 \pm 0.6 \mu\text{A cm}^{-2}$, regression coefficient $R^2 = 0.98$).

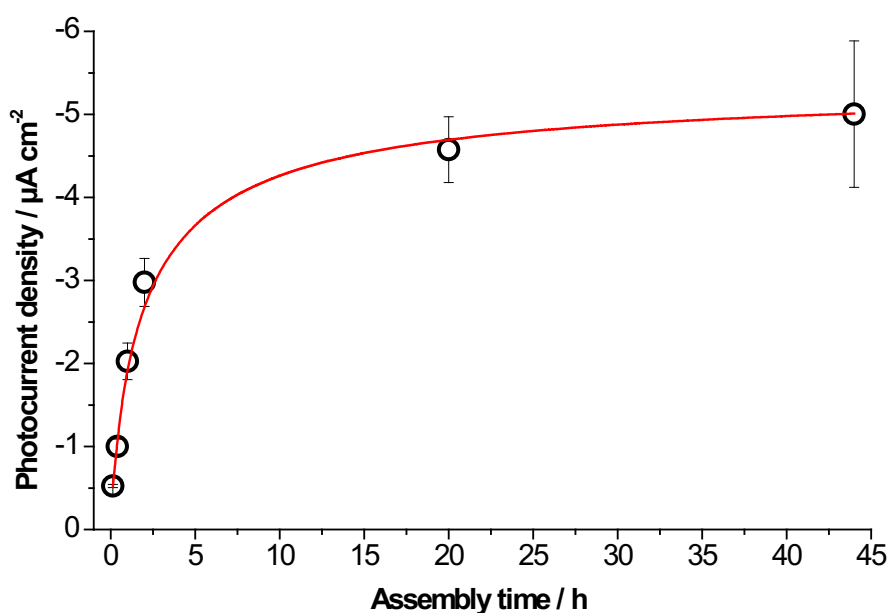


Fig. 1: Photocurrent density in dependence on the assembly time. Electrodes have been modified with a cyt *c* ML, then PSI and cyt *c* have been co-assembled for different time periods from a 1:100 mixture of both proteins. Photochronoamperometric measurements have been carried out under aerobic conditions at RT in phosphate buffer (5 mM, pH 7) at a potential of -100 mV vs. Ag|AgCl using white light of 20 mW cm^{-2} ($n = 4$).

To gain further insights in the co-assembly process, surface plasmon resonance (SPR) experiments have been carried out, elucidating the mass accumulation on the cyt *c* ML (see Fig. 2). Thus, repeated injections of the protein mixture are used to verify both the mass deposition and the adsorption kinetics of the co-assembly. Here, two different molar ratios of cyt *c* and PSI have been tested, which have resulted in a significantly different photocurrent density: 1:100 ($5 \pm 0.9 \mu\text{A cm}^{-2}$) and 1:20 ($1.6 \pm 0.4 \mu\text{A cm}^{-2}$). For the experiment 6 subsequent flushes of PSI:cyt *c* complexes over the surface with intermittent buffer flow have been performed. For short assembly times (up to 16 min), no significant difference of mass deposition on the surface is detected. For longer exposure times the mass deposition from a

solution of a molar ratio of 1:100 yields a higher mass correlated signal. For both cases a saturation behaviour is observed, however saturation for 1:20 solution starts earlier. The total amount of proteins on the surface (proportional to the SPR signal) is lower compared to the deposition from a 1:100 solution.

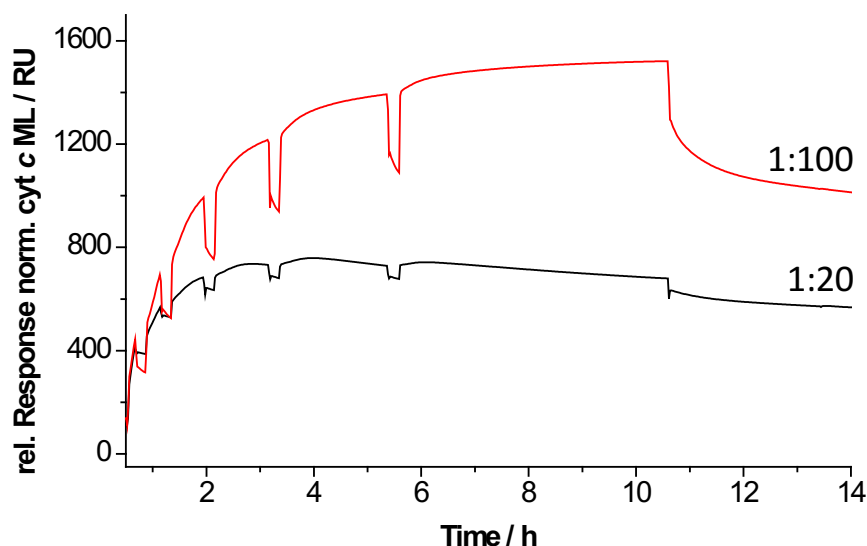


Fig. 2: Surface plasmon resonance (SPR) sensorgram of the co-assembly of PSI:cyt *c* complexes on modified gold surfaces. All experiments have been performed in phosphate buffer (5 mM, pH 7) at RT in a flow system (1 mL min^{-1}). A mixture of 11-mercaptopundecanoic acid (MUA) and 11-mercapto-1-undecanol (MU) (1:3) has been used for SAM formation on the gold surface prior to the protein assembly. First, a cyt *c* monolayer (cyt *c* ML) was formed on the surface by flushing cyt *c* ($30 \text{ } \mu\text{M}$, 1 mL min^{-1}) over the surface (not shown). Afterwards a pre-mixed solution of PSI:cyt *c* (1:100 – red curve, 1:20 – black curve) was injected for 8, 16, 36, 60, 120 and 300 min, respectively with intermittent buffer flushes. The SPR signal has been normalized to the mass signal of the cyt *c* ML.

Via cyclic voltammetry the redox reaction of immobilized cyt *c* in the co-assembly on the gold electrode can be verified, while the transferred charge in the film corresponds to the electro-active amount of deposited cyt *c*. The redox protein can be detected within the protein architecture even when fixed further away from the electrode surface because of self exchange between the cyt *c* molecules. This property does not only result in the electrochemical addressability of many layers of cyt *c* but has also been exploited in connecting enzyme molecules in different layers with the electrode.^{178,271}

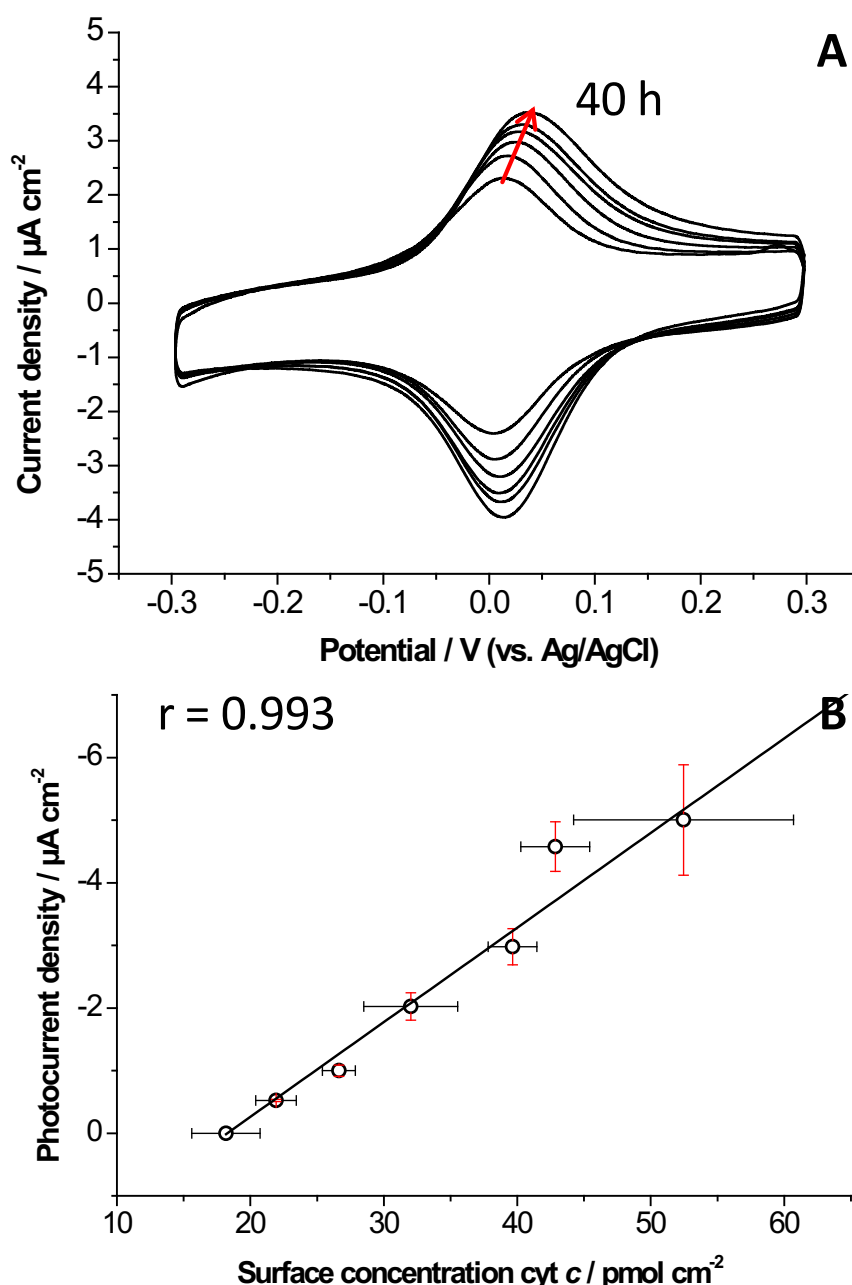


Fig. 3: (A) Cyclic voltammetry of Au-ML-(PSI:cyt *c*) electrodes for different assembly times (0, 8, 24, 60, 120 min, 20 and 40 h) in phosphate buffer (5 mM, pH 7) at RT using a scan rate of 100 mV s^{-1} . The red arrow indicates the increase in peak current with the incubation time. (B) Correlation plot of photocurrent density against electro active surface concentration of cyt *c*, determined *via* cyclic voltammetry (Pearson's correlation coefficient $r = 0.993$, $n = 4$).

In Fig. 3A the increase in peak current and thus the transferred charge from/to cyt *c* within the PSI:cyt *c* assemblies can be followed with the incubation time of the electrode in the protein mixture. Additionally, there is a slight increase in peak separation (from 15 mV to 22 mV) and the half peak width (from $92 \pm 8 \text{ mV}$ to $144 \pm 11 \text{ mV}$) on raising assembly times. This indicates that with increasing protein mass on the surface the electron transfer through the

assembly is slowing down. Furthermore, the heterogeneity of the cyt *c* micro-environment rises. For electrodes, which have been obtained after different assembly times, the cyt *c* surface concentration can be plotted against the generated photocurrent density. A correlation between the electro-active cyt *c* amount and the functional PSI - indicated by the photocurrent - is received (Fig. 3B, Pearson's correlation coefficient $r = 0.993$). This corresponds to the idea of well connected PSI molecules within the 3D architecture and reveals that both proteins assemble jointly to the surface.

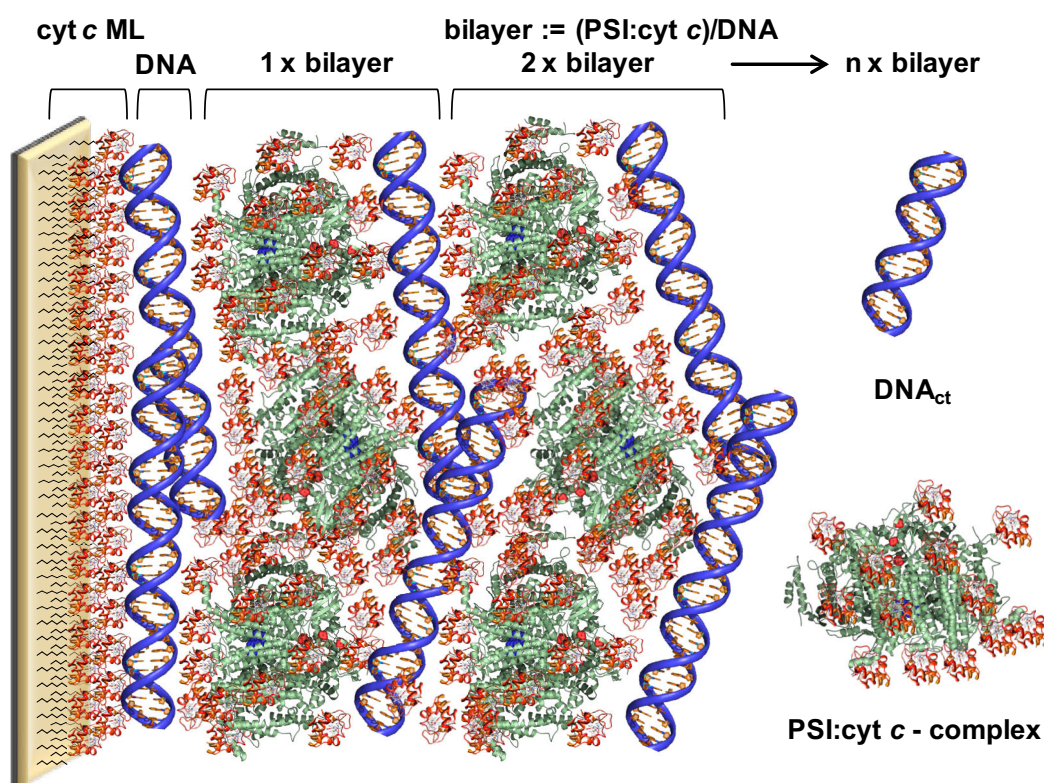
Taken together, a higher molar excess of cyt *c* to PSI results not only in a faster adsorption on the electrode, but displays an increase in photocurrent. Within these architectures the cyt *c*–cyt *c* electron self-exchange, which is necessary for the reduction of PSI, is not the limiting parameter. Even PSI molecules far away from the electrode surface can still be electrically addressed, which improves the efficiency compared to a 2D photo-reactive electrode design.²⁶⁷ The equilibrium condition at which the rate of adsorption equals the rate of desorption can be tuned by the molecular excess of cyt *c*. We conclude, that cyt *c* by itself plays a major role for the structural integrity of the deposited film. Hence, in addition to its function to create electron pathways within the structure, cyt *c* acts as molecular scaffold between the PSI molecules and may also stabilizes the large membrane protein in detergent-diminished solution.

Multilayer electrodes: Au-ML/DNA-[PSI:cyt *c*/DNA]_n

To address the limiting features of the co-assembly PSI:cyt *c* electrode with respect to the structural thickness and stability, the assembly strategy has been further improved. Therefore, the idea of stabilizing the assembly *via* a further building block is applied to extend the photoactive and connected protein amount on the surface. Here, the natural biopolymer DNA from *calf thymus* is used to increase the cohesion of the photoactive protein arrangement mainly because of the strong interaction of cyt *c* and DNA (see scheme 2).

Cyt *c* binds electrostatically with mainly positively charged residues to the backbone of DNA, the strongest complex formation between both biomolecules occurring in a low ionic strength buffer at pH 5. The biomolecular interaction has been studied previously²⁷³ and shown to allow a high mass deposition of the redox protein on surfaces. Additionally, it has been verified that DNA does not hinder cyt *c*-cyt *c* electron transfer and thus allows the preparation of protein multilayer electrodes with a rather high amount of redox-active cyt *c*.¹⁷⁸

These properties are exploited here for the construction of PSI electrodes. Basically the layer-by-layer technique is used to alternately deposit DNA and PSI:cyt *c* complexes for a specific time, to build up multilayered PSI:cyt *c*/DNA biocomposites. A simultaneous adsorption of these three molecules from solution is not suitable, since for the deposition of DNA on cyt *c* low ionic strength and pH 5 have to be used.¹⁷⁸ In such a layered surface structure each biological building block has its own unique function: DNA acts as stabilizing matrix and scaffold, cyt *c* as electron shuttle and assembly template for PSI and PSI as a photo-functional building block.



Scheme 2: Schematic representation of the construction of Au-ML-DNA-[PSI:cyt *c*/DNA]_n electrodes. The gold surface is modified with mercaptoundecanoic acid / mercaptoundecanol 1:3 (MUA/MU) adsorbing a monolayer of cyt *c* (cyt *c* ML). Successive assembly of DNA and PSI:cyt *c* complexes (bilayer) is performed by the layer-by-layer technique for the construction of a photo-functional biomolecular multilayer electrode. Three different matrix elements are used here, cyt *c* – conductive element, PSI – photo-sensitive element, DNA – structural element.

SPR measurements show an alternating deposition of DNA on top of the PSI:cyt *c* surface, as *vice versa* (Fig. S5). An assembled PSI:cyt *c* structure with DNA exhibits a ~1.6 fold increased mass deposition on the surface under the same experimental conditions compared to a control without DNA (both prepared with 6 deposition steps).

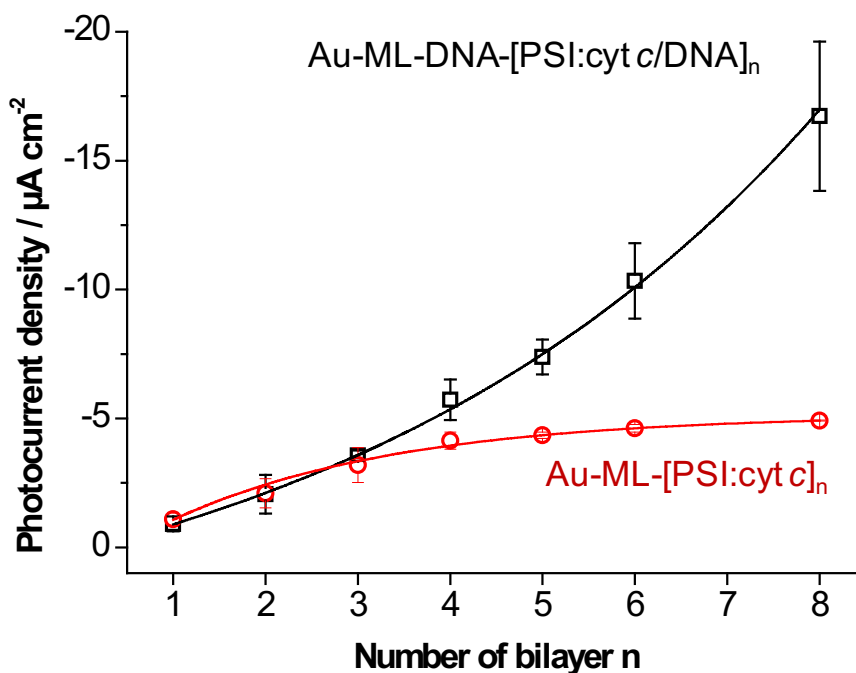


Fig. 4: Dependence of the photocurrent density on the number of deposition steps n of the DNA-electrode (Au-ML-DNA-[PSI:cyt c /DNA] $_n$, black) and the co-assembly electrode (Au-ML-[PSI:cyt c] $_n$, red). Photochronoamperometric measurements have been carried out under aerobic conditions at RT in phosphate buffer (5 mM, pH 7) at a potential of -100 mV vs. Ag|AgCl using white light of 20 mW cm $^{-2}$ ($n = 4$).

In Fig. 4 a comparison of photocurrent densities of DNA-based electrodes (Au-ML-[PSI:cyt c /DNA] $_n$) and electrodes prepared by simple co-assembly of PSI:cyt c (Au-ML-[PSI:cyt c] $_n$) for a different number of deposition steps is shown. Since there is no second building block for the co-assembly electrode, the electrode was prepared from a PSI:cyt c solution maintaining the same incubation times as for the DNA-based electrode to guarantee a better comparability. Until three incubation steps in the PSI:cyt c solution there is no significant difference found between the construction of the electrode with or without DNA. After the 4th assembly step a saturation of photocurrent density is observed with the co-assembly electrodes (as already mentioned in the first section). The generated photocurrent of the DNA-based electrode increases exponentially and no saturation is found up to the 8th bilayer. The DNA-based electrodes circumvent the limiting issue of the co-assembly electrode by allowing further protein deposition followed by a strong rise in photocurrent output. By investigating the PSI:cyt c /DNA systems by means of cyclic voltammetry a clear cyt c signal has been obtained (see Fig. 5A).

With each bilayer the peak current and thus the transferred charge increases. A high electroactive surface concentration of cyt c is found for 6x bilayer (231 ± 28 pmol cm $^{-2}$, $n = 4$).

Furthermore, the DNA-based electrode exhibits a quasi-reversible electron transfer with a formal potential of 39 ± 5 mV vs. Ag|AgCl and a peak current ratio ($I_{\text{pox}}/I_{\text{pred}}$) of ~ 1 for different numbers of bilayers. The half peak width changed from 92 ± 8 mV for a cyt *c* ML ($n = 5$) to 140 ± 3 mV for a 6x bilayer ($n = 5$). These results can be explained by the different microenvironment of bound cyt *c* in the multilayer assembly with the large membrane protein PSI. The resulting distribution of redox states and orientation of the cyt *c* heme exhibits a broadening in redox peaks. The peak separation also increases with the number of bilayers (Fig. S3) from 13 ± 4 mV (cyt *c* ML, $n = 5$) to 66 ± 9 mV (6x bilayer, $n = 5$), thus the electron transfer kinetics is more and more influenced by the electron transport between the assembled cyt *c* molecules. If the resulting photocurrent density of each electrode is plotted against the surface concentration of cyt *c* (which was obtained *via* cyclic voltammetry), a good correlation can be seen (Fig. 5B, Pearson's correlation coefficient $r = 0.995$). This indicates that also with the newly developed assembly strategy both proteins adsorb as a complex from the solution to the surface. In comparison to the co-assembly electrode, the increase in photocurrent is due to a higher amount of assembled proteins. If cyt *c* is left out during the assembly process, only minor non-directional photocurrents are achieved (see Fig. S6). This shows that DNA does not take part in the light induced electron transfer to the electrode and cyt *c* is needed for the connection of the PSI molecules in the different layers. This also seems to be reasonable considering the redox potential of G-bases in DNA (0.81 V vs. SHE)²⁷⁴ and the potential of P₇₀₀ (0.42 V vs. SHE)⁵⁷. Furthermore the photoaction spectrum of this system demonstrates that the photocurrent follows the absorption spectrum of PSI in solution, and also the absorption of a 6x bilayer assembly, and therefore originates from the photoexcitation of PSI (Fig. S10).

At least for the tested assembly numbers of PSI:cyt *c*/DNA, the photocurrent correlates with the PSI concentration, thus verifying that cyt *c* self exchange within the architecture can provide the necessary electrons for PSI reduction even when PSI is located far away from the electrode surface. A second result is the feature of DNA, which does not alter the working properties of the co-assembly, acting only as a structural framework without any electrochemical activity within this potential range. This overcomes the limitation of the co-assembly method and extends the electrode structure towards a larger photo-functional film thickness.

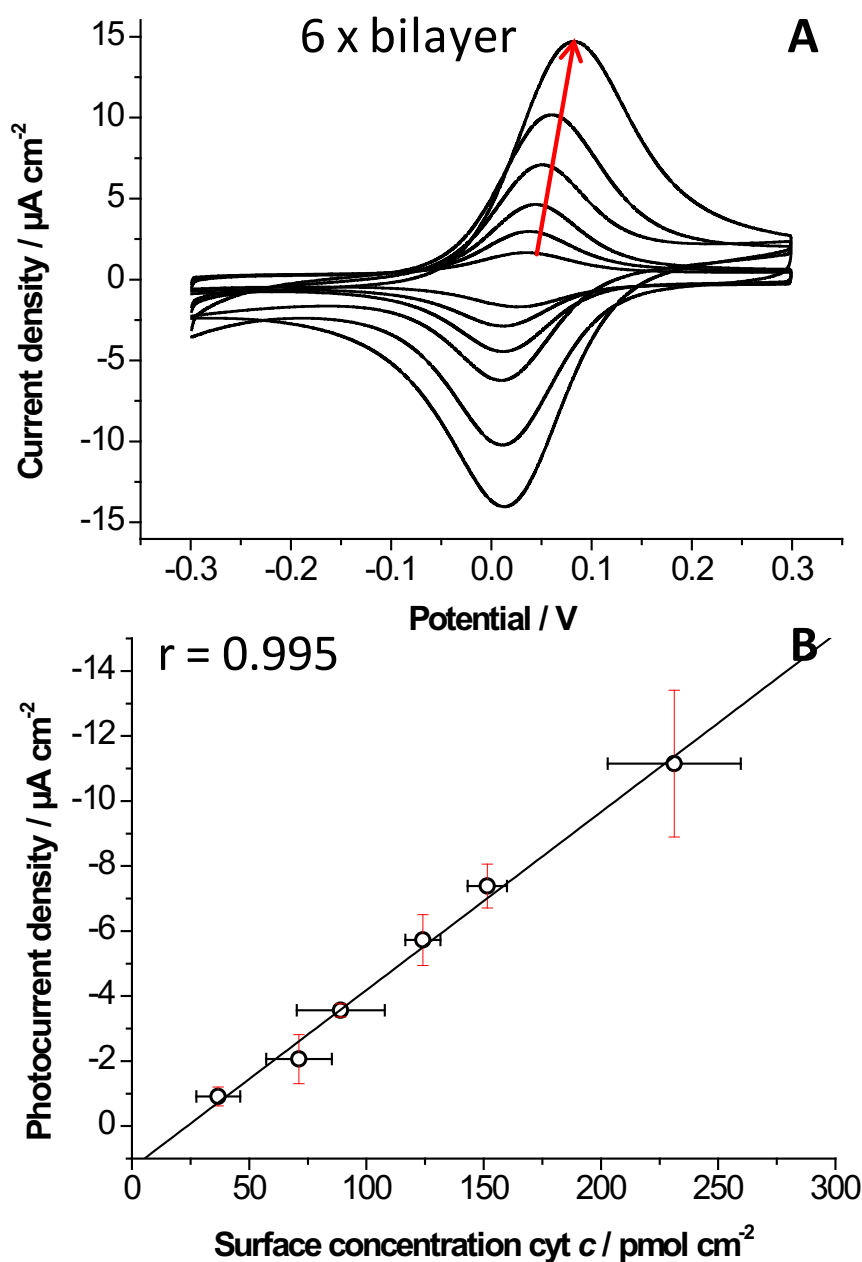


Fig. 5: (A) Cyclic voltammograms of Au-ML-DNA-[PSI:cyt *c*/DNA]_{*n*} electrodes with different bilayers (1x-6x) in phosphate buffer (5 mM, pH 7) at RT using a scan rate of 100 mV s⁻¹. The red arrow indicates the increase in peak current with the bilayer number. The potential is given vs. Ag|AgCl, 3 M KCl. **(B)** Correlation plot of photocurrent density obtained with Au-ML-DNA-[PSI:cyt *c*/DNA]_{*n*} electrodes against the electro-active cyt *c* concentration of these electrodes determined *via* cyclic voltammetry (Pearson's correlation coefficient $r = 0.995$, $n = 4$).

Features of the Au-ML-[PSI:cyt *c*/DNA]_n electrode

One of the indicated features of DNA-based assemblies is the surface enlargement during the deposition of multiple layers. Scanning electron microscopy images have been displayed to verify this claim (see Fig. 6).

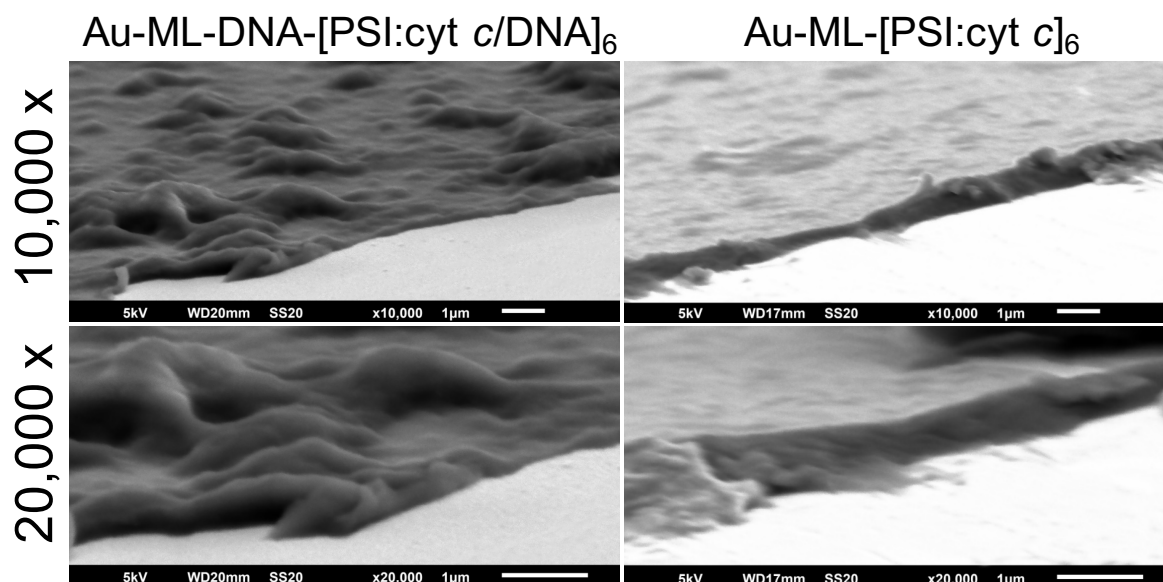


Fig. 6: Scanning electron microscopy (SEM) images of 6 bilayer assemblies prepared in the presence or absence of DNA: Au-ML-DNA-[PSI:cyt *c*/DNA]₆ and Au-ML-[PSI:cyt *c*]₆. A magnification of 10,000x, 20,000x and a voltage of 5 kV were used. White bars indicate the scale (1 µm).

A rather high surface roughness can be seen for the DNA-based electrode compared to the co-assembly electrode. Here, the DNA-based PSI:cyt *c* assemblies form films of different height (250 – 700 nm) with additional islands. On the contrary, the PSI:cyt *c* co-assembly form a rather flat and smooth film. The height of this deposition is much more uniform and around 500 nm. The comparatively rough surface of the DNA-based electrodes indicates an increased overall biomolecule mass on the surface and correlates well with the higher photocurrent densities found for this system.

This is also in very good agreement with the photocurrent differences found between the electrodes. The output of the DNA-electrode is for 6x bilayers twice as high as for the co-assembly electrode with the same number of assembly steps (see Fig. 4). Since, there is no additional photoactive element used in the DNA-assembly, the overall output corresponds only to the amount of connected PSI on the surface. While DNA could also disturb the

connection between cyt *c* and PSI, and lower the active amount of PSI, the relatively good correlation between the surface structure and the photocurrent contradicts to this assumption.

In this section we also provide insight into the photoelectrochemical properties of the DNA-based electrode. For the photocurrent densities it has to be mentioned that no additional electron acceptor has been used in the solution so far. Under such conditions electrons from the reduced F_B^- ($E^{0'} = -0.58$ V vs. SHE ²⁴) can be transferred to molecular oxygen. A high photocurrent density with only oxygen in the solution can be obtained with 8x bilayers ($17 \pm 3 \mu\text{A cm}^{-2}$, $n = 3$). In order to elucidate the limiting step of the electron transfer cascade methyl viologen (MV^{2+}) has been used as an additional electron acceptor for F_B^- (in addition to the presence of molecular oxygen). This approach in testing photocatalytic systems with MV^{2+} has been used previously, since it was reported that the presence of MV^{2+} can enhance the electron withdrawal from photo-excited PSI.^{275,276} A recent study has proposed that this is probably caused by a first reaction of oxygen with MV^{2+} , which then oxidizes the reduced F_B cluster of PSI.²⁷⁷

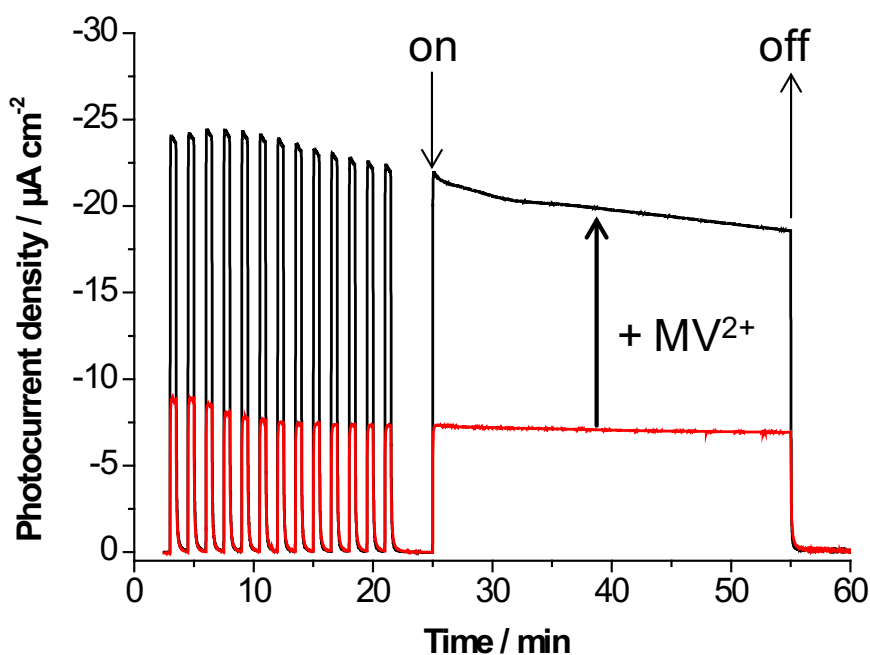


Fig. 7: Photochronoamperometric measurement of an Au-ML-DNA-[PSI:cyt *c*/DNA]₆ electrode (6x bilayer) at RT in phosphate buffer (5 mM, pH 7) with 1 mM MV^{2+} (black) and without (red). A 20 mW cm^{-2} light intensity (white light) was used for light pulses of 15 s and for a longer exposure time of 30 min. The potential was fixed at -100 mV vs. Ag|AgCl.

This would also agree with our experiments since in the absence of oxygen, MV^{2+} additions have no effect on the photocurrent. By the addition of MV^{2+} one can test whether the photobiohybrid system is limited by electron transfer to the excited PSI or electron withdrawal from PSI. Consequently, the influence of MV^{2+} in solution on the photocurrent has been evaluated with a 6x bilayer electrode. A remarkable photocurrent density increase can be obtained by adding MV^{2+} , here the current becomes a factor of 2.7 higher (increase from ~ 9 to $\sim 24 \mu A cm^{-2}$).

This verifies that the overall electron transfer process in the system is not mainly limited by cyt *c*, but by electron withdrawal from the excited PSI. The photo-induced cathodic electron transfer for these electrodes starts at about 60 mV vs. Ag|AgCl, which can be seen from voltammetric experiments with and without illumination of the surface (see Fig. S4). Here, the onset of photocurrent is mainly determined by the redox properties of cyt *c*, which demonstrates the wiring properties of the redox protein, i.e. cyt *c* needs to be reduced before electrons can be transferred to PSI. This is in agreement with previously reported findings²⁶⁷. No anodic catalysis has been found verifying the photodiode character of the protein architecture. The proposed mechanism of electron transfer in the assembly starts at the electrode where cyt *c* is reduced and is followed by subsequent interprotein electron transfer steps between the cyt *c* molecules and cyt *c* to PSI finally resulting in electron transfer from PSI to oxygen (or oxygen+ MV^{2+}). This is schematically shown in the supporting information (Fig. S11).

Another interesting feature of these electrodes is the photocurrent stability, which is shown in Fig. 7. After several times of 30 s light exposition, the electrode exhibits a rather stable photocurrent. When illuminated for 30 min with constant light (power of $20 mW cm^{-2}$) a moderate photocurrent decrease of about 16 % is observed using MV^{2+} in solution. On the contrary the reduction of photocurrent without MV^{2+} by exposing the electrode to light is very small (~ 3 %). This finding might be explained by a rather fast depletion of MV^{2+} near the electrode surface. Nevertheless, remarkable photocurrent stability has been found, additionally underpinning the pronounced stability of the protein-DNA framework. Ancillary, long term storage experiments have been performed. Storing the electrodes in buffer solution results in a reduction of photocurrent within the time frame of several days. Cyclic voltammetric experiments suggest that the framework tends to lose connection with the electrode (data not shown).

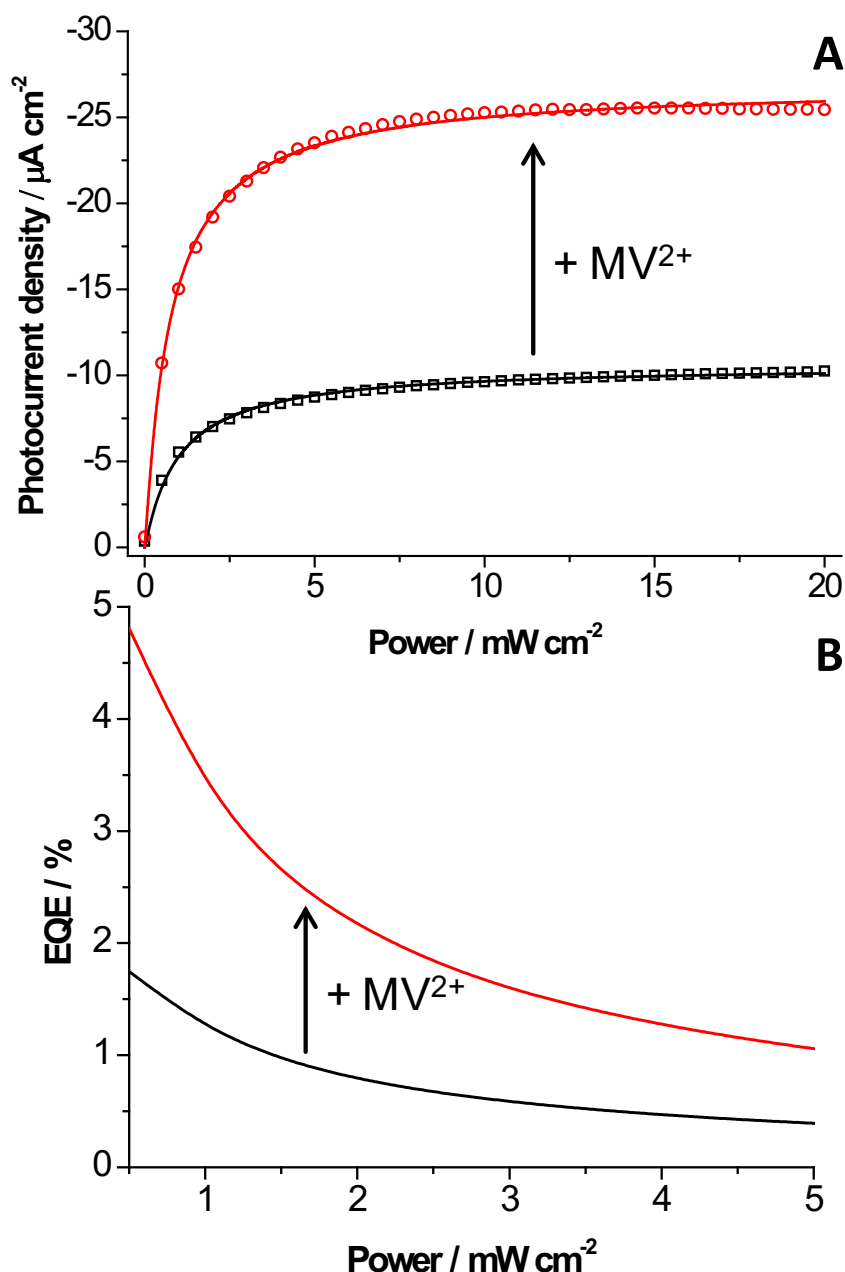


Fig. 8: (A) Dependence of the photocurrent density of an Au-ML-DNA-[PSI:cyt *c*/DNA]₆ electrode on the light intensity with (red) and without (black) MV^{2+} . Experiments have been performed under aerobic conditions at RT in phosphate buffer (5 mM, pH 7). Data were fitted with the Michaelis-Menten equation. Parameters have been elucidated with MV^{2+} ($K_M = 0.77 \pm 0.02 \text{ mW cm}^{-2}$, $I_{\text{max}} = 26.8 \pm 0.1 \mu\text{A cm}^{-2}$, regression coefficient $R^2 = 0.994$) and without ($K_M = 1 \pm 0.02 \text{ mW cm}^{-2}$, $I_{\text{max}} = 10.6 \pm 0.1 \mu\text{A cm}^{-2}$, regression coefficient $R^2 = 0.994$). (B) Calculated external quantum efficiency (EQE) of an Au-ML-DNA-[PSI:cyt *c*/DNA]₆ electrode as a function of light intensity with (red) and without (black) MV^{2+} .

However, when the electrodes are stored dry at 4 °C after 9 d of storage the DNA-based electrodes exhibit still $94 \pm 13 \%$ ($n = 3$) of its starting activity, which is in comparison to the co-assembly electrode much more stable (only $25 \pm 10 \%$, $n = 3$). Even after 1 month of

storage ~65 % of the activity is retained with the DNA-electrode (see Fig. S7). This is remarkable particularly since the electrodes have been measured several times during the storage period. The usability of the electrode over a longer time period provides the next advantageous feature of the system.

In the following set of experiments the dependency of the photocurrent density on the light power has been investigated (see Fig. 8A). Considering photons as the substrate for a photo-reactive enzyme such as PSI, the Michaelis-Menten equation can be used to fit the experimental data, which was proposed previously.^{214,266,267} As there is no additional photon-to-current converting species in the system, the cooperativity n was chosen to be 1. The parameters of K_M and v_{max} can be calculated for a 6x bilayer electrode ($K_M = 1 \pm 0.02 \text{ mW cm}^{-2}$, $J_{max} = 10.6 \pm 0.1 \mu\text{A cm}^{-2}$, regression coefficient $R^2 = 0.994$). When using MV^{2+} as an additional electron acceptor in solution, the overall photocurrent density increases significantly ($J_{max} = 26.8 \pm 0.1 \mu\text{A cm}^{-2}$, regression coefficient $R^2 = 0.994$), as already mentioned (see Fig 7). The light power at the half-maximum of photocurrent undergoes a slight decrease ($K_M = 0.77 \pm 0.02 \text{ mW cm}^{-2}$). This result points out, that without MV^{2+} the withdrawal of electrons from the F_B is the rate-limiting step of electron flow in the system, because of either low electron acceptor concentration in solution or slow electron transfer rate of the oxidation of F_B with oxygen. This behaviour changes after the addition of MV^{2+} . Under these conditions the light-to-current conversion of the PSI multilayer electrode seems to be limited by the electron transfer of the electron shuttle to PSI. This can be concluded considering the fast intramolecular rate of charge separation ($\sim 1 \mu\text{s}$) upon PSI illumination and a quantum yield of PSI of nearly 100 %.^{25,59} The lower K_M value after the addition of MV^{2+} indicates, that the efficiency of light conversion is improved by the additional electron acceptor in this system. Proux-Delrouyre *et al.* have also shown, that at a high molecular excess of MV^{2+} with respect to the natural electron donor $\text{cyt } c_6$ the apparent rate constant reaches the rate constant of P_{700} reduction by $\text{cyt } c_6$ and thus the latter process becomes the rate-limiting step.²⁵¹ PSI concentration has been determined for a 6x bilayer electrode following chlorophyll extraction. The total density of PSI in this assembly is $13 \pm 2 \text{ pmol cm}^{-2}$ ($n = 3$). With MV^{2+} in solution a turnover number of $21 \pm 2 \text{ s}^{-1}$ can be calculated.

For the usage in a photovoltaic setup, the external quantum efficiency (EQE) can be estimated, which is defined as the ratio of the collected number of carriers (n_e) to the number of incident photons (n_p) at a given energy:

$$EQE = \frac{n_e}{n_p}.$$

In Fig. 8B the EQE is calculated and plotted against the light power used for excitation. Here, for all light intensities an overall higher quantum efficiency can be obtained, when MV^{2+} is used. At light intensities of half maximum (0.77 mW cm^{-2}) an EQE of 4.1 % is achieved. This is in the same order of magnitude of values found for other 3D PSI architectures.²¹⁴ The internal quantum efficiency (IQE), considering only the absorbed photons, has also been estimated from the PSI absorption spectrum in solution corrected for the number of PSI complexes in a 6x bilayer assembly (and considering the spectral properties of the white light source used for the photocurrent measurements). At half-maximum light intensities (0.77 mW cm^{-2}) an IQE of about 24 % is achieved, which is about 6 times larger compared to the EQE.

Conclusions

This study demonstrates a feasible proof of concept for the artificial connection of biological building blocks exploiting different biomolecular features. First, we have shown that the redox protein, *cyt c*, and a solar energy converting protein, PSI are able to form complexes in solution. Second, this biomolecular interaction has been exploited for the co-assembly of both proteins on electrode surfaces. Here, *cyt c* acts as the conductive biomolecular element, building up an electrical wiring network, which embeds PSI as the photo-functional component. As for most deposition processes from solution, self-assembly on a surface is limited by the adsorption equilibrium or the available 2D area. To overcome this problem a structural matrix element, DNA, is introduced, giving the opportunity to successively enhance the functional film thickness and thus the photocurrent output, in a layer-by-layer approach. Together these building blocks form an artificial 3D architecture exhibiting several features for future applications: A rather high stability compared to other photo-biohybrid electrodes, a reasonable and tuneable photocurrent, and a renewable biological interface for the incorporation of other biomolecules. Prospects of this system can be seen since the biological assembly is not restricted to one surface or electrode material, it can be used in conjunction with different kinds of electrodes; nano-, semiconductor-, transparent or polymer-based materials. Furthermore, the biological nature of the photobiohybrid electrode allows an excellent embedment and communication with additional biomolecules of different functions.

This may raise the opportunity to develop photo-enzymatic electrodes for synthesis generating simultaneously electrical energy.

Acknowledgements

We gratefully acknowledge the support of this research by the Bundesministerium für Bildung und Forschung BMBF, Germany (Biotechnologie 2020+, projects: 031A154A+B).

Supporting Information

D) MALDI verification of PSI:cyt *c* complex formation in solution

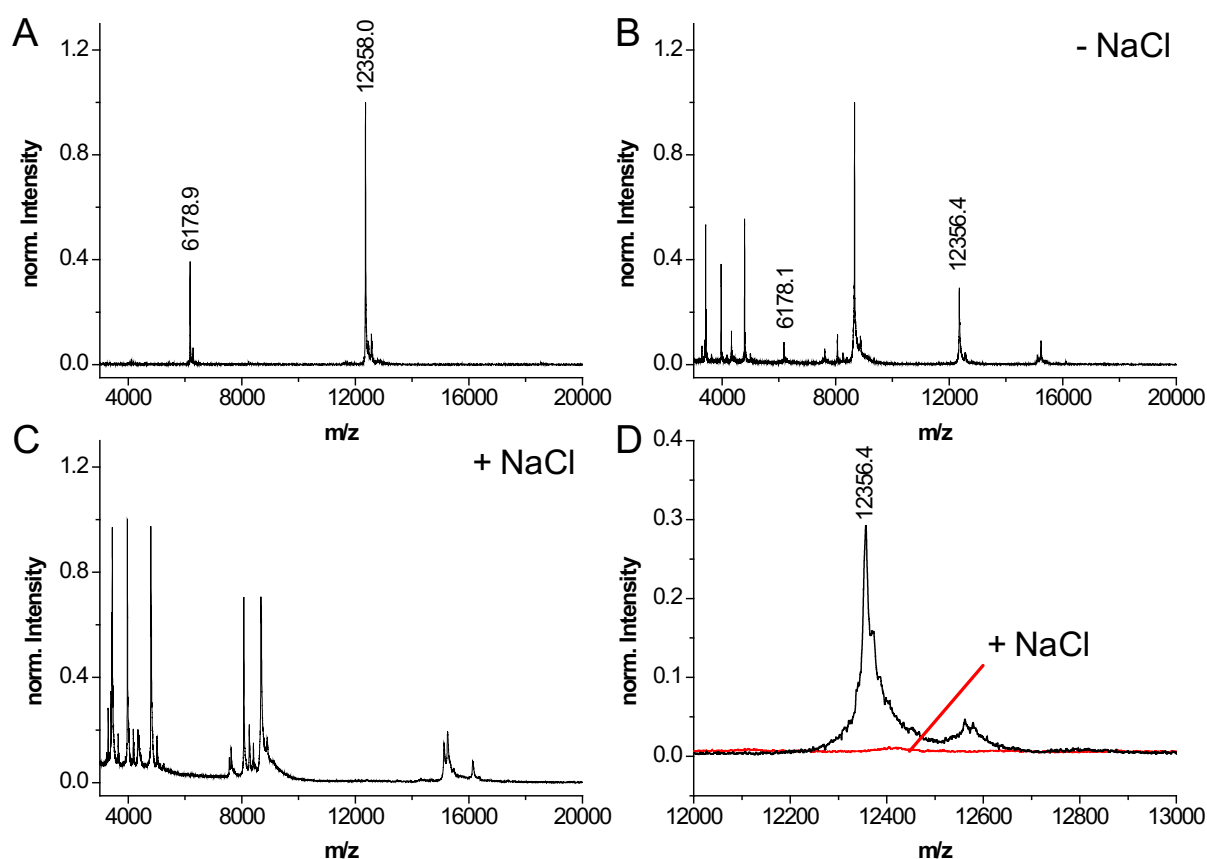


Fig. S1: Mass spectrometry analysis of PSI:cyt *c* complexes. **(A)** MALDI-TOF spectrum of cyt *c*. The characteristic peaks at 12,358 and 6,179 correspond to the molecular mass of cyt *c* (one and two protonated mass, respectively). **(B)** MALDI-TOF spectrum of PSI:cyt *c* complexes formed in solution with a molecular ratio of 1:50 in phosphate buffer (5 mM, pH 7). Cyt *c* can be found in the spectrum with peaks at 12,356 and 6,178. **(C)** MALDI-TOF spectrum of PSI:cyt *c* complex solution after addition of 100 mM NaCl. Cyt *c* characteristic peaks at 12,358 and 6,179 are missing due to disassembly of the PSI:cyt *c* complexes and removal of free cyt *c* by filtration. **(D)** Comparison between mass spectra of the molecule ion peak of cyt *c*. After addition of 100 mM NaCl to the complex solution and filtration of the PSI:cyt *c* complex solution to remove the free cyt *c* molecules the peak at 12,356 is missing. Spectra have been normalized to the highest peaks.

II) Photocurrent response of different PSI:cyt *c* mixtures

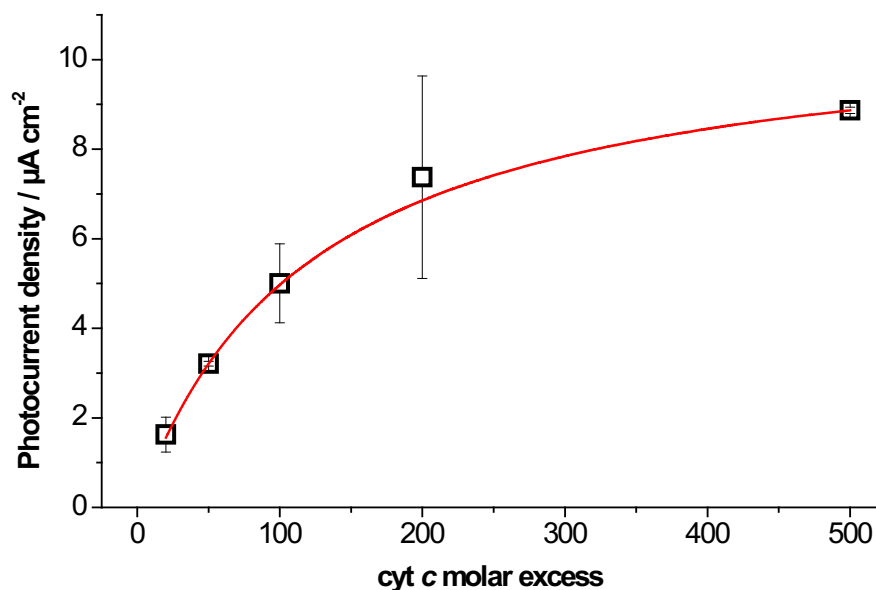


Fig. S2: Photocurrent density in dependency of the molar excess of cyt *c* to PSI. Electrodes have been first modified with a cyt *c* ML, then cyt *c* and PSI are co-assembled from protein mixtures with different molar excess of cyt *c* versus PSI. Photochronoamperometric measurements have been carried out under aerobic conditions, phosphate buffer (5 mM, pH 7) at a potential of -100 mV (vs. Ag|AgCl) using white light of 20 mW cm^{-2} ($n = 4$).

III) Peak separation of Au-ML-DNA-[PSI:cyt *c*/DNA]_{*n*} electrodes

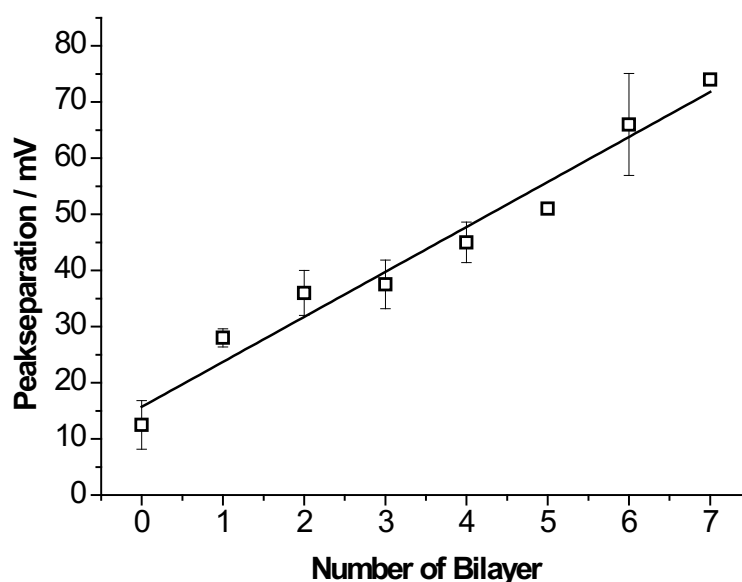


Fig. S3: Peak separation of Au-ML-DNA-[PSI:cyt *c*/DNA]_{*n*} electrodes in dependence of the number *n* of bilayers. Peak separation increases linearly with the number of bilayers. Measurements have been performed with a scan rate of 100 mV s^{-1} between -300 mV and 300 mV in phosphate buffer (5 mM, pH 7) in the dark. Linear fit was performed with an adjusted $R^2 = 0.962$.

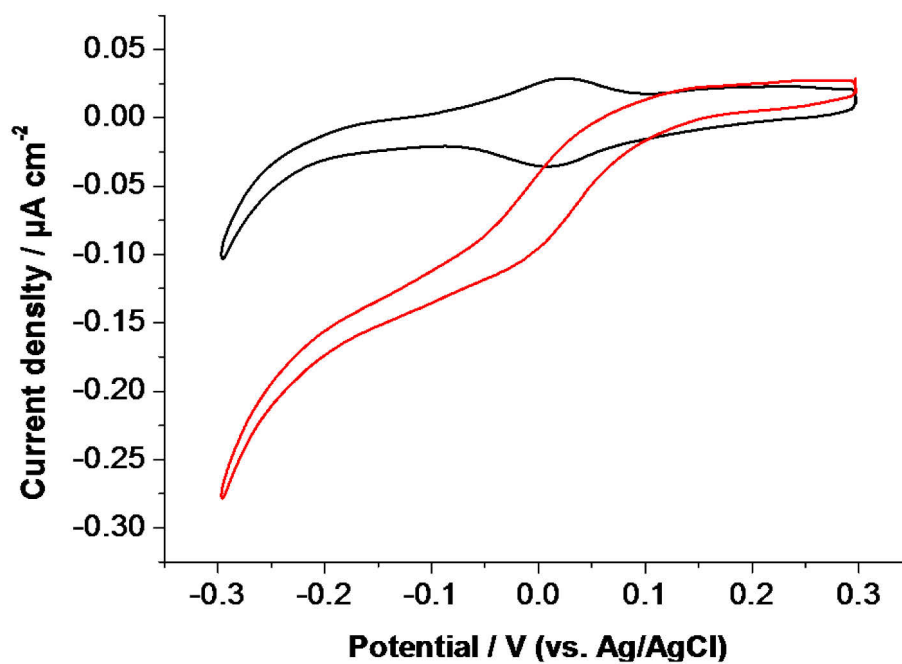
IV) Photocatalysis of Au-ML-DNA-[PSI:cyt *c*/DNA]_n electrodes

Fig. S4: Photo-induced catalytic current of the Au-ML-DNA-[PSI:cyt *c*/DNA]_n electrode. The experiment has been performed in the dark (black) and with 50 mW cm⁻² of white light (red) at a scan rate of 10 mV s⁻¹ in aerobic phosphate buffer (5 mM, pH 7) containing 1 mM MV²⁺. Cathodic catalysis starts at 80 mV vs. Ag|AgCl.

V) SPR of Au-ML-DNA-[PSI:cyt *c*/DNA]_n assembly

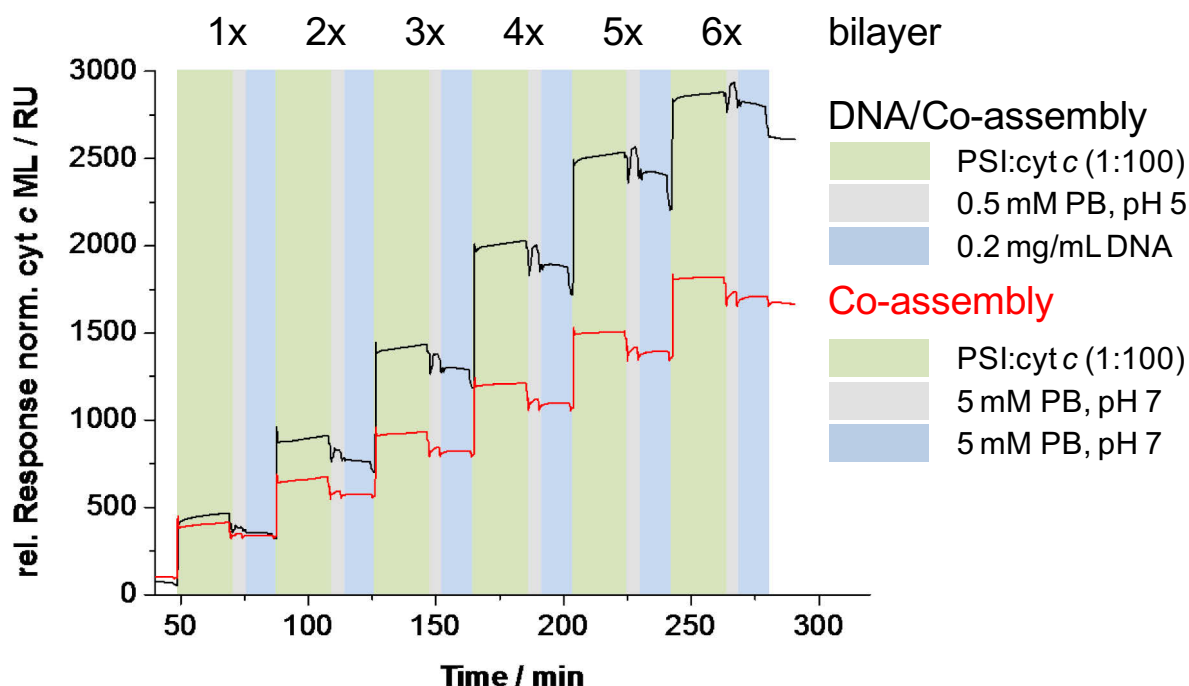


Fig. S5: Surface plasmon resonance measurements of the assembly of photosystem I (PSI) and cytochrome *c* (cyt *c*) on a cyt *c* monolayer (cyt *c* ML) with and without the use of DNA (Au-ML-DNA-[PSI:cyt *c*/DNA]_n and Au-ML-[PSI:cyt *c*]_n assembly for *n* = 1, 2, 3, 4, 5, 6). An intermittent buffer wash with phosphate buffer (PB) between the PSI:cyt *c* and DNA layer has been performed. The sensorgram starts after the incubation of a cyt *c* ML (both systems) and one DNA layer (only for the DNA/co-assembly system) and have been normalized to the cyt *c* mass signal of the cyt *c* ML. The rather minor differences for the first bilayer between the control (co-assembly) and the DNA/co-assembly can be explained by a small increase of surface roughness after the first DNA layer incubation, which raises the accessible area for the protein complexes. Here, for all assembly steps (both control and DNA assembly) the same injection time was chosen, which exhibit a different kinetic behaviour compared to Fig. 2 (the experiment has been performed under varying injection times of the PSI:cyt *c* complex solution).

VI) Photocurrent control without cyt *c* in the multilayer assembly: Au-ML-DNA-[PSI/DNA]₆

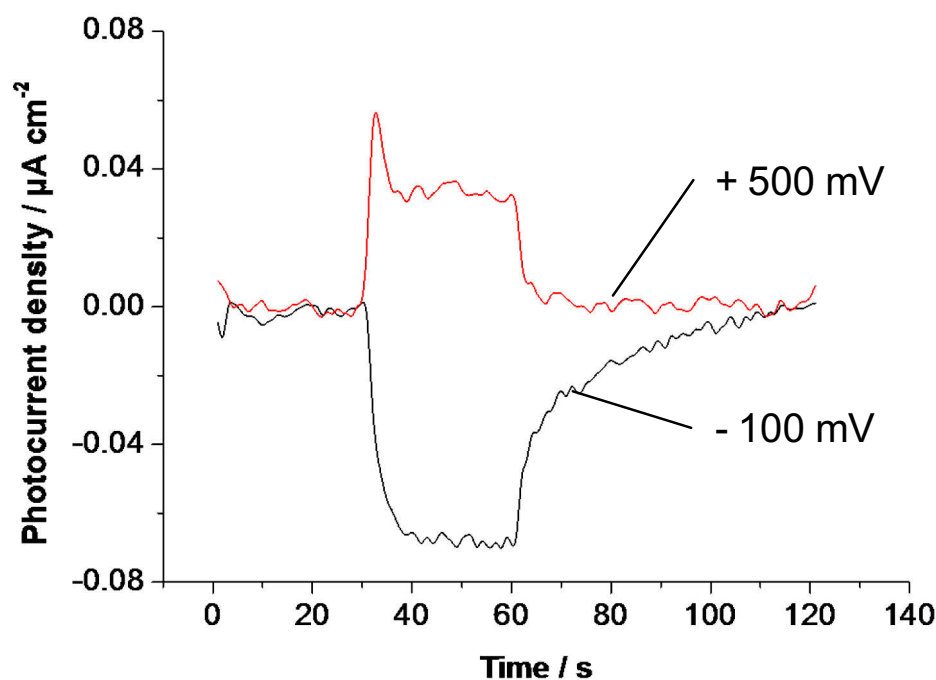


Fig. S6: Photocurrent measurements of the Au-ML-DNA-[PSI/DNA]₆ electrode. The electrode assembly contains a cyt *c* monolayer (ML) separated by DNA from the PSI/DNA assembly. The photocurrent measurement at two different potentials (-100 mV, +500 mV vs. Ag|AgCl) exhibit only minor photocurrent densities and cathodic and anodic photocurrents are observed. This experiment shows, that cyt *c* is necessary for the high unidirectional photocurrent generation of a multilayer assembly – DNA does not contribute to the electron transfer. The experiments have been performed at RT in phosphate buffer (5 mM, pH 7) using white light (20 mW cm⁻², 30 s pulse) at a potential of -100 mV (black) and +500 mV (red) vs. Ag|AgCl.

VII) Long term storage experiments of the Au-ML-DNA-[PSI:cyt *c*/DNA]₆ electrode

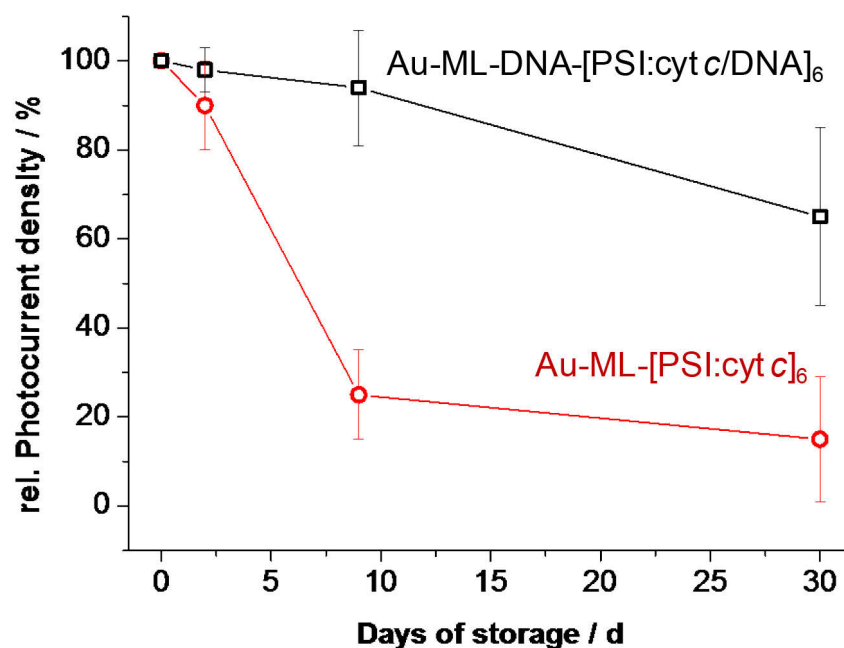


Fig. S7: Relative photocurrent density of the Au-ML-DNA-[PSI:cyt *c*/DNA]₆ (black) and Au-ML-[PSI:cyt *c*]₆ electrode vs. storage time. The experiment shows the measurement of each type of electrodes after a certain time of storage (dry at 4 °C in the dark). The electrodes have been measured first after preparation, than subsequently after 2, 9 and 30 days of storage. The experiments have been performed at RT in phosphate buffer (5 mM, pH 7) using white light (20 mW cm⁻²) at a potential of -100 mV vs. Ag|AgCl.

VIII) Light source spectrum (white light)

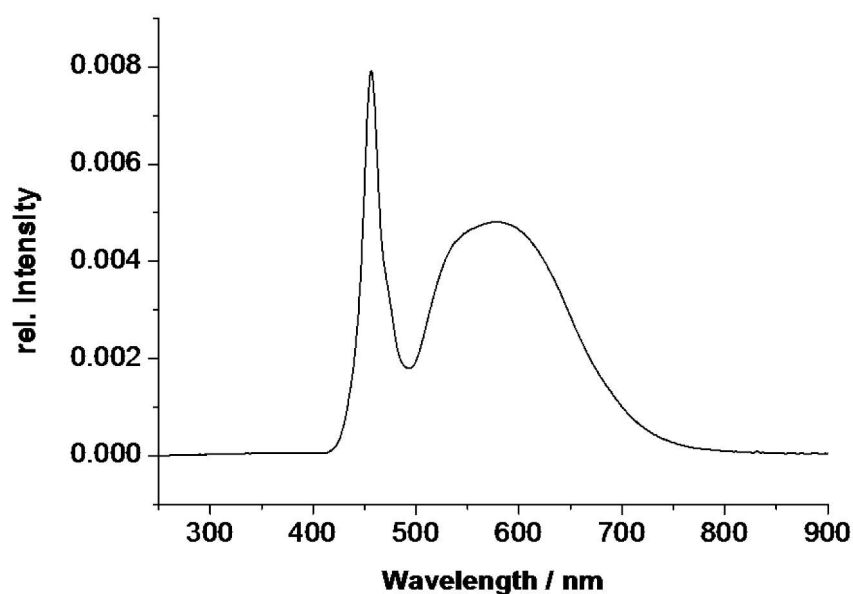


Fig. S8: Spectrum of the white light source used in all experiments. The spectrum was normalized to an integral area of 1. Characteristic peak values are at 456 nm and 576 nm.

IX) Interaction between cyt *c* and PSI in solution

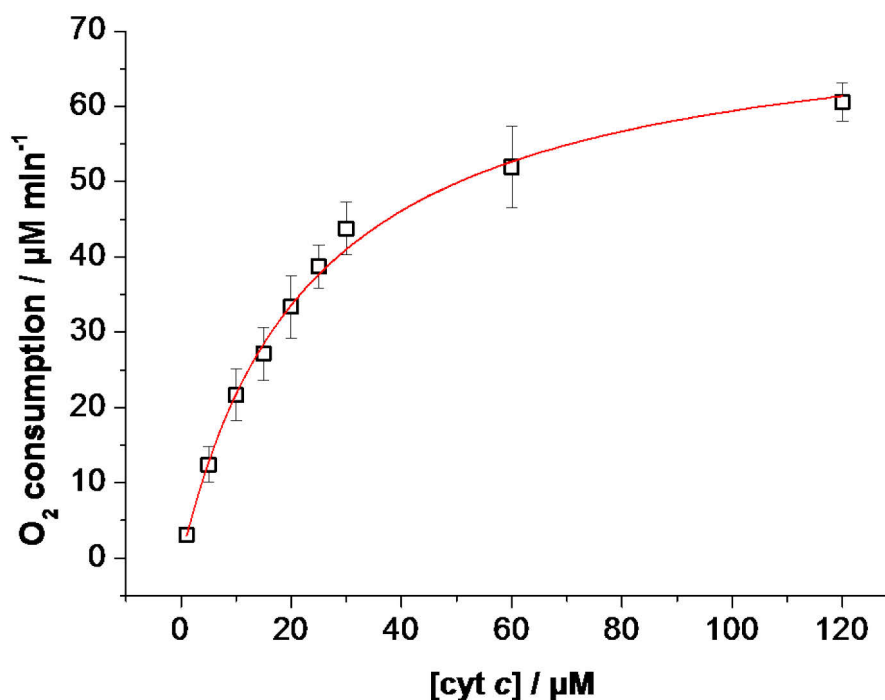


Fig. S9: O_2 consumption of PSI vs. cyt *c* concentration in solution. The experiment has been performed at 20 °C under aerobic conditions and saturating light ($700 \mu\text{mol m}^{-2} \text{s}^{-1}$) in phosphate buffer (5 mM, pH 7) containing $170 \mu\text{M MV}^{2+}$, 0.05 % β -DM, 1 mM Na-ascorbate, 20 nM PSI and a variable concentration of cyt *c*. Data have been fitted with a Michaelis-Menten equation with a K_M value of $23 \pm 3 \mu\text{M}$ and a v_{max} value of $74 \pm 2 \mu\text{M min}^{-1}$. For the interaction of PSI with cyt *c* a catalytic rate of $20 \pm 1 \text{s}^{-1}$ can be calculated. The experiment shows, that cyt *c* enhances the oxygen consumption of PSI dramatically, as it provides the electrons for the photoexcited P_{700} reduction.

X) Photoaction spectra of the Au-ML-DNA-[PSI:cyt *c*/DNA]₆ electrode

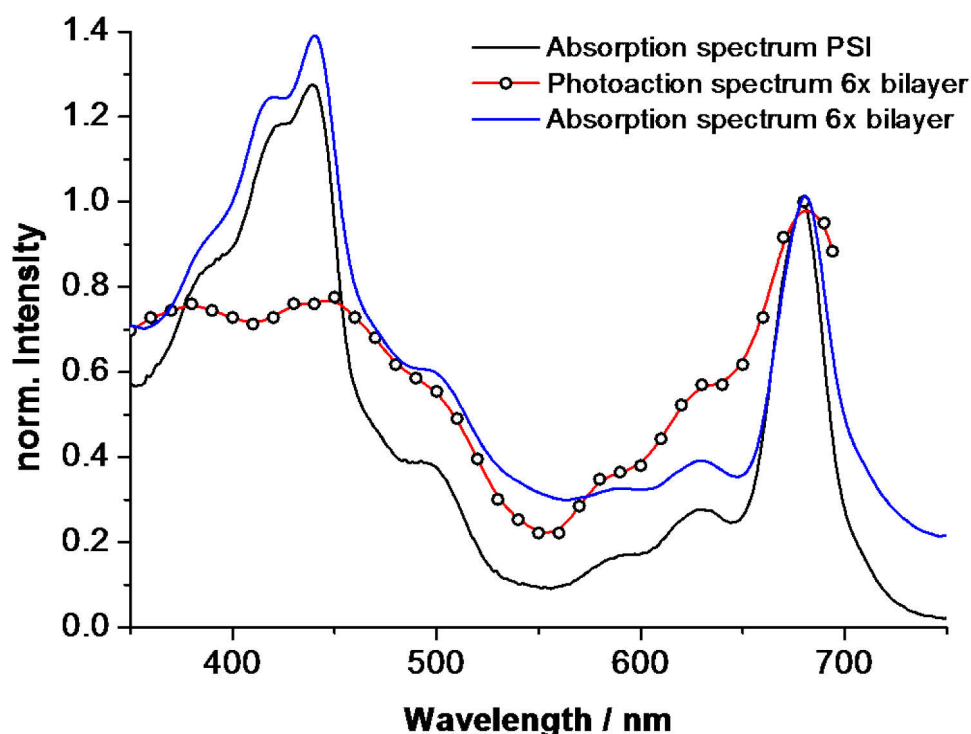


Fig. S10: Photoaction spectrum of an Au-ML-DNA-[PSI:cyt *c*/DNA]₆ electrode in comparison to the absorption spectrum of PSI in phosphate buffer (5 mM, pH 7) and with the absorption spectrum of a glass-APTES-DNA-[PSI:cyt *c*/DNA]₆ surface, all normalized at the peak at 680 nm. The spectra verify the origin of the photocurrent, since the photoaction spectrum follows the general line shape of absorption spectra of PSI in solution and in the assembly. Additionally, comparison between the absorption spectra of PSI in solution and the one on the glass-APTES-DNA-[PSI:cyt *c*/DNA]₆ surface reveals a similar wavelength dependence. However, due to incorporation of cyt *c* and DNA into the assembly the surface spectrum has an increased background. Photoaction spectra have been obtained with monochromatic light (bandwidth 15 nm, intensities > 10 mW cm⁻²) in aerobic phosphate buffer (5 mM, pH 7). The broadening of the peaks is due the relatively high bandwidth of the monochromatic light. The lower photocurrent generation in the region of 400 to 450 nm is possibly due to competing absorption of the cyt *c* Soret band. Spectra are the averages of 3 independent measurements.

XI) Proposed electron transfer mechanism for the Au-ML-DNA-[PSI:cyt *c*/DNA]_n electrode

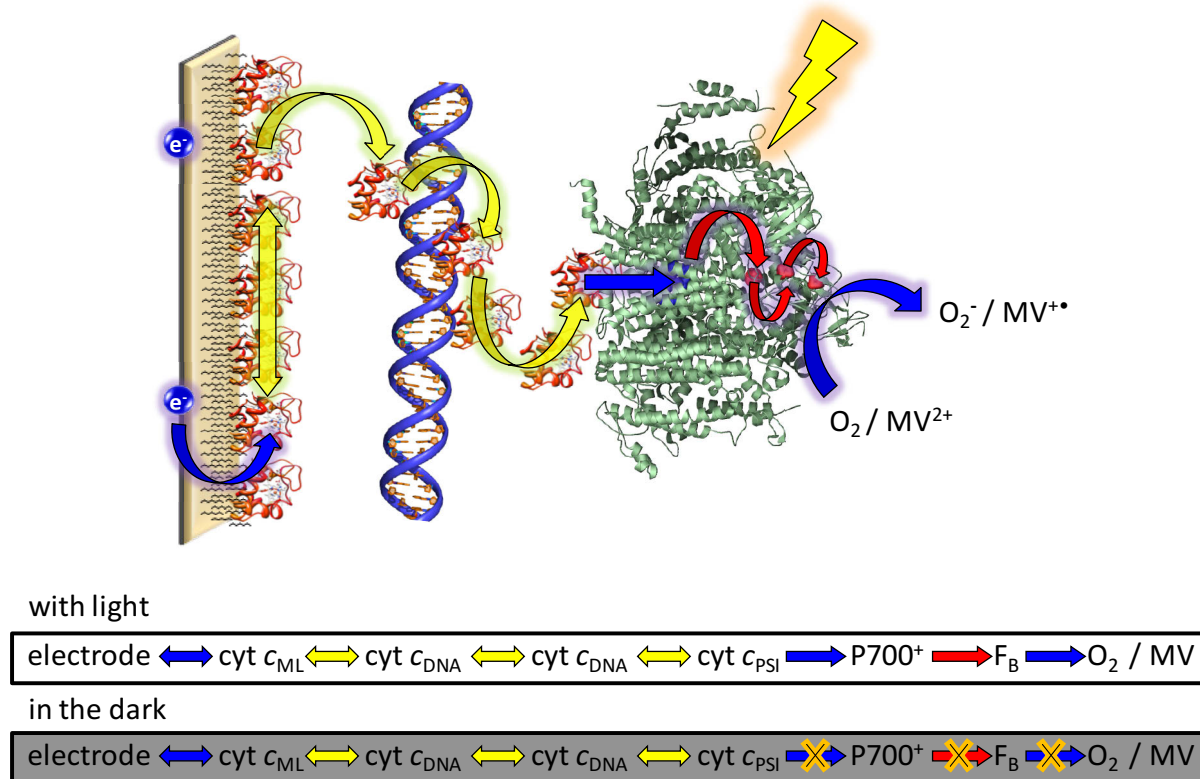


Fig. S11: Schematic representation of the proposed cathodic electron transfer mechanism for the Au-ML-DNA-[PSI:cyt *c*/DNA]_n electrode. Electrons are injected into the cyt *c* monolayer (cyt *c* ML) and relayed *via* cyt *c* – cyt *c* self exchange. Cyt *c* molecules bound to DNA molecules in proximity can exchange electrons. Finally, electrons are transferred to PSI-bound cyt *c* and reduce photoexcited P700⁺. Within PSI complex, electrons flow to the terminal iron-sulfur cluster F_B which is oxidized by oxygen or methyl viologen. Heterogeneous electron transfer processes are indicated with blue, homogenous with yellow, and intramolecular ones with red arrows.

4.3 Biohybrid architectures for efficient light-to-current conversion based on photosystem I within scalable 3D mesoporous electrodes

Authors: Kai R. Stieger, Sven C. Feifel, Heiko Lokstein, Mahdi Hejazi, Athina Zouni and Fred Lisdat

Abstract

The combination of advanced materials and defined surface design with complex proteins from natural photosynthesis is currently one of the major topics in the development of biohybrid systems and biophotovoltaic devices. In this study transparent mesoporous indium tin oxide (μ ITO) electrodes have been used in combination with the trimeric supercomplex photosystem I (PSI) from *Thermosynechococcus elongatus* and the small redox protein cytochrome *c* (cyt *c*) from *horse heart* to fabricate advanced and efficient photobiocathodes. The preparation of the μ ITO *via* spin coating allows an easy scalability and ensures a defined increase in electrochemically active surface area with accessibility for both proteins. Using these 3D electrodes up to a 40 μ m thickness, the immobilization of cyt *c* and PSI with full monolayer coverage and their electrical communication to the electrode can be achieved. Significant improvement can be made when the heterogeneous electron transfer rate constant of cyt *c* with the electrode is increased by proper surface treatment. The photocurrent follows linearly the thickness of the μ ITO and current densities of up to 150 μ A cm⁻² can be obtained without indications of a limitation. The internal quantum efficiency is determined to be 39 % which demonstrates that the wiring of PSI *via* cyt *c* can be advantageously used in a system with high protein loading and efficient electron pathways inside 3D transparent conducting oxides.

Introduction

The construction and development of photobiohybrid electrodes incorporating key components of natural photosynthesis – mainly the solar-to-charge carrier converting complexes – have been strongly emerged over the past few years.^{258,259} These biohybrid electrodes are suitable for potential future applications such as photo-switchable biosensors, solar-to-chemical²⁶⁰ or solar-to-electrical energy converting systems and establish the basis towards a bio-based renewable economy.^{193,230,239,261–263}

Learning from nature, light-to-charge carrier converting proteins from oxygenic photosynthesis of plants and cyanobacteria are of high interest for the construction of new functional devices.¹⁹² One of the most promising light-converting complexes is photosystem I (PSI), because of a very high quantum efficiency (~100 %), fast and stable charge separation, and a proper spectral overlap with our sun.^{25,192} In the thermophilic cyanobacterium *Thermosynechococcus elongatus* (*T. elongatus*) PSI is a trimeric pigment-protein super-complex, consisting of 12 different protein subunits, harbouring 96 chlorophylls *a* (Chl *a*) and 22 carotenoids – per monomeric subunit. Most Chls serve as light-harvesting antenna pigments and 6 Chls form an electron transport chain.⁷⁸ In PSI charge separation occurs at the luminal pigment dimer, Chl *a*/Chl *a*' (P₇₀₀) finally leading to a reduction of the stromally-located terminal iron-sulfur-cluster (F_B).^{83,244} Light-induced electron-hole pairs are restocked *via* cytochrome *c*₆ (cyt *c*₆), which reduces P₇₀₀, whereas the oxidation of PSI takes place at the F_B cluster, which is done by the redox protein ferredoxin (Fdx).⁵²

The effective electrical wiring of PSI to various electrode structures and materials is of fundamental importance for functional photobiohybrid devices generating higher photocurrent densities.¹⁹¹ A vast number of strategies has been published applying different surface design and chemistry.^{196–198,201,245,246,264,265} A strong improvement in electrode performance can be seen if electrical signal chains with electron shuttling systems or conducting junctions have been used.^{206,210,229,266,267}

In order to overcome the limitations of 2D arrangements and to generate higher photocurrents per geometrical electrode area, various strategies have been explored, which can be divided mainly into three groups: Multilayer architectures^{211,217,241,269,278,279}, 3D polymer gels^{212–214,216,231,268} and 3D electrode surfaces^{204,205,280}. Particularly in the latter group application potential can be seen, since limitations of electron transport in PSI multilayer architectures due to long electron transfer pathways can be circumvented. The light induced charge carriers can be injected directly into a high conductive material without being restricted to a planar surface dimension. Hence, photoactive PSI-containing 3D electrodes have been developed – often using semiconductor materials, such as ZnO/TiO₂ nanowires²²⁰ or nanostructured TiO₂ columns²²⁸. In addition, also porous structures such as silica nanopores show the possibility of PSI integration, but lack the electrical connection to an electrode.²⁸¹ Moreover, other light-harvesting components like the bacterial reaction center - light harvesting complex 1 (RC-LH1) could be connected to mesoporous silver electrodes.²⁸²

In this study, we exploit the features of a mesoporous indium tin oxide (μ ITO) electrode. Transparent conducting oxides (TCO) provide the advantage of high transparency with reasonable conductance. So far, direct electrochemistry of large proteins with TCOs is often rather difficult. Different reasons can be seen for this such as improper surface groups, low intrinsic charge carrier density and low electron tunneling rates. However by surface modification efficient functional systems with enzymes have been demonstrated.^{283–285} In addition photosystem II (PSII) has been functionally attached to such surfaces.^{286,287}

Here, we use cytochrome *c* (cyt *c*) as a wiring agent for PSI molecules, which has been previously investigated in mono- and multilayer architectures by us.^{267,278} The small redox protein cyt *c* is oxidized by the photo-excited PSI and subsequently reduced at the electrode. Furthermore, cyt *c* adsorbs and exhibits reasonable heterogeneous electron transfer rate constants (k_s) on planar^{159,288}, meso-^{161,289} and nanostructured¹⁶² ITO. As an obvious consequence, we combine the cyt *c*-PSI system with a mesoporous indium tin oxide electrode (μ ITO) to construct a tuneable photobiocathode. We characterize the (photo-) electrochemical properties in terms of efficiency so as scalability and demonstrate ways to improve the light-to-current conversion performance.

Experimental Methods

Isolation of Photosystem I from *T. elongatus*

Growth of *Thermosynechococcus elongatus* BP-1 and extraction of membrane proteins from thylakoids were performed according to Kern *et al.* 2005.²⁷² For the purification of PSI two chromatography steps were used. The first column was packed with Toyo Pearl DEAE 650 S (GE Healthcare) and pre-equilibrated with buffer A (20 mM MES-NaOH, pH 6.0, 20 mM CaCl₂, 0.02 % β -DM, 5 % glycerol). After sample loading and washing the column with buffer A, PSI was separated from PSII using a linear gradient with buffer B (20 mM MES-NaOH, pH 6.0, 20 mM CaCl₂, 0.02 % β -DM, 5 % glycerol, 100 mM MgSO₄). PSI eluted at 80-90 mM MgSO₄ was pooled and diluted with the same volume of buffer C (5 mM MES-NaOH, pH 6.0, 0.02 % β -DM). The second column was packed with Q-Sepharose™ Fast Flow (GE Healthcare) and pre-equilibrated with buffer D (5 mM MES-NaOH, pH 6.0, 0.02 % β -DM, 60 mM MgSO₄). PSI trimer was separated from remaining PSI monomer by a linear gradient with buffer E (5 mM MES-NaOH, pH 6.0, 0.02 % β -DM, 150 mM MgSO₄). The PSI trimer eluted at 150 mM MgSO₄. The fractions were pooled and concentrated in an Amicon

stirring cell using a Biomax 100 membrane (Millipore). Finally, the PSI trimer was crystallised by dilution with buffer C at 4 °C until a concentration of 5 mM MgSO₄ was reached. The crystals were collected by centrifugation (5 min, 4 °C, 4000 g), washed with buffer C, re-solubilized by adding buffer F (5 mM MES-NaOH, pH 6.0, 30 mM MgSO₄) and re-crystallised as described above. For the assembly experiments the crystals were dissolved in 10 mM tricine, 50 mM MgSO₄, 0.02 % β -DM, pH 8.

Preparation of μ ITO electrodes

ITO slides (20 Ω / sq, Sigma) have been cut to a rectangle with dimensions of 0.5 and 1.5 cm. The slides have been cleaned with acetone, isopropanol, ethanol for 30 min each in an ultrasonication bath and stored in an oven at 150 °C prior to use. The cleaned ITO slides have been allowed to cool down to RT and placed on a spin coater (SCC-200, KLM). Slides have been covered with parafilm to result in a free area of 0.2 cm². A mixture of 800 nm diameter latex beads (LB, Sigma) and 50 nm ITO nanoparticles (ITO_{NP}, Sigma) has been produced according to Mersch *et al.*²⁸⁷ 35 mg of ITO_{NP} has been suspended in 300 μ L (6:1 methanol/water) and ultrasonicated for at least 1 h. 1 mL of a 2.5 % LB methanol suspension was centrifuged for 10 min at 25,000 g. After removal of the supernatant the LB precipitate was re-suspended with 300 μ L ITO_{NP} solution and thoroughly vortexed. The mixture was then ultrasonicated in an ice bath for at least 5 min. Afterwards 4 μ L of the ITO_{NP}/LB suspension was spin coated at 60 rps for each layer onto a geometrical area of 0.2 cm². Between each layer there was a waiting time of 5 s after the next layer was drop casted. The as-deposited μ ITO electrodes have been sintered for 2 h at 500 °C in a custom-made chamber under either air or argon atmosphere. The air sintered μ ITO electrodes have been cleaned with air plasma for 5 min at 50 % power (Diener electronic).

Preparation of μ ITO-PSI-cyt *c* electrodes

A volume of 2 μ L of a 20 μ M PSI solution (10 mM tricine, 50 mM MgSO₄, 0.02 % β -DM, pH 8) has been drop casted onto the μ ITO electrode and incubated for 2 min. The unbound protein was removed by repeated washing in phosphate buffer (5 mM, pH 7). Afterwards the electrodes have been drop casted with 10 μ L of 1 mM cyt *c* (horse heart, Sigma) in phosphate buffer (5 mM, pH 7) and incubated for 2 min. Unbound cyt *c* was washed away by dipping into solution containing phosphate buffer (5 mM, pH 7). This procedure appeared to be optimal, because changing the incubation order or protein concentrations yields less photocurrent.

Protein concentration determination

For PSI protein concentration determination, chlorophyll *a* has been extracted by incubating the electrode in 80 % acetone for 2 h at RT followed by measuring the extinction at 664 nm using an extinction coefficient of $76.79 \text{ L mmol}^{-1} \text{ cm}^{-1}$.²⁴⁸ The cyt *c* surface concentration has been determined by cyclic voltammetry at 100 mV s^{-1} in a potential range of $-300 - 400 \text{ mV vs. Ag|AgCl}$. Electro-active protein amount was calculated from the peak area and using Faraday's law.¹⁴⁴

Electrochemical experiments

Electrochemical measurements have been performed using the potentiostat CHI660E (CHI) and a custom-made electrochemical cell containing 1 mL of phosphate buffer (5 mM, pH 7), a Pt counter electrode and an Ag|AgCl (3 M KCl) reference electrode. Cyclic voltammetric measurements have been performed at a scan rate of 100 mV s^{-1} or 10 mV s^{-1} if not otherwise stated and in a potential range from $+400$ to $-300 \text{ mV vs. Ag|AgCl}$. The heterogeneous electron transfer rate constant (k_s) has been determined according to the method of Laviron.²⁹⁰ Experiments have been performed with scan rates of 5 to 3000 mV s^{-1} under ohmic drop compensation in phosphate buffer (5 mM, pH 7).

Photoelectrochemical experiments

Photoelectrochemical measurements have been performed using an integrated system (CIMPS, Zahner) containing a white LED light source (4300 K, Zahner) with adjustable intensity (max. 100 mW cm^{-2}), an electrochemical cell and a photodiode with feedback control to the light source *via* a potentiostat (PP211, Zahner). Electrochemical investigations have been carried out through a coupled potentiostat (Zennium, Zahner). In all experiments a Pt counter electrode and an Ag|AgCl (3 M KCl) reference electrode have been used in an aqueous solution containing phosphate buffer (5 mM, pH 7). Experiments have been performed under air saturation of the solutions. Photochronoamperometric experiments have been performed at RT and $-100 \text{ mV vs. Ag|AgCl}$, while using an illumination time of 6 min and a light power of 20 mW cm^{-2} (white light source spectrum see Fig. S8). Light power dependent photocurrent experiments have been done at -100 mV using a power range of $0.5 - 60 \text{ mW cm}^{-2}$ of white light. Photoaction spectra have been achieved at a potential of $-100 \text{ mV vs. Ag|AgCl}$ in aerobic phosphate buffer (5 mM, pH 7) using a monochromator (Polychrome V, Till Photonics) with a bandwidth of 20 nm.

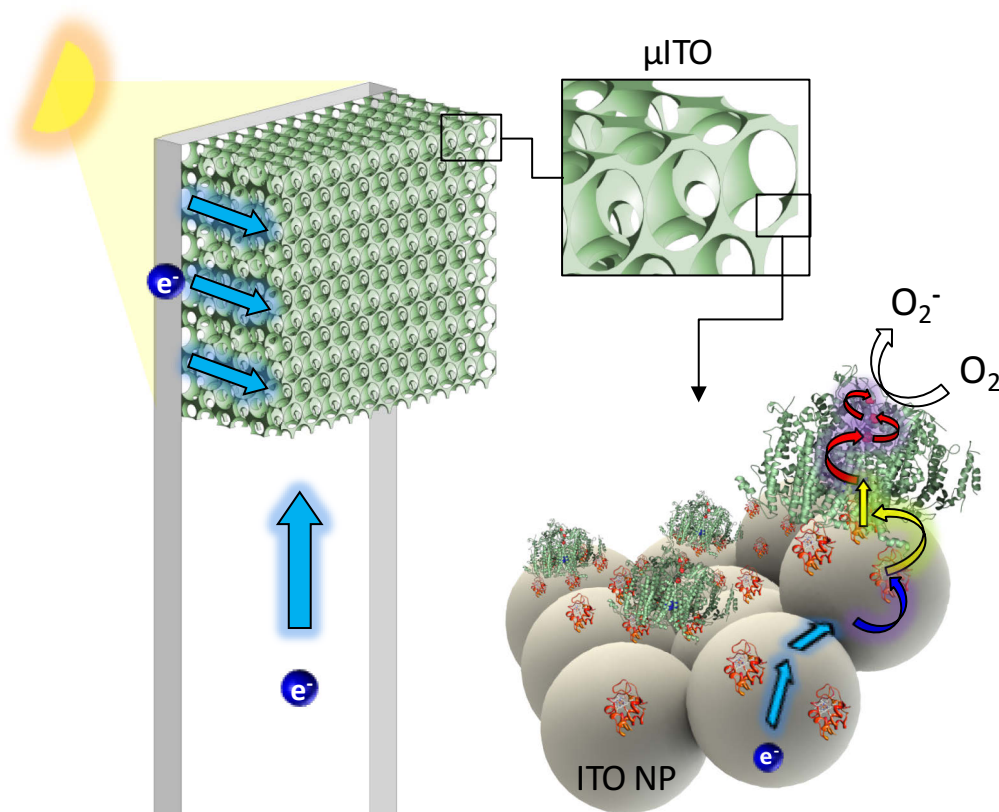
Scanning electron microscopy

6x layer μ ITO electrodes have been prepared, according to the previously described procedure in this study. For visualization of morphology of the prepared electrodes, scanning electron microscopy (JSM-6510, JEOL) has been employed. The acceleration voltage was 10 kV. A working distance of 10 mm and a magnification of 12,000 fold were chosen. Images have been recorded from the top and under an approximate angle of 45° relative to the surface normal.

Results and Discussion

In this study we exploit the transparency and conductivity of ITO with the possibility of 3D structure preparation and combine it with PSI and cyt *c* to develop a functional photocathode system. In scheme 1 electrode design and electron transfer pathways are displayed. To produce a μ ITO electrode, a mixture of ITO nanoparticles (ITO_{NP}) and latex beads (LB) have been spin coated onto an ITO slide in various deposition steps (see experimental section). The sintering process at high temperatures is performed only once after the layers have been deposited on the surface. It forms an inverse opal mesoporous structure, because of the thermal decomposition of LB. The generated hollow structure is then first incubated with PSI, followed by an incubation with cyt *c*, yielding a greenish-coloured electrode (see experimental methods). After light exposure a cathodic photocurrent is obtained verifying that electrons are transported from the planar ITO electrode towards the deposited porous ITO structure, reducing the bound cyt *c* and further the assembled PSI. At the stromal side of PSI electrons can be finally transferred to an acceptor in solution (here oxygen, see scheme 1). The signal chain is switched on and off by the light excitation of PSI.

First of all, the prepared μ ITO electrodes have been characterized with scanning electron microscopy (SEM) and cyclic voltammetry (CV) to clarify the successful and reproducible construction of these basic electrodes. SEM measurements show a regular structure with circle shaped holes comprising interconnections to the next layer of removed latex particles (Fig. 1). Highly uniform holes with a diameter of 640 ± 10 nm ($n = 20$) are observed. In comparison with the used LB diameter (~ 800 nm) in the deposition mixture, the produced holes are shrunk by about 160 nm in diameter during the baking step. Interconnections are of different size and range from 200 to 400 nm. This may ensure access to deeper layers of the μ ITO even for large proteins like PSI.



Scheme 1: Schematic representation of a μ ITO electrode with integrated photosystem I (PSI) and cytochrome *c* (cyt *c*). The μ ITO structure displays an inverse opal mesoporous structure with nanoparticulate surface roughness. Cyt *c* binds to the surface and allows the electrical connection of PSI to the μ ITO electrode surface. After light excitation, electrons flow from base ITO electrode in the μ ITO structure consisting of sintered ITO nanoparticles (ITO_{NP}) further to cyt *c*, which subsequently reduces PSI. The photo-excited electron within PSI can be transferred to molecular oxygen. Light blue arrows display intrinsic electron transfer in ITO, the dark blue arrow indicates the heterogeneous electron transfer, yellow arrows show the protein-protein electron transfer and red arrows display the PSI intramolecular electron transfer cascade.

The μ ITO electrodes can be prepared with various numbers of spin coating steps allowing a defined adjustment of the thickness of the electrode structure. The individual preparation steps can also be seen in Fig. 1. The average layer thickness for one spin coating step is $5.2 \pm 0.4 \mu\text{m}$. The gain in electro-active surface area can be verified by CV measurements. Since the double layer capacity scales with the electrode area in electrolyte contact, the electro-active area is calculated from the charging current of flat ITO and the different μ ITOs (for procedure details see ESI, section A). This results in a linear function with the number of layers ($R^2 = 0.999$) with a slope of $5.5 \pm 0.01 \text{ cm}^2 / \text{layer}$. The results taken from CV and SEM measurements indicate that the surface area and height of μ ITO electrodes can directly be controlled *via* the number of deposited layers. Here, no saturation behaviour has been

observed. Moreover, structural properties like hole diameters, interconnections and uniformity are highly conserved within all produced electrodes.

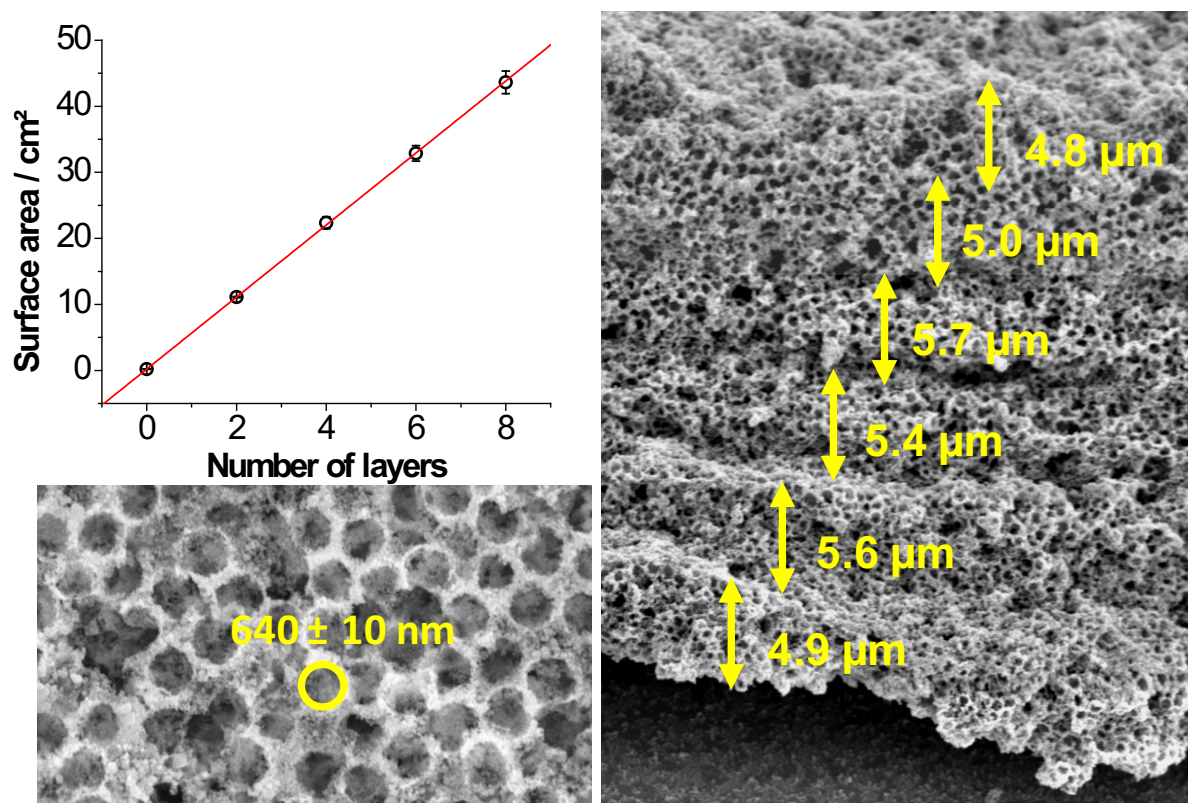


Fig. 1: Scanning electron microscopy images of sintered μ ITO electrodes, prepared by 6 spin coating steps (6x μ ITO). Bottom left: Top view of the 6x μ ITO electrode. After thermal removal of latex beads, hole diameter can be determined to 640 ± 10 nm ($n = 20$). Right: Side view of the 6x μ ITO electrode. Defined separation between the successively added spin-coated layers with a height of 5.2 ± 0.4 μ m / layer are visible. Top left: Electro-active surface area increase dependent on the number of applied layers. Surface increases by 5.5 ± 0.01 cm^2 / layer ($R^2 = 0.999$, $n = 4$).

Photoelectrochemical properties of μ ITO-PSI-cyt *c* electrodes

In this section the focus is on the construction of a photobiohybrid system using the above described μ ITO electrodes. Here different strategies for combining PSI and cyt *c* with the 3D electrode have been studied. The current behaviour of these electrodes after illumination has been used as success criteria. Besides the approaches of solution incubation and drop casting, the order of protein contacts and protein concentration has been varied. The highest photocurrent density can be achieved, when the following preparation procedure is used: First, a highly concentrated PSI solution (> 20 μ M) is drop-casted and the electrode is incubated for several minutes, then the electrode is washed with phosphate buffer. Second, a 1 mM cyt *c* solution is drop-casted afterwards and incubated for several minutes, followed by

washing with phosphate buffer prior to any photoelectrochemical measurement (see experimental section). After the incubation steps the greenish colour of the electrode already indicates the binding of PSI to the μ ITO surface. The second incubation step with cyt *c* ensures the binding of the redox protein to PSI and the μ ITO surface, which results in the connection of PSI with the electrode. To clarify the electron transfer mechanism of such a μ ITO-PSI-cyt *c* electrode, CV experiments have been performed. They reveal the direct electrochemistry of cyt *c* incorporated in the μ ITO electrode (see Fig. S1), which is in accordance to results obtained at other porous ITO electrodes.¹⁶¹ Clear oxidation/reduction peaks are visible with a peak-to-peak separation of 80 mV and a full peak width at half maximum of 93 mV indicating a quasi-reversible heterogeneous electron transfer of the redox protein with the electrode.¹²⁶ It has to be noted here that the electrochemistry of cyt *c* is not disturbed by the presence of PSI in the 3D electrode structure (see Fig. S1). Under illumination a distinct solely cathodic catalytic current is detected starting at around 70 mV vs. Ag|AgCl (see Fig. S2). This indicates that cyt *c* is reduced by the electrode to further inject electrons into PSI, as previously proven by us at modified gold.^{267,278} The open circuit potential of this electrode is in the range of -50 to -100 mV vs. Ag|AgCl.

Fig. 2 displays the photocurrent density of a μ ITO-PSI-cyt *c* electrode under constant illumination at a potential of -100 mV vs. Ag|AgCl. A peak cathodic photocurrent density of $103 \pm 8 \mu\text{A cm}^{-2}$, as well as a steady-state photocurrent of $35 \pm 2 \mu\text{A cm}^{-2}$ ($n = 4$) is measured. The fast decay in photocurrent over time can be addressed to diffusion limitation of the final electron acceptor (oxygen). When diffusion has been accelerated by constant stirring, the decay can be drastically reduced and a rather stable photocurrent output is obtained. The small drop observed even under stirring can be attributed to the transport limitation of oxygen within the 3D μ ITO structure, which cannot be influenced by external stirring. During the photo-excitation process dissolved oxygen is consumed by PSI and thus, has to diffuse from the bulk of the solution to the surface-fixed proteins. Due to the mesoporous nature of the electrode, the diffusion of reactants is slowed down, consequently becoming a rate-limiting step. At this point it should be added that the photocurrent can be further enhanced when the electron transfer from the F_B cluster is enhanced by addition of methyl viologen (by 45 %).

The incorporation of cyt *c* in this assembly is essential for the functioning of the photocathode, since without cyt *c* only minor photocurrents of about $1 \mu\text{A cm}^{-2}$ are detected (with PSI alone, Fig. S3). This means that only few PSI molecules can directly exchange electrons with the electrode. Furthermore the μ ITO and the μ ITO-cyt *c* electrode do not show

any detectable photocurrent, indicating the necessity of the presence of the photoactive enzyme (see Fig. S3).

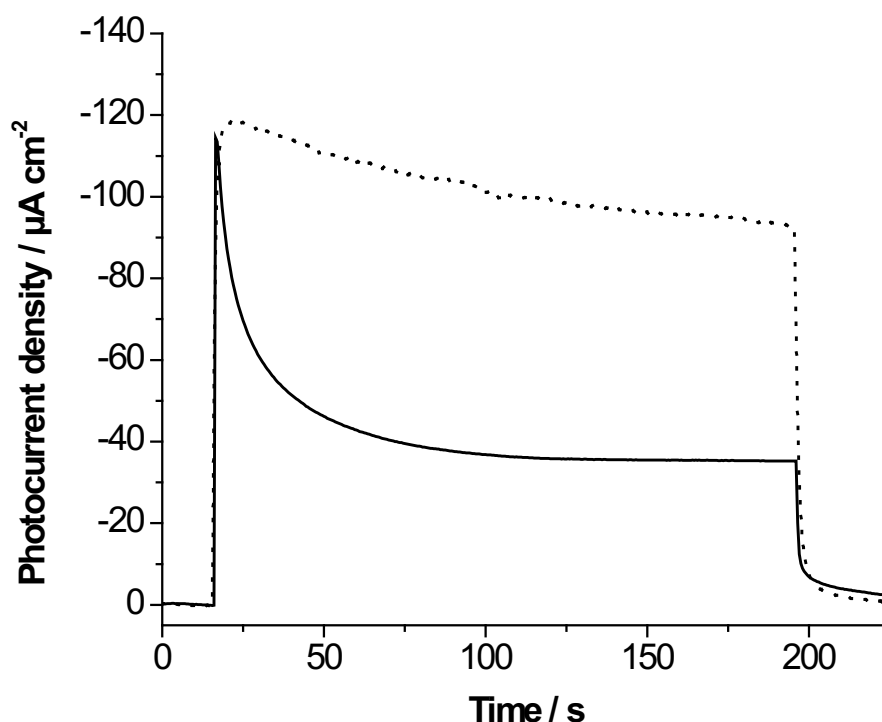


Fig. 2: Photocurrent response of a 6x $\mu\text{ITO-PSI-cyt } c$ electrode. Experiments have been performed at RT in phosphate buffer (5 mM, pH 7) using white light (20 mW cm^{-2} , 3 min) at a potential of -100 mV vs. Ag|AgCl with constant stirring (dotted) or without (solid). Geometrical electrode area: 0.2 cm^2 .

Operation of the photobiohybrid cathode is based on the strong interaction of *cyt c* with the ITO surface on the one hand and with PSI on the other. This view is supported by experiments of such an electrode in buffer of higher ionic concentration (100 mM). Here much smaller photocurrents have been found (reduction of about 70 %) which can be attributed to the lowering of interaction forces between the essential components of the system and the electrostatic nature of this interaction (see Fig. S4).

For a better understanding of the limitations within such a complex structure, two different preparation procedures for the μITO electrode have been investigated. The μITO electrodes have been sintered either under standard air conditions (P_{Air}) or under argon atmosphere (P_{Argon}). This strategy has been chosen, since oxygen vacancies in ITO are supposed to improve conductivity and electron mobility.²⁹¹ In Fig. 3 a comparison of different electrodes prepared according to both procedures (P_{Air} , P_{Argon}) is displayed. Here the photocurrent densities of $\mu\text{ITO-PSI-cyt } c$ electrodes are plotted against the number of μITO layers used during electrode preparation. From 2 to 8 layers a linear increase in photocurrent output is

achieved. The procedure under argon (P_{Argon}) results in the highest overall photocurrents. They increase linearly with a slope of $17.5 \pm 0.4 \mu\text{A cm}^{-2} / \text{layer}$ ($R^2 = 0.992$, $n = 4$).

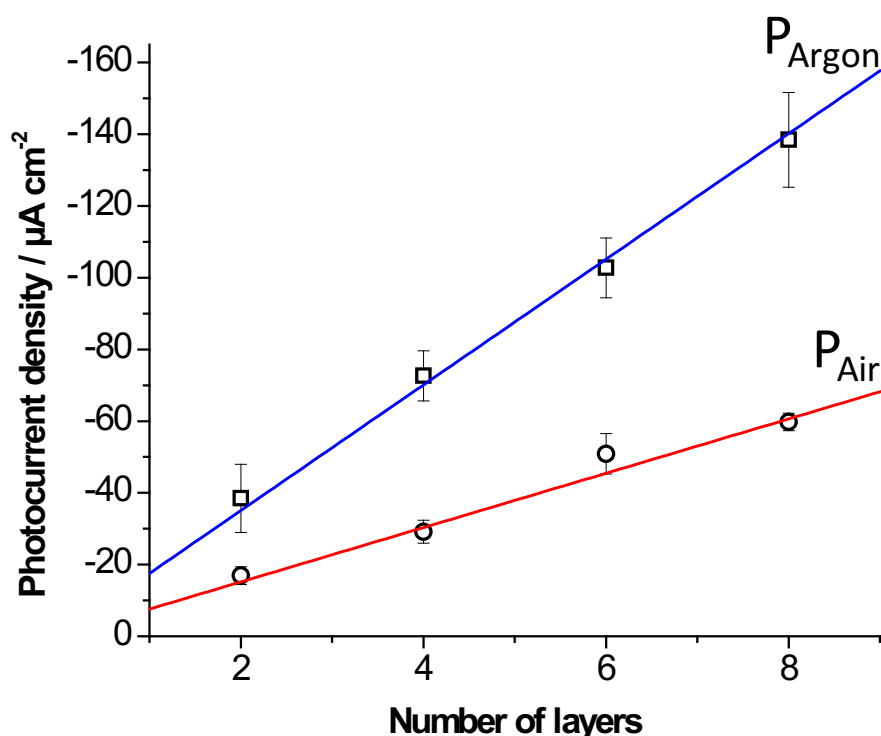


Fig. 3: Photocurrent density dependent on the number of applied μITO layers of a μITO -PSI-cyt *c* electrode and different sintering procedures (P_{Air} = sintering under air = circles, P_{Argon} = sintering under argon = squares). A linear relationship between photocurrent and the number of layers can be found (P_{Argon} : $17.5 \pm 0.4 \mu\text{A cm}^{-2} / \text{layer}$, $R^2 = 0.992$; P_{Air} : $7.7 \pm 0.2 \mu\text{A cm}^{-2} / \text{layer}$, $R^2 = 0.989$). Experiments have been performed at RT in phosphate buffer (5 mM, pH 7) using white light (20 mW cm^{-2}) at a potential of -100 mV vs. Ag|AgCl ($n = 4$). Geometrical electrode area: 0.2 cm^2 .

Sintering under air atmosphere (P_{Air}) also give defined photocurrents, but with significantly lower current output ($7.7 \pm 0.2 \mu\text{A cm}^{-2} / \text{layer}$, $R^2 = 0.989$). A comparison between P_{Argon} and P_{Air} in terms of electro-active surface area (for a given number of μITO layers) reveals no significant difference (see Fig. S5). Furthermore the protein concentration in the structure, either cyt *c* or PSI, is very similar (in the limits of error, see discussion below), and thus cannot be the reason for the drastic change in photocurrent magnitude. Therefore, we focus on the heterogeneous electron transfer rate (k_s) of cyt *c* to the μITO electrode being possibly the reason for a higher current density of the photobiohybrid system when prepared under argon atmosphere. By using the method of Laviron²⁹⁰ a k_s of $1.1 \pm 0.1 \text{ s}^{-1}$ for P_{Argon} and $0.54 \pm 0.03 \text{ s}^{-1}$ for P_{Air} can be derived (see Fig. S6). The values compare well with other findings on porous TCO materials. Oxygen vacancies, conductivity, surface roughness, and

protein orientation have been elucidated as key factors for the heterogeneous electron transfer rate between cyt *c* and the TCO material.^{161,162,166} Thermal treatment of ITO under air leads to a higher concentration of oxygen in the material, thus lowering the carrier density. This seems to be the reason for the higher k_s using P_{Argon}, since all other parameters (e. g. sintering temperature and time) have been kept constant. When all the other electron transfer steps (cyt *c*-cyt *c*, cyt *c*-PSI, PSI-oxygen) are faster than the heterogeneous electron transfer of cyt *c* on ITO, the overall current flow through the system is not only limited by acceptor diffusion but also by the rate of cyt *c* reduction. These experiments show that analysing limiting steps in complex systems can help to improve the performance. As a consequence, in the following experiments we use sintering under argon for the μ ITO preparation.

In the next set of experiments, the focus is on the protein amount that can be integrated in the μ ITO structure for different layers. The concentration of cyt *c* has been analysed *via* CV by evaluating the charge of the redox reaction, whereas PSI concentration can be determined by UV/Vis measurements evaluating the chlorophyll concentration extracted from the electrode (see experimental section). Fig. 4 displays the determined protein concentration related to the geometrical surface. Here, a linear relationship of both the cyt *c* and PSI concentration to the number of μ ITO layers deposited during preparation of the base electrode is found. A concentration increase related to the geometrical area of $4.5 \pm 0.2 \text{ pmol cm}^{-2} / \text{layer}$ ($R^2 = 0.997$, $n = 5$) can be detected for PSI, whereas the value for cyt *c* is $0.46 \pm 0.01 \text{ nmol cm}^{-2} / \text{layer}$ ($R^2 = 0.998$, $n = 5$). Related to the electro-active surface area (see Fig. 1) a surface coverage of $0.2 \pm 0.01 \text{ pmol cm}^{-2}$ for PSI is calculated, which is close to an entire monolayer coverage. The same encounters for cyt *c*, which assembles also in monolayer coverage of $15.5 \pm 0.4 \text{ pmol cm}^{-2}$. These values indicate that both proteins can penetrate the whole 3D structure and we can make use of the full electro-active surface of the electrode.

In order to describe the electron transfer efficiency per molecule, the turnover number (T_e) has been calculated. T_e is the number of electrons, which are processed by each individual protein per second. The result of this analysis is given in Fig. 4. At a minimum of 4x μ ITO layers T_e for both proteins become constant to a value of $0.42 \pm 0.01 \text{ e}^- \text{ cyt } c^{-1} \text{ s}^{-1}$ and $35 \pm 3 \text{ e}^- \text{ PSI}^{-1} \text{ s}^{-1}$. The T_e for μ ITO-PSI-cyt *c* with respect to PSI is two orders of magnitude higher than without cyt *c* (μ ITO-PSI, $0.3 \pm 0.1 \text{ e}^- \text{ PSI}^{-1} \text{ s}^{-1}$). This clearly explains the strong effect on performance, when cyt *c* is added to the system. A comparison of the T_e value of cyt *c* to the determined k_s

shows, that not all of the *cyt c* molecules contribute to the reduction of PSI, but are connected to the electrode.

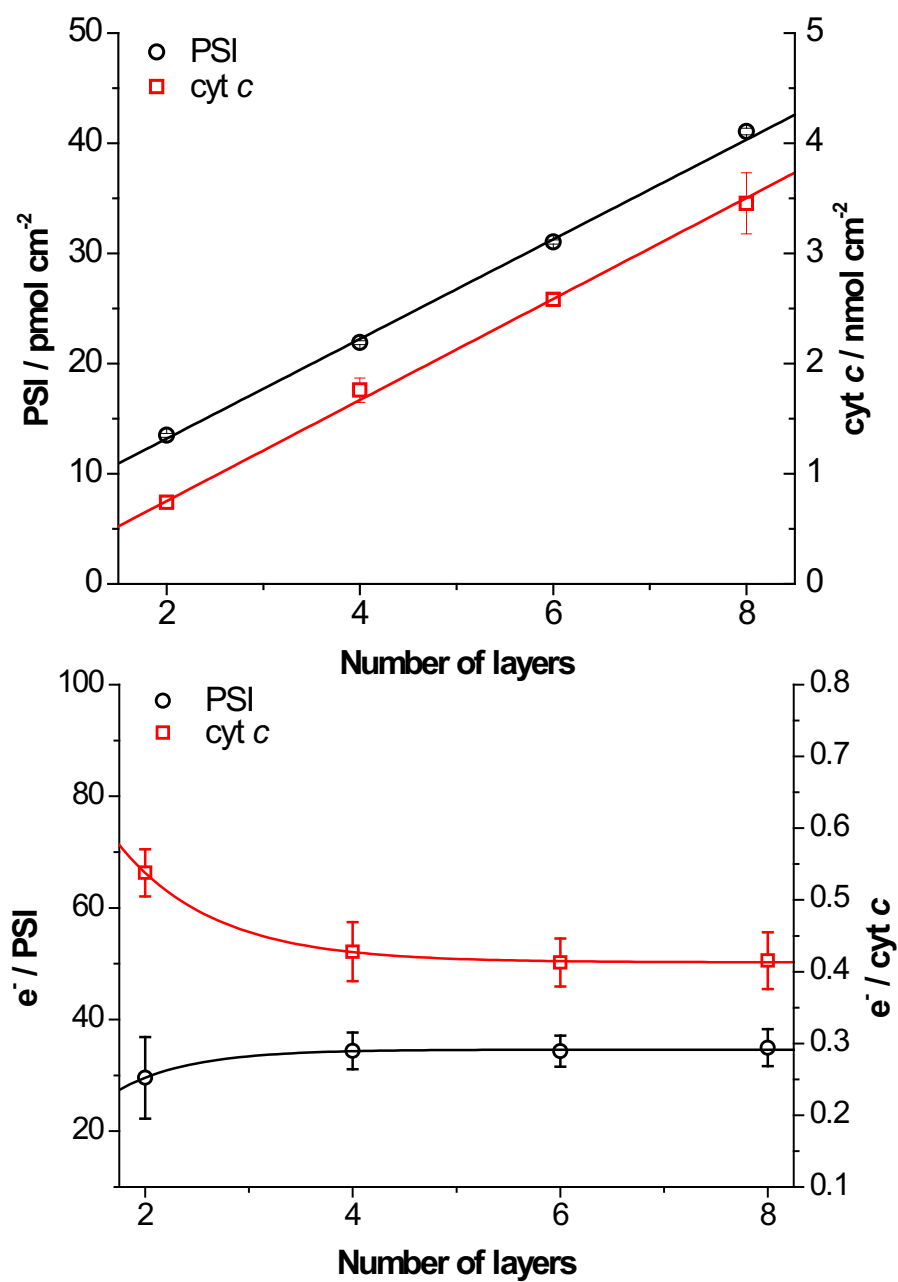


Fig. 4: Protein concentration (top) and turnover number (bottom) in dependency on the number of μ ITO layers. A linear relationship between the protein amount and the number of layers can be found (PSI: 4.5 ± 0.2 pmol cm⁻² / layer, $R^2 = 0.997$; *cyt c*: 0.46 ± 0.01 nmol cm⁻² / layer, $R^2 = 0.998$; $n = 4$). Geometrical electrode area: 0.2 cm².

Photophysical features of μ ITO-PSI-cyt *c* electrodes

In this section, we characterize the photo-physical features of the μ ITO-PSI-cyt *c* electrode demonstrating its potential as an efficient, biohybrid and transparent photocathode. In Fig. 5 the photocurrent density of a 6x μ ITO-PSI-cyt *c* electrode is plotted against the incident light power. The Michaelis-Menten equation can be applied to fit the experimental data, since photons can be considered as a substrate for PSI. The light intensity at half maximum (K_M) is determined to be $2.6 \pm 0.2 \text{ mW cm}^{-2}$ with a maximum photocurrent (J_{\max}) of $148 \pm 2 \text{ } \mu\text{A cm}^{-2}$. The cooperativity (n) of this behaviour is calculated to be 1.0 ± 0.1 . This means that PSI excitation by photons can be seen as multiple parallel single events, taking place independently. The K_M value derived from these experiments is very similar to our findings of a cyt *c*/PSI monolayer system²⁶⁷ and more than a factor of 2 higher as in a multilayer setup²⁷⁸ on planar gold electrodes. The nature of light absorption here seems to be more similar to a monolayer system as compared to a complex multilayer environment with additional assembled components. In addition, this behaviour also corresponds to the determined monolayer coverage of the proteins within the 3D structure.

As a next experiment for characterization, a photoaction spectrum has been recorded and compared with the absorption spectrum of PSI in solution as well as immobilized in the μ ITO structure. Fig. 6 displays the spectra normalized to the peak at 680 nm. The photoaction spectrum follows the overall wavelength distribution of PSI in solution and with the spectrum measured for a 6x μ ITO-PSI-cyt *c* electrode. Peaks are observed at 680, 620 and 440 nm corresponding either to the Q_y , Q_x and the Soret band of chlorophyll *a*.²⁴⁸ Due to scattering and the heterogeneity of surface confined proteins the absorption of the μ ITO-PSI-cyt *c* in the typical green gap is higher compared with PSI in solution. For shorter wavelength the photoaction spectrum decreases as expected from the absorption behaviour. Due to the other assembled component cyt *c* and the high protein loading the Soret absorption at 410 nm (ferric) and 416 nm (ferrous) are lowering the effective photon-to-charge carrier conversion of PSI.¹⁶¹ From the transmission spectra of ITO and μ ITO a decrease in transmission over the visible light spectrum going to shorter wavelength is recognizable. If both spectra are compared, the transmission at 680 nm reduces from 86 % to 24 % for the 3D electrode (see Fig. S7). This points to an increased scattering effect in the μ ITO. During the construction of the 3D electrodes ITO nanoparticles are used as starting material. Due to their diameter much smaller than the incident light wavelength higher Rayleigh scattering can be expected (more pronounced at shorter wavelengths).

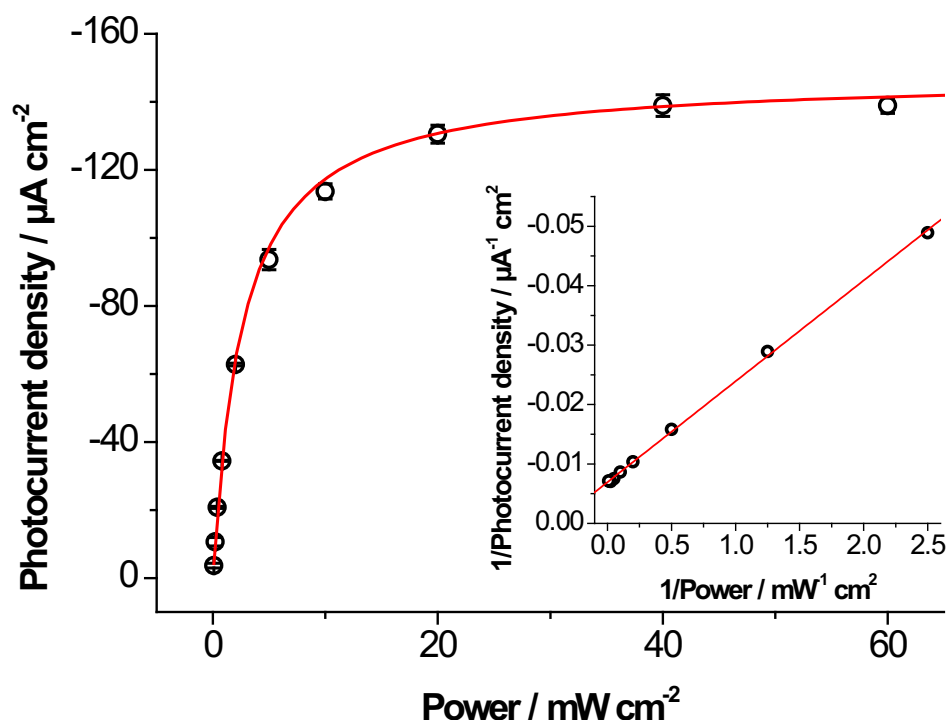


Fig. 5: Photocurrent density of a 6x $\mu\text{ITO-PSI-cyt } c$ electrode in dependency on the illumination intensity. Data have been fitted with the Michaelis-Menten equation ($K_M = 2.6 \pm 0.2 \text{ mW cm}^{-2}$, $J_{\max} = 148 \pm 2 \mu\text{A cm}^{-2}$, $n = 1.0 \pm 0.1$, $R^2 = 0.998$). Inset: Lineweaver-Burk plot of the same data. Experiments have been performed at RT in phosphate buffer (5 mM, pH 7) using white light at a potential of -100 mV vs. Ag|AgCl ($n = 3$). Geometrical electrode area: 0.2 cm^2 .

The quantum efficiency has also been calculated for various light intensities of the $\mu\text{ITO-PSI-cyt } c$ electrode, whereas the incident light-to-current efficiency is referred to as external quantum efficiency (EQE). Here, a peak value of about 11 % (6.6 % at the apparent K_M) is determined. The internal quantum efficiency (IQE) represents the ratio between the number of absorbed photons to the number of produced charge carriers in a given time. For this reason the absorption spectrum of a $\mu\text{ITO-PSI-cyt } c$ electrode is taken and the number of photons absorbed by the electrode can be calculated from the light source spectrum (see Fig. S8). The calculation does not take into account, that due to the light scattering nature of the mesoporous structure, the real absorption of the electrode will be lower. A plot of the IQE against the light power displays also a peak value at low light intensities of about 30 % (and 18 % at the apparent K_M). These values represent one of the highest efficiencies of PSI electrodes to date.^{210,212,214,227,239,278} If we assume, that only PSI contributes to the photocurrent, which can even be seen from the photoaction spectra, the IQE can also be

calculated from the absorption spectra of PSI in solution corrected for the respective PSI concentration in a 6x layer μ ITO electrode.

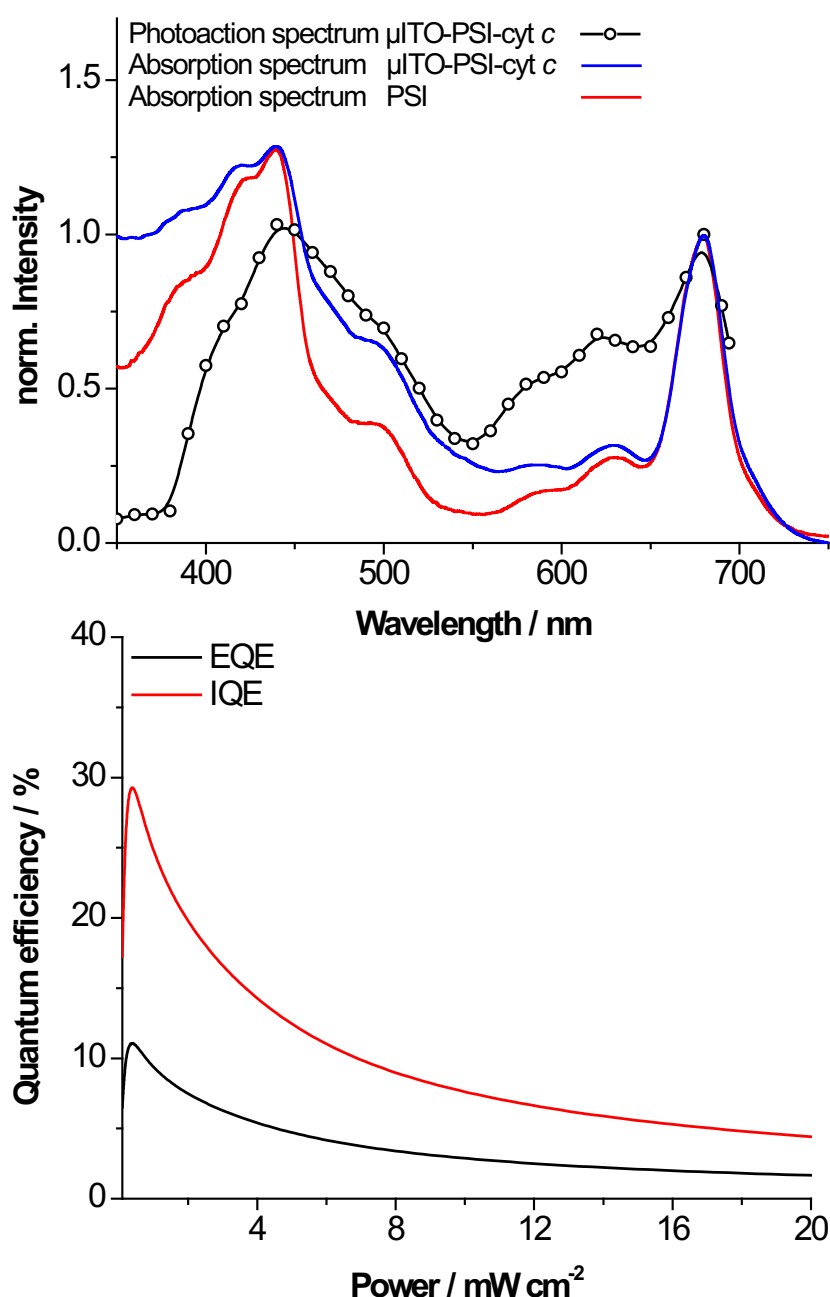


Fig. 6: (Top) Photoaction spectrum of a 6x μ ITO-PSI-cyt *c* electrode in comparison to the absorption spectrum of PSI in phosphate buffer (5 mM, pH 7) and to the absorption spectrum of a 6x μ ITO-PSI-cyt *c*, all normalized to the peak at 680 nm. Photoaction spectrum has been obtained with monochromatic light (bandwidth 15 nm, intensities $<10 \text{ mW cm}^{-2}$) in aerobic phosphate buffer (5 mM, pH 7). Spectra are the averages of 3 independent measurements. (Bottom) External (EQE) and internal (IQE) Quantum efficiencies of a 6x μ ITO-PSI-cyt *c* electrode calculated for different light intensities.

Here, an IQE of even 39 % (and 23 % at the apparent K_M) is achieved. This value clearly demonstrates that either scattering/reflectivity effects, or the additional cyt *c* absorption influence the efficiency of the electrode. Nevertheless this system provides very good performances already at low intensities, in contrast to approaches which need more than one order of magnitude higher light intensities.²⁸²

Conclusions

In this study a mesoporous scalable 3D electrode structure has been successfully combined with PSI, which is electrically wired by means of the redox protein cyt *c* resulting in a highly efficient photocathode. The experiments suggest a linear scalability of the photocurrent output over various layer thicknesses of the μ ITO electrode without boundaries (at least up to 40 μ m). The thickness of the μ ITO can easily be adjusted during the preparation of the electrode by the number of spin coating steps. The electro-active area follows the thickness of the 3D structure linearly. Due to the fast and easy preparation procedure of μ ITO, electrode production speed can be significantly enhanced compared to other preparation protocols. Additionally the study of different fabrication procedures allows a deeper understanding of the functionality and limiting steps of the photo-biohybrid structure. PSI and cyt *c* can be well integrated into the 3D electrode structure. Remarkably the entire inner electrode surface can be used for protein immobilisation and photocurrent generation. On this basis it is possible to generate high cathodic photocurrents, which are scalable with the number of μ ITO layers used during electrode preparation. The system shows high quantum efficiencies and follows the spectral properties of PSI. The biohybrid approach enables the construction of more complex light-to-current converting devices, like the integration of enzymes or nanomaterials for the light-to-chemical energy conversion. The study demonstrates that the cyt *c*-PSI wiring system can be applied to a variety of materials and surfaces, and allows photocurrent densities of more than 150 μ A cm⁻². Thus, it has shown its potential for further developments and applications.

Acknowledgements

We gratefully acknowledge the support of this research by the Bundesministerium für Bildung und Forschung BMBF, Germany (Biotechnologie 2020+, projects: 031A154A+B). HL wishes to acknowledge GACR grant No. P501/12/G055, too.

Supporting Information

A) Calculation of the electro-active surface of a μ ITO structure

The electro-active surface of μ ITO structure was calculated as follows: First cyclic voltammetry measurements of a defined surface area (geometrical surface: 0.2 cm^2) of flat ITO (pre-cleaned by ultrasonication in acetone, isopropanol and water) and of 2, 4, 6, 8 x μ ITO (geometrical surface: 0.2 cm^2) have been performed from $-300 - +400 \text{ mV vs. Ag|AgCl}$ at RT in phosphate buffer (5 mM, pH 7) without any redox species. At 0 mV vs. Ag|AgCl ($dI/dV = 0$) the charging currents (anodic and cathodic) have been determined and averaged ($n = 4$). Here, we assume that the electro-active surface of flat ITO is corresponding to its geometrical surface and that the electrochemical double layer structure is similar for ITO and μ ITO. This means higher charging currents are only caused by a higher surface area in contact with the electrolyte. Consequently, the electro-active surface area is calculated for the μ ITO out of the charging current increase of μ ITO compared to flat ITO.

I) Cyclic voltammetry of 6x μ ITO, 6x μ ITO-cyt *c*, 6x μ ITO-PSI-cyt *c* and μ ITO-PSI electrodes

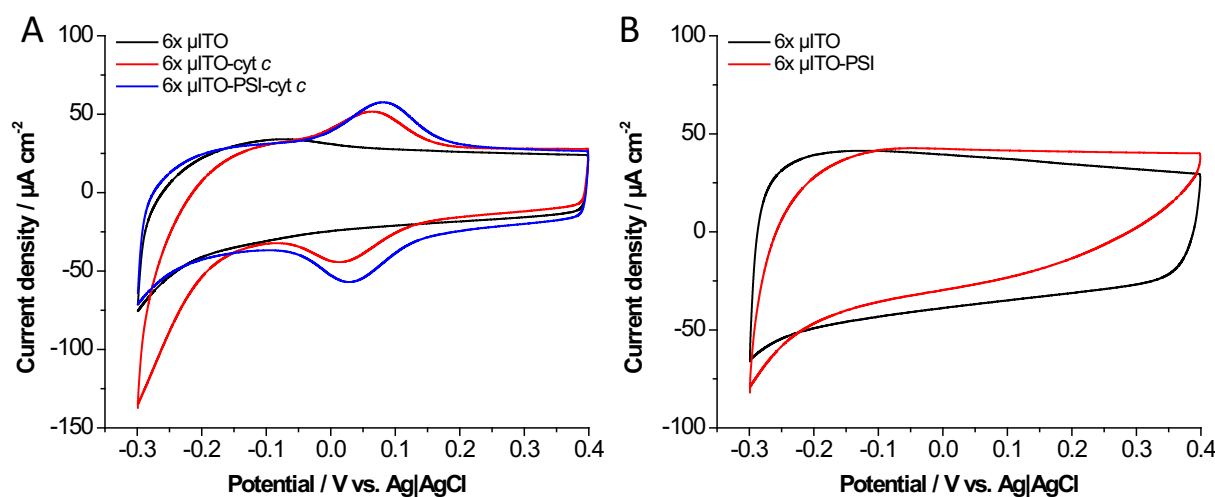


Fig. S1: Cyclic voltammograms of different 6x μ ITO electrodes: A) CV of a bare 6x μ ITO, a 6x μ ITO-cyt *c* and a 6x μ ITO-PSI-cyt *c* electrode. (B) CV of a bare 6x μ ITO and a 6x μ ITO/PSI electrode. No redox signals can be detected when only PSI is immobilized in the structure. The experiments have been performed in the dark at a scan rate of 10 mV s^{-1} in aerobic phosphate buffer (5 mM, pH 7).

II) Photocatalysis of 6x μ ITO-PSI-cyt *c* electrodes

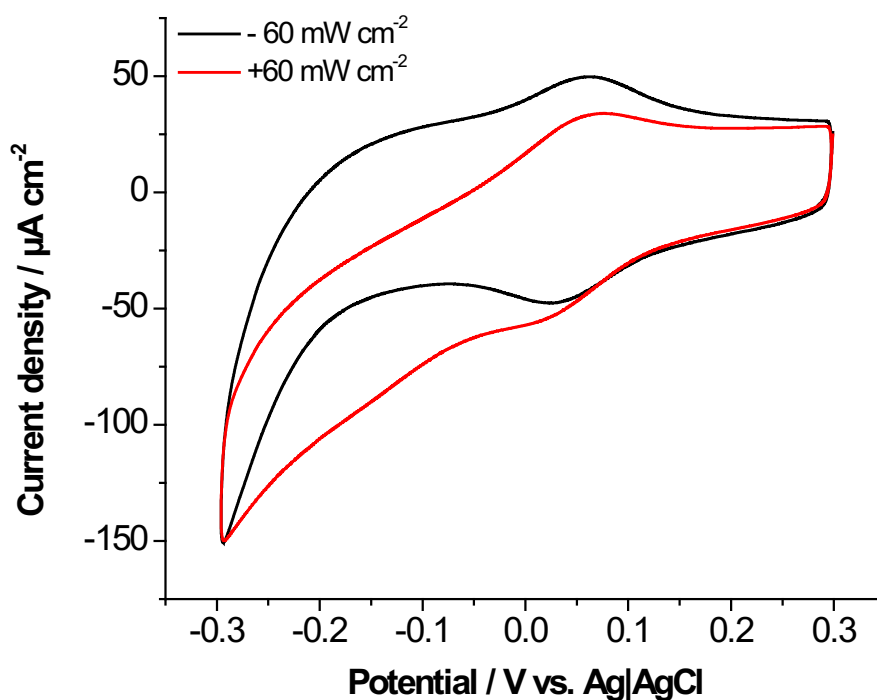


Fig. S2: Photo-induced catalytic current of the 6x μ ITO-PSI-cyt *c* electrode. The experiment has been performed in the dark (black) and with 60 mW cm^{-2} of white light (red) at a scan rate of 10 mV s^{-1} in aerobic phosphate buffer (5 mM, pH 7) as well as 1 mM methyl viologen. Cathodic catalysis starts at 70 mV vs. Ag|AgCl and decreases when oxygen reduction starts at the electrode. In the dark only the redox conversion of cyt *c* can be seen at around 45 mV vs. Ag|AgCl. Cathodic catalysis under illumination starts at a potential at which cyt *c* can be reduced by the electrode. This means that first electrons are transferred from the μ ITO to cyt *c* before PSI reduction by cyt *c* occurs.

III) Photocurrent control: μ ITO-PSI, μ ITO-cyt *c*, μ ITO

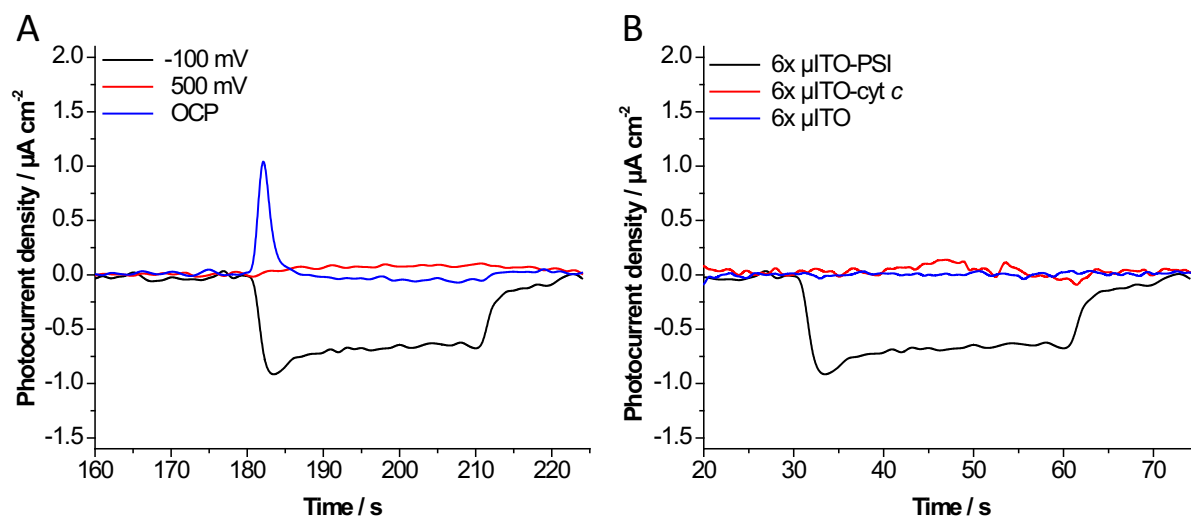


Fig. S3: Photocurrent measurements of the $6x \mu\text{ITO-PSI}$, $6x \mu\text{ITO-cyt } c$ and $6x \mu\text{ITO}$ electrodes. (A) The photocurrent measurements at three different potentials of a $6x \mu\text{ITO-PSI}$ (-100 mV , $+500 \text{ mV}$, $\text{OCP} = 196 \text{ mV}$ vs. $\text{Ag}|\text{AgCl}$) exhibit only minor photocurrent densities, cathodic but no anodic photocurrents are observed (left). This experiment shows, that cyt *c* is necessary for the high unidirectional photocurrent generation. The direct electron transfer from PSI to the μITO electrode is highly limited. (B) Comparison of photocurrents achieved at a potential of -100 mV vs. $\text{Ag}|\text{AgCl}$ between $6x \mu\text{ITO-PSI}$, $6x \mu\text{ITO-cyt } c$ and $6x \mu\text{ITO}$ electrodes. Without PSI in the structure there is no photocurrent detected. All experiments have been performed at RT in phosphate buffer (5 mM , $\text{pH } 7$) using white light (20 mW cm^{-2} , 30 s pulse).

IV) Photocurrent of 6x μ ITO-PSI-cyt *c* electrodes in buffer consisting of higher ionic strength

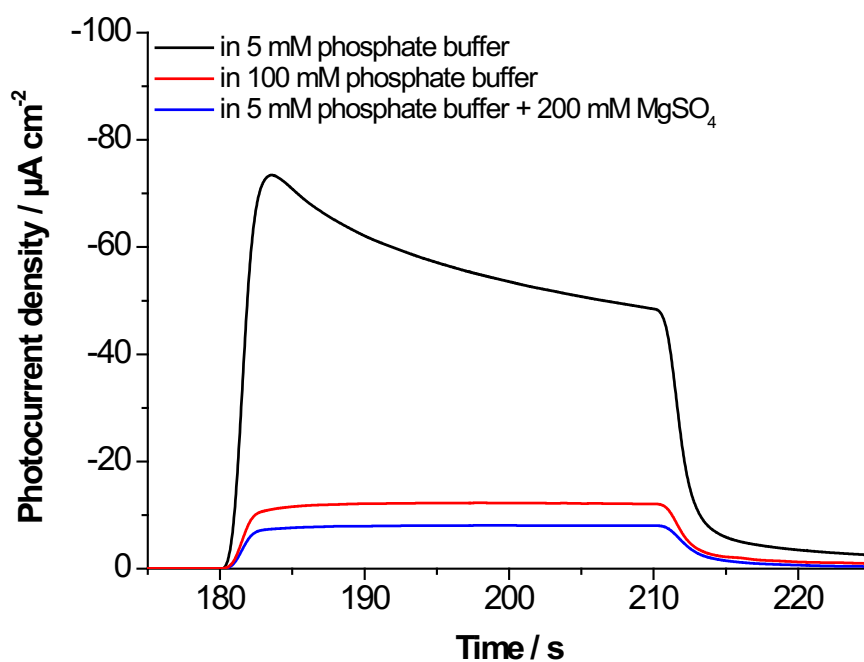


Fig. S4: Photocurrent measurements of the 6x μ ITO-PSI-cyt *c* electrode. Due to higher concentration of either buffer substance (100 mM phosphate) or addition of 200 mM MgSO_4 , photocurrents decrease significantly. The experiments have been performed at RT in phosphate buffer (5 mM, pH 7) using white light (20 mW cm^{-2} , 30 s pulse) at a potential of -100 vs. Ag|AgCl.

V) Surface area of air sintered/air plasma treated μ ITO electrodes

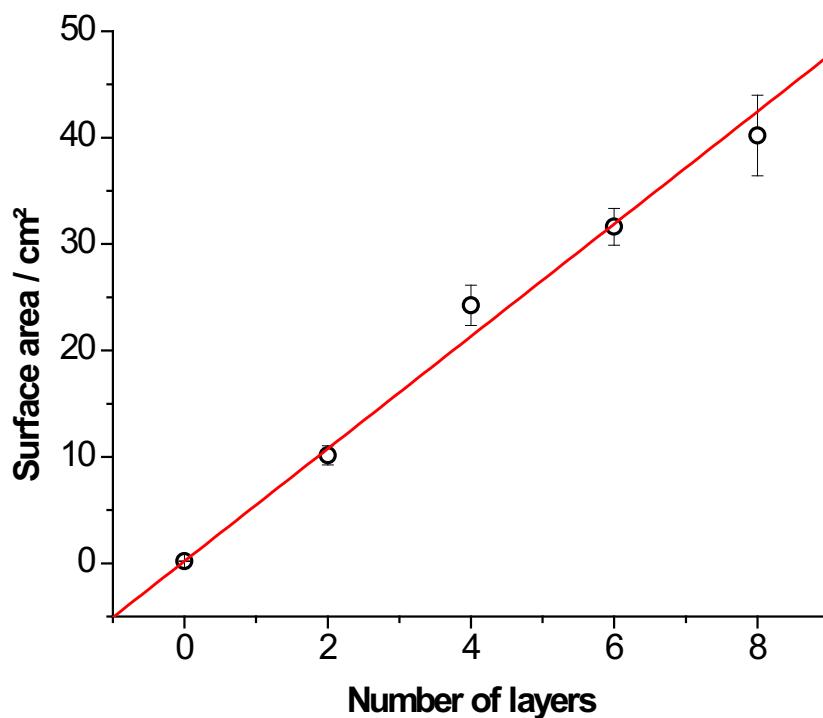


Fig. S5: Surface area increase dependent on the number of applied layers. The surface increases by $5.3 \pm 0.2 \text{ cm}^2$ / layer ($R^2 = 0.995$, $n = 4$).

VI) Determination of heterogeneous electron rate constant (k_s) for a μ ITO-cyt *c* electrode

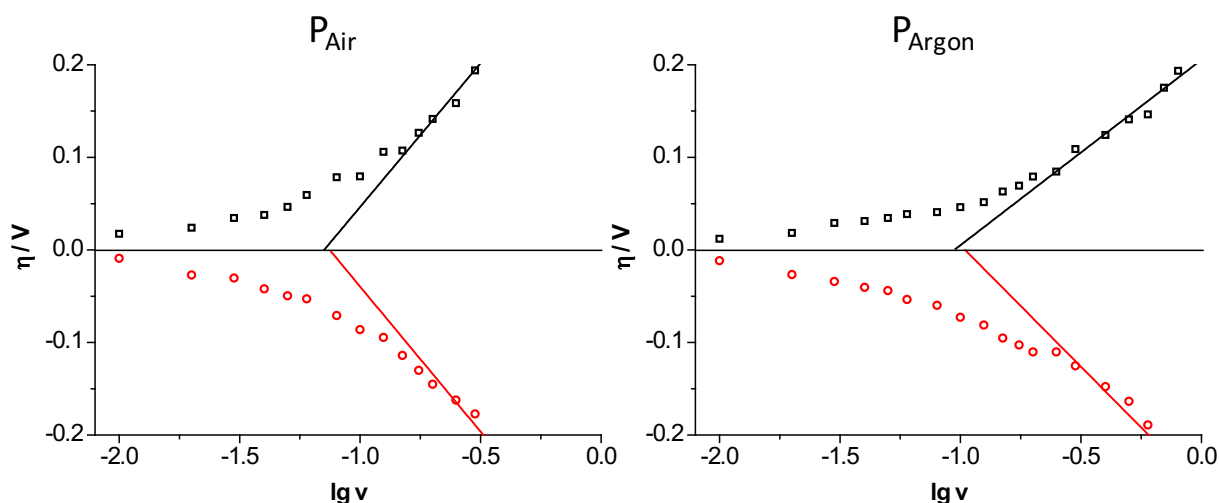


Fig. S6: Trumpet plot for the determination of k_s after the method of Laviron for P_{Air} (left) and P_{Argon} (right). The overpotential ($E_0 - E_p$) for both anodic (black) and cathodic (red) peaks is plotted against the decadic logarithm of the scan rate ($\lg v$). A linear fit of the data with a peak separation of $> 200 \text{ mV}$ results in a slope proportional to the charge transfer coefficient (α) with an intercept proportional to k_s .

VII) Transmission spectra of ITO and 6x μ ITO structures

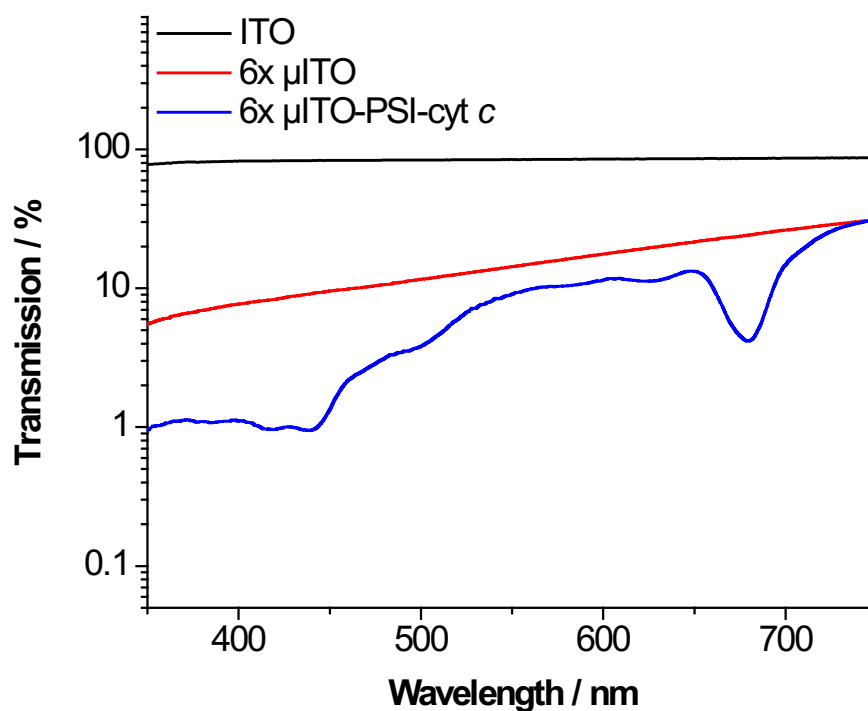


Fig. S7: Transmission spectrum of ITO, 6x μ ITO and 6x μ ITO-PSI-cyt *c* electrodes.

VII) White light source spectrum

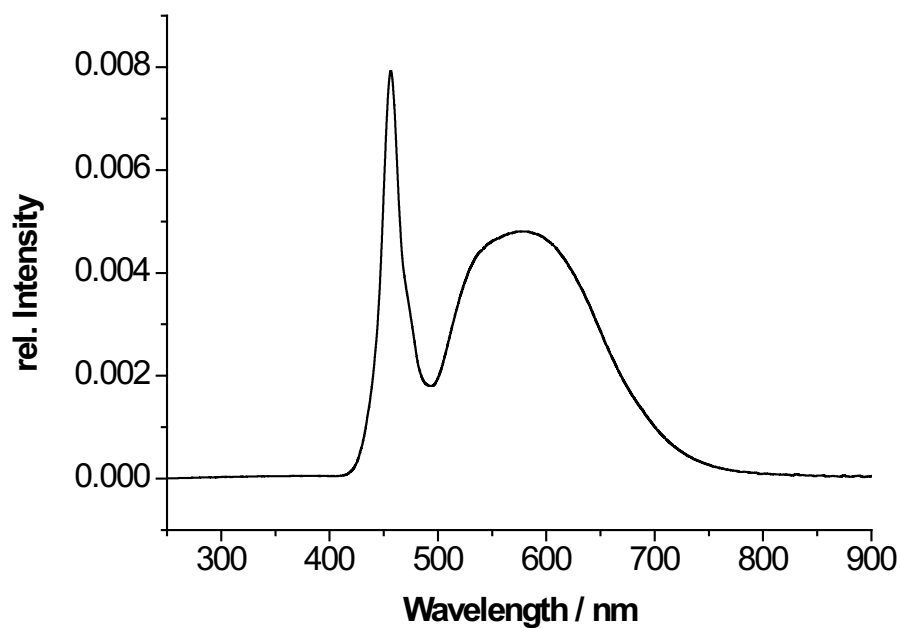


Fig. S8: Spectrum of the white light source used in all experiments. The spectrum was normalized to an integral area of 1. Characteristic peaks are found at 456 nm and 576 nm.

5. Discussion

In the following chapter the results obtained during the doctorate will be discussed. There are three different topics studied within this thesis:

1. The cytochrome *c* / photosystem I monolayer electrode (P4.1, see chapter 4.1),
2. The cytochrome *c* / photosystem I multilayer electrode (P4.2, see chapter 4.2),
3. 3D mesoporous indium tin oxide electrodes incorporating cytochrome *c* / photosystem I (P4.3, see chapter 4.3).

These three systems share a common underlying concept – the connection of PSI to an electrode *via* cyt *c*. This aspect will be discussed in this chapter in more detail, while the performance and efficiency will be compared and classified with other systems of state of the art. This provides the basis for the final analysis of advantages and drawbacks of the cyt *c* / PSI systems, including the evaluation of critical parameters. In the last sub chapter, an outlook and putative future perspectives of the cyt *c* / PSI system will be given.

5.1 The interaction and communication between cytochrome *c* and photosystem I

The non-natural interaction between cyt *c* and PSI has been exploited for the connection of the large super-complex to electrodes. To understand the nature of binding of the small redox protein to PSI, insights have to be given into the native protein interaction of cyt *c*. In the natural system the binding process and ET reaction of cyt *c* to its partners is more complex and can be divided into two steps: 1. Long-range interaction and 2. Short-range interaction. In the first one, cyt *c* is docking *via* positively charged lysine residues to an acidic patch on the opposing protein.²⁹² Site-mutagenesis on these acidic residues have a strong effect on the docking to cytochrome *c* oxidase, where complex formation needs lower ionic strength and changes kinetic parameters, such as K_M (getting higher) and k_{cat} (getting lower).^{293,294} The next step of ET complex formation is mediated by short-range hydrophobic van der Waals contact interactions by means of apolar residues on the opposing protein site.²⁹⁵ Changes to theses residues, will primarily have a negative effect on the k_{ET} and thus this region is also being considered to be the electron entry point of ET.²⁹² Nonetheless, cyt *c* is also able to bind

non-natural partners, which is often ensured by the electrostatic nature of cyt *c*, exhibiting a strong dipole momentum at neutral pH. Examples for this have already been shown in several studies, where cyt *c* can interact with various biomolecules, such as enzymes, phospho-lipid membranes and DNA.^{182,270,273,284,296} This demonstrates, that cyt *c* binds to other biomolecules rather nonspecifically, but retains its natural function. As can be seen in chapter 3.2.2.3, cyt *c* can keep its function as a redox shuttle also in a surface-fixed state and can exchange electrons with an electrode, whereas self-exchange between cyt *c* molecules helped the connection of enzymes to electrodes.^{182,185,270} Nevertheless, the situation of how cyt *c* connects these enzymes is often not well understood.

In this thesis, the interaction partner for cyt *c* is PSI, which interacts very transient with its natural electron donor proteins (cyt *c*₆ and PC).²⁵ In contrast to cyt *c*, cyt *c*₆ displays a more homogeneous surface potential with a pI of 5.5 (negative charges are dominant) and is only slightly charged with apolar patches around the heme pocket (vacuum electrostatic analysis of PDB:3DR0).²⁹⁷ Thus, interaction between cyt *c* and PSI differs from the natural situation with freely diffusible redox proteins. These shuttles must leave the ET complex after electron transition, to regain electrons from the cyt b₆/f complex. This is in contrast to the cyt *c* / PSI system, where electrons are transferred *via* the electrode or *via* self-exchange of surface-confined cyt *c* molecules. Thus, a simple analogy to the natural system is not helpful for understanding the interaction between cyt *c* and PSI. At the moment, a complete picture on the cyt *c* / PSI system cannot be given, but first conclusions can be drawn.

The light-harvesting super-complex PSI has a strong dipole momentum itself between the luminal (negatively charged) and stromal side (positively charged) of the protein with a hydrophobic transmembrane intersection (see 4.1 Fig. S3). From P4.1 it is reasonable to assume that PSI assembles preferentially with its luminal side on a cyt *c* monolayer. This assembly takes time (as can be seen from SPR, P4.1, Fig. 2) and is more pronounced compared to a SAM-modified electrode only, while producing a complete PSI layer (AFM, P4.1, Fig. 1). Additionally, the interaction is very sensitive to variations in pH having the maximal protein deposition in the experimental range at pH 7 (P4.1, Fig. S1A). Reasons for this can be seen in the charge situation on the proteins. Both biomolecules have different pI values, whereas cyt *c* (pI = 10.5) has a positive net charge and PSI (pI = 6.4) a slightly negative one at pH 7. At higher pH (> 7) the positive charges on the protein surface of cyt *c* will be lowered, at a lower pH (< 7), the negative charges at PSI will be reduced. The charge situation on both proteins supports the experimental findings of an interaction maximum at a

certain pH. From MALDI-TOF experiments (P4.2, Fig. S1) it is verified, that cyt *c* binds strongly to PSI in solution under these conditions, while this binding can only be prevented in a buffer of higher ionic strength. Photocurrent experiments of the mesoporous photobioelectrode (P4.3, S4) with higher salt concentration in the buffer decrease the produced photocurrent density at least by a factor of 7. Due to a suppressed binding of cyt *c* to PSI as well as to the electrode by means of buffer ions, the electrical connection of PSI is prevented. These experiments make the electrostatic interaction scenario between both biomolecules most likely, since it is very sensitive to changes in pH and in ionic strength.

The electron transfer pathway from the electrode to PSI must involve cyt *c* as the electrical wire and cyt *c* acts as the electron donor molecule for PSI. This has been found in all photobioelectrodes produced within this thesis (P4.1, Fig. 3B, P4.2, Fig. S4, P4.3, Fig. S2). Electrons are transferred first to cyt *c* from the electrode and can also be exchanged under the neighbouring cyt *c* molecules. This is supported by cyclic voltammetry, since light-induced catalysis starts at the redox potential of cyt *c*. To generate a photocurrent, there must be a cyt *c* molecule bound in the near of P₇₀₀, which is able to reduce P₇₀₀⁺. Other cyt *c* molecules, which may also be bound to PSI, must be in ET distance to the P₇₀₀ associated cyt *c* for its re-reduction. Only this would lead to a steady-state photocurrent, which has been observed all photobioelectrodes (P4.1, P4.2 and P4.3). As can be seen from Fig. 7 the heme group of cyt *c* is located at one side of the protein. An efficient electron transport can be achieved, when interprotein distances are small between the redox groups of the proteins. Hence, a rotational freedom at RT of bound cyt *c* on either the electrode, as well as on PSI must exist, resulting in the ET to P₇₀₀. A proof of the self-exchange can be seen in the results of the CV measurements of multiple layer of cyt *c*, giving an electro-active amount of cyt *c* much higher than a monolayer in contact with the modified gold electrode (P4.1, Fig. 4; P4.2, Fig. 3A, 5A).

Another phenomenon is observed, when PSI and cyt *c* are assembled on top each other. Both proteins reach deposition saturation, when deposited onto a terminal layer of the other molecule, resulting in a dense packed bilayer (cyt *c*/PSI, see P4.1). If the proteins are alternately assembled on each other, multiple layers can be build up, with connecting PSI molecules to the electrode. Cyt *c* has a molecular weight which is around 85 times lower than the large trimeric PSI, drawing the conclusion, that under buffer and pH conditions used in this thesis, there must be several binding sites for cyt *c* at PSI. Fig. S3 from P4.1 shows that there are negative potential surface patches at the stromal side of PSI, being large enough that cyt *c* molecules can dock to these places. Despite the high positive surface potential, cyt *c*

displays also hydrophobic patches, being located around the heme pocket (crystal structure analysis of hydrophobicity, PDB:1HRC).¹¹³ It can be assumed, that the small redox protein can also bind in the hydrophobic area of PSI, but further studies are necessary for verification.

Under buffer conditions of low ionic strength and without a further stabilizing tenside molecule in solution, PSI is often only semi-stable and tends to agglomerate within hours. If cyt *c* is present, this mixed solution is much more stable (several days, data not provided in the three publications). From these findings it can be concluded, that the cyt *c*/PSI hybrid complex is being better adapted to the situation in aqueous solutions, even under buffer conditions of low ionic strength. This is clearly a new feature, because large membrane proteins often require a complex buffer composition containing a surfactant for stabilizing the membrane regions. At this point the role of cyt *c* as a bridging molecule between complexes can only be guessed, which would explain the co-assembly of both proteins on the surface, but without further experiments it cannot be fully elucidated. Nonetheless, these complexes can slowly (several hours) assemble from solution to a surface, while the total protein amount deposited is depending on several parameters, such as the ratio of cyt *c* with respect to PSI (P4.2, Fig. 2, Fig. S2), or the assembly time (P4.2, Fig. 1). A higher excess not only accelerates the deposited protein amount, but also enhances the assembled protein amount. This means, that binding of cyt *c* to PSI is probably nonstoichiometric, while the low affinity suggests an unspecific binding phenomenon. If several cyt *c* binding sites on PSI are assumed with each having a different affinity, not all binding sites will be populated by a given molecular ratio of both proteins. When some of these binding sites are needed for the co-assembly onto an electrode surface, a raise in the cyt *c* excess and thus subsequently in the population of these crucial binding sites, would help to accelerate the adsorption process to the surface. Another finding shows, that the photocurrent of the system correlates with the amount of electrically addressable cyt *c* molecules, which also underpins that both proteins must assemble jointly.

To further elucidate the conclusions on the interaction between cyt *c* and PSI, a docking analysis of both proteins reveals putative binding sites of cyt *c* at the monomeric PSI (see Fig. 9). The analysis has been done using crystal structure information of both proteins and ClusPro 2.0 (cyt *c*: 1HRC, PSI: 4FE1).^{115,253,298–300} This analysis can be seen only qualitatively since the binding behaviour can be different under various buffer conditions used in this thesis. Nevertheless, the analysis reveals, that several cyt *c*-interaction spots at the luminal side of PSI can be found, while also some binding sites are located at the stromal side. This

was guessed before, since it can explain, that after deposition of PSI, cyt *c* can be assembled again and that on top of this another layer of PSI can be adsorbed.

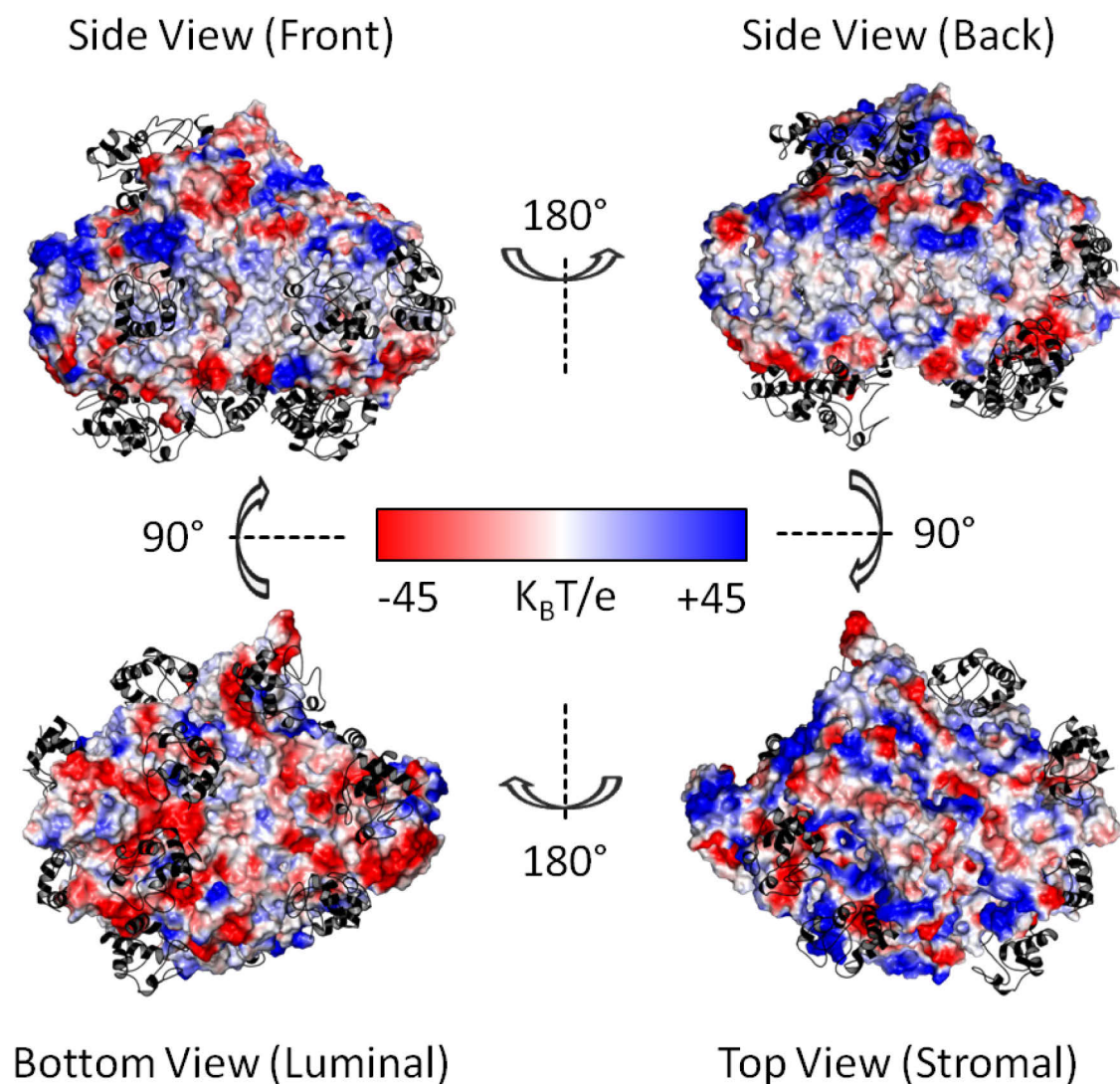


Fig. 9: Crystal structure visualization from protein-protein docking analysis (ClusPro 2.0) between cytochrome *c* (black, cartoon, PDB:1HRC) and monomeric photosystem I (vacuum electrostatic surface, red-white-blue, PyMOL, PDB:4FE1). A selection of different putative interaction spots is displayed. The selection has been done according to the highest cluster values. If there are multiple binding conformations of cyt *c* at one individual cyt *c*-PSI interaction site, only one is displayed for a better visualization.^{115,253,298–300}

Nevertheless, it has to be mentioned here, that in the assembly solution the hydrophobic region of PSI is covered by β -dodecyl maltoside (β -DM), which was not taken into account for the analysis presented in Fig. 9. Therefore the exact situation of cyt *c* binding to PSI cannot yet be fully enlightened. Interestingly, from these *in silico* binding analysis, no direct binding of cyt *c* is found at the putative binding site for the natural electron donor cyt *c*₆ below the P₇₀₀ at the luminal side of PSI. This may indicate a larger distance of cyt *c*

molecules to P₇₀₀, and may explain, that the ET rate of cyt *c* to PSI is smaller as compared with the natural system (will be discussed more in detail in the next chapter). For the electrical connection of photoactive protein layers to the electrode, electrons have to be transferred *via* cyt *c* to the next PSI layer. The analysis can also help to explain this, because of two findings: 1. Interaction sites can be found in the hydrophobic region of PSI, 2. Neighbouring binding sites of cyt *c* enable self-exchange between cyt *c* molecules. When electrons are to be transferred to the next protein layer, cyt *c* molecules need to have a close distance to each other and the redox molecules thus form a protein network surrounding PSI.

To further elucidate the binding situation of cyt *c* / PSI hybrids assembled on the surface, a closer look has to be taken into P4.2, where the introduction of DNA can greatly enhance the overall protein amount on the surface. While a saturation behaviour is observed for the assembly of PSI and cyt *c* on the surface from the protein mixture, assembling DNA as separating layer provides a new surface for the start of another cyt *c*/PSI deposition. The consequence from this finding is, that the cyt *c*/PSI layer loose cohesion after a certain number of complexes have been deposited onto the surface. This means, that at one time the rate of assembly equals the rate of disassembly at specific buffer and temperature conditions. DNA can protect complexes from detachment from the surface and strengthen interlayer forces by means of a strong cyt *c*-DNA binding, which has been found previously and can also be seen from various experiments (P4.2, Fig. 4, S5, S7).²⁷³ Furthermore, DNA does not hinder the ET between the photoactive protein layers, because here also the amount of electrically connected cyt *c* molecules correlates well with the photocurrent density (P4.2, Fig. 5B).

The co-assembly has also been tested at the 3D ITO electrodes, but does not result in high photocurrents. Here, a separate deposition of PSI and cyt *c* is more beneficial for the connection of a large amount of photoactive protein. Thus the binding situation of both proteins to the electrode is different as has been seen on planar electrodes. From SEM analysis of the electrode (P4.3, Fig. 1), the interconnections between the μ ITO structure are around 100-150 nm. This means that large cyt *c*/PSI complexes can get stuck and prevent mass transfer to the deeper layer of the structure. The benefit of the one-by-one assembly is, that the small redox protein can manage to bind between electrode and PSI to achieve a productive connection. Both proteins can be detected at a monolayer coverage if the electroactive surface area of the μ ITO structure have been taken into account. Furthermore it can remove loosely bound PSI molecules from the surface and thus clean the surface from

inefficient connected molecules. This can be observed, when the electrode is incubated with cyt *c*. After the cyt *c* deposition step, the colour intensity of the greenish electrode decrease. Because of the strong green colour of PSI, the presumption is, that cyt *c* removes PSI from the surface.

In P4.3 it has been clearly shown, that the overall electrode performance mainly relies on the ET rate of cyt *c* to the electrode (P4.3, Fig. 3, Fig. S6). This means also, that the basic findings about the interaction, communication and productive assembly of the cyt *c*-PSI biohybrid system is not affected on other materials, which results in the possibility to even extend the use of various electrode materials and structures. This new system in the photobiovoltaic research, where biomolecules with different tasks are coupled together generating a new kind of photobioelectrode, can be the starting point of further more advanced developments. In the next chapter, the focus is turned to the performance and efficiency of such a biohybrid approach in comparison to other systems.

5.2 Photobioelectrode performance and efficiency

So far new insights into the interaction between the biomolecules used in this thesis have been discussed. To bring this strategy in a broader context, a comparative analysis to other developed photobioelectrode systems will be given in this chapter. Besides the construction strategy of biohybrid electrodes, the performance and the efficiency of the electrodes are a set of parameters, which has an important role in optimisation and evaluation. This chapter will give conclusions about the quality of PSI photobioelectrodes and will present the most superior concepts.

The first parameter discussed here is the photocurrent density (I_p) of the photobioelectrodes produced within this thesis in comparison with other systems reported in the literature. It can be expressed as the number of light-induced generated electrons per second by the electrode. Higher photocurrents are desirable, since they reflect the maximum capacity of the electrode to transfer electrons to the counter electrode in a solar cell or to a useful acceptor, like an enzyme producing energy-rich chemicals. Nevertheless, this important parameter is difficult to compare, since photocurrent values and kinetics are dependent on the applied overpotential relative to the redox potential of the oxidized or the reduced redox center in PSI, the kind and concentration of the electron acceptor/donor used and the power or wavelength of the incident light. Therefore photocurrent densities have been extracted at their reported maximum values

and are highlighted if very unconventional experimental conditions have been used. Within the series of publication 4.1 to 4.3 (P4.1, P4.2, P4.3), the photocurrent density has been improved by 2 orders of magnitude: $1.6 \rightarrow 25 \rightarrow 150 \mu\text{A cm}^{-2}$. Compared with another cyt *c*-based approach reported in the literature, P4.1 already exceeds their produced photocurrents ($0.225 \mu\text{A cm}^{-2}$).²²⁹ So far, about 35 photobioelectrodes have been published using PSI as their main light-to-current converting component. To evaluate the results achieved in this thesis, these publications have been analysed according to their reported maximum I_p , as well as to their I_p normalized to the light intensity used. It has to be mentioned at this point, that such an analysis requires the light intensity applied in the study, since in most publications different light sources have been used (e. g. illumination at 680 nm, sun light emulating sources, or others). The normalized values can be considered only as a rough estimation, but may help to evaluate the efficiency better than only maximum values. Publications have been excluded if a) no electrode area or b) no light intensities have been given.

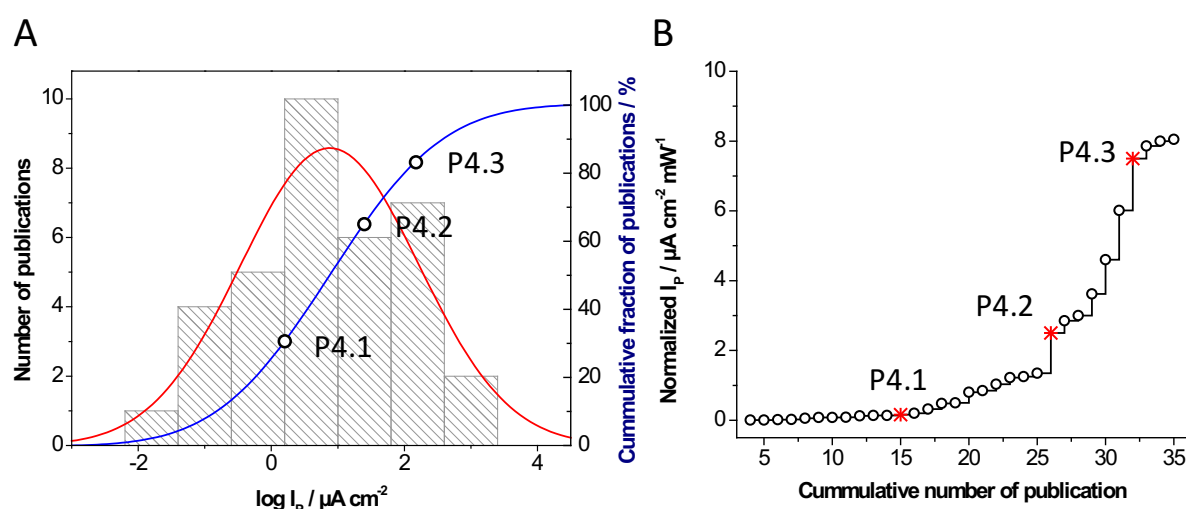


Fig. 10: Reported and light intensity-normalized photocurrent densities of analysed photobioelectrodes (number of publications = 35). **(A)** Distribution of reported maximum photocurrent densities (have been displayed as their logarithmic values, bin size = 0.8, bin range = -1.8 to 3, centred). Data have been fitted according to a Gaussian distribution, whereas the cumulative fractions of publications with the position of publication 4.1-4.3 (P4.1-4.3) have been added. **(B)** Photocurrent densities normalized to the respective light intensity against the cumulative number of publication with the position of P4.1-4.3 added. Photocurrent values have been sorted from low to high. Data have been taken from references.^{201–214,216,217,220,222–224,228,229,231,237,241,266,267,269,278,301–305}

Figure 10 describes the context of P4.1-4.3 with respect to other PSI containing systems. If the reported photocurrent densities are analysed, the maximum of the distribution of analysed publications peaked at a value of $7.5 \mu\text{A cm}^{-2}$. The basic cyt *c*/PSI monolayer system on gold electrodes (P4.1) is below this average. Nonetheless it shows higher photocurrent densities

than 30 % of the reported systems. The co-assembly of cyt *c*/PSI combined with a layer by layer approach increases the photoactive protein amount by means of DNA (P4.2), which is thus already clearly above average. With the incorporation of cyt *c*/PSI into a mesoporous ITO structure (P4.3) this value further increases, only 17 % of all publication can show higher photocurrents.

The evaluation changes clearly, when the light intensity-normalized values are considered, because in most studies high light intensities are needed to achieve high photocurrents. This is especially the case for the top 3 systems and other photobioelectrodes based on semiconductors.^{217,220,228} Here, the photocurrent values drop significantly, if normalized to the light intensities applied. On top of this, the photocurrent of the basic material used in such approaches often show already high photocurrents, while also the origin of the light-induced charge separation and the mechanism of electron transfer in these systems are not clear. For example, Leblanc *et al.* 2012 have used vacuum-deposited PSI multilayers on a p-doped silicon electrode and reached high, but only transient photocurrents of $875 \mu\text{A cm}^{-2}$ ($4.6 \mu\text{A cm}^{-2} \text{ mW}^{-1}$) with the need of a very high electron acceptor concentration in solution (200 mM).²¹⁷ However, the p-doped silicon already shows 50 % of the photocurrent in control experiments. This draws the speculation, that an additional electron transfer pathway may have been created, where electrons also can be transferred directly from the electrode to the acceptor after charge separation in the p-doped silicon.

When the light intensity-normalized photocurrents are considered, the performance of P4.3 belongs to the top 4 produced photobioelectrodes to date (when PSI is used as light-sensitive biocomponent). But even among these electrodes care has to be taken to the detailed experimental conditions. In the experiments reported by Yehezkeli *et al.* 2013 a very low light intensity at 680 nm has been used (0.28 mW cm^{-2}). This is a spectral and light intensity illumination condition, where PSI is most efficient with respect to the light-to-current conversion. This condition is far away from the light intensity or spectrum of the sun, thus the natural situation. Most studies report their photocurrent values at light saturation conditions by using lamp sources covering the whole visible light spectrum. Yehezkeli *et al.* 2013 have not provided the photocurrent dependency upon the light intensity, and without normalizing the photocurrent to the light intensity, their electrode performance is only below average.²¹¹ Hence, a clear classification of this study cannot be done and the low light-intensity used here does probably not reflect the high efficiency of this system. Kothe *et al.* 2014 supersaturated the buffer with oxygen to yield high photocurrents, whereby under air saturation the

normalized photocurrent density reached only $2.45 \mu\text{A cm}^{-2} \text{mW}^{-1}$, which is comparable to P4.2 ($2.5 \mu\text{A cm}^{-2} \text{mW}^{-1}$).²¹⁶ In another strategy of wiring PSI based on Osmium-redox polymers have been used, conducting the hole from PSI to the electrode. Here, a large amount of electrically connected PSI can be integrated in the hydrogel, while electron donation to P_{700} is very efficient.²¹⁴ When the solvated hydrogel is collapsed by means of a buffer containing high concentrations of ions, the connection to the luminal side of PSI can be further improved, increasing the photocurrents by a factor of 2.²¹⁶

However with the examples discussed so far, it is obvious, that photocurrents and their light-normalized values often cannot fully be evaluated and a comparison of efficiencies between studies is difficult, because they strongly depend on the experimental conditions applied. Owing to this, another important parameter has also to be considered – the turnover number (T_e). This parameter can be seen as the molecular apparent electron transfer rate of the system and has to be maximized for a high efficiency. T_e is the number of light-induced electrons per second and per PSI molecule. Owing to this, systems with high photocurrents not necessarily have a high T_e . In cyanobacteria a T_e of approximately $47 \text{ e}^- \text{PSI}^{-1} \text{s}^{-1}$ has been determined.²³⁵ With systems developed during this thesis the T_e could be increased from 10 (P4.1) over 21 (P4.2) to $35 \text{ e}^- \text{PSI}^{-1} \text{s}^{-1}$ (P4.3). In P4.1 the concentration of PSI was determined by SPR and exceeds the theoretical value for a monolayer. It can be seen that not all PSI molecules have been connected to the electrode, since the photocurrent increases after another deposition of cyt *c* on top. If only the actively connected PSI molecules are considered, the real T_e would have been higher, since for the calculation of T_e the whole amount of deposited PSI has been used. Considering a monolayer coverage of 0.4 pmol cm^{-2} PSI, the T_e of P4.1 would have been $26 \text{ e}^- \text{PSI}^{-1} \text{s}^{-1}$, which is close to P4.2 and P4.3. However the T_e of all three systems lies beyond the natural system as well as beyond the T_e for cyt *c* and PSI in solution ($61 \text{ e}^- \text{PSI}^{-1} \text{s}^{-1}$, see 4.2, S9). The latter experiment suggests that there are possibilities to further improve the turnover and thus the photocurrent output. Not many other studies have given the T_e values, which would show a better comparison of the molecular efficiency of systems. Compared with another study using cyt *c*, the T_e achieved in this thesis are one order of magnitude higher ($3.76 \text{ e}^- \text{PSI}^{-1} \text{s}^{-1}$, calculated).²²⁹

Another fact, which is often not mentioned in detail for PSI-semiconductor systems is the high amount of PSI molecules, deposited onto the electrode surface ($1 - 10 \mu\text{mol cm}^{-2}$). When the T_e number is calculated from the provided data in these studies, only very slow rates can be estimated ($1-90 \cdot 10^{-5} \text{ e}^- \text{PSI}^{-1} \text{s}^{-1}$, calculated).^{223,224,227,279} The electrodes developed within

this thesis provide more than 6 orders of magnitude higher T_e values. This shows again that the above mentioned studies failed to efficiently wire PSI to the electrode and also highlights the importance of a PSI connection network. When PSI is connected to gold electrodes *via* a SAM a T_e of $4.5 \text{ e}^- \text{ PSI}^{-1} \text{ s}^{-1}$ can already be achieved.²⁰¹ The use of a molecular wiring network, like cyt *c*, conducting polymers and redox polymers improve these values. But not every wiring network approach seems to be efficient, for example the embedment of PSI into a polyaniline network provides only $1.4 \text{ e}^- \text{ PSI}^{-1} \text{ s}^{-1}$.²¹² The use of a poly-benzylviologen polymer increases this value only to $2.5 \text{ e}^- \text{ PSI}^{-1} \text{ s}^{-1}$ (calculated).²¹¹ Using Osmium-redox polymers as a PSI embedding hydrogel, extraordinary values of $335 \text{ e}^- \text{ PSI}^{-1} \text{ s}^{-1}$ ($102 \text{ e}^- \text{ PSI}^{-1} \text{ s}^{-1}$ under air saturation), have been achieved, when the gel is collapsed.²¹⁶ Very recently, Peters *et al.* 2016 used a macroporous ATO structure with immobilized PSI (similar to P4.3), but PSI connection to the electrode have been done by the adsorption of an electro-active guest (molybdenum polyoxometalate anion). They achieved a reasonable T_e ($8.4 \text{ e}^- \text{ PSI}^{-1} \text{ s}^{-1}$), which is nevertheless beyond the values achieved with the cyt *c* based systems provided by this thesis.

Another interesting parameter is the quantum efficiency (QE), which describes the efficiency in terms of photon-to-charge carrier conversion including all limiting effects (e. g. absorption by other non- light-to-current converting components of the electrode). The QE is the ratio of the light-induced electrons to the incident photons per second. There are two different QE's, which divide into the external and internal QE (EQE, IQE). For calculating the EQE, all irradiating photons per second are used, while for the IQE only the absorbed photons per second will be taken into account. In most cases the IQE is therefore higher, because there is a loss in usable photons due to reflection, scattering or spectral mismatch of the electrode. The QE is not often calculated for most photobioelectrodes, but is commonly used in solar cell publications to validate the spectral efficiency of a system. In this thesis, the EQE and IQE was only determined for P4.2 and P4.3 in dependence on the applied light intensity. For P4.2 the EQE reached a maximum value of 4.9 %, with an IQE of about 27 %. With the introduction of μ ITO electrodes in P4.3, values of 11 % (EQE) and 30 % (IQE) have been evaluated. These efficiencies are extraordinary high compared to other studies, underlining the high functionality of PSI within these systems. The IQE of PSI in the natural system can reach nearly 100 %, which shows that there is still room for improvements.²⁵

A comparison with other PSI electrode systems can only be done qualitatively, since most studies are not using the same light source, intensity distribution and light intensity. For

example, Leblanc *et al.* 2014 used a 633 nm high pass filter, which resulted in a 15 % higher photocurrent as compared by using a standard solar irradiance simulator as light source.²²³ Without a given light source spectrum the QE can have strong variations, e. g. when the typical green gap of PSI is not included in the incident light spectrum. For the purpose of a better comparability, a white light source should be used, simulating the solar intensity distribution.

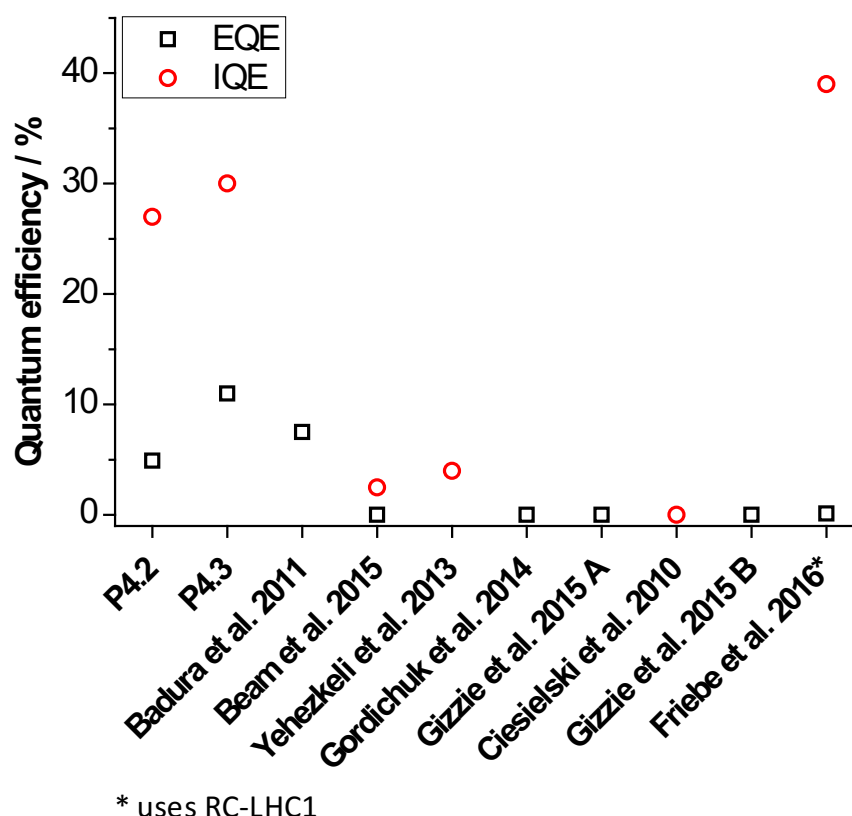


Fig. 11: Reported maximum quantum efficiencies (EQE, black and IQE, red) of different electrode systems using PSI.^{211,212,214,227,239,240,269} As comparison one of the most efficient systems using another biological light-harvesting component (RC-LH1) is also shown (Friebe *et al.* 2016).²⁸²

Figure 11 summarizes the EQE as well as the IQE of different PSI containing electrodes. A clear tendency can be seen: Most electrode systems are beyond the values achieved in P4.2 and P4.3. Despite high and moderate reported photocurrent densities achieved in those studies, their quantum efficiency is relatively low. This can be attributed to high light intensities, which are needed to produce a decent photocurrent in these studies. Additionally, a high amount of unconnected PSI molecules will also lower the QE, because these molecules competitively absorb light and a higher light intensity is needed. In addition, there are often more light-absorbing components in a photobioelectrode and in the cell solution, lowering the

photons absorbed by PSI. Another fact is the usage of materials, which strongly scatters or absorbs the incident photons, while producing no charge carriers. In terms of EQE, only Badura *et al.* 2011 are in the same magnitude as P4.2 and P4.3. The IQE often cannot be measured due to the opaque nature of the electrode. For this reason the absorption spectrum of the light-harvesting component is taken and corrected for the protein amount in the structure, which have been also done in P4.2.

At this point, a non-PSI containing photobioelectrode has to be discussed and compared with the cyt *c* approach used in this thesis. Friebe *et al.* 2016 used also cyt *c* to connect a different light-harvesting protein-complex, the reaction-center light harvesting-1 complex (RC-LH1) from *Rhodobacter sphaeroides*, to a mesoporous silver electrode.²⁸² Here, the 3D photobioelectrode has shown photocurrents of $166 \mu\text{A cm}^{-2}$, which is comparable to P4.3. But when I_p is normalized to the light intensity used in this study, P4.2 and P4.3 outperform this system by at least a factor of 2 (1.66 vs. 2.5 and $7.5 \mu\text{A cm}^{-2} \text{mW}^{-1}$). The maximum possible photocurrent density reported by Friebe *et al.* 2016 could reach up to $416 \mu\text{A cm}^{-2}$ using 4 suns (400mW cm^{-2}), which can be explained by the plasmonic nature of silver. This system therefore is not limited by the illumination intensity as can be seen in P4.1-4.3, where maximum currents are reached already at 20mW cm^{-2} , but needs extra high light intensities for high current densities.²⁸² The connection of silver electrodes with cyt *c* yields a turnover number of $142 \text{e}^- \text{RC-LH1}^{-1} \text{s}^{-1}$ at 1 sun. Furthermore, they reported one of the highest IQE value to date of $\sim 300 \%$ for small light intensities and even 39% at 1 sun. Nevertheless, for the calculation of the IQE, the RC-LHC1 solution spectrum was used, while corrected for the number of molecules in the structure. Because of the strong plasmonic effect of the porous silver, the apparent IQE is much higher as they would be if absorption and scattering of the silver structure was taken into account. This can be seen also by the lower EQE compared to the IQE, which is a factor of $\sim 2,300$ smaller than the apparent IQE.

This system clearly demonstrates that cyt *c* is well suited of connecting light-harvesting protein-complexes to electrodes and also shows that especially mesoporous structures with plasmonic field effects have a great potential for photobioelectrode performance improvements. Interestingly, when basic concepts are compared with respect to efficiency, the use of a wiring network for the indirect connection of PSI with the electrode seems to be a very powerful approach. These wiring networks exhibit a connection on a very molecular level to each individual PSI molecule and are able to connect a large protein amount to an electrode. Following this strategy, the cyt *c* / PSI approaches presented by this thesis, are

comparable to the best PSI electrode systems in terms of photocurrent density and turnover number, and can be seen as one of the most efficient photon-to-charge carrier converting photobioelectrodes.

5.3 Advantages and drawbacks of the cytochrome *c* / photosystem I photobioelectrodes

The starting point of this discussion will be the interaction of cyt *c* and PSI itself. To generate a beneficial connection of both components, certain conditions have to be used, including ionic strength and pH of the assembly solution. This clearly shows the first drawback of the system, because these conditions have to stay constant even when assembled on an electrode surface. A high magnitude of photocurrent strongly requires a buffer with low ionic strength. Nonetheless higher salt concentrations in electrolyte solutions of electrochemical cells are often applied, because this enhances the conductivity of the medium and reduces the ohmic loss. Consequently, the usage of the cyt *c*/PSI photobioelectrodes in a bio-electrochemical cell is potentially not beneficial. This can be seen as the first drawback of the system, since the ET reactions as well as the conductivity cannot be improved by a higher ionic strength, due to the disassembly of the biomolecules, which will lose connection to the electrode.

There are 4 basic ET reactions in this system, a) the ET between cyt *c* and PSI, b) the self-exchange between adjacent cyt *c* molecules, c) the heterogeneous ET between cyt *c* and the electrode and d) the ET from PSI to an acceptor in solution. All four processes can be the rate-limiting step of overall electron flow and need to be improved for a high photocurrent density. As has been discussed before (5.2), the turnover number in this non-natural system is superior to most strategies but still below the natural system, and other artificial systems based on Os-polymers. It has not been verified that cyt *c* binds to the putative electron donor binding site of PSI. Therefore distances of redox groups between the respective proteins may be rather long, demanding cyt *c*-cyt *c* ET before cyt *c* to PSI ET can take place. To address this issue, possible actions like site-directed mutagenesis of PSI as well as of cyt *c* may improve the binding situation of the small redox protein at the luminal electron donor-binding site of PSI. Other redox proteins can have also the potential to increase the T_e of PSI, e. g. because of a different redox-active prosthetic group or a more beneficial match with the surface patch below the P_{700} . For instance, the T_e of PSI in solution is much higher compared to cyt *c*, when cyt *c*₆, the natural interaction partner, is used.²³⁵ Nonetheless, the ET reaction of cyt *c*₆ to

electrodes has only been achieved from solution, but its electro-active immobilization on electrodes has not yet been accomplished.²⁵¹ This issue further demonstrates, that also the electrical connection of a redox shuttle in a surface-fixed state needs to be considered.

In this thesis two materials (gold and ITO) with a different structure (planar and 3D), a different surface-electrolyte interface (carboxyl-/hydroxyl terminated SAM and partial hydroxyl-terminated) and a distinct carrier density/mobility have been used, but nonetheless in both cases it has been possible to construct photobioelectrodes based on *cyt c* and PSI. These systems share a high similarity by means of the cathodic direction of photocurrents, the onset potential of photocatalysis, the light dependence of the photocurrent, the turnover numbers of PSI and the interaction between both biomolecules under buffer conditions of low ionic strength. But especially the heterogeneous ET of *cyt c* with the electrode can be a crucial point. On gold electrodes, the k_s of *cyt c* is already rather fast, but on ITO k_s is much slower and shows a strong variation depending on the sintering conditions. Since, it has been demonstrated, that if the k_s is already slow, small improvements on the rate constant by modification of the electrode material (from 0.58 s^{-1} to 1.1 s^{-1} , see P4.3, Fig. 3, S6) have a strong direct impact on the photocurrent output. From these findings one essential note is, that the *cyt c*/PSI system is solely beneficial, if a fast electrical connection of *cyt c* to the electrode can be established. The parameter, which needs to be determined for evaluating the utility of such materials, is the heterogeneous electron transfer constant of *cyt c* with such an electrode. These aspects draw the conclusion, that there is a need for the improvement of the ET reaction of *cyt c* to 3D electrodes, but also for ensuring that the interaction of *cyt c* with PSI itself is not becoming the rate-limiting step for the overall electron flow.

The use of *cyt c* along with PSI has another not yet discussed parameter, which is needed to be addressed here: the onset potential of the photocurrent. To use the entire transformed energy provided by PSI (difference between P_{700} and F_B , $\sim 1\text{ V}$), for a photocathodic system, the differences between the electrode potential and P_{700} ($+0.42\text{ V vs. SHE}$) and the electron acceptor and F_B (-0.58 V vs. SHE) have to be small. The potential difference can be considered as the additional electrical energy, which is needed to be applied for overcoming the energy barrier for the electron transfer in the system. Because electrons are first transferred from the electrode to *cyt c*, the redox potential of this small protein determines the start of the ET reaction (see P4.1, Fig. 3). There is a potential gap between *cyt c* and P_{700} of about 0.185 V . Within photobioelectrodes produced in this thesis, an applied electrode potential of $-0.1\text{ V vs. Ag|AgCl}$ is at least needed for generating maximum photocurrents. This

also displays, that an additional overpotential is necessary for a fast ET reaction with cyt *c*, whereby the heterogeneous ET rate can be the rate-limiting step in the overall ET kinetics. This clearly demonstrates also a drawback of this system, because additional electrical energy is needed for driving the light-induced ET reaction. However, solutions for this issue can be potentially applied in the future, because other redox proteins with a higher redox potential can be used, or the redox potential of cyt *c* can be changed by a change in the iron-coordinating axial ligands or surrounding amino acids at the heme group.

Another set of parameters, which has to be mentioned here, is the reliability, sustainability, simplicity and stability of the cyt *c*/PSI system. One major advantage can be found if the procedure of electrode production is analysed. The protocol of mixing or assembling both biocomponents is rather simple as compared with other procedures, which often includes a high number of preparation steps. Here, there is only one step of assembling cyt *c* and PSI, which can be done over night (P4.1), in a couple of hours (P4.2) or even in several minutes (P4.3). This clearly depends on the electrode structure and modification used, whereas especially in 3D electrodes, strong capillary forces support the mass-transfer of the biocomponents to the electrode surface. This seems to be even more convincing, when combined with a fast preparation of the basic 3D electrode. The protocol for the μ ITO structure could be speeded up enormously, when compared to other μ ITO photobioelectrodes, which often need several days.^{287,305}

Another aspect is the stability of cyt *c*/PSI photobioelectrodes. This has only been addressed in detail in P4.2, because here the role of DNA has been pointed out. In this study long term photocurrent experiments revealed that DNA improves the stability of the assembly, whereas electrodes can be stored up to 9 days without a loss in activity. Even 1 month of storage will still retain 65 % of activity, which is extraordinary high, when using biocomponents. Nevertheless, the co-assembly of cyt *c*/PSI in a large amount seems to be sensitive to a buffer exchange and the applied potential, where cohesion can be lost between the assembled molecules. To date little effort has been undertaken for improving this situation, which remains as a future task to be addressed. Under permanent illumination, the photocurrent stability of the photobioelectrodes from P4.1, P4.2 and P4.3 exhibits strong differences. Here, two processes turn out to influence the photocurrent-time dependence. The first process is mainly driven by depletion of diffusible electron acceptor molecules close to the electrode. At planar electrodes (as can be seen in P4.1 and P4.2) the delivery of acceptor molecules from bulk solution to the electrode surface is fast, thus photocurrent stability is only less influenced

by this process. In the 3D electrode setup this situation changes dramatically, since photocurrents drop fast over a certain time period under diffusion-controlled conditions (see P4.3, Fig. 2). If the solution is stirred, the photocurrent becomes much more stable, clearly showing, that diffusion is the dominant process in the degradation of photocurrents in this electrode setup. As a consequence, 3D electrodes indeed have the potential to produce high photocurrents, but without addressing their diffusion problem, the permanent illumination stability is less pronounced compared to planar electrodes. A solution can be seen, if the concentration of electron acceptors can be increased, or more important, if the stromal side of the PSI can be connected by means of a conducting molecule, like a polymer, to another electrode. Thus, electrons from the F_B cluster can be transferred directly to the counter electrode. This means that there is no need for an electron acceptor in solution and the diffusion limitation will not be present. The stromal side of the PSI can also be connected to an enzyme, which uptakes electrons for substrate conversion. Nevertheless, the substrate must also diffuse to the electrode surface, but can be put at high concentrations in the solution. Besides diffusion of the electron acceptor, other processes can be identified to degrade the photocurrent over time, which is seen in all produced photobioelectrodes within this thesis. This behaviour has not been investigated in detail so far, but possible reasons can be seen in the damage of PSI by reactive oxygen species, the loss of protein-electrode or protein-protein cohesion on the surface, due to an applied potential and/or the photobleaching of the PSI molecules.

In this thesis it has also been shown, that the cyt *c*/PSI system can be applied to different electrode materials, which demonstrates the great reliability of the invented biocomponent connection. The prerequisite for this is the establishment of a fast electron transfer between the electrode and cyt *c*. As has been previously described in chapter 3.2.2.3, numerous electrode materials for electrical connection of cyt *c* have already been successful used, which shows again the great prospective for the cyt *c*/PSI system.

A different aspect to be discussed is the dependence of the photocurrent on the intensity of the applied light illumination. For all photobioelectrodes within this thesis, the dependence upon illumination intensity has been rather similar. By considering photons as the substrate for the light-harvesting super-complex PSI, the Michaelis-Menten equation has been applied, resulting in comparable parameters. The Michaelis constant K_M is 2.4 (P4.1), 0.77 (P4.2), 2.6 (P4.3) mW cm^{-2} , respectively. Interestingly, K_M seems to be higher for systems where cyt *c* and PSI are assembled in a monolayer fashion, and lower for a multilayer approach. An

explanation here can be seen if adjacent PSI molecules and their chlorophylls have an energetically coupling with each other. This is not the case if only a monolayer of PSI molecules is present. On the other side, there can be a limitation in ET in the multilayer system. Electrons have to travel by means of cyt *c* self-exchange far through the large network to transport them to every connected PSI molecule. This takes time and slows down the entire ET process, therefore the photocurrent saturation will be observed at smaller light intensities. Nonetheless, all K_M values are rather small, which on the one hand shows a that this system is already efficient at low light intensities, making these electrodes a candidate to be used as a photosensor, or in regions, where the solar irradiation is low. On the contrary, under full sun light, the photobioelectrode is not able to make use of the excess solar intensity, because it already reached saturation at 20 mW cm^{-2} . This makes it highly efficient under lower light conditions, which has similarities with cloudy days in northern Europe.

6. Outlook and Future Perspectives

The benefits of the cyt *c*/PSI approach to be used as a light-harvesting biological electrode are: 1. The creation of an artificial signal chain on electrodes, 2. The generation of a high photocurrent density by means of a multilayer approach or on 3D electrodes and 3. The achievement of high external and internal quantum efficiencies. Moreover, certain aspects still need to be improved, while first solutions for this have been shown in the discussion. The most important issues are: a) The ET rate between cyt *c* and PSI, b) the redox potential of cyt *c* with respect to P₇₀₀ and c) the ET rate of cyt *c* to the electrode. Since there are several other electrode materials and structures available, the benefits of them can be explored in the future, which may allow an even more efficient biohybrid combination.

The use of nanomaterials as either electrode material or to improve the connection of the biocomponents has not been exploited to their limits. Benefit can be seen here in enhancing the light conversion efficiency over a broader light spectrum. PSI typically has a low absorption in the green area of the visible spectrum, while additionally the sun provides also light energy in the infrared or ultraviolet electromagnetic radiation. Nanomaterials, like quantum dots, may improve the energy transfer towards the photosynthetic reaction center. Furthermore they are able to conduct charge carriers, which can be used for the acceleration of the electron transfer of the system or as artificial catalysts for the production of energy-rich molecules. First examples, like silver nanostructures, which have been reported recently show great potential for increasing the electrode efficiency by exploitation of plasmonic effects.

For an application, the overall stability has to be considered; one strategy has been developed within this thesis due to the use of DNA as a structural matrix element. Other building blocks, like polymers or nanomaterials can also be considered for increasing the stability. The integration of the complex PSI in a matrix can increase the operational stability. Protein stability in liquid phases has some limitations and to overcome this issue, protein crystals or another solid state strategy might be explored, although, the state of the protein is not easy to control in the latter approach. Additionally, the adsorption of the proteins from a solution to a surface displays room for improvements, as other techniques, like electro-spraying, can help to assemble proteins in a different manner.

To date the system lacks an important component, which transfers the solar energy to storable chemical energy. In the future, enzymes or catalytic nanomaterials have to be integrated in the

electrode construction, to produce energy-rich compounds, for example NADPH (ferredoxin-NADP⁺-reductase), H₂ (hydrogenase, Pt nanoparticles) or reducing the climate problematic CO₂ (formate dehydrogenase). A different area of application of the cyt *c* / PSI interaction can be seen in light-switchable biosensors. PSI can be the photo-active gate in the enzymatic signal cascade and thus a photocurrent could become the analytical signal changing in the presence of a certain enzymatic substrate.

The basic working principle provided by this thesis has the potential to be used to study these further developments, like understanding and establishing the interaction between enzymes and PSI in a productive manner. This thesis can therefore be considered as contributions to the development towards a biobased photosynthetic economy, which uses the benefits from nature combined with artificial materials.

7. Summary

The construction of light-harvesting electrodes based on the integration and exploitation of components from the natural photosynthesis is an emerging field in current research and potential can be seen to contribute to the development of a bio-based economy. In this thesis the focus was applied to produce photobioelectrodes by the utilization of photosystem I, as one of the major light-to-charge separating super-complexes from the thylakoid membrane in the oxygenic photosynthesis. The electrical connection of this complex with an inorganic electrode material is often rather difficult. Hence, a new strategy has been investigated by coupling PSI by means of the small redox protein from the respiratory chain *cyt c* to the electrode. The essential features of the biohybrid photoelectrodes will be summarized hereinafter.

In the first part of this thesis (P4.1), the direct interaction between both biocomponents has been addressed, whereas the experimental conditions for the assembly on a SAM modified gold electrode have been revealed. Here, PSI was able to assemble in a densely packed layer on a *cyt c* monolayer under buffer conditions of low ionic strength and at a neutral pH. It has further found, that *cyt c* promotes the binding of PSI to the surface. The photobioelectrode exhibited a photocurrent of about $1 \mu\text{A cm}^{-2}$ at $-0.1 \text{ V vs. Ag|AgCl}$. The direction of the photocurrent is solely cathodic, since at higher potentials ($+0.5 \text{ V vs. Ag|AgCl}$) only very small anodic currents have been observed. The light-induced catalysis started at the redox potential of *cyt c*. This demonstrates, that the electrons are first transferred from the electrode to *cyt c* further reducing the PSI in a second step. It also shows, that PSI can be assembled on *cyt c* preferentially with the luminal side down. The study also reveals, that multiple alternately assembled layers of *cyt c* and PSI can be built up with an additional contribution to the overall detected photocurrent.

The second part of this thesis (P4.2) has aimed for the further improvement of the photobioelectrode and for the elucidation of a deeper understanding of the connection of PSI with *cyt c*. It was found that *cyt c* and PSI were able to produce artificial complexes already in solution. Both biocomponents can be deposited as a thick layer from a mixed solution on a modified gold surface. The deposited amount strongly depends on the molecular ratio of *cyt c* to PSI and on the assembling time. The surface concentration of electrically addressable *cyt c* molecules strongly correlates with the generated photocurrents, which demonstrates that both biocomponents assemble jointly to the surface. Nonetheless, the amount of proteins on the

surface was limited and DNA, as a polyelectrolyte structural scaffold, was introduced to circumvent the saturation of biomolecules on the electrode. With a layer-by-layer approach, the photocurrent was greatly enhanced up to $27 \mu\text{A cm}^{-2}$ for an 8 bilayer electrode. In addition the long-term stability of the photobioelectrode was improved (65 % activity after 1 month's storage). The photophysical parameters of the *cyt c* / PSI electrode revealed high quantum efficiencies of 4.9 % (EQE) and 27 % (IQE), with a moderate turnover number of PSI ($21 \text{ e}^- \text{ PSI}^{-1} \text{ s}^{-1}$).

In the third part of this thesis (P4.3) mesoporous indium tin oxide electrodes have been developed for the integration of *cyt c* and PSI into a 3D transparent electrode. The construction process of μITO electrodes has been investigated in detail with respect to structural scalability. It was possible to integrate the large membrane super-complex PSI and the small redox protein *cyt c* with monolayer coverage with respect to the electrochemically active surface area of the μITO electrode. The produced photocurrents reached up to $150 \mu\text{A cm}^{-2}$ (for a $40 \mu\text{m}$ thick or a 6x layer electrode) and the improvement of the heterogeneous electron transfer constant, k_s of *cyt c* to the electrode has been identified to play a crucial role in this system. The internal quantum efficiency of this photobioelectrode achieved a very high value of 39 %, which is extraordinary high if compared with other strategies using PSI. A further advantage of this biohybrid electrode can be seen in the ease of preparation. The 3D electrode can be produced using a spin-coating procedure within hours, while the integration of the protein components takes only several minutes.

From all studies performed within this thesis it can be concluded, that the interaction and communication of *cyt c* with PSI plays a crucial role. The binding of both biocomponents seems to be of non-specific mainly electrostatic nature. Computational analysis of putative contact sites shows, that *cyt c* is able to bind to different parts of PSI, including the luminal and stromal side, as well as hydrophobic regions in the membrane section of the protein complex. This feature explains, why both biocomponents can be assembled onto each other and form co-complexes in solution, whereby a protein multilayer or co-assembly are feasible.

However a preferential binding to the luminal side can also be shown and explains the docking of PSI to a *cyt c* monolayer. In the multilayer system PSI molecules far away from the electrode surface can be functionally connected, and the generated photocurrent exhibits a linear relationship with the protein amount deposited. This can be explained by the efficient self-exchange between the *cyt c* network surrounding PSI.

The comparison to other photobioelectrode strategies using PSI displays a remarkable development over the studies provided by this thesis. In terms of performance, quantum or molecular efficiency, the cyt *c* / PSI photobioelectrodes P4.2, but especially P4.3 belong to the best systems to date, making them candidates for the generation of more complex signal chains. Especially the light-to-current conversion efficiency of P4.3, expressed by the internal quantum efficiency can reach up to 39 %, while the molecular efficiency expressed by the turnover number can be as high as $35 \text{ e}^- \text{ PSI}^{-1} \text{ s}^{-1}$. Furthermore, the systems even provide a high performance under lower light conditions, which once again shows that efficient signal pathways have been created.

Taken together, these three studies demonstrate the potential and limitations of constructing a photobiohybrid electrode based on PSI, when cyt *c* was used for the wiring to the electrode. Within this thesis, the working conditions of the cyt *c*/PSI system have been revealed, while optimization of performance have been done by the choice of electrode material and protein arrangement, e. g. by using DNA. The photo-induced signal chain was analysed and experimental evidence was presented, that cathodic photodiodes have been produced. The limiting factors and the potential for application have been discussed based on supporting experiments, clearly showing the high capability of being used in a photobioenzymatic device or in a photo-switchable biosensor application.

8. References

- 1 N. S. Lewis and D. G. Nocera, *Proc. Natl. Acad. Sci.*, 2006, **103**, 15729–15735.
- 2 R. E. Blankenship, *Photosynth. Res.*, 1992, **33**, 91–111.
- 3 D. I. ARNON, M. B. ALLEN and F. R. WHATLEY, *Nature*, 1954, **174**, 394–396.
- 4 H. Gest, *FEMS Microbiol. Lett.*, 1993, **112**, 1–5.
- 5 R. E. Blankenship, M. T. Madigan and C. E. Bauer, *Anoxygenic Photosynthetic Bacteria*, Springer Science & Business Media, 1995.
- 6 K. Sauer, *Annu. Rev. Phys. Chem.*, 1979, **30**, 155–178.
- 7 A. BENSON and M. CALVIN, *Science (80-.)*, 1947, **105**, 648–649.
- 8 P. E. Jensen and D. Leister, *F1000Prime Rep.*, 2014, **6**.
- 9 T. Cavalier-Smith, *Trends Plant Sci.*, 2000, **5**, 174–82.
- 10 J. P. Dekker and E. J. Boekema, *Biochim. Biophys. Acta - Bioenerg.*, 2005, **1706**, 12–39.
- 11 D. Bald, J. Kruip and M. Rögner, *Photosynth. Res.*, 1996, **49**, 103–118.
- 12 U. Enser and U. Heber, *Biochim. Biophys. Acta - Bioenerg.*, 1980, **592**, 577–591.
- 13 W. Haehnel, *Annu. Rev. Plant Physiol.*, 1984, **35**, 659–693.
- 14 P. Manna and W. Vermaas*, *Plant Mol. Biol.*, 1997, **35**, 407–416.
- 15 N. Nelson and A. Ben-Shem, *Nat. Rev. Mol. Cell Biol.*, 2004, **5**, 971–982.
- 16 G. T. Babcock, B. A. Barry, R. J. Debus, C. W. Hoganson, M. Atamian, L. McIntosh, I. Sithole and C. F. Yocum, *Biochemistry*, 1989, **28**, 9557–9565.
- 17 M. D. Lambrev, D. Russo, F. Polticelli, V. Scognamiglio, A. Antonacci, V. Zobnina, G. Campi and G. Rea, *Curr. Protein Pept. Sci.*, 2014, **15**, 285–95.
- 18 J. Kern and G. Renger, *Photosynth. Res.*, 2007, **94**, 183–202.
- 19 H. Kirchhoff, U. Mukherjee and H.-J. Galla, *Biochemistry*, 2002, **41**, 4872–4882.
- 20 J. M. Anderson, *Photosynth. Res.*, 1992, **34**, 341–357.
- 21 S. S. Hasan, E. Yamashita, D. Baniulis and W. A. Cramer, *Proc. Natl. Acad. Sci.*, 2013, **110**, 4297–4302.
- 22 E. L. Gross, *Photosynth. Res.*, 1993, **37**, 103–16.

-
- 23 M. Hippler, F. Drepper, J. Farah and J.-D. Rochaix, *Biochemistry*, 1997, **36**, 6343–6349.
- 24 P. R. Chitnis, *Annu. Rev. Plant Physiol. Plant Mol. Biol.*, 2001, **52**, 593–626.
- 25 N. Nelson and C. F. Yocum, *Annu. Rev. Plant Biol.*, 2006, **57**, 521–65.
- 26 R. Masaki, S. Yoshikawa and H. Matsubara, *Biochim. Biophys. Acta - Protein Struct. Mol. Enzymol.*, 1982, **700**, 101–109.
- 27 P. MITCHELL, *Nature*, 1961, **191**, 144–148.
- 28 N. Nelson, *Photosynth. Res.*, 2013, **116**, 145–151.
- 29 G. W. Brudvig, *Philos. Trans. R. Soc. B Biol. Sci.*, 2008, **363**, 1211–1219.
- 30 D. M. Kramer, C. A. Sacksteder and J. A. Cruz, *Photosynth. Res.*, 1999, **60**, 151–163.
- 31 L. I. Krishtalik, *Biochim. Biophys. Acta - Bioenerg.*, 1986, **849**, 162–171.
- 32 Y.-C. Cheng and G. R. Fleming, *Annu. Rev. Phys. Chem.*, 2009, **60**, 241–262.
- 33 P. Horton, A. V. Ruban and R. G. Walters, *Annu. Rev. Plant Physiol. Plant Mol. Biol.*, 1996, **47**, 655–684.
- 34 A. R. Grossman, D. Bhaya, K. E. Apt and D. M. Kehoe, *Annu. Rev. Genet.*, 1995, **29**, 231–88.
- 35 C. J. Law, A. W. Roszak, J. Southall, A. T. Gardiner, N. W. Isaacs and R. J. Cogdell, *Mol. Membr. Biol.*, 2004, **21**, 183–191.
- 36 A. R. Holzwarth, M. G. Muller, M. Reus, M. Nowaczyk, J. Sander and M. Rogner, *Proc. Natl. Acad. Sci.*, 2006, **103**, 6895–6900.
- 37 B. A. Diner and G. T. Babcock, in *Oxygenic Photosynthesis: The Light Reactions*, Kluwer Academic Publishers, Dordrecht, 1996, pp. 213–247.
- 38 B. A. Diner and F. Rappaport, *Annu. Rev. Plant Biol.*, 2002, **53**, 551–580.
- 39 F. Rappaport, M. Guergova-Kuras, P. J. Nixon, B. A. Diner and J. Lavergne, *Biochemistry*, 2002, **41**, 8518–8527.
- 40 Y. Kato, M. Sugiura, A. Oda and T. Watanabe, *Proc. Natl. Acad. Sci. U. S. A.*, 2009, **106**, 17365–70.
- 41 H. Dau and I. Zaharieva, *Acc. Chem. Res.*, 2009, **42**, 1861–1870.
- 42 J. H. Nugent, *Eur. J. Biochem.*, 1996, **237**, 519–31.
- 43 T. Shibamoto, Y. Kato, M. Sugiura and T. Watanabe, *Biochemistry*, 2009, **48**, 10682–10684.
-

-
- 44 K. Saito, A. W. Rutherford and H. Ishikita, *Proc. Natl. Acad. Sci.*, 2013, **110**, 954–959.
- 45 B. A. Barry, *Photochem. Photobiol.*, 1993, **57**, 179–188.
- 46 C. Tommos and G. T. Babcock, *Biochim. Biophys. Acta - Bioenerg.*, 2000, **1458**, 199–219.
- 47 P. E. M. Siegbahn, *Biochim. Biophys. Acta - Bioenerg.*, 2013, **1827**, 1003–1019.
- 48 M. Suga, F. Akita, K. Hirata, G. Ueno, H. Murakami, Y. Nakajima, T. Shimizu, K. Yamashita, M. Yamamoto, H. Ago and J. Shen, *Nature*, 2014, **517**, 99–103.
- 49 B. KOK, B. FORBUSH and M. McGLOIN, *Photochem. Photobiol.*, 1970, **11**, 457–475.
- 50 D. J. Vinyard, G. M. Ananyev and G. Charles Dismukes, *Annu. Rev. Biochem.*, 2013, **82**, 577–606.
- 51 H. H. Stiehl and H. T. Witt, *Zeitschrift für Naturforsch. B*, 1969, **24**.
- 52 W. A. Cramer, H. Zhang, J. Yan, G. Kurisu and J. L. Smith, *Annu. Rev. Biochem.*, 2006, **75**, 769–90.
- 53 S. Veit, K. Takeda, Y. Tsunoyama, D. Rexroth, M. Rögner and K. Miki, *Acta Crystallogr. Sect. D Biol. Crystallogr.*, 2012, **68**, 1400–1408.
- 54 A. N. Tikhonov, *Plant Physiol. Biochem.*, 2014, **81**, 163–183.
- 55 H. T. Witt, *Biochim. Biophys. Acta - Rev. Bioenerg.*, 1979, **505**, 355–427.
- 56 K. K. Ho and D. W. Krogmann, *Biochim. Biophys. Acta - Bioenerg.*, 1984, **766**, 310–316.
- 57 A. Nakamura, T. Suzawa, Y. Kato and T. Watanabe, *Plant Cell Physiol.*, 2011, **52**, 815–23.
- 58 I. V. Shelaev, F. E. Gostev, M. D. Mamedov, O. M. Sarkisov, V. A. Nadtochenko, V. A. Shuvalov and A. Y. Semenov, *Biochim. Biophys. Acta - Bioenerg.*, 2010, **1797**, 1410–1420.
- 59 K. Brettel and W. Leibl, *Biochim. Biophys. Acta*, 2001, **1507**, 100–14.
- 60 V. V. Ptushenko, D. A. Cherepanov, L. I. Krishtalik and A. Y. Semenov, *Photosynth. Res.*, 2008, **97**, 55–74.
- 61 K. Brettel, *FEBS Lett.*, 1988, **239**, 93–98.
- 62 P. Setif and K. Brettel, *Biochemistry*, 1993, **32**, 7846–7854.
- 63 P. Fromme, P. Jordan and N. Krauß, *Biochim. Biophys. Acta - Bioenerg.*, 2001, **1507**, 5–31.
-

-
- 64 P. Q. Y. Setif and H. Bottin, *Biochemistry*, 1994, **33**, 8495–8504.
- 65 N. Fischer, P. Setif and J.-D. Rochaix, *J. Biol. Chem.*, 1999, **274**, 23333–23340.
- 66 A. van der Est, C. Bock, J. Golbeck, K. Brettel, P. Setif and D. Stehlik, *Biochemistry*, 1994, **33**, 11789–11797.
- 67 K. Brettel, *Biochim. Biophys. Acta - Bioenerg.*, 1997, **1318**, 322–373.
- 68 G. Kurisu, M. Kusunoki, E. Katoh, T. Yamazaki, K. Teshima, Y. Onda, Y. Kimata-Ariga and T. Hase, *Nat. Struct. Biol.*, 2001, **8**, 117–121.
- 69 H. Bottin and B. Lagoutte, *Biochim. Biophys. Acta - Bioenerg.*, 1992, **1101**, 48–56.
- 70 N. Carrillo and E. A. Ceccarelli, *Eur. J. Biochem.*, 2003, **270**, 1900–1915.
- 71 J. J. PUEYO, C. GOMEZ-MORENO and S. G. MAYHEW, *Eur. J. Biochem.*, 1991, **202**, 1065–1071.
- 72 Y. Munekage, M. Hashimoto, C. Miyake, K.-I. Tomizawa, T. Endo, M. Tasaka and T. Shikanai, *Nature*, 2004, **429**, 579–582.
- 73 I. Yacoby, S. Pochekailov, H. Toporik, M. L. Ghirardi, P. W. King and S. Zhang, *Proc. Natl. Acad. Sci.*, 2011, **108**, 9396–9401.
- 74 D. B. Knaff and M. Hirasawa, *Biochim. Biophys. Acta - Bioenerg.*, 1991, **1056**, 93–125.
- 75 N. Krauss, W. Hinrichs, I. Witt, P. Fromme, W. Pritzkow, Z. Dauter, C. Betzel, K. S. Wilson, H. T. Witt and W. Saenger, *Nature*, 1993, **361**, 326–331.
- 76 N. Krauß, W.-D. Schubert, O. Klukas, P. Fromme, H. T. Witt and W. Saenger, *Nat. Struct. Biol.*, 1996, **3**, 965–973.
- 77 O. Klukas, W.-D. Schubert, P. Jordan, N. Krauss, P. Fromme, H. T. Witt and W. Saenger, *J. Biol. Chem.*, 1999, **274**, 7351–7360.
- 78 P. Jordan, P. Fromme, H. T. Witt, O. Klukas, W. Saenger and N. Krauss, *Nature*, 2001, **411**, 909–17.
- 79 M. Rögner, U. Mühlenhoff, E. J. Boekema and H. T. Witt, *Biochim. Biophys. Acta - Bioenerg.*, 1990, **1015**, 415–424.
- 80 J. H. Golbeck, *Annu. Rev. Plant Physiol. Plant Mol. Biol.*, 1992, **43**, 293–324.
- 81 N. V. Karapetyan, A. R. Holzwarth and M. Rögner, *FEBS Lett.*, 1999, **460**, 395–400.
- 82 E. J. Boekema, J. P. Dekker, M. G. van Heel, M. Rögner, W. Saenger, I. Witt and H. T. Witt, *FEBS Lett.*, 1987, **217**, 283–286.
- 83 I. Grotjohann and P. Fromme, *Photosynth. Res.*, 2005, **85**, 51–72.
-

-
- 84 W. Xu, P. Chitnis, A. Valieva, A. van der Est, Y. N. Pushkar, M. Krzystyniak, C. Teutloff, S. G. Zech, R. Bittl, D. Stehlik, B. Zybailov, G. Shen and J. H. Golbeck, *J. Biol. Chem.*, 2003, **278**, 27864–27875.
- 85 P. Sétif, *Biochim. Biophys. Acta - Bioenerg.*, 2001, **1507**, 161–179.
- 86 P. Fromme, H. Bottin, N. Krauss and P. Sétif, *Biophys. J.*, 2002, **83**, 1760–1773.
- 87 F. Rousseau, P. Sétif and B. Lagoutte, *EMBO J.*, 1993, **12**, 1755–65.
- 88 V. P. Chitnis and P. R. Chitnis, *FEBS Lett.*, 1993, **336**, 330–334.
- 89 T. Förster, *Ann. Phys.*, 1948, **437**, 55–75.
- 90 A. N. Melkozernov, *Photosynth. Res.*, 2001, **70**, 129–153.
- 91 B. Gobets and R. van Grondelle, *Biochim. Biophys. Acta - Bioenerg.*, 2001, **1507**, 80–99.
- 92 A. J. Young and H. A. Frank, *J. Photochem. Photobiol. B Biol.*, 1996, **36**, 3–15.
- 93 S. Akimoto, S. Takaichi, T. Ogata, Y. Nishimura, I. Yamazaki and M. Mimuro, *Chem. Phys. Lett.*, 1996, **260**, 147–152.
- 94 K. R. Naqvi, *Photochem. Photobiol.*, 1980, **31**, 523–524.
- 95 P. Fromme, E. Schlodder and S. Jansson, 2003, pp. 253–279.
- 96 D. R. Baker, A. K. Manocchi, M. L. Lamicq, M. Li, K. Nguyen, J. J. Sumner, B. D. Bruce and C. A. Lundgren, *J. Phys. Chem. B*, 2014, **118**, 2703–11.
- 97 M. K. Şener, C. Jolley, A. Ben-Shem, P. Fromme, N. Nelson, R. Croce and K. Schulten, *Biophys. J.*, 2005, **89**, 1630–1642.
- 98 T. Ritz, S. Park and K. Schulten, *J. Phys. Chem. B*, 2001, **105**, 8259–8267.
- 99 M. Yang, A. Damjanović, H. M. Vaswani and G. R. Fleming, *Biophys. J.*, 2003, **85**, 140–158.
- 100 A. R. Holzwarth, M. G. Müller, J. Niklas and W. Lubitz, *Biophys. J.*, 2006, **90**, 552–565.
- 101 P. Joliot and A. Joliot, *Biochemistry*, 1999, **38**, 11130–11136.
- 102 O. G. Poluektov, S. V. Paschenko, L. M. Utschig, K. V. Lakshmi and M. C. Thurnauer, *J. Am. Chem. Soc.*, 2005, **127**, 11910–11911.
- 103 N. Dashdorj, W. Xu, R. O. Cohen, J. H. Golbeck and S. Savikhin, *Biophys. J.*, 2005, **88**, 1238–1249.
- 104 P. Q. Y. Setif and H. Bottin, *Biochemistry*, 1995, **34**, 9059–9070.
-

-
- 105 M. Hervás, J. A. Navarro and M. A. De La Rosa, *Acc. Chem. Res.*, 2003, **36**, 798–805.
- 106 M. Hervás, J. a Navarro, a Díaz, H. Bottin and M. a De la Rosa, *Biochemistry*, 1995, **34**, 11321–6.
- 107 M. Hervás, J. A. Navarro, F. P. Molina-Heredia and M. A. De La Rosa, *Photosynth. Res.*, 1998, **57**, 93–100.
- 108 M. A. De la Rosa, J. A. Navarro, A. Díaz-Quintana, B. De la Cerda, F. P. Molina-Heredia, A. Balme, P. del S. Murdoch, I. Díaz-Moreno, R. V Durán and M. Hervás, *Bioelectrochemistry*, 2002, **55**, 41–45.
- 109 D. M. A. Smith, K. M. Rosso, M. Dupuis, M. Valiev and T. P. Straatsma, *J. Phys. Chem. B*, 2006, **110**, 15582–15588.
- 110 Y. K. Shin, M. D. Newton and S. S. Isied, *J. Am. Chem. Soc.*, 2003, **125**, 3722–3732.
- 111 C. C. Page, C. C. Moser, X. Chen and P. L. Dutton, *Nature*, 1999, **402**, 47–52.
- 112 M. J. Eddowes and H. A. Hill, *J. Am. Chem. Soc.*, 1979, **101**, 4461–4464.
- 113 G. W. Bushnell, G. V. Louie and G. D. Brayer, *J. Mol. Biol.*, 1990, **214**, 585–595.
- 114 B. F. Van Gelder and E. C. Slater, *Biochim. Biophys. Acta*, 1962, **58**, 593–595.
- 115 S. E. J. Bowman and K. L. Bren, *Nat. Prod. Rep.*, 2008, **25**, 1118–1130.
- 116 W. H. Koppenol, J. D. Rush, J. D. Mills and E. Margoliash, *Mol. Biol. Evol.*, 1991, **8**, 545–58.
- 117 W. H. Koppenol and E. Margoliash, *J. Biol. Chem.*, 1982, **257**, 4426–4437.
- 118 I. Bertini, G. Cavallaro and A. Rosato, *Chem. Rev.*, 2006, **106**, 90–115.
- 119 X. Liu, C. N. Kim, J. Yang, R. Jemmerson and X. Wang, *Cell*, 1996, **86**, 147–157.
- 120 Y.-L. P. Ow, D. R. Green, Z. Hao and T. W. Mak, *Nat. Rev. Mol. Cell Biol.*, 2008, **9**, 532–542.
- 121 Y. Zhao, Z.-B. Wang and J.-X. Xu, *J. Biol. Chem.*, 2003, **278**, 2356–60.
- 122 U. Kappler and S. Bailey, *J. Biol. Chem.*, 2005, **280**, 24999–5007.
- 123 T. M. Cotton, S. G. Schultz and R. P. Van Duyne, *J. Am. Chem. Soc.*, 1980, **102**, 7960–7962.
- 124 M. R. Tarasevich and V. A. Bogdanovskaya, *Bioelectrochemistry Bioenerg.*, 1976, **3**, 589–595.
- 125 E. F. Bowden, F. M. Hawkridge and H. N. Blount, *J. Electroanal. Chem. Interfacial Electrochem.*, 1984, **161**, 355–376.
-

-
- 126 R. S. Nicholson and I. Shain, *Anal. Chem.*, 1964, **36**, 706–723.
- 127 D. E. Reed and F. M. Hawkrige, *Anal. Chem.*, 1987, **59**, 2334–2339.
- 128 P. Yeh and T. Kuwana, *Chem. Lett.*, 1977, **6**, 1145–1148.
- 129 M. J. Eddowes and H. A. O. Hill, *J. Chem. Soc. Chem. Commun.*, 1977, 771b.
- 130 I. Taniguchi, T. Murakami, K. Toyosawa, H. Yamaguchi and K. Yasukouchi, *J. Electroanal. Chem. Interfacial Electrochem.*, 1982, **131**, 397–401.
- 131 P. M. Allen, H. Allen, O. Hill and N. J. Walton, *J. Electroanal. Chem. Interfacial Electrochem.*, 1984, **178**, 69–86.
- 132 F. Lisdat, B. Ge and F. W. Scheller, *Electrochem. commun.*, 1999, **1**, 65–68.
- 133 S. Song, R. A. Clark, E. F. Bowden and M. J. Tarlov, *J. Phys. Chem.*, 1993, **97**, 6564–6572.
- 134 M. J. Tarlov and E. F. Bowden, *J. Am. Chem. Soc.*, 1991, **113**, 1847–1849.
- 135 P. L. Dutton, D. F. Wilson and C.-P. Lee, *Biochemistry*, 1970, **9**, 5077–5082.
- 136 J. Vanderkooi and M. Erecińska, *Arch. Biochem. Biophys.*, 1974, **162**, 385–391.
- 137 A. Avila, B. W. Gregory, K. Niki and T. M. Cotton, *J. Phys. Chem. B*, 2000, **104**, 2759–2766.
- 138 Z. Qiang Feng, S. Imabayashi, T. Kakiuchi and K. Niki, *J. Chem. Soc. Faraday Trans.*, 1997, **93**, 1367–1370.
- 139 J. Wei, H. Liu, D. E. Khoshtariya, H. Yamamoto, A. Dick and D. H. Waldeck, *Angew. Chemie - Int. Ed.*, 2002, **41**, 4700–4703.
- 140 K. Niki, W. R. Hardy, M. G. Hill, H. Li, J. R. Sprinkle, E. Margoliash, K. Fujita, R. Tanimura, N. Nakamura, H. Ohno, J. H. Richards and H. B. Gray, *J. Phys. Chem. B*, 2003, **107**, 9947–9949.
- 141 D. H. Murgida and P. Hildebrandt, *J. Am. Chem. Soc.*, 2001, **123**, 4062–4068.
- 142 H. Yue, D. Khoshtariya, D. H. Waldeck, J. Grochol, P. Hildebrandt and D. H. Murgida, *J. Phys. Chem. B*, 2006, **110**, 19906–13.
- 143 W. Scheller, W. Jin, E. Ehrentreich-Förster, B. Ge, F. Lisdat, R. Büttemeier, U. Wollenberger and F. W. Scheller, *Electroanalysis*, 1999, **11**, 703–706.
- 144 B. Ge and F. Lisdat, *Anal. Chim. Acta*, 2002, **454**, 53–64.
- 145 J. Wei, H. Liu, A. R. Dick, H. Yamamoto, Y. He and D. H. Waldeck, *J. Am. Chem. Soc.*, 2002, **124**, 9591–9599.
-

-
- 146 H. Ju, S. Liu, B. Ge, F. Lisdat and F. W. Scheller, *Electroanalysis*, 2002, **14**, 141–147.
- 147 C. XIANG, Y. ZOU, L. SUN and F. XU, *Talanta*, 2007, **74**, 206–211.
- 148 Y.-C. Liu, S.-Q. Cui, J. Zhao and Z.-S. Yang, *Bioelectrochemistry*, 2007, **70**, 416–420.
- 149 A. Zhu, Y. Tian, H. Liu and Y. Luo, *Biomaterials*, 2009, **30**, 3183–3188.
- 150 F. A. Armstrong, A. M. Bond, H. A. O. Hill, I. S. M. Psalti and C. G. Zoski, *J. Phys. Chem.*, 1989, **93**, 6485–6493.
- 151 F. A. Armstrong, A. M. Bond, H. A. O. Hill, B. N. Oliver and I. S. M. Psalti, *J. Am. Chem. Soc.*, 1989, **111**, 9185–9189.
- 152 M. Eguílaz, L. Agüí, P. Yáñez-Sedeño and J. M. Pingarrón, *J. Electroanal. Chem.*, 2010, **644**, 30–35.
- 153 G.-C. Zhao, Z.-Z. Yin, L. Zhang and X.-W. Wei, *Electrochem. commun.*, 2005, **7**, 256–260.
- 154 J.-F. Wu, M.-Q. Xu and G.-C. Zhao, *Electrochem. commun.*, 2010, **12**, 175–177.
- 155 X. Zuo, S. He, D. Li, C. Peng, Q. Huang, S. Song and C. Fan, *Langmuir*, 2010, **26**, 1936–1939.
- 156 K.-P. Lee, A. I. Gopalan and S. Komathi, *Sensors Actuators B Chem.*, 2009, **141**, 518–525.
- 157 L. Zhang, *Biosens. Bioelectron.*, 2008, **23**, 1610–1615.
- 158 A. F. Runge and S. S. Saavedra, *Langmuir*, 2003, **19**, 9418–9424.
- 159 A. El Kasmi, M. C. Leopold, R. Galligan, R. T. Robertson, S. S. Saavedra, K. El Kacemi and E. F. Bowden, *Electrochem. commun.*, 2002, **4**, 177–181.
- 160 T. Daido and T. Akaike, *J. Electroanal. Chem.*, 1993, **344**, 91–106.
- 161 S. Frasca, T. von Graberg, J. J. Feng, A. Thomas, B. M. Smarsly, I. M. Weidinger, F. W. Scheller, P. Hildebrandt and U. Wollenberger, *ChemCatChem*, 2010, **2**, 839–845.
- 162 D. Schaming, C. Renault, R. T. Tucker, S. Lau-Truong, J. Aubard, M. J. Brett, V. Balland and B. Limoges, *Langmuir*, 2012, **28**, 14065–72.
- 163 X. Xu, B. Z. Tian, J. L. Kong, S. Zhang, B. H. Liu and D. Y. Zhao, *Adv. Mater.*, 2003, **15**, 1932–1936.
- 164 Z. Dai, S. Liu and H. Ju, *Electrochim. Acta*, 2004, **49**, 2139–2144.
- 165 P. Kwan, D. Schmitt, A. M. Volosin, C. L. McIntosh, D.-K. Seo and A. K. Jones, *Chem. Commun.*, 2011, **47**, 12367.
-

-
- 166 V. Müller, J. Rathousky and D. Fattakhova-Rohlfing, *Electrochim. Acta*, 2014, **116**, 1–8.
- 167 R. Geng, G. Zhao, M. Liu and M. Li, *Biomaterials*, 2008, **29**, 2794–2801.
- 168 E. Topoglidis, Y. Astuti, F. Duriaux, M. Grätzel and J. R. Durrant, *Langmuir*, 2003, **19**, 6894–6900.
- 169 X. Zhang, J. Wang, W. Wu, S. Qian and Y. Man, *Electrochem. commun.*, 2007, **9**, 2098–2104.
- 170 R. K. Gupta and A. G. Redfield, *Science (80-.)*, 1970, **169**, 1204–1206.
- 171 R. K. Gupta, *Biochim. Biophys. Acta - Bioenerg.*, 1973, **292**, 291–295.
- 172 D. W. Dixon, X. Hong and S. E. Woehler, *Biophys. J.*, 1989, **56**, 339–351.
- 173 S. M. Andrew, K. A. Thomasson and S. H. Northrup, *J. Am. Chem. Soc.*, 1993, **115**, 5516–5521.
- 174 D. W. Concar, H. A. O. Hill, G. R. Moore, D. Whitford and R. J. P. Williams, *FEBS Lett.*, 1986, **206**, 15–19.
- 175 M. K. Beissenhirtz, F. W. Scheller, W. F. M. Stöcklein, D. G. Kurth, H. Möhwald and F. Lisdat, *Angew. Chem. Int. Ed. Engl.*, 2004, **43**, 4357–60.
- 176 D. Sarauli, J. Tanne, C. Xu, B. Schulz, L. Trnkova and F. Lisdat, *Phys. Chem. Chem. Phys.*, 2010, **12**, 14271–7.
- 177 S. M. Bonk and F. Lisdat, *Biosens. Bioelectron.*, 2009, **25**, 739–44.
- 178 D. Sarauli, J. Tanne, D. Schäfer, I. W. Schubart and F. Lisdat, *Electrochem. commun.*, 2009, **11**, 2288–2291.
- 179 S. C. Feifel and F. Lisdat, *J. Nanobiotechnology*, 2011, **9**, 59.
- 180 S. C. Feifel and F. Lisdat, *J. Nanobiotechnology*, 2011, **9**, 59.
- 181 R. E. McGovern, S. C. Feifel, F. Lisdat and P. B. Crowley, *Angew. Chemie - Int. Ed.*, 2015, **54**, 6356–6359.
- 182 F. Wegerich, P. Turano, M. Allegrozzi, H. Möhwald and F. Lisdat, *Langmuir*, 2011, **27**, 4202–11.
- 183 S. C. Feifel, A. Kapp and F. Lisdat, *Langmuir*, 2014, **30**, 5363–7.
- 184 S. C. Feifel, R. Ludwig, L. Gorton and F. Lisdat, *Langmuir*, 2012, **28**, 9189–9194.
- 185 C. Wettstein, K. Kano, D. Schäfer, U. Wollenberger and F. Lisdat, *Anal. Chem.*, 2016, **88**, 6382–6389.
-

-
- 186 R. Dronov, D. G. Kurth, H. Möhwald, R. Spricigo, S. Leimkühler, U. Wollenberger, K. V. Rajagopalan, F. W. Scheller and F. Lisdat, *J. Am. Chem. Soc.*, 2008, **130**, 1122–1123.
- 187 R. Spricigo, R. Dronov, F. Lisdat, S. Leimkühler, F. W. Scheller and U. Wollenberger, *Anal. Bioanal. Chem.*, 2009, **393**, 225–233.
- 188 S. C. Feifel, A. Kapp, R. Ludwig and F. Lisdat, *Angew. Chemie - Int. Ed.*, 2014, **53**, 5676–5679.
- 189 I. Willner and E. Katz, *Angew. Chem. Int. Ed. Engl.*, 2000, **39**, 1180–1218.
- 190 W. Schuhmann, *Rev. Mol. Biotechnol.*, 2002, **82**, 425–441.
- 191 K. Nguyen and B. D. Bruce, *Biochim. Biophys. Acta*, 2014, **1837**, 1553–66.
- 192 F. Wang, X. Liu and I. Willner, *Adv. Mater.*, 2013, **25**, 349–77.
- 193 A. Badura, T. Kothe, W. Schuhmann and M. Rögner, *Energy Environ. Sci.*, 2011, **4**, 3263.
- 194 P. N. Ciesielski, D. E. Cliffel and G. K. Jennings, *J. Phys. Chem. A*, 2011, **115**, 3326–34.
- 195 I. Lee, J. Lee and E. Greenbaum, *Phys. Rev. Lett.*, 1997, **79**, 3294–3297.
- 196 H. A. Kincaid, T. Niedringhaus, M. Ciobanu, D. E. Cliffel and G. K. Jennings, *Langmuir*, 2006, **22**, 8114–20.
- 197 B. S. Ko, B. Babcock, G. K. Jennings, S. G. Tilden, R. R. Peterson, D. Cliffel and E. Greenbaum, *Langmuir*, 2004, **20**, 4033–38.
- 198 M. Ciobanu, H. A. Kincaid, V. Lo, A. D. Dukes, G. Kane Jennings and D. E. Cliffel, *J. Electroanal. Chem.*, 2007, **599**, 72–78.
- 199 D. Mukherjee, M. Vaughn, B. Khomami and B. D. Bruce, *Colloids Surf. B. Biointerfaces*, 2011, **88**, 181–90.
- 200 D. Mukherjee, M. May, M. Vaughn, B. D. Bruce and B. Khomami, *Langmuir*, 2010, **26**, 16048–54.
- 201 A. K. Manocchi, D. R. Baker, S. S. Pendley, K. Nguyen, M. M. Hurley, B. D. Bruce, J. J. Sumner and C. A. Lundgren, *Langmuir*, 2013, **29**, 2412–9.
- 202 L. Frolov, O. Wilner, C. Carmeli and I. Carmeli, *Adv. Mater.*, 2008, **20**, 263–266.
- 203 C. J. Faulkner, S. Lees, P. N. Ciesielski, D. E. Cliffel and G. K. Jennings, *Langmuir*, 2008, **24**, 8409–12.
- 204 P. N. Ciesielski, A. M. Scott, C. J. Faulkner, B. J. Berron, D. E. Cliffel and G. K. Jennings, *ACS Nano*, 2008, **2**, 2465–72.
-

-
- 205 N. Terasaki, N. Yamamoto, T. Hiraga, I. Sato, Y. Inoue and S. Yamada, *Thin Solid Films*, 2006, **499**, 153–156.
- 206 N. Terasaki, N. Yamamoto, T. Hiraga, Y. Yamanoi, T. Yonezawa, H. Nishihara, T. Ohmori, M. Sakai, M. Fujii, A. Tohri, M. Iwai, Y. Inoue, S. Yoneyama, M. Minakata and I. Enami, *Angew. Chem. Int. Ed. Engl.*, 2009, **48**, 1585–7.
- 207 N. Terasaki, N. Yamamoto, K. Tamada, M. Hattori, T. Hiraga, A. Tohri, I. Sato, M. Iwai, M. Iwai, S. Taguchi, I. Enami, Y. Inoue, Y. Yamanoi, T. Yonezawa, K. Mizuno, M. Murata, H. Nishihara, S. Yoneyama, M. Minakata, T. Ohmori, M. Sakai and M. Fujii, *Biochim. Biophys. Acta - Bioenerg.*, 2007, **1767**, 653–659.
- 208 N. Terasaki, N. Yamamoto, M. Hattori, N. Tanigaki, T. Hiraga, K. Ito, M. Konno, M. Iwai, Y. Inoue, S. Uno and K. Nakazato, *Langmuir*, 2009, **25**, 11969–74.
- 209 A. Efrati, O. Yehezkeli, R. Tel-Vered, D. Michaeli, R. Nechushtai and I. Willner, *ACS Nano*, 2012, **6**, 9258–66.
- 210 O. Yehezkeli, O. I. Wilner, R. Tel-Vered, D. Roizman-Sade, R. Nechushtai and I. Willner, *J. Phys. Chem. B*, 2010, **114**, 14383–8.
- 211 O. Yehezkeli, R. Tel-Vered, D. Michaeli, R. Nechushtai and I. Willner, *Small*, 2013, **9**, 1–9.
- 212 E. A. Gizzie, G. LeBlanc, G. K. Jennings and D. E. Cliffel, *ACS Appl. Mater. Interfaces*, 2015, **7**, 9328–9335.
- 213 D. R. Baker, R. F. Simmerman, J. J. Sumner, B. D. Bruce and C. A. Lundgren, *Langmuir*, 2014, **30**, 13650–5.
- 214 A. Badura, D. Guschin, T. Kothe, M. J. Kopczak, W. Schuhmann and M. Rögner, *Energy Environ. Sci.*, 2011, **4**, 2435.
- 215 F. Zhao, K. Sliozberg, M. Rogner, N. Plumere and W. Schuhmann, *J. Electrochem. Soc.*, 2014, **161**, H3035–H3041.
- 216 T. Kothe, S. Pöller, F. Zhao, P. Fortgang, M. Rögner, W. Schuhmann and N. Plumeré, *Chemistry*, 2014, **20**, 11029–34.
- 217 G. LeBlanc, G. Chen, E. a Gizzie, G. K. Jennings and D. E. Cliffel, *Adv. Mater.*, 2012, **24**, 5959–62.
- 218 L. Frolov, Y. Rosenwaks, S. Richter, C. Carmeli and I. Carmeli, *J. Phys. Chem. C*, 2008, **112**, 13426–13430.
- 219 V. V. Nikandrov, Y. V. Borisova, E. A. Bocharov, M. A. Usachev, G. V. Nizova, V. A. Nadtochenko, E. P. Lukashev, B. V. Trubitsin, A. N. Tikhonov, V. N. Kurashov, M. D. Mamedov and A. Y. Semenov, *High Energy Chem.*, 2012, **46**, 200–205.
- 220 A. Mershin, K. Matsumoto, L. Kaiser, D. Yu, M. Vaughn, M. K. Nazeeruddin, B. D. Bruce, M. Graetzel and S. Zhang, *Sci. Rep.*, 2012, **2**, 234.
-

-
- 221 I. Carmeli, M. Mangold, L. Frolov, B. Zebli, C. Carmeli, S. Richter and A. W. Holleitner, *Adv. Mater.*, 2007, **19**, 3901–3905.
- 222 D. Gunther, G. LeBlanc, D. Prasai, J. R. Zhang, D. E. Cliffl, K. I. Bolotin and G. K. Jennings, *Langmuir*, 2013, **29**, 4177–80.
- 223 G. LeBlanc, K. M. Winter, W. B. Crosby, G. K. Jennings and D. E. Cliffl, *Adv. Energy Mater.*, 2014, **4**, 1301953.
- 224 E. Darby, G. LeBlanc, E. A. Gizzie, K. M. Winter, G. K. Jennings and D. E. Cliffl, *Langmuir*, 2014, **30**, 8990–4.
- 225 H. O'Neill and E. Greenbaum, *Chem. Mater.*, 2005, **17**, 2654–2661.
- 226 G. Chen, G. LeBlanc, G. K. Jennings and D. E. Cliffl, *J. Electrochem. Soc.*, 2013, **160**, H315–H320.
- 227 J. C. Beam, G. LeBlanc, E. A. Gizzie, B. L. Ivanov, D. R. Needell, M. J. Shearer, G. K. Jennings, C. M. Lukehart and D. E. Cliffl, *Langmuir*, 2015, **31**, 10002–10007.
- 228 V. B. Shah, W. R. Henson, T. S. Chadha, G. Lakin, H. Liu, R. E. Blankenship and P. Biswas, *Langmuir*, 2015, **31**, 1675–82.
- 229 A. Efrati, R. Tel-Vered, D. Michaeli, R. Nechushtai and I. Willner, *Energy Environ. Sci.*, 2013, **6**, 2950.
- 230 T. Kothe, N. Plumeré, A. Badura, M. M. Nowaczyk, D. A. Guschin, M. Rögner and W. Schuhmann, *Angew. Chem. Int. Ed. Engl.*, 2013, **52**, 14233–6.
- 231 V. Hartmann, T. Kothe, S. Pöller, E. El-Mohsnawy, M. M. Nowaczyk, N. Plumeré, W. Schuhmann and M. Rögner, *Phys. Chem. Chem. Phys.*, 2014, **16**, 11936–41.
- 232 M. Ihara, H. Nishihara, K.-S. Yoon, O. Lenz, B. Friedrich, H. Nakamoto, K. Kojima, D. Honma, T. Kamachi and I. Okura, *Photochem. Photobiol.*, 2006, **82**, 676–682.
- 233 L. M. Utschig, S. C. Silver, K. L. Mulfort and D. M. Tiede, *J. Am. Chem. Soc.*, 2011, **133**, 16334–16337.
- 234 L. M. Utschig, N. M. Dimitrijevic, O. G. Poluektov, S. D. Chemerisov, K. L. Mulfort and D. M. Tiede, *J. Phys. Chem. Lett.*, 2011, **2**, 236–241.
- 235 C. E. Lubner, A. M. Applegate, P. Knorzer, A. Ganago, D. A. Bryant, T. Happe and J. H. Golbeck, *Proc. Natl. Acad. Sci.*, 2011, **108**, 20988–20991.
- 236 H. Krassen, A. Schwarze, B. Friedrich, K. Ataka, O. Lenz and J. Heberle, *ACS Nano*, 2009, **3**, 4055–61.
- 237 F. Zhao, F. Conzuelo, V. Hartmann, H. Li, M. M. Nowaczyk, N. Plumeré, M. Rögner and W. Schuhmann, *J. Phys. Chem. B*, 2015, **119**, 13726–31.
- 238 R. Das, P. J. Kiley, M. Segal, J. Norville, a. A. Yu, L. Wang, S. a. Trammell, L. E.
-

- Reddick, R. Kumar, F. Stellacci, N. Lebedev, J. Schnur, B. D. Bruce, S. Zhang and M. Baldo, *Nano Lett.*, 2004, **4**, 1079–1083.
- 239 P. I. Gordiichuk, G.-J. A. H. Wetzelaer, D. Rimmerman, A. Gruszka, J. W. de Vries, M. Saller, D. A. Gautier, S. Catarci, D. Pesce, S. Richter, P. W. M. Blom and A. Herrmann, *Adv. Mater.*, 2014, **26**, 4863–4869.
- 240 E. A. Gizzie, J. Scott Niezgoda, M. T. Robinson, A. G. Harris, G. Kane Jennings, S. J. Rosenthal and D. E. Cliffler, *Energy Environ. Sci.*, 2015, **8**, 3572–3576.
- 241 K. Ocakoglu, T. Krupnik, B. van den Bosch, E. Harputlu, M. P. Gullo, J. D. J. Olmos, S. Yildirimcan, R. K. Gupta, F. Yakuphanoglu, A. Barbieri, J. N. H. Reek and J. Kargul, *Adv. Funct. Mater.*, 2014, **24**, 7467–7477.
- 242 C. F. Meunier, X.-Y. Yang, J. C. Rooke and B.-L. Su, *ChemCatChem*, 2011, **3**, 476–488.
- 243 H. W. Trissl and C. Wilhelm, *Trends Biochem. Sci.*, 1993, **18**, 415–419.
- 244 A. Díaz-Quintana, W. Leibl, H. Bottin and P. Sétif, *Biochemistry*, 1998, **37**, 3429–39.
- 245 I. Carmeli, L. Frolov, C. Carmeli and S. Richter, *J. Am. Chem. Soc.*, 2007, **129**, 12352–12353.
- 246 X. Yan, C. J. Faulkner, G. K. Jennings and D. E. Cliffler, *Langmuir*, 2012, **28**, 15080–6.
- 247 S. Song and R. Clark, *J. Phys. ...*, 1993, **97**, 6564–6572.
- 248 F. Müh and A. Zouni, *Biochim. Biophys. Acta*, 2005, **1708**, 219–28.
- 249 F. Müh and A. Zouni, *Biochim. Biophys. Acta*, 2008, **1778**, 2298–307.
- 250 C. A. Kerfeld and D. W. Krogmann, *Annu. Rev. Plant Physiol. Plant Mol. Biol.*, 1998, **49**, 397–425.
- 251 V. Proux-Delrouyre, C. Demaille, W. Leibl, P. Sétif, H. Bottin and C. Bourdillon, *J. Am. Chem. Soc.*, 2003, **125**, 13686–92.
- 252 L. Malmgren, Y. Olsson, T. Olsson and K. Kristensson, *Brain Res.*, 1978, **153**, 477–493.
- 253 A. T. Brunger, P. D. Adams, P. Fromme, R. Fromme, M. Levitt and G. F. Schröder, *Structure*, 2012, **20**, 957–966.
- 254 N. A. Baker, D. Sept, S. Joseph, M. J. Holst and J. A. McCammon, *Proc. Natl. Acad. Sci.*, 2001, **98**, 10037–10041.
- 255 M. Holst and F. Saied, *J. Comput. Chem.*, 1993, **14**, 105–113.
- 256 M. J. Holst and F. Saied, *J. Comput. Chem.*, 1995, **16**, 337–364.

-
- 257 F. Lisdat, R. Dronov, H. Möhwald, F. W. Scheller and D. G. Kurth, *Chem. Commun. (Camb.)*, 2009, 274–83.
- 258 A. Sassolas, L. J. Blum and B. D. Leca-Bouvier, *Biotechnol. Adv.*, 2012, **30**, 489–511.
- 259 N. Czechowski, H. Lokstein, D. Kowalska, K. Ashraf, R. J. Cogdell and S. Mackowski, *Appl. Phys. Lett.*, 2014, **105**, 43701.
- 260 X. Dominguez-Benetton, S. Srikanth, Y. Satyawali, K. Vanbroekhoven and D. Pant, *J. Microb. Biochem. Technol.*, 2013, **S6**, 7.
- 261 D. Leech, P. Kavanagh and W. Schuhmann, *Electrochim. Acta*, 2012, **84**, 223–234.
- 262 A. Operamolla, R. Ragni, F. Milano, R. Roberto Tangorra, A. Antonucci, A. Agostiano, M. Trotta and G. Farinola, *J. Mater. Chem. C*, 2015, **3**, 6471–6478.
- 263 N. Plumeré, *Nat. Nanotechnol.*, 2012, **7**, 616–7.
- 264 R. A. Grimme, C. E. Lubner, D. A. Bryant and J. H. Golbeck, *J. Am. Chem. Soc.*, 2008, **130**, 6308–9.
- 265 R. A. Grimme, C. E. Lubner and J. H. Golbeck, *Dalton Trans.*, 2009, 10106–13.
- 266 S. C. Feifel, K. R. Stieger, H. Lokstein, H. Lux and F. Lisdat, *J. Mater. Chem. A*, 2015, **3**, 12188–12196.
- 267 K. R. Stieger, S. C. Feifel, H. Lokstein and F. Lisdat, *Phys. Chem. Chem. Phys.*, 2014, **16**, 15667–74.
- 268 F. Zhao, F. Conzuelo, V. Hartmann, H. Li, M. M. Nowaczyk, N. Plumeré, M. Rögner and W. Schuhmann, *J. Phys. Chem. B*, 2015, **119**, 13726–31.
- 269 P. N. Ciesielski, C. J. Faulkner, M. T. Irwin, J. M. Gregory, N. H. Tolk, D. E. Cliffel and G. K. Jennings, *Adv. Funct. Mater.*, 2010, **20**, 4048–4054.
- 270 C. Wettstein, H. Möhwald and F. Lisdat, *Bioelectrochemistry*, 2012, **88**, 97–102.
- 271 S. C. Feifel, A. Kapp, R. Ludwig, L. Gorton and F. Lisdat, *RSC Adv.*, 2013, **3**, 3428.
- 272 J. Kern, B. Loll, C. Lüneberg, D. DiFiore, J. Biesiadka, K.-D. Irrgang and A. Zouni, *Biochim. Biophys. Acta*, 2005, **1706**, 147–57.
- 273 C. Wettstein, C. Kyne, A. M. Doolan, H. Möhwald, P. B. Crowley and F. Lisdat, *Nanoscale*, 2014, **6**, 13779–86.
- 274 H. Xie, D. Yang, A. Heller and Z. Gao, *Biophys. J.*, 2007, **92**, L70-2.
- 275 E. Y. Katz, Y. N. Kozlov and B. A. Kiselev, *Energy Convers.*, 1979, **19**, 73–75.
- 276 T. Fujii, E. Yokoyama, K. Inoue and H. Sakurai, *Biochim. Biophys. Acta - Bioenerg.*, 1990, **1015**, 41–48.
-

-
- 277 T. Bennett, H. Niroomand, R. Pamu, I. Ivanov, D. Mukherjee and B. Khomami, *Phys. Chem. Chem. Phys.*, 2016, **18**, 8512–21.
- 278 K. R. Stieger, D. Ciornii, A. Kölsch, M. Hejazi, H. Lokstein, S. C. Feifel, A. Zouni and F. Lisdat, *Nanoscale*, 2016, **8**, 10695–10705.
- 279 G. LeBlanc, E. Gizzie, S. Yang, D. E. Cliffel and G. K. Jennings, *Langmuir*, 2014, **30**, 10990–11001.
- 280 D. Yu, M. Wang, G. Zhu, B. Ge, S. Liu and F. Huang, *Sci. Rep.*, 2015, **5**, 9375.
- 281 C. Kamidaki, T. Kondo, T. Noji, T. Itoh, A. Yamaguchi and S. Itoh, *J. Phys. Chem. B*, 2013, **117**, 9785–9792.
- 282 V. M. Friebe, J. D. Delgado, D. J. K. Swainsbury, J. M. Gruber, A. Chanaewa, R. Van Grondelle, E. Von Hauff, D. Millo, M. R. Jones and R. N. Frese, *Adv. Funct. Mater.*, 2016, **26**, 285–292.
- 283 D. Sarauli, K. Peters, C. Xu, B. Schulz, D. Fattakhova-Rohlfing and F. Lisdat, *ACS Appl. Mater. Interfaces*, 2014, **6**, 17887–93.
- 284 D. Sarauli, C. Xu, B. Dietzel, B. Schulz and F. Lisdat, *J. Mater. Chem. B*, 2014, **2**, 3196–3203.
- 285 S. Frasca, A. Molero Milan, A. Guet, C. Goebel, F. Pérez-Caballero, K. Stiba, S. Leimkühler, A. Fischer and U. Wollenberger, *Electrochim. Acta*, 2013, **110**, 172–180.
- 286 M. Kato, T. Cardona, A. W. Rutherford and E. Reisner, *J. Am. Chem. Soc.*, 2012, **134**, 8332–5.
- 287 D. Mersch, C. Y. Lee, J. Z. Zhang, K. Brinkert, J. C. Fontecilla-Camps, A. W. Rutherford and E. Reisner, *J. Am. Chem. Soc.*, 2015, **137**, 8541–9.
- 288 Z. O. Araci, A. F. Runge, W. J. Doherty and S. S. Saavedra, *J. Am. Chem. Soc.*, 2008, **130**, 1572–1573.
- 289 Y. Liu, K. Peters, B. Mandlmeier, A. Müller, K. Fominykh, J. Rathousky, C. Scheu and D. Fattakhova-rohlfig, *Electrochim. Acta*, 2014, **140**, 108–115.
- 290 E. Laviron, *J. Electroanal. Chem. Interfacial Electrochem.*, 1979, **101**, 19–28.
- 291 S. N. Luo, A. Kono, N. Nouchi and F. Shoji, *J. Appl. Phys.*, 2006, **100**, 113701.
- 292 O. Maneg, F. Malatesta, B. Ludwig and V. Drosou, *Biochim. Biophys. Acta - Bioenerg.*, 2004, **1655**, 274–281.
- 293 H. Witt, F. Malatesta, F. Nicoletti, M. Brunori and B. Ludwig, *Eur. J. Biochem.*, 1998, **251**, 367–373.
- 294 V. Drosou, F. Malatesta and B. Ludwig, *Eur. J. Biochem.*, 2002, **269**, 2980–2988.
-

-
- 295 H. Witt, *J. Biol. Chem.*, 1998, **273**, 5132–5136.
- 296 M. Rytomaa and P. K. J. Kinnunen, *J. Biol. Chem.*, 1995, **270**, 3197–3202.
- 297 W. Bialek, S. Krzywda, M. Jaskolski and A. Szczepaniak, *FEBS J.*, 2009, **276**, 4426–4436.
- 298 D. Kozakov, D. Beglov, T. Bohnuud, S. E. Mottarella, B. Xia, D. R. Hall and S. Vajda, *Proteins Struct. Funct. Bioinforma.*, 2013, **81**, 2159–2166.
- 299 D. Kozakov, R. Brenke, S. R. Comeau and S. Vajda, *Proteins Struct. Funct. Bioinforma.*, 2006, **65**, 392–406.
- 300 S. R. Comeau, D. W. Gatchell, S. Vajda and C. J. Camacho, *Bioinformatics*, 2004, **20**, 45–50.
- 301 J. Ridge Carter, D. R. Baker, T. Austin Witt and B. D. Bruce, *Photosynth. Res.*, 2016, **127**, 161–170.
- 302 P. N. Ciesielski, F. M. Hijazi, A. M. Scott, C. J. Faulkner, L. Beard, K. Emmett, S. J. Rosenthal, D. Cliffler and G. Kane Jennings, *Bioresour. Technol.*, 2010, **101**, 3047–53.
- 303 P. O. Saboe, C. E. Lubner, N. S. McCool, N. M. Vargas-Barbosa, H. Yan, S. Chan, B. Ferlez, G. C. Bazan, J. H. Golbeck and M. Kumar, *Adv. Mater.*, 2014, **26**, 7064–7069.
- 304 S. C. Feifel, K. R. Stieger, H. Lokstein, H. Lux and F. Lisdat, *J. Mater. Chem. A*, 2015, **3**, 12188–12196.
- 305 K. Peters, H. N. Lokupitiya, D. Sarauli, M. Labs, M. Pribil, J. Rathouský, A. Kuhn, D. Leister, M. Stefik and D. Fattakhova-Rohlfing, *Adv. Funct. Mater.*, 2016, 1–11.

Danksagung

Ich möchte den folgenden Personen für ihren vielfältigen Anteil an meiner Doktorarbeit danken:

- **Prof. Dr. Fred Lisdat** für die äußerst kompetente, fachliche Unterstützung und intensive Betreuung während meiner Promotion, für die hilfreichen und zielbringenden Diskussionen rund um ein vielschichtiges Promotionsthema, der umfassenden Auseinandersetzung mit der Dissertationsschrift, als auch den gemeinsamen Publikationen, aber auch der konstruktiven Kritik in persönlichen Gesprächen, besonders aber für den Einsatz seiner Zeit.
- **Prof. Dr. Athina Zouni** für ihren fachlichen und menschlichen Rat, ihre immer offen stehende Tür für persönliche Fragen, aber auch für unsere gelungene Zusammenarbeit, ohne welche die gemeinsamen wissenschaftlichen Erfolge nicht denkbar gewesen wären.
- **Prof. Dr. Holger Dobbek** und **Prof. Dr. Frank Bier** für die unkomplizierte Bereitstellung ihrer Zeit zur Begutachtung meiner Dissertation.
- **Dr. Sven Feifel** für seinen fachlichen Rat bzw. seiner hilfreichen, sowie konstruktiven Kritik, der stets offenen Tür für alle Belange meiner Arbeit, sowie persönlichen Problemen und für das fachkritische Korrekturlesen.
- **Marc Riedel** für unsere Abendstunden ohne Bier, dafür aber mit äußerst fachlichen Diskussionen am S-Bahnhof Frankfurter Allee und für unsere Kreativ-„Frei“-tage, aus denen so manche innovative Idee entsprungen ist.
- Dem Feinschmecker, **Dmitri Ciornii** für seinen exquisiten Gaumen, seinem positiven und freundschaftlichen Charakter und für stets heitere Momente in der Kaffeeküche.
- **Mahdi Hejazi**, **Adrian Kölsch** und **Heiko Lokstein** für die Bereitstellung der qualitativ hochwertigen Proteine, insbesondere des Photosystem I. Ihnen danke ich für die gelungene Zusammenarbeit im Projekt, sowie für die experimentellen Beiträge zu unseren Publikationen.
- Der gesamten Abteilung Biosystemtechnik, die nicht nur für ein entspanntes Arbeitsklima sorgten, sondern mich moralisch und fachlich unterstützten. **Andreas Wiese**, **Dr. Christoph Wettstein** und **Arthur Fandrich** danke ich für die nette, produktive Atmosphäre im Büro, die auch häufig sehr lustige Momente hatte. **Gero Göbel** für viele interessante, politische Diskussionen, sowie das gemeinsame

Grübeln über Problemstellungen. **Dr. Anke Renger** und **Dr. David Sarauli** für ihre Motivation und Erfahrungen in Hinblick auf persönliche Zukunftsaussichten. **Daniel Schäfer** für einen unkomplizierten Ablauf im Laboralltag und der Hilfestellung bei allen technischen Fragen. **Andreas Kapp** für seine gute Seele und für viele schöne Stunden an der frischen Luft. Allen gilt mein Dank für die tatkräftige Unterstützung in verschiedenen Phasen und Bereichen meiner Promotion.

- Meiner Freundin **Sophie Melzer** für ihren vielfältigen persönlichen Einsatz in allen Bereichen meines Lebens. Besonders die Geschichte unseres Kennenlernens während meiner Promotionsphase und die darauffolgende gemeinsame Zeit versüßte mir meine Arbeit in der Promotion und wird mir immer als eines der wichtigsten Ereignisse meines Lebens in Erinnerung bleiben.
- Größtmöglicher Dank gilt meiner Familie, die mich in jeder erdenklichen Weise unterstützt hat. Ohne ihr andauerndes Vertrauen in mich und ihre Erfahrungen wäre ich in meinem Leben nicht bis an diesen Punkt gekommen.

Ehrenwörtliche Erklärung

Hiermit erkläre ich, die Dissertation selbstständig und nur unter Verwendung der angegebenen Hilfen und Hilfsmittel angefertigt zu haben. Ich habe mich anderwärts nicht um einen Doktorgrad beworben und besitze keinen entsprechenden Doktorgrad. Ich erkläre, dass ich die Dissertation oder Teile davon nicht bereits bei einer anderen wissenschaftlichen Einrichtung eingereicht habe und dass sie dort weder angenommen noch abgelehnt wurde. Ich erkläre die Kenntnisnahme der dem Verfahren zugrunde liegenden Promotionsordnung der Lebenswissenschaftlichen Fakultät der Humboldt-Universität zu Berlin vom 5. März 2015. Weiterhin erkläre ich, dass keine Zusammenarbeit mit gewerblichen Promotionsberaterinnen/-Promotionsberatern stattgefunden hat und dass die Grundsätze der Humboldt-Universität zu Berlin zur Sicherung guter wissenschaftlicher Praxis eingehalten wurden.

Ort, Datum

Unterschrift